



**HAL**  
open science

# 3D printed photonic circuits towards efficient and scalable integration of hybrid photonic platforms

Adrià Grabulosa

► **To cite this version:**

Adrià Grabulosa. 3D printed photonic circuits towards efficient and scalable integration of hybrid photonic platforms. Optics / Photonic. Université Bourgogne Franche-Comté, 2023. English. ⟨NNT : 2023UBFCD060⟩. ⟨tel-04478167v2⟩

**HAL Id: tel-04478167**

**<https://hal.science/tel-04478167v2>**

Submitted on 22 Mar 2024

HAL is a multi-disciplinary open access archive for the deposit and dissemination of scientific research documents, whether they are published or not. The documents may come from teaching and research institutions in France or abroad, or from public or private research centers.

L'archive ouverte pluridisciplinaire HAL, est destinée au dépôt et à la diffusion de documents scientifiques de niveau recherche, publiés ou non, émanant des établissements d'enseignement et de recherche français ou étrangers, des laboratoires publics ou privés.



HAL Authorization

**THÈSE DE DOCTORAT DE L'ÉTABLISSEMENT UNIVERSITÉ BOURGOGNE FRANCHE-COMTÉ**

**PRÉPARÉE À L'UNIVERSITÉ DE FRANCHE-COMTÉ**

École doctorale n°37

Sciences Pour l'Ingénieur et Microtechniques

Doctorat d'Optique et Photonique

par

**ADRIÀ GRABULOSA I VALLMAJÓ**

**3D printed photonic circuits towards efficient and scalable integration of  
hybrid photonic platforms**

Circuits photoniques imprimés en 3D pour une intégration efficace et évolutive des  
plates-formes photoniques hybrides

Thèse présentée et soutenue à Besançon, le 15 Décembre 2023

Composition du Jury :

COURVOISIER FRANÇOIS	Directeur de Recherche CNRS, Institut Femto-st	Président du jury
SUNADA SATOSHI	Professeur, Kanazawa University (Japan)	Rapporteur
MOSER CHRISTOPHE	Professeur, École polytechnique fédérale de Lausanne (EPFL)	Rapporteur
BRUNNER DANIEL	Chargé de Recherche CNRS, Institut Femto-st	Directeur de thèse



**Title:** 3D printed photonic circuits towards efficient and scalable integration of hybrid photonic platforms

**Keywords:** 3D photonic integration, 3D photonic waveguides, Additive fabrication, One-photon polymerization, Two-photon polymerization, CMOS compatibility

**Abstract:**

In the last decades, the prolonged miniaturization of modern electronic integrated circuits (ICs) has reached a fundamental limit at  $\sim 2$  nm feature sizes. At the same time, emerging computing concepts such as neural networks (NNs), which are already playing a major role in modern societies, further amplifying this challenge. The energy consumption required for communicating across dense and numerous channels is severely hampering further improvements in high-performing electronic ICs. However, most of today's leading-edge technologies leverages dense integration in two-dimensional (2D) silicon-based platforms, and adopting the third-dimension is a promising strategy for achieving scalability of connections over the microchip's dimensions. Here, based on additive one- (OPP) and two-photon polymerization (TPP) processes and combined with direct-laser writing (DLW) settings, a complete toolbox of optical components towards three-dimensional (3D) photonic integration is presented. A novel lithography configuration

leveraging OPP and TPP, i.e. *flash*-TPP, is developed for constructing single-mode air- and polymer-cladded photonic waveguides and splitters, all while boosting performances and reducing fabrication times by 90% compared to classical DLW-TPP methods. Crucially, this lithographic concept enables a monolithic and single-step fabrication, using commercially available photoresists, making the overall process fully compatible with CMOS platforms. This is validated by printing 3D photonic waveguides onto semiconductor (GaAs) substrates integrating quantum dot micro-lasers, demonstrating promising performances. This first-of-its-kind integrated hybrid device lays the foundation for scalable integration of multi-chip photonic and electronic platforms in hardware, which is challenging if not impossible in 2D. Overall, these building blocks are highly appealing for realizing fully-parallel and efficient communication throughout a densely-connected network, which are pivotal concepts for future NN computing topologies.

**Titre :** 3D printed photonic circuits towards efficient and scalable integration of hybrid photonic platforms

**Mots-clés :** Photonique intégrée 3D, Guides d'ondes photoniques en 3D, Fabrication additive, Polymérisation à un photon, Polymérisation à deux photons, Compatibilité CMOS

**Résumé :**

Ces dernières années, la miniaturisation des circuits intégrés électroniques modernes a atteint une limite fondamentale à 2 nm, tandis que de nouveaux concepts tels que les réseaux de neurones, qui jouent déjà un rôle majeur dans les sociétés modernes, amplifient encore ce défi. La quantité d'énergie utilisée pour la communication sur des canaux denses et multiples limite les améliorations des circuits électroniques à haute performance. Les technologies modernes sont basées sur des plates-formes bidimensionnelles (2D), et l'utilisation de la troisième dimension est une stratégie prometteuse pour réaliser des connexions efficaces dans de petits volumes. En utilisant les processus de polymérisation à un et deux photons avec des paramètres d'écriture directe par laser, une boîte à outils complète de composants optiques pour l'intégration photonique tridimensionnelle (3D) est présentée. Une nouvelle

configuration de lithographie nommé *flash*-TPP est développée pour construire des guides d'ondes photoniques et des séparateurs, tout en augmentant les performances et en réduisant les temps de fabrication de 90 %. Ce concept permet une fabrication monolithique et en une seule étape, en utilisant des résines photosensibles commerciales, ce qui rend le processus entièrement compatible avec plateformes CMOS. Cela a été confirmé par l'impression de guides d'ondes photoniques 3D sur des substrats semi-conducteurs intégrant des micro-lasers à points quantiques. Les composants optiques réalisés présentent des performances prometteuses pour réaliser une communication complètement parallèle et efficace à travers un réseau densément connecté, ce qui constitue un aspect fondamental pour les futurs réseaux de neurones.



# ACKNOWLEDGMENTS

I would like to thank my supervisor Daniel Brunner. He gave me the opportunity of joining his amazing research group, where I not only learnt about science, but always felt at home. I really value his unique way of leadership, in a work environment, but mostly in his personal approach, together with his wife Lidia and little Kiara. Thanks, Dani, for making me grow personal and academically, and for teaching me fancy words such as scalability, post-Turing and, my favourite, hallmark.

I also thank all the members of the group for their support during these years. Anas, Hajar, Nadia, Ria, Romain, Soro and Vova: it was a pleasure to work with you and share good moments in and outside the workplace. To Johnny and Xavi, you both taught me everything I know about 3D printing and optics. Special mention to Erik, even just for a short time, we had an amazing time playing table tennis during working hours and, sometimes, discussing about 3D waveguides. It would have been nice having you here for a longer time, but I wish you, Melle and little Jule the best.

To my mother, father, grandmothers, uncles and aunts: it is not easy to stay away from you, but knowing that I have your unconditional support and we will be always there for each other comforts me. Thanks for being the most important part of my life. I also miss walking you Lluna, your clumsiness while playing and your snoring.

This adventure would have not been the same without all the friends and mates in Besançon. To the latino, Erasmus and Femto crew, thank you for the memories, the several parties from night until early morning, hikes, barbecues and mutual teasing and annoying. Also, I would like to thank people with a shared passion for sports. I really enjoyed playing tennis and football (even after breaking my Aquiles tendon), it has been fundamental for having a balance between work and health.

To my friends in Catalunya, I miss spending time with you and the amazing moments we shared. I thank you for being a vital support and making every part of my living journey an absolutely amazing experience. I have been more absent than I should have, but you are the reason for who I am today. You all are the best family that one could choose.

Specially I would like to thank the amazing administration team at Femto-ST. Aline, Sarah and Valérie: your work is amazing, thanks for making an already stressful life for academic people easier. Without you, I would be still struggling to register for the first year of my PhD.

Last but not least, thank you Ria for spending your days with me, together. I couldn't have been luckier, even sharing half of our name, you really make me whole.

To all of you, *Gràcies*.



# PUBLICATIONS AND CONFERENCES

## Articles in international peer-reviewed journals

Grabulosa, A., Moughames, J., Porte, X., Kadic, M., Brunner, D., "Additive 3D photonic integration that is CMOS compatible", *Nanotechnology* **34**, 322002 (2023).

Grabulosa, A., Porte, X., Jung, E., Moughames, J., Kadic, M., Brunner, D., "(3+ 1)D printed adiabatic 1-to-M broadband couplers and fractal splitter networks", *Optics Express* **31**, 20256-20264 (2023).

Grabulosa, A., Porte, X., Moughames, J., Brunner, D., "Combining one and two photon polymerization for accelerated high performance (3+1)D photonic integration," *Nanophotonics* **11**, 1591 (2022).

## Invited international conferences

Grabulosa, A., Porte, X., Moughames, J., Brunner, D., "3D integration towards scalability for photonic neural network integration", *2nd workshop on Neuromorphic computing and applications, University of West Attica, Athens* (2023).

## International conferences

Grabulosa, A., Porte, X., Moughames, J., Brunner, D., "Combining (3+1)D printed photonic circuits and CMOS technology for future high-performance integration", *CLEO Europe, Munich* (2023).

Grabulosa, A., Porte, X., Moughames, J., Brunner, D., "3D printing towards the scalable and efficient integration of high- performance hybrid platforms", *EOSAM, Dijon* (2023).

Grabulosa, A., Porte, X., Moughames, J., Brunner, D., "(3+1)D printing towards the scalable and efficient integration of hybrid platforms", *JNOG, Lyon* (2023).

Grabulosa, A., Porte, X., Moughames, J., Brunner, D., "(3+1)D-printed adiabatic 1-to-N couplers", *SPIE Optics + Photonics, San Diego* (2022).

Grabulosa, A., Moughames, J., Porte, X., Brunner, D., "Three-dimensional two-photon polymerization: breakthrough towards scalable integration of photonic neural networks.", *SPIE Optics + Photonics, San Diego* (2021).

## Poster presentations

Grabulosa, A., Moughames, J., Porte, X., Brunner, D., “Next generation of 3D printed photonic circuits for scalability and high-performance hybrid integration.”, *NNPC*, Hannover (2023).

Grabulosa, A., Moughames, J., Porte, X., Brunner, D., “Three-dimensional two-photon polymerization: breakthrough towards scalable integration of photonic neural networks.”, *EPFL-Photonic Day*, Lausanne (2021).

## Workshops

Grabulosa, A., Moughames, J., Porte, X., Brunner, D., “Three-dimensional two-photon polymerization: breakthrough towards scalable integration of photonic neural networks.”, *Femto-ST Annual Seminar*, Sevenans (2021).

Grabulosa, A., Moughames, J., Porte, X., Brunner, D., “Three-dimensional two-photon polymerization: breakthrough towards scalable integration of photonic neural networks.”, *EPFL-Photonic Day*, Lausanne (2021).

# CONTENTS

<b>Acknowledgments</b>	<b>v</b>
<b>Publications and conferences</b>	<b>vii</b>
<b>Introduction</b>	<b>1</b>
<b>1 Towards scalable and CMOS compatible integration of photonic networks</b>	<b>5</b>
1.1 Scientific motivation: photonic neural networks . . . . .	6
1.1.1 2D/2.5D platforms for photonic integration . . . . .	8
1.1.1.1 On-chip neural network implementations . . . . .	10
1.1.2 3D photonic integration: state-of-the-art . . . . .	11
1.1.2.1 Other platforms for 3D photonic integration . . . . .	13
1.2 Theory of photonic waveguides . . . . .	15
1.2.1 Optical waveguide theory: ray analysis . . . . .	15
1.2.1.1 Total internal reflection . . . . .	16
1.2.1.2 Step- and graded-index profile waveguides . . . . .	17
1.2.1.3 Creation of modes . . . . .	18
1.2.2 Electromagnetic wave description of guided light . . . . .	21
1.2.2.1 Maxwell's equation . . . . .	21
1.2.2.2 Eigenmodes of step-index cylindrical waveguides . . . . .	22
1.2.2.3 Weakly-guiding approximation . . . . .	25
1.2.3 Optical coupling between waveguides . . . . .	26
1.2.3.1 Adiabatic tapers . . . . .	27
1.2.3.2 Coupling between waveguides . . . . .	28
1.3 3D photonic integration via photo-induced polymerization . . . . .	29
1.3.1 Photo-polymerization . . . . .	30
1.3.2 One-photon polymerization . . . . .	30
1.3.3 Two-photon polymerization induced via femtosecond pulses . . . . .	33
1.3.3.1 Direct-laser writing lithography . . . . .	35
1.3.4 Dynamic power range of photoresists . . . . .	37

1.3.5	Advantages and challenges of additive DLW-TPP fabrication . . . . .	39
1.3.6	DLW-TPP fabrication commercial system . . . . .	40
1.3.6.1	IP-resins overview . . . . .	40
1.3.6.2	Operational workflow . . . . .	41
1.3.7	(3+1)D printing of photonic waveguides . . . . .	43
1.3.8	Optical characterization . . . . .	45
<b>2</b>	<b>Flash-TPP: combining one- and two-photon polymerization</b>	<b>47</b>
2.1	Accelerate 3D waveguide printing with flash-TPP . . . . .	47
2.1.1	Two-photon polymerization fabrication parameters . . . . .	49
2.2	Flash-TPP waveguide properties . . . . .	52
2.2.1	Modal confinement . . . . .	52
2.2.2	Propagation and injection losses . . . . .	54
2.2.3	Temporal stability . . . . .	55
2.3	Flash-TPP printing time . . . . .	57
2.4	Conclusions and outlook . . . . .	58
<b>3</b>	<b>3D printed adiabatic 1 to M broadband couplers and fractal splitter networks</b>	<b>61</b>
3.1	3D adiabatic 1 to M couplers . . . . .	61
3.1.1	Design and fabrication . . . . .	62
3.1.2	Optical performance . . . . .	63
3.1.3	Broadband functionality . . . . .	66
3.2	Fractal networks of 3D splitters . . . . .	67
3.3	Conclusions and outlook . . . . .	69
<b>4</b>	<b>Single-mode and air-cladded waveguides for increased 3D photonic integration</b>	<b>71</b>
4.1	Analysis method for highly-confined waveguides . . . . .	72
4.2	Straight and tapered waveguides . . . . .	73
4.3	Curved waveguides: circular and Euler-bends . . . . .	74
4.3.1	Design and fabrication . . . . .	76
4.3.2	S-bends . . . . .	79
4.3.3	U-bends . . . . .	79
4.4	Air-cladded 3D splitters . . . . .	81
4.5	Conclusions and outlook . . . . .	83
<b>5</b>	<b>Interfacing 3D photonic circuits with semiconductor quantum dot micropillar</b>	

<b>arrays</b>	<b>85</b>
5.1 Quantum dot micro-cavity lasers . . . . .	86
5.2 Challenges of integrating DLW-TPP fabrication and semiconductor technology . . . . .	88
5.3 DLW-TPP fabrication on semiconductor substrates . . . . .	89
5.3.1 TPP fabrication parameter calibration . . . . .	89
5.3.2 Alignment protocol . . . . .	91
5.3.3 Optical reflection performance . . . . .	93
5.4 Optical pumping and emission of QDMLs via 3D waveguides . . . . .	94
5.4.1 Cryogenic system and optical characterization . . . . .	94
5.4.2 Optical pumping and emission of QDMLs performance . . . . .	97
5.4.3 Optical pumping and emission of QDMLs via 3D waveguides performance . . . . .	97
5.5 Conclusions and outlook . . . . .	99
<b>6 General conclusions and perspectives</b>	<b>101</b>
<b>Bibliography</b>	<b>105</b>



# INTRODUCTION

- **Adrià:** *Hello, how are you today?*
- **ChatGPT:** *Hello! I'm just a computer program, so I don't have feelings, but I'm here and ready to assist you. How can I help you today?*
- **Adrià:** *I will start by explaining my situation. I am writing the introduction of my PhD thesis about 3D photonic integration for applications in photonic neural networks and neuromorphic computing. In this thesis, we demonstrate some proof of concept regarding the fabrication of 3D photonic waveguides and splitters leveraging a process called two-photon polymerization (TPP). I am a bit short on time, and I need to finish the introduction as soon as possible. Could you tell me what should I include?*
- **ChatGPT:** *Of course, I'd be happy to help you outline the introduction for your PhD thesis on 3D photonic integration for applications in photonic neural networks and neuromorphic computing. The introduction is a critical part of your thesis, as it sets the stage for the entire document and provides context for your research. Here's a general structure and some key points to include:*
  1. *Begin with a Hook: start with an engaging opening statement or anecdote that piques the reader's interest and highlights the significance of your research.*
  2. *Background and Context: provide an overview of the broader field of photonics, emphasizing its importance in various technological applications. Discuss the limitations of current photonic systems and the need for advancements in 3D photonic integration.*
  3. *Problem Statement: clearly state the problem or challenge your research aims to address. In your case, it could be the limitations of traditional photonic components in the context of neuromorphic computing.*
  - ...
  10. *Transition to the Next Chapter: end the introduction by smoothly transitioning into the next chapter, which could be a literature review or the methodology section.*

*Remember to keep the introduction concise and focused while conveying the importance and novelty of your research. It should provide enough information to orient the reader without overwhelming them with details. Good luck with your PhD thesis!*
- **Adrià:** *Thank you! This is so helpful! Regarding the first point "Begin with a Hook": do you think it is a good idea to pick the reader's interest by showing our conversation and then discuss your performance as the state-of-the-art of a neural network?*
- **ChatGPT:** *Using our conversation as a hook in your thesis introduction is an innovative and engaging approach, especially if you want to highlight the advanced capabilities of natural language processing models like mine. However, you should*

*be cautious when comparing my performance to a "state-of-the-art" neural network. While I can generate human-like text and provide valuable information, I have limitations and may not be considered state-of-the-art in all natural language processing tasks. This approach can be effective in making your introduction more engaging, but be sure to strike a balance between the conversational hook and the technical content of your thesis. The transition should smoothly guide the reader into the main subject matter of your research.*

- **Adrià:** *Thank you! Let's hope this works for the thesis!*
- **ChatGPT:** *You're very welcome! I hope this approach indeed engages your thesis readers and sets a captivating tone for your research. If you have any more questions or need further assistance as you work on your thesis or any other aspect of your research, feel free to reach out. Best of luck with your PhD thesis on 3D photonic integration, and may your research be both impactful and well-received!*

These lines were generated on September 15th, 2023, less than 1 year since the world-wide release of Chat GPT by OpenAI (GPT-3.5 version, dated on November 30th, 2022). Chat GPT stands for Chat Generative Pre-trained Transformer. Based on artificial neural network (NN) architectures, its design is capable of processing and generate human-machine interaction for sequences of 'input' characters, including diverse spoken languages, programming languages, and mathematical equations [1]. GPT by OpenAI has rapidly (< 1 year de facto is fast) become an advantageous tool for multiple applications in fields such as economics, cybersecurity, education, financial markets, medicine, law and academic research [2]. For the latter, it has found to be potentially useful as a 'hook' to engage the reader's attention in this thesis.

While providing a tremendous boost in artificial intelligence (AI) conceptions and having currently over 100M users, OpenAI is expected to file for bankruptcy before the end of 2024 [3]. ChatGPT may be crucially useful, but it certainly is not cheap to run. The cost per query is estimated to be roughly 0.36 cents and the overall daily cost for GPT to operate increases to approximately 700.000 \$. Crucially, GPT-3 consumed 1287 MWh during training [4], with a corresponding electricity bill of 2M €, while the human brain operates at approximately 20 Wh. ChatGPT relies on a combination of high-performance CPU and GPU clusters, state-of-the-art deep learning models and advanced hardware in order to meet a rapidly increasing demand [5]. This also requires a massive amount of computing power, memory and resources to store all this large volume of data.

The birth of universal computation can be dated to the late 1930s, when the mathematician Alan Turing introduced a theoretical model known as the Turing machine, which states that any computable function is solvable by leveraging the concept of serial bits, sequentially executed digital logic as well as infinite memory [6, 7]. Several decades later, very important advances in Turing's ideas, their practical realization and an exponential sophistication of the machines have been achieved, so as to reach the impressive capabilities of the actual modern computers. Yet, his fundamental ideas are still the basis of the current computers, while AI and NN concepts are fundamentally different in terms of the required operations.

The traditional electronic computer differs fundamentally from the inherent topology of neural networks. Neural network architectures leverage extensive and simultaneous parallel connections between artificial neurons, i.e. nodes, whereas current computers adhere to the von Neumann architecture and predominantly operate in serial sequences.

Over the past 15 years, advances in computing power have primarily relied on augmenting the number of processors employed and the development of new hardware designed to enhance electronic parallelism. The major future hardware challenge for artificial NNs lies in achieving highly parallel connectivity, which, however, is currently and potentially fundamentally out of reach considering classical electronic integration approaches [8].

To this aim, the use of photons enables to potentially boost performances of present and future generations of photonic NNs. Unlike electrons, photons are not electrically charged particles and hence do not suffer from inductive or capacitive energy dissipation [9]. This fundamentally results in a reduction of latency, which limits the maximum rate at which information can be transmitted. In electronics, switching a wire consumes  $>1/2CV^2$ , while in optics it consumes only absorption losses which are an engineering problem. For telecommunications, the inherent properties of light are currently enabling the optical encoding and transmission of information through a single communication channel such as optical fibers, achieving remarkable data transfer rates. Additionally, the possibility of optically modulating information in, both, the temporal and spatial domains with minimal crosstalk opens new avenues towards enhancing connectivity parallelization.

Crucially, continued miniaturization in electronic integrated circuits (ICs) appears to have reached its fundamental limit at  $\approx 2$  nm feature sizes, making it increasingly challenging to enhance computing power by increasing the number of components per processor [10]. While not reaching the current capabilities in standard electronic ICs, photonic integration has significantly advanced. To ensure maximum compatibility and synergy with electronic systems, photonic integration based on silicon substrates emerged in the 1980s with the introduction of silicon waveguides [11, 12], which serve as the photonic counterparts to the metallic wires of electronic ICs. These predominantly rely on complementary metal-oxide-semiconductor (CMOS) technology, which primarily employs silicon as the semiconductor substrate. The fundamental importance of achieving CMOS compatibility is fundamental for the complete maturation of next-gen photonic ICs.

In this thesis, a novel approach is presented based on additive fabrication technology towards the scalable and efficient integration of photonic NNs. Via additive photo-induced polymerization of standard photo-resins, high-performing three-dimensional (3D) photonic circuits are demonstrated. An important application of such circuits is the interconnects of optical NNs, where 3D integration enables scalability in terms of network size versus overall geometric dimensions, which is challenging to address via standard two-dimensional (2D) platforms [13].

Chapter 1 serves as a general overview of pivotal concepts presented in this thesis such as the theoretical notion of photonic waveguides and diverse photo-induced fabrication methods. This further includes a basic description of the NN architecture and its operation principle. Crucially, the state-of-the-art of technology platforms leveraging 2D, 2.5D and 3D integration schemes for realizing NN computing are reviewed. The research output derived from activities conceived during this thesis is presented throughout Chapter 2, Chapter 3 and Chapter 4. Here, 3D printed air- and polymer-cladded photonic waveguides and optical splitters leveraging adiabatic coupling are constructed via one-photon polymerization (OPP) and two-photon polymerization (TPP) combined with direct-laser writing (DLW) of commercial photoresists, and their performances are further evaluated. The concept's CMOS compatibility is demonstrated in Chapter 5 by fabricating such polymer-based photonic ICs onto semiconductor (GaAs) substrates integrating quantum dot micro-lasers (QDMLs). Preliminary characterization of these structures shows encouraging perfor-

mance in terms of optical losses and mechanical stability. Lastly, Chapter 6 provides future perspectives of the demonstrated 3D photonic ICs, including preliminary guidelines towards their implementation in NN frameworks.

# TOWARDS SCALABLE AND CMOS COMPATIBLE INTEGRATION OF PHOTONIC NETWORKS

Today's cutting-edge technology relies on the intricate integration of 2D electronic circuits. However, these circuits are currently facing a multitude of challenges. The task of further enhancing the performance of 2D computing chips is becoming progressively more complex [14, 15]. Meanwhile, emerging platforms, particularly those related to NNs, artificial intelligence and data-driven computing, are posing a fundamental hurdle to the dominance of CMOS circuits. To sustain the remarkable technological advancements of recent decades, it is imperative to develop novel integration concepts and manufacturing techniques. Crucially, these novel concepts must acknowledge the fundamental characteristics that have established the success of 2D electronic ICs, and their compatibility towards hybrid integration is essential.

Raising a novel integration technology to a level comparable to that of 2D electronic ICs is a formidable and long-term undertaking. Ever since the initial demonstration of a planar 2D monolithic IC by Fairchild in 1957, this classical form of integration has been steadily advancing for over six decades, with contributions from across the globe. The success of this integration concept has facilitated decades of exponential growth in electronic ICs, with the number of transistors per chip doubling approximately every two years as described by Moore's law [10], see Fig. 1.1. Critically, while the transistor's size is reduced, its power density remains constant with a power consumption proportional to the chip's area, as described by Dennard scaling.

Likewise, as the world's population continuously increases, the number of internet users will correspondingly rise, presenting new infrastructural, technological, and environmental challenges, while exacerbating the current carbon footprint's concern [16]. Overcoming this barrier is crucial if the demand for increased processing power is to be met. The thermal energy dissipation derived from the switching of electronic signal lines represents a fundamental bottleneck for truly electronic 3D integration [9]. Photonics addresses this issue, and as a result, 3D photonic integration has become an immensely desirable technology. Its significance is growing rapidly, particularly in response to the demand for scalable application-specific ICs designed for NNs [17].

## 1.1/ SCIENTIFIC MOTIVATION: PHOTONIC NEURAL NETWORKS

Several decades have passed between the inception and the widespread exploration of NNs. Ever since the proposal of simple NNs in 1943 [18], the field has undergone numerous cycles of excitement and challenges before ultimately arriving at today's extensive interest and utilization [19]. Neural networks are fundamentally rooted in a connectionist approach to computation, a concept that was developed based on simplified features of biological neurons. Currently, NNs are driving a revolution across various domains of the economy, technology and society.

As schematically depicted in Fig. 1.2 (a), an NN is based on densely interconnecting a vast number of artificial neurons throughout layers. Conceptually, each neuron receives information from neurons in the previous layer as its input, performing a linear sum of these different input information channels to determine its own activation level. The activation of this neuron is further outputted via weighted channels to become the input of other neurons in the network. Typically, a non-linear monotonic function that saturates at 0 and 1 is used to determine the activation of the artificial neuron [20]. Importantly, all the artificial neurons simultaneously perform their transformations of input signals, creating an intrinsic link between NNs and parallelism. In doing so, it is possible to design computer systems capable of solving complicated tasks. For a network to be a computational tool, its topology must be structured appropriately, with weights and biases correctly adjusted during the learning process.

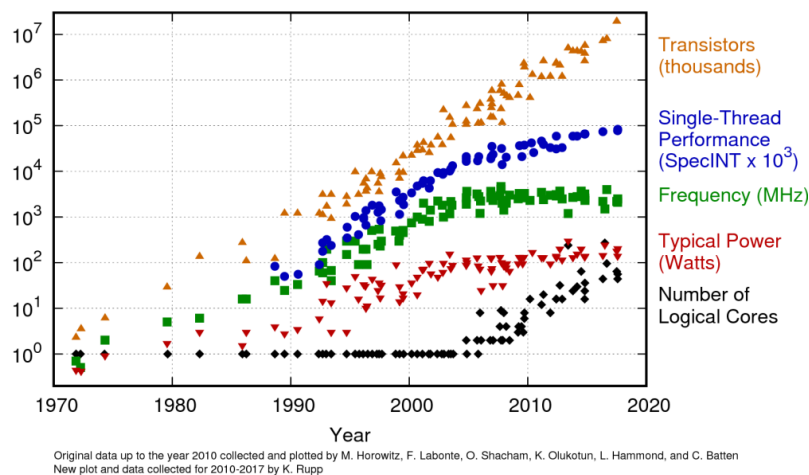


Figure 1.1: 42 years of microprocessor trend data comparing their relevant performance metrics, i.e. frequency (MHz), power consumption (Watts), number of transistors (thousands), number of logical cores and single-thread performance (SpecINT  $\cdot 10^3$ ). The trends reveal that the number of transistors per chip still double every two years (Moore's law), while several other performance metrics clearly stagnate [21].

Presently, easily accessible high-performance computing systems enable the emulation of powerful NN architectures, where connections are optimized through computationally intensive learning techniques like gradient back-propagation [22]. NNs are therefore currently excelling on scales never before witnessed [23, 24]. For instance, Google's most heavily employed NN model (MLP0) comprises five layers and approximately 20 million parameters, which implies around 2200 neurons in each layer [17]. Northwesterly, even significantly smaller networks with just two layers and 800 neurons in total can achieve

a remarkable 99% recognition rate in the well-known Modified National Institute of Standards and Technology (MNIST) database task [25].

However, creating electronic 3D circuits is intrinsically lossy, notably due to capacitive coupling and the associated energy dissipation when transmitting information along signalling wires in serial operation [26, 27]. Efficiently disposing of the energy dissipated by these circuits is a major bottleneck, even for the primarily serial and 2D von Neumann processors [28]. Likewise, electronic connections suffer from harsh trade-offs between bandwidth and interconnectivity, which limits the development of high-speed communications. At present, NN computing concepts are therefore emulated, leading to significant energy consumption and speed overheads. Future NN circuits that aim to eliminate these overheads necessitate ICs with a significantly higher degree of connectivity, meaning a greater number of connections for transmitting signals across the chip.

Photonics can address the issues related to heat dissipation and provide an efficient means of interconnecting NN components [29]. The multiple dimensions of light, i.e. wavelength, polarization, and spatial mode, enable multiple feasible strategies for multiplexing the numerous parallel connections of an NN. It allows for the incorporation of all-optical and electro-optical components as neurons, and the 3D photonic interconnect can be realized through various methods.

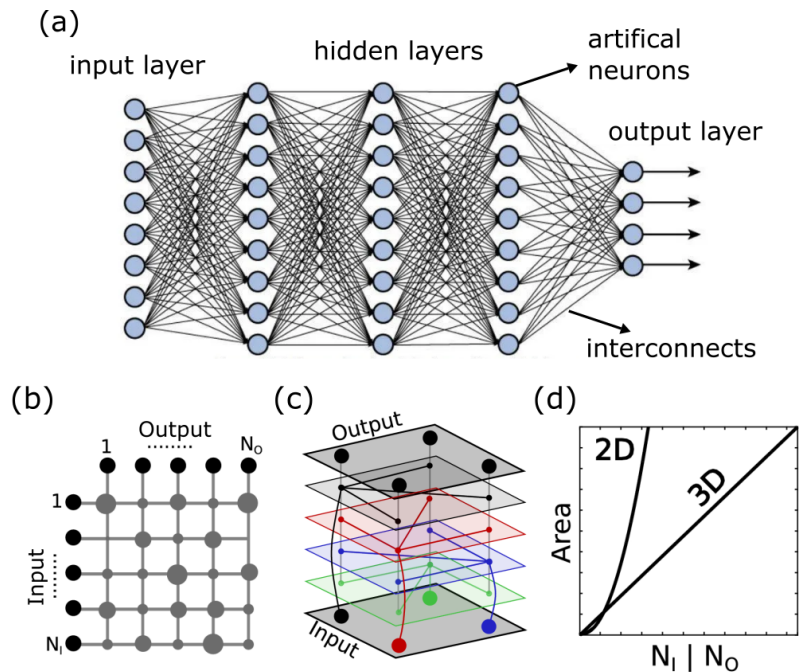


Figure 1.2: Motivation for 3D photonic integration. (a) Schematic representation of a typical NN architecture; numerous artificial neurons are densely-interconnected throughout layers. Connectivity arrangement leveraging (b) 2D topologies with input and output channels (IO-channels) and (c) 3D schemes with neurons arranged in 2D sheets with connections implemented in the third dimension. (d) The result is that the chip's area and height in 3D scales linearly with the number of IO-channels, whereas it quadratically grows in 2D. Extracted from [30].

One of the key challenges in hardware integration for NNs is achieving fully parallel and scalable interconnections within each neuron, and the physical realization of dense connections with  $>1000$  nodes hampers its implementation. In 2D configurations, routing

takes place through discrete contacts between two layers that contain input and output channels (IO-channels), see Fig. 1.2 (b). The input ( $N_I$ ) and output ( $N_O$ ) channels are typically arranged in columns or rows, i.e. cross-bar arrays, and the overall area for interconnecting scales as  $A \propto (N_I \cdot N_O)$ . In 2D topologies, the interconnect's footprint therefore grows quadratic with the number of IO-channels. The inclusion of the third dimension fundamentally eases scalability, see Fig. 1.2 (c), where input and output ports occupy a 2D plane each, while the third dimension allows the circuit's volume to be utilized for out-of-plane interconnections. In a 3D configuration, for each of the  $N_I$  channels, there is a dedicated plane that accommodates all its connections to the  $N_O$  channels. Here, artificial neurons are therefore arranged in 2D sheets, while the connections are realized via 3D connections. For this relatively simple routing strategy, the scaling of the system's area  $A \propto (N_I|N_O)$  and height  $H \propto N_I$  becomes linear, see Fig. 1.2 (d). Due to this linear scaling, the interconnection between the layers of an NN within a 3D photonic IC can be accommodated within a compact volume of  $\text{mm}^3$ . This addresses the scalability challenge, and 3D routing may indeed be a fundamental prerequisite for achieving scalability and parallelism in NN chips.

### 1.1.1/ 2D/2.5D PLATFORMS FOR PHOTONIC INTEGRATION

Silicon photonics is the most widespread and disruptive platform for 2D photonic integration with applications in communication systems, data interconnects, sensors and wavelength-division-multiplexing (WDM) telecommunications products. Since its birth in 1985 and further commercialization by Bookham Technology Ltd [31], the potential of integrated silicon photonics has been patent in primer studies of waveguides in silicon-on-insulator (SOI) wafers [32, 33]. Several remarkable breakthroughs endorse this fact [34, 35, 36], boosting research efforts towards its implementation in emerging fields such as optics, material science, neuroscience and computer science. The primary catalyst of silicon photonics maturation is its compatibility with CMOS platforms, enabling high-volume production at a reduced cost. The large refractive index contrast ( $\Delta n \approx 2.3$  at  $\lambda = 1550$  nm) between silicon and its oxide alloys ( $\text{SiO}_2$ ) is crucial for dense integration of waveguides due to the extremely low bending radii, in the other of tens of  $\mu\text{m}$  [37, 38, 39]. Typically, standard silicon waveguides have propagation losses of 0.06 dB/cm [40, 41], and can be extensively reduced to 0.0007dB/cm for waveguides based on silicon nitride ( $\text{Si}_3\text{N}_4$ ) [42, 43, 44]. However, the large number of connections throughout layers makes traditional 2D lithographic fabrication impractical for the dimensionality demanded in NNS architectures.

For the most part, both, electronic and photonic integration rely on manufacturing techniques initially developed for planar, silicon-based substrates. The process involves engraving the layout of a circuit onto a thin surface composed mainly of metal or semiconductor materials, a procedure known as 2D lithography [45, 46, 47, 48]. In this process, a layer of photoresist is typically applied to shield specific surface areas from etching. All the steps involved in the 2D lithography process can be performed together in a single operation for a significant surface area or an entire wafer. This includes applying the photoresist, exposing it using a photo-mask, the etching process, and subsequent cleaning steps. The striking feature size of  $\approx 10$  nm achievable via electron-beam (e-beam) or immersion deep ultraviolet (DUV,  $\lambda = 193$  nm) lithography is advantageous for several applications [49, 50]. However, for the stacking several layers using this conventional 2D fabrication approach requires precise alignment of the photo-mask multiple times in each

photo-lithographic step, which is challenging, time-consuming and hence expensive when targeting fabrication in 3D.

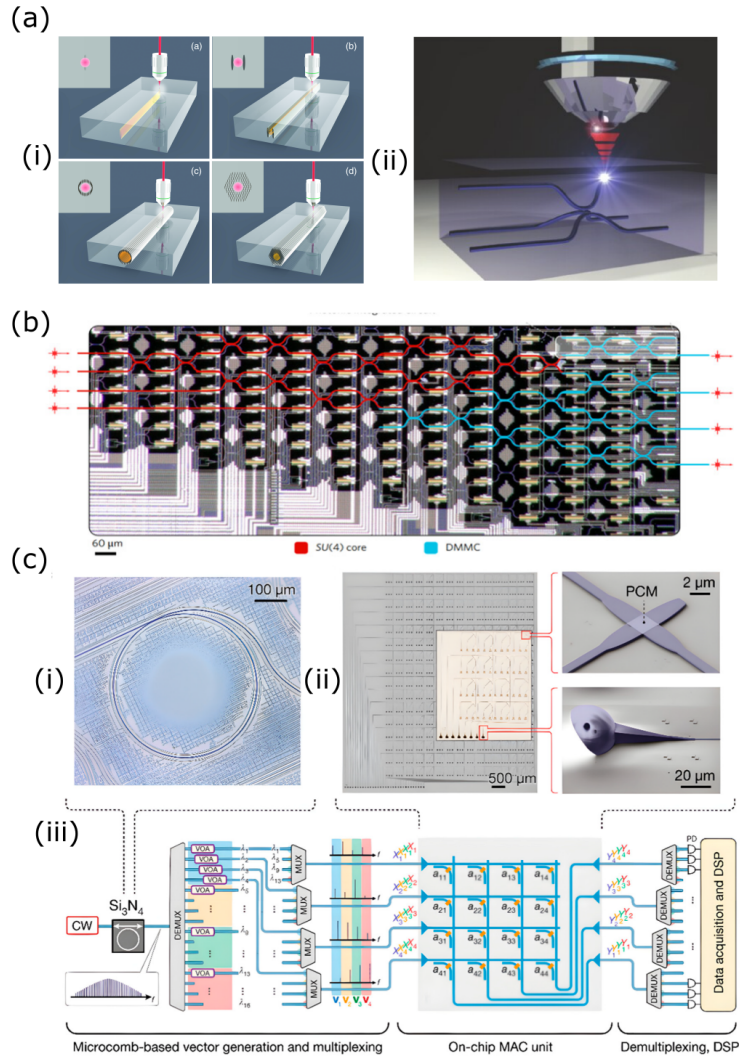


Figure 1.3: State-of-the-art of 2D and 2.5D photonic integration. (a) 2.5D integration leveraging DLW-inscription into glass for (i) photonic waveguides with single-line (top-left panel), double-line (top-right panel), depressed-cladding (bottom-left panel) and optical-lattice-like (bottom-right panel) configurations, and (ii) 3x3 directional couplers. Extracted from [51, 52]. (b) Schematic representation of an integrated mesh of Mach-Zehnder interferometer used to perform NN computing based on coherent light. Extracted from [53]. (c) Schematic overview of an integrated 2D photonic tensor core for parallel convolutional processing: (i) frequency comb generator, (ii) phase-chase material 16x16 arrays and (iii) overall integration of the photonic circuit. Extracted from [54].

For further photonic integration, femtosecond (fs)-laser inscription, or commonly named DLW into bulk materials, has been recognized as a powerful technique for engineering diverse 2.5D materials and produce large number of optical devices such as photonic chips integrating waveguides [55, 56, 57, 58, 59], directional couplers [60, 61, 62], optical splitters [63, 64, 65], waveguide lasers [66], wavelength converters [67, 68], optical (de)multiplexers [69, 70], quantum memories [71, 72, 73] and photonic lanterns [74]. This DLW technique relies on the modification of material properties of dielectric crystal, i.e.

crystalline quartz, fused silica,  $\text{KTiOPO}_4$ ,  $\beta$ -BBO,  $\text{LiNbO}_3$ , BGO or sapphire, achieving feature sizes beyond the diffraction limit of  $\approx 200$  nm [75, 76]. The high optical intensity associated with fs-laser beams leverages the strong-field ionization of dielectrics, breaking of large amount of electrons away from the atoms. These free electrons, by continuously interacting with the laser field, generate an avalanche ionization that leads to a hot and dense electronic plasma [77, 78]. The material breakdown occurs if the quantity of free electrons is similar to the plasma density associated with the laser wavelength, leading to surface ablation and significant modifications to the irradiated lattices within the material. The fs-laser modification results in some effects in dielectrics, such as refractive index changes [79], stress [80], birefringence [81] or thermal melting [82].

For fabricating photonic waveguides, the creation of an enduring refractive index modification (ranging from  $\Delta n \approx 10^{-2}$  to  $10^{-4}$ ) within the focal volumes requires a meticulous engineering of the fs-pulse intensity and shape. For modifying the refractive index  $n$ , type 1 processes are referred to when the laser-induced variations result in positive refractive index changes  $\Delta n > 0$  that are due to slight structural lattice modifications in the dielectric crystals, while for type 2 these variations result in negative  $\Delta n < 0$ . Figure 1.3 (a) depicts (i) photonic waveguides and (ii) 3x3 directional couplers fabricated via DLW-inscription into glass. For such waveguides, a single-line (top-left panel), double-line (top-right panel), depressed-cladding (bottom-left panel) and optical-lattice-like (bottom-right panel) laser-induced track configurations are followed [52, 83]. Typically, these DLW-inscribed waveguides exhibit propagation losses as low as 0.21 dB/cm [84, 85].

However, DLW inscription into bulk glass suffers from several drawbacks [86, 87] that prevent its widespread utilization in NN applications. Tightly focusing a fs-laser beam within a transparent dielectric produces spherical aberrations [88, 89] induced by the difference in refractive index between the immersion medium (air) and the sample material (glass). These aberrations are a major bottleneck for the truly implementation of DLW-laser inscription into bulk materials, constraining its capabilities of fabricating 'tall' mm-size structures in 3D. Moreover, the short working distance of high numerical aperture (NA) objectives limits the height of such integrated circuits. The ultra-high peak power of such fs-laser can trigger the so-called Kerr self-focusing effect [90], which is a nonlinear phenomena that distorts the waveguide shape (or even spatial collapse) due to change of the spatial laser's intensity distribution. Furthermore, DLW glass-inscribed waveguides suffer from very high injection losses. This is due to the non-circular geometry of the waveguides in the transverse writing direction, which is defined by the elliptical cross-section of the fs-laser beam, and differs from the Gaussian-like field profile of standard lasers or waveguide modes. Overall, DLW inscription in bulk glasses is considerably challenging and time-consuming when compared to polymer TPP-based fabrication configurations.

### 1.1.1.1/ ON-CHIP NEURAL NETWORK IMPLEMENTATIONS

In a NN framework, and despite the scalability challenges, exciting achievements have been recently demonstrated via silicon photonics involving phase-change materials (PCM) [91, 92], soliton micro-combs [93, 94, 95], metasurfaces [96] and different (de)multiplexing methods [97, 98]. An alternative strategy for NN computing in hardware is illustrated in Fig. 1.3 (b), where an architecture based on a mesh of Mach-Zehnder interferometer (MZIs) is used to implement coherent fully-optical computing [53, 99], demonstrating levels of accuracy comparable to a conventional digital computer using a fully

connected NN algorithm. This was the first practical demonstration using a photonic IC, where the layers of this architecture consisting of an optical interference unit, i.e. mesh of MZI, and the singular value decomposition (SVD)-based methodology [100]. While MZIs have demonstrated significant potential in addressing the limitations of cutting-edge electronics, it suffers from a larger footprint, hence the constraints of today's CMOS-based computing technology represent a potential limitation to the scope of the NN revolution.

More recently, a photonic tensor core was used for implementing parallel convolutional processing [54], which uses Kerr soliton micro-combs and PCM memories for executing NN tasks, see Fig. 1.3 (c). Such a processor performs the data encoding by combining (i) high-quality factor (Q) micro-combs and (ii) matrix–vector multiplication (MVM) via a non-volatile configuration of integrated PCM (16x16) arrays. This on-chip micro-comb and PCMs integrated onto Si<sub>3</sub>N<sub>4</sub> waveguides [101, 102] locally store convolutional kernels, enabling parallelized in-memory photonic computing via wavelength-division-multiplexing (WDM). Overall, such an integrated NN circuit yields a high prediction accuracy of 95.3 % in tasks such as digit recognition [54].

### 1.1.2/ 3D PHOTONIC INTEGRATION: STATE-OF-THE-ART

Additive manufacturing via 3D printing stands out as an innovative tool for creating intricate 3D photonic components. Direct-laser writing combined with TPP enables fabricating 3D structures ranging from mm to sub- $\mu\text{m}$  scales across various scientific and engineering domains, including micromechanical systems [103], components for micro-robotics [104], applications in biosciences [105] and optics [106]. In DLW, a tightly focused fs-laser beam is guided through a photosensitive resin, solidifying it within the TPP reactive volume, potentially yielding sub- $\mu\text{m}$  voxels [107]. Within the field of photonics, DLW-TPP has found applications in the production of free-form and transformative components [108, 109], point-to-point photonic wire-bondings [110], waveguides [111], spatial filters [30], graded-index lenses [29], and integrated photonics [112, 113]. Crucially, the processes and materials involved in the entire fabrication via DLW-TPP are CMOS compatible [114].

Photonic waveguides play a pivotal role in various optical components and are essential for their incorporation into everyday technologies [115, 116]. The capability to additively integrate photonic circuits with  $\mu\text{m}$ -size features opens up exciting possibilities for a wide range of applications, including the scalability of integrated NN circuits [30], chip-to-chip interconnections [117, 118], quantum and optical communications [119, 120], and the construction of building blocks for 3D photonic waveguide integration [121, 14]. Compared to DLW into solid dielectric substrates, see Section 1.1.1, additive DLW allows to fabricate directly on top of an existing IC. This removes post-fabrication bonding of the classical, e.g. CMOS, chip to the equally solid 3D photonic dielectric chip, a substantial simplification that also increases the compatibility of the technique. Research efforts currently include the micromachining of photonic waveguides using additive DLW-TPP with diverse materials, including glasses, crystals, and polymers [122].

For highly-dense photonic integration, it is crucial to connect multiple photonic platforms, and most of today's photonic devices are based on silicon-on-insulator (SOI) and CMOS technology. Merging the advantages of multiple photonic and electronic systems into a unified, hybrid, and multi-chip platform, would potentially result in universal computing tools, while simultaneously boosting overall performance. The polymer-based 3D printing

technology via DLW-TPP is particularly advantageous in tackling these obstacles, as evidenced by several investigations [123, 118, 124, 117]. Figure 1.4 (a) depicts a schematic illustration of the so-called photonic wire-bonding (PWB), which involves the creation of a 3D photonic waveguides to establish point-to-point links for a chip-to-chip connection between multiple SOI chips. Here shown for (i) SiP-to-SiP chip and (ii) SiP-to-SMF connections, with SiP (SMF) standing for silicon phosphide (single-mode fiber), this work demonstrated the fundamental potential of DLW-TPP fabrication compatible with CMOS platforms, wafer-scale integration, and chip-to-chip connections.

More recently, 3D optical splitters with 1 to 4, 1 to 9, and 1 to 16 IO-channels were demonstrated [115], see Fig. 1.4 (b). These air-cladded waveguides, having polymer as core and air as their cladding, are prime candidates for dense photonic integration due to their high optical confinement resulting in low bending radii [125, 126, 127]. For large-scale network interconnect applications, parallel interconnects having 225 inputs and 529 outputs only occupying a volume of  $(460 \times 460 \times 300) \mu\text{m}^3$  were demonstrated [30]. Such highly-dense connections are based on fractal topologies, which efficiently connect large numbers of input and output channels [128], cascading a double-layer of 1 to 9 splitters and spatially multiplexing arrays of such 1 to 81 splitters to accommodate a  $15 \times 15$  array of input waveguides, see bottom-panel in Fig. 1.4 (b).

Similarly, 3D waveguide architectures capable of performing spatial filtering were demonstrated via DLW-TPP [30]. Nine different  $3 \times 3$  Boolean convolutional filtering kernels were realized to implement Haar-like kernels of a convolutional NN layer, which is a fundamental operation in deep NNs [130, 131, 132, 133]. These Haar-like filters can process images containing  $21 \times 21$  pixels when arranged in a 2D array with a stride of two [30]. Figure 1.4 (c) shows the scanning electron microscope (SEM) micrograph (left panel) of such Haar-like filtering 3D waveguide topologies and its experimental characterization (right panel), where each filter kernel's  $3 \times 3$  input weight is associated with a single output. Despite the asymmetric coefficients of each kernel, this realization proves the significant potential for truly 3D integration via DLW-TPP. Furthermore, optical volume elements (OVEs) enable implementing such spatial filtering operations via multi-layer diffractive optical elements [134, 113]. For such OVEs' topologies, mode-division multiplexing is achieved by learning tomography (LT), which operates as an angular multiplexer or 'lantern' that translates plane waves with varying incidence angles into linearly polarized (LP) multimode fiber modes. Figure 1.4 (d) shows the SEM micrograph (left panel) of a three-layer volume element, the phase distribution of distinct layers (central panel) and the experimental output intensities (right panel) for two different incident angles  $\pm(-)3^\circ$  yielding two  $\text{LP}_{21}$  ( $\text{LP}_{02}$ ) modes [111].

Finally, 3D printed building blocks have been recently shown to be an impact tool for hybrid photonic multi-chip platforms [129]. Figure 1.4 (e) shows SEM micrographs of free-form 3D printed elements such as lenses, mirrors, high-NA lenses, total internal reflection mirrors, beam expanders and multi-lens beam expanders (left to right panels), with application in hybrid integration [135, 136]. These optical components were experimentally tested, obtaining  $\approx 88\%$  coupling efficiencies while connecting the emission of an edge-emitting InP laser to a single-mode fiber (SMF) input-facet.

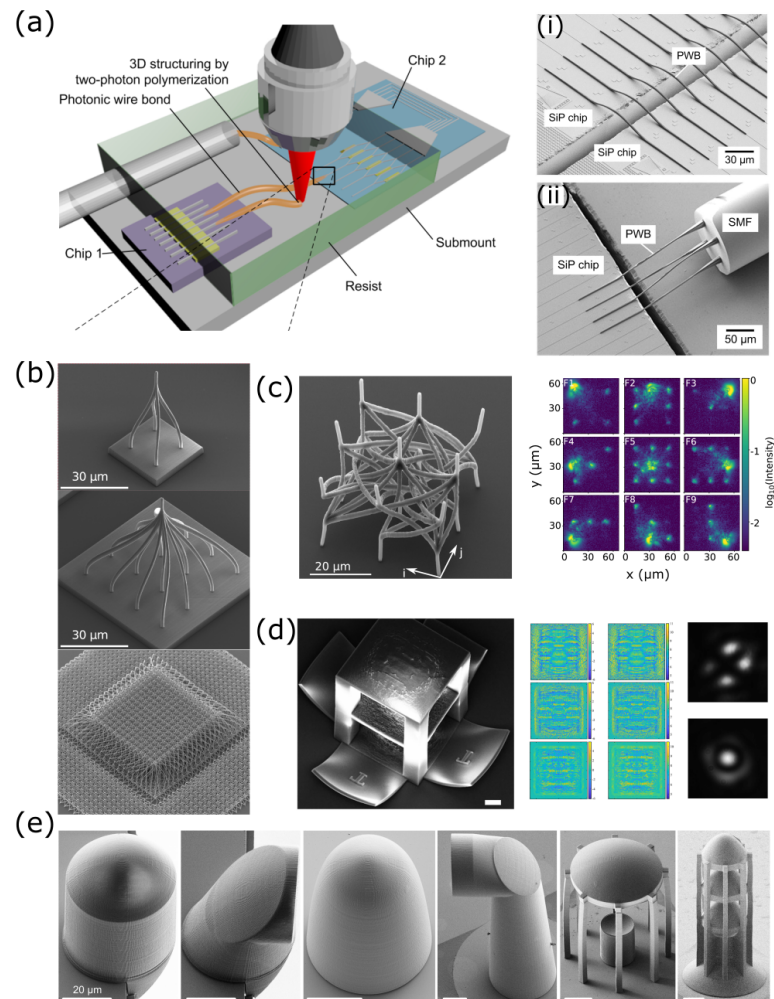


Figure 1.4: State-of-the-art of 3D photonic integration. (a) Schematic representation of the photonic wire-bonding concept (PWB) for chip-to-chip interconnects via DLW-TPP, here for (i) SiP-to-SiP chip and (ii) SiP-to-SMF connections. Reproduced from [110, 117]. (b) SEM micrographs of air-cladded optical splitters leveraging 1 to 4 (top panel), 1 to 8 (middle panel) and 225 to 529 (bottom panel) input and output connections. Reproduced from [115]. (c) SEM micrograph (left panel) and optical characterization (right panel) of a 3D printed spatial Haar-like filter for a convolutional neural network. Reproduced from [30]. (d) SEM micrograph (left panel), phase mask (middle panel) and output intensity profiles (right panel) for a three-layer optical volumetric element (OVE) used for spatial filtering via learning tomography (LT). Reproduced from [113]. (e) 3D printed universal building blocks such as lenses, mirrors, high-NA lenses, total internal reflection mirrors, beam expanders and multi-lens beam expanders (from left to right panels) for hybrid multi-chip interconnection. Reproduced from [129].

### 1.1.2.1/ OTHER PLATFORMS FOR 3D PHOTONIC INTEGRATION

Other than DLW-TPP fabrication, alternative photolithographic methods are suitable for manufacturing complex 3D components. Projection micro-stereolithography (P $\mu$ SL) combined with micro-continuous liquid interface production ( $\mu$ CLIP), stands out as a remarkable technique for producing large-scale optical components, such as a 3 mm diameter

aspherical lens printed at a high speed of  $4.85 \text{ mm}^3/\text{h}$  [137]. Crucially,  $P_{\mu}\text{SL-}\mu\text{CLIP}$  fails to achieving the accurate control of refractive indices essential for constructing single-mode waveguides or high-resolution volume holograms [138, 139, 140, 141, 142]. Furthermore, the maximum feature resolution achievable with  $P_{\mu}\text{SL-}\mu\text{CLIP}$  is  $\approx 50 \text{ }\mu\text{m}$  [143], which is far from the  $200 \text{ nm}$  achievable with DLW-TPP [144, 145].

A further 3D printing strategy is the subsurface controllable refractive index via beam exposure (SCRIBE), which eliminates the need for mechanical support during printing by polymerizing the photoresist within a porous thin film [146, 147]. However, a crucial drawback inherent to this approach is that the quality of focus deteriorates due to spherical aberrations when fabricating large structures, as the process involves focusing deep inside the medium, similarly to DLW into glass. In contrast, DLW-TPP printing is advantageous for constructing tall (mm-size) 3D structures with a high aspect-ratio via the 'dip-in' configuration [148, 149, 150]. An additional limitation related to the SCRIBE method is its compatibility with diverse substrates, primarily being suitable for materials like porous silicon and silicon oxide. These substrates exhibit dissimilarity in their optical properties over extended periods, particularly when exposed to humid environments [151].

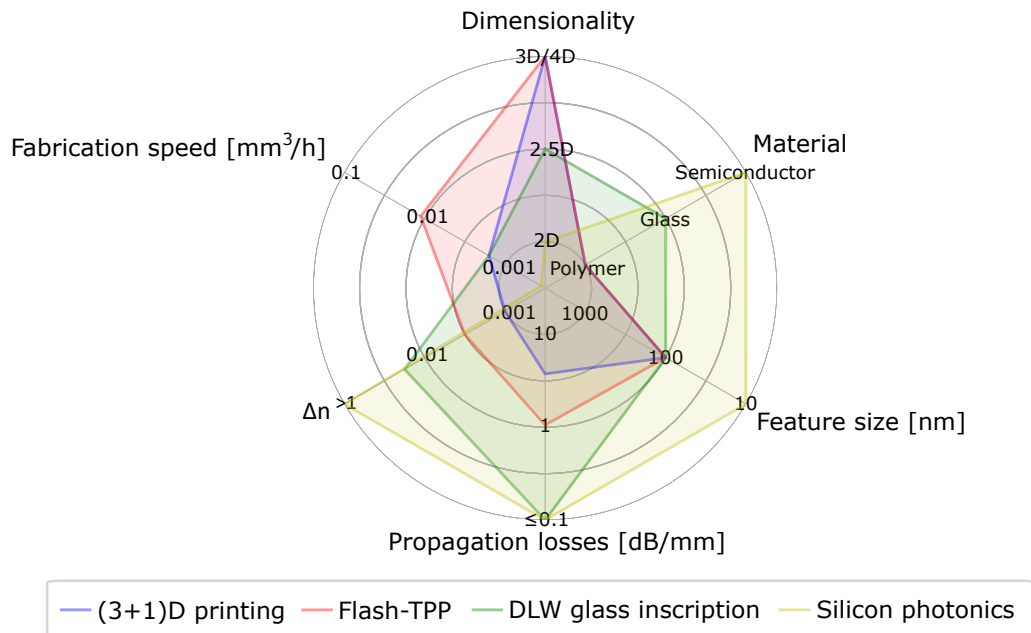


Figure 1.5: Radar chart diagram comparing key performances of the most relevant technology platforms for 3D photonic integration: (3+1)D printing (blue color), *flash*-TPP (red color), DLW inscription into glass (green color) and silicon photonics (yellow color). Extracted from [114].

Figure 1.5 illustrates a radar chart comparing several performance metrics, including dimensionality (2D, 2.5D, 3D), 3D fabrication speed ( $\text{mm}^3/\text{h}$ ), refractive index contrast ( $\Delta n$ ), propagation losses (dB/mm), minimal feature size (nm), and substrate materials, for diverse technology platforms playing a major role in photonic integration such as silicon photonics and DLW inscription in bulk glass. These performances are compared for additive manufacturing techniques based on TPP combined with DLW, which are the pivotal fabrication methodologies exploited in this thesis, i.e. (3+1)D printing and *flash*-TPP. As seen, DLW-TPP fabrication methods offer significant advantages in achieving truly 3D integration of complex and large-scale photonic circuits, all with relatively rapid

fabrication speeds. However, further efforts are to be invested in elevating the potential of photo-induced fabrication methods and approaching the standard metric performances of standard silicon photonics platforms [152, 41, 153, 154] and DLW glass inscription [52, 83, 155, 156].

## 1.2/ THEORY OF PHOTONIC WAVEGUIDES

The concept of optical waveguides arises from the phenomena in which light is guided in the form of waves, and this Section 1.2 covers the essential theoretical aspects. Firstly, a general description of the light-wave propagation in waveguides is introduced via ray analysis of classical geometric optics and the total internal reflection principle. The transmission characteristics of step- (STIN) and graded-index (GRIN) waveguides are explored in the framework of 2D planar waveguides, which is the most general representation of stacked dielectric waveguides. Special attention is given to the creation of optical modes in cylindrical STIN waveguides following classical geometric theory. Secondly, the 3D electromagnetic representation of light is of vital importance towards photonic integration applications, hence the electromagnetic analysis of light propagation in 3D waveguides is introduced based on the solutions of Maxwell's equations. With these, basic concepts such as the propagation of electromagnetic field distributions, the modal parameters of light propagation, the dispersion relation and propagation constants in 3D waveguides are described.

Importantly, waveguides in which only one optical mode can propagate are named single-mode waveguides, and these are particularly reviewed under the weakly-guiding approximation. Finally, exciting a specific optical mode in a waveguide requires accurate mode-matching of, both, the mode from an external light source and the one propagating in the waveguide. The most common strategy to achieve efficient mode-matching is the addition of adiabatic tapers at the input-facet of the waveguides. Furthermore, when two independent waveguides are placed aside, the mutual light-wave interaction between these waveguides results in perturbations, and the overall optical power can be transferred between them. Here, the case of tapered velocity couplers is introduced.

The relevant information presented in Section 1.2 is strongly based on the concepts that are extensively contained in the following books: *Fundamentals of Photonics* by Saleh and Teich [157], *Fundamentals of Optical Waveguides* by Katusnari Okamoto [158], *Optical Waveguide Theory* by Snyder and Love [159], *Theory of Dielectric Optical Waveguides* by Marcuse [160] and *Foundations for Guided-Wave Optics* by Chin-Lin Chen [161].

### 1.2.1/ OPTICAL WAVEGUIDE THEORY: RAY ANALYSIS

In Section 1.2.1, the ray optics model is utilized to describe the propagation of light within optical waveguides. This simple theory considers that light waves propagate through objects whose dimensions are larger than the wavelength  $\lambda$ , and the wave nature of light is not readily discerned. In such a scenario, its behavior can be described by rays obeying a set of geometrical rules. This simple geometrical optics theory is adequate for studying light transmission in photonic waveguides in an approximate manner, yet a complete analysis will be done in Section 1.2.2 via its electromagnetic representation by solving Maxwell's equations. Here, general concepts for understating crucial aspects

such as total internal reflection, step- and graded-index profiles and the creation of modes in photonic waveguides are described via ray analysis.

### 1.2.1.1/ TOTAL INTERNAL REFLECTION

In the simplest form, an optical waveguide is a long 2D planar structure having two dielectric regions, as schematically illustrated in Fig. 1.6 (a). The central region is the core, which is surrounded by the cladding, with associated refractive indices  $n_{\text{core}}$  and  $n_{\text{cladding}}$ , respectively, being the optical properties associated with each region independent. The first condition for optical guidance is that the refractive index of the core must be larger than the one of the cladding  $n_{\text{core}} > n_{\text{cladding}}$ . When this condition is fulfilled, light that is coupled to the input-facet of a waveguide can be confined in the region with a greater refractive index, i.e. the waveguide core  $n_{\text{core}}$ , via total internal reflection. The second condition for optical guidance, i.e. total internal reflection, is that the reflected ray at the core-cladding interface leaves at the same angle  $\theta$  as the incident ray (see Fig. 1.6 (b)), and by using Snell's law this results in

$$\theta_c = \sin^{-1} \left( \frac{n_{\text{cladding}}}{n_{\text{core}}} \right) = \cos^{-1} \left( 1 - \frac{n_{\text{cladding}}^2}{n_{\text{core}}^2} \right)^{1/2}, \quad (1.1)$$

where  $\theta_c = \theta_1$  is the critical angle of the incident ray such as  $\theta_2 = \pi/2$ . Therefore, a ray with angle  $\theta$  is totally internally reflected at the core-cladding interface if  $0 \leq \theta < \theta_c$  and it will be partly refracted in the cladding region if  $\theta_c < \theta \leq \pi/2$ . The totally internally reflected ray that is named guided ray, and it repeatedly reflects within the core at the same angle  $\theta$ , creating successive zig-zag reflections along the pathway. Consequently, a guided ray can ideally propagate indefinitely with zero loss as at every reflection the power of the ray is conserved, and allows to transfer optical signals over long distances.

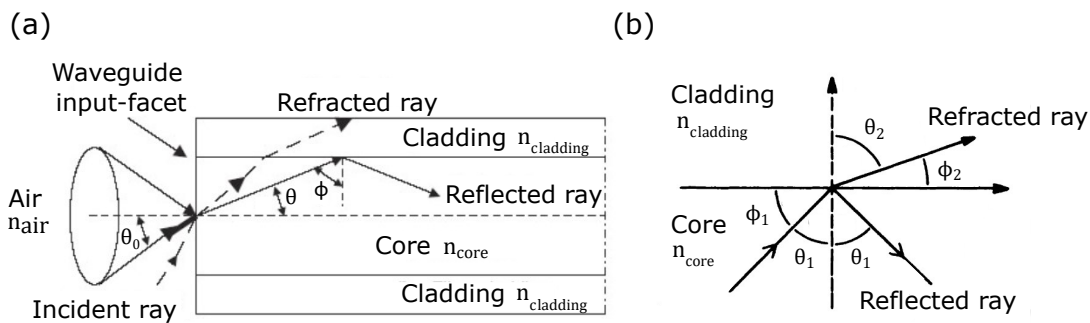


Figure 1.6: Total internal reflection in photonic waveguides. (a) At the input-facet of a waveguide, an incident ray light is confined within the core due to total internal reflection, the refracted ray is damped towards the cladding. For this, the refractive index of the core must be larger than the cladding's  $n_{\text{core}} > n_{\text{cladding}}$ . (b) Reflection and refraction of a plane wave at a dielectric interface, i.e. waveguide's core-cladding interface. Reproduced from [160].

Figure 1.6 (a) shows that at the waveguides' input-facet the incident (reflected) ray with angle  $\theta_0$  ( $\theta$ ) are related  $n_{\text{air}} \sin \theta_0 = n_{\text{core}} \sin \theta \leq \sqrt{n_{\text{core}}^2 - n_{\text{cladding}}^2}$ . The condition for an

incident ray coming from air ( $n_{\text{air}} = 1$ ) to be guided into the waveguide core is

$$\theta \leq \sin^{-1} \sqrt{n_{\text{core}}^2 - n_{\text{cladding}}^2} \equiv \theta_{\text{max}}, \quad (1.2)$$

with  $\theta_{\text{max}}$  denoting the maximum acceptance angle and known as the numerical aperture  $\text{NA} = \sin \theta$ , which is defined as the maximum angle at which light can be injected into the waveguide's core as a totally internally reflected ray.

### 1.2.1.2/ STEP- AND GRADED-INDEX PROFILE WAVEGUIDES

At the waveguide's core, the refractive index profile can be uniform or vary as a function of the radial distance to the core's center  $n(\mathbf{r})$ , while the cladding index  $n_{\text{cladding}}$  is typically uniform. When  $n(\mathbf{r})$  is uniform along the core, it is assumed to take the maximum value of the refractive index at the core  $n(r) = n_{\text{core}}$ , while if it varies throughout the vicinity of the core, the refractive index value depends on the spatial position at the core as

$$\frac{d}{ds} \left( n(\mathbf{r}) \frac{d\mathbf{r}}{ds} \right) = \nabla n(\mathbf{r}), \quad (1.3)$$

where  $s$  is the distance along the ray path and  $\mathbf{r}$  is the position vector of a point on the ray path. These two situations correspond to STIN and GRIN profile waveguides, and their typical ray trajectories under total internal reflection are shown in Fig. 1.7 (a) and (b), respectively. For the STIN waveguides, all bound rays propagate at angles within the range  $0 \leq \theta < \theta_c$  at any position in the core cross-section. For GRIN waveguides, the range of values of  $\theta_c$  varies over  $\mathbf{r}$ . The light-wave analysis of STIN profile waveguides is of vital interest as it is the most common configuration for waveguides, hence the following sections are focused on these.

For STIN waveguides, when the refractive index contrast between core and cladding  $\Delta n = n_{\text{core}} - n_{\text{cladding}}$  is small ( $\Delta n \ll 1$ ), waveguides are considered to be in the weakly-guiding regime, and the complementary critical angle  $\theta_c$  from Eq. 1.1 is reformulated as

$$\sin \theta_c \cong \theta_c \cong (1 - n_{\text{cladding}}^2 / n_{\text{core}}^2)^{1/2}. \quad (1.4)$$

Within this framework, the range of angles  $\theta$  of guided rays becomes small, and each ray propagates nearly parallel to the propagation axis. This is known as the paraxial approximation. An important parameter to describe the general properties of optical waveguides is the relative refractive index difference between core and cladding  $\Delta$ , which is defined under the paraxial approximation as

$$\Delta = \frac{n_{\text{core}}^2 - n_{\text{cladding}}^2}{2n_{\text{core}}^2} \cong \frac{n_{\text{core}} - n_{\text{cladding}}}{2n_{\text{core}}}, \quad (1.5)$$

which is typically  $\Delta \ll 1$ . Moreover, the NA of a waveguides is related to the relative refractive index difference  $\Delta$  as

$$\text{NA} = \theta_{\text{max}} \cong n_{\text{core}} \sqrt{2\Delta}, \quad (1.6)$$

hence the maximum angle for light to be propagated within the core becomes  $\theta_{\max}/n_{\text{core}} \cong \sqrt{2\Delta}$ .

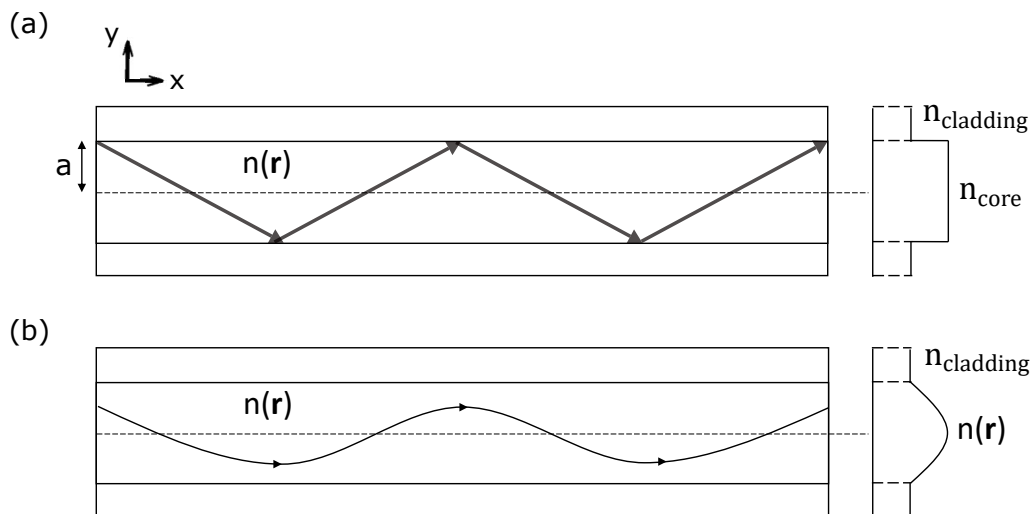


Figure 1.7: Ray path for STIN and GRIN profile waveguides. (a) Typical zig-zag-like ray path within the core of a STIN planar waveguide. The light is confined at the core-cladding interface. (b) Sinusoidal-like ray path within the core of a GRIN planar waveguide. Light is tightly confined at the center of the waveguide core. Reproduced from [159].

### 1.2.1.3/ CREATION OF MODES

For 2D planar dielectric waveguides, when a plane wave undergoes total internal reflection at the core-cladding interface, the phase of the reflected wave changes with respect to the phase of the incident wave. The phase shift between the two wave-fronts depends on the polarization of the light, whether the electric or the magnetic field is parallel to the interface. For both of the cases, the direction of the electric or magnetic fields remains unaltered after the reflection. The geometrical analysis of this phase-shift of propagating rays describes in a simple way the formation of modes in a waveguide, where each mode is associated with light rays at a discrete angle of propagation.

Figure 1.8 illustrates plane waves propagating along the  $z$ -direction in a 2D planar dielectric waveguide with angle  $\phi$  and phase fronts perpendicular to the ray's direction. The propagation constants  $\beta$  ( $\kappa$ ) along the  $z$ -direction ( $x$ -direction) are expressed as

$$\beta = kn_{\text{core}} \cos \phi, \quad (1.7)$$

$$\kappa = kn_{\text{core}} \sin \phi, \quad (1.8)$$

where  $kn_{\text{core}}$  is the wavenumber of light in the core. The reflection coefficient  $t$  of the totally internally reflected ray and its associated fields polarized perpendicular to the incident plane is

$$t = \frac{A_t}{A_i} = \frac{n_{\text{core}} \sin \phi + j \sqrt{n_{\text{core}}^2 \cos^2 \phi - n_{\text{cladding}}^2}}{n_{\text{core}} \sin \phi - j \sqrt{n_{\text{core}}^2 \cos^2 \phi - n_{\text{cladding}}^2}}. \quad (1.9)$$

The amount of phase shift between the incident and reflected rays in terms of the complex reflection coefficient  $t = \exp(-j\Phi)$  is expressed as

$$\Phi = -2 \tan^{-1} \frac{\sqrt{n_{\text{core}}^2 \cos^2 \phi - n_{\text{cladding}}^2}}{n_{\text{core}} \sin \phi} = -2 \tan^{-1} \sqrt{\frac{2\Delta}{\sin^2 \phi} - 1}. \quad (1.10)$$

Figure 1.8 illustrates a light ray propagating from point P to Q, or PQ, with a constant phase front. On the contrary, the ray RS undergoes reflection twice (lower and upper interface) and therefore the phase front between these points (PQ and RS) is different. However, since points P and R (Q and S) lie on the same phase front after multiple reflections, their optical paths are equal or differ by an integral multiple of  $2\pi$ . The phase-matching condition for the optical paths PQ and RS is given by

$$\tan\left(kn_{\text{core}}a \sin \phi - \frac{m\pi}{2}\right) = \sqrt{\frac{2\Delta}{\sin^2 \phi} - 1}, \quad (1.11)$$

where  $m$  is an integer number and  $a$  is the radius of the waveguide. The optical field distribution that satisfies the phase-matching condition is named mode  $m$  that corresponds to a bounce angle, and the discrete solution of the propagation constant  $\beta$  is its eigenvalue.

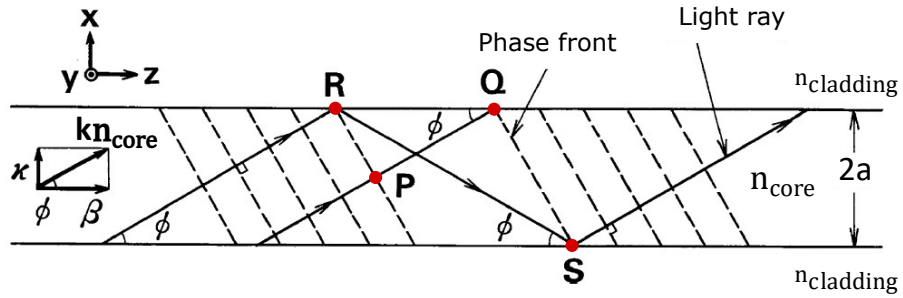


Figure 1.8: Schematic illustration of the phase-matching condition for ray trajectories and their phase fronts that lead to the eigenvalue equation. All rays that travel in the same direction belong to the same planar wave. Reproduced from [158].

Figure 1.9 illustrates the formation of modes in the exemplary case of STIN 2D planar waveguides for (a) the fundamental mode and (b) higher-order modes, respectively. The fundamental mode, with minimum angle  $\phi$  ( $m = 0$ ), and the higher-order mode, with a larger angle ( $m \geq 1$ ), are constructed after the interference of the guided light waves along the waveguide core. The electric field amplitude  $\mathbf{E}$  becomes maximum (minimum) at the point where two positive (negative) phase fronts interfere. Positive (solid lines) and negative (dotted lines) phase fronts cancel each other out at the core-cladding interfaces, and the electric field amplitude becomes nearly zero in these regions. Consequently, the field distribution along the transversal  $x$ -direction represents a standing wave that varies periodically ( $\lambda_p = (\lambda/n_{\text{core}})/\cos \phi = 2\pi/\beta$ ) along the  $z$ -direction, see Fig. 1.9.

Equation 1.11 can be reformulated in terms of the normalized parameter  $\xi = \sin \phi / \sqrt{2\Delta}$  from Eq. 1.6 as

$$kn_{\text{core}}a \sqrt{2\Delta} = \frac{\cos^{-1} \xi + m\pi/2}{\xi}, \quad (1.12)$$

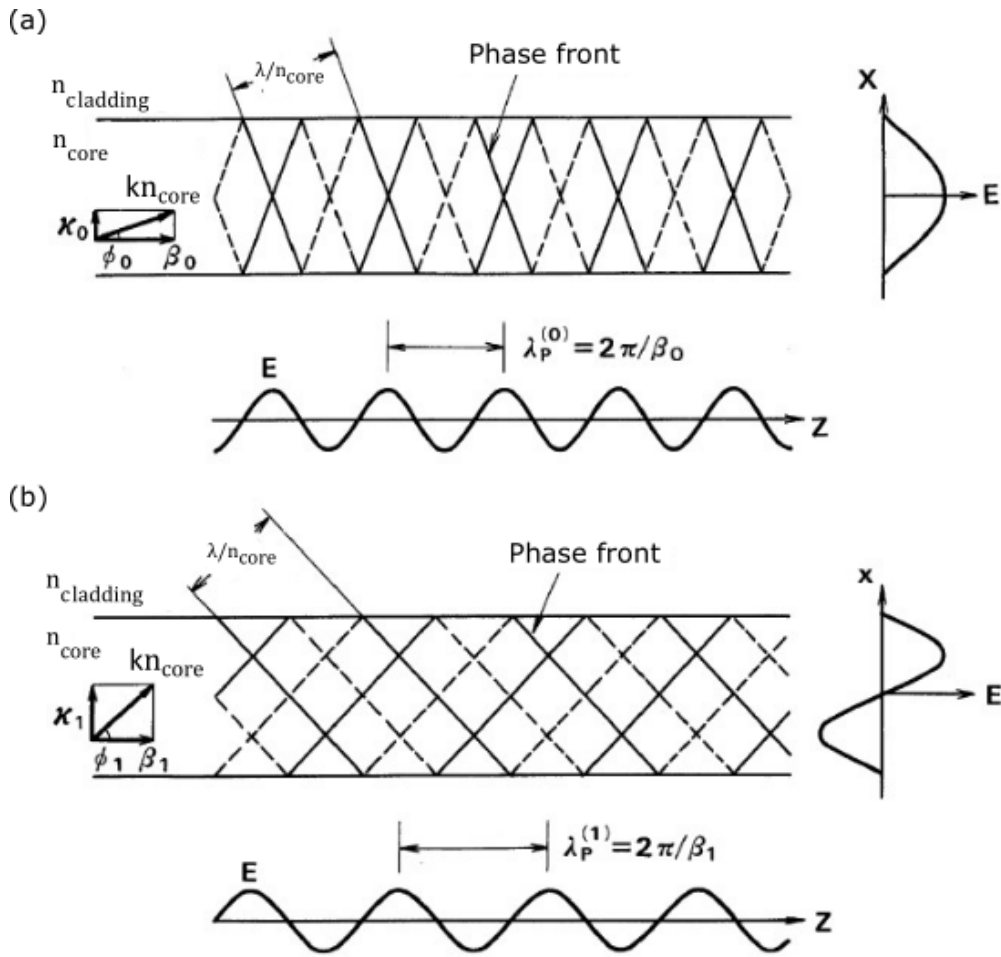


Figure 1.9: Formation of modes for (a) fundamental ( $m = 0$ ) and (b) higher-order modes ( $m = 1$ ) for ray paths with corresponding phase fronts. Their respective electric field  $\mathbf{E}$  distribution is illustrated in the right-side panels. Extracted from [158].

which is the so-called normalized frequency  $V$  that is expressed as

$$V = kn_{\text{core}}a \sqrt{2\Delta} = \frac{2\pi a}{\lambda_0} \sqrt{n_{\text{core}}^2 - n_{\text{cladding}}^2}. \quad (1.13)$$

From the normalized frequency  $V$ , the number of guided modes in a waveguide  $M$  is extracted as

$$M = \frac{1}{2}V^2 \text{ for } V \gg 1. \quad (1.14)$$

The relationship between  $V$  and  $\xi$  provides the different solutions for each mode number  $m$  and its associated propagation constant  $\beta$ . Noteworthy, this relation will be further derived also for the case of cylindrical STIN waveguides under the electromagnetic approach via solving Maxwell's equations. Therefore, the general behavior of a guided ray in a waveguide, which is intrinsically linked to the normalized frequency  $V$ , can be fully described by the waveguide core radius  $a$ , the numerical aperture  $\text{NA} = \sqrt{n_{\text{core}}^2 - n_{\text{cladding}}^2}$

and wavelength  $\lambda_0$  of the light. Generally, the threshold value for single-mode propagation of STIN waveguides is given by

$$V_{\text{cut-off}} < \frac{2\pi a}{\lambda_0} \text{NA}, \quad (1.15)$$

above which higher modes can propagate, too.

### 1.2.2/ ELECTROMAGNETIC WAVE DESCRIPTION OF GUIDED LIGHT

The previously discussed classical geometrical ray method is a simple and approximate description for the analysis of light transmission in photonic waveguides, and it is often valid for multimode waveguides. However, the classical approach is inaccurate to fully describe waveguides in which only one or few modes propagate. For these waveguides, the electromagnetic representation of light provides an exact solution by solving Maxwell's equations. Chapter 2, Chapter 3 and Chapter 4 introduce experimental demonstrations of cylindrical 3D photonic waveguides with STIN profile in which the fundamental mode is guided, hence a fully electromagnetic description of guided light is required. All these aspects are specifically discussed in the following sections.

#### 1.2.2.1/ MAXWELL'S EQUATION

Generally, the electromagnetic  $\mathbf{E}(\mathbf{r}, \omega)$  and magnetic  $\mathbf{H}(\mathbf{r}, \omega)$  fields are described as sinusoidal functions that vary over time, with angular frequency  $\omega$  and propagation constant  $\beta$ . These are usually represented by complex amplitudes as

$$\mathbf{E}(\mathbf{r}, \omega) = \mathbf{E}_0 e^{j(\omega t - \beta z) + \phi_0}, \quad (1.16)$$

$$\mathbf{H}(\mathbf{r}, \omega) = \mathbf{H}_0 e^{j(\omega t - \beta z) + \phi_0}, \quad (1.17)$$

where  $\mathbf{r}$  denotes the position in the plane transverse to the  $z$ -axis,  $\mathbf{E}_0$  ( $\mathbf{H}_0$ ) are the amplitudes of the electric (magnetic) fields and  $\phi_0$  is the phase angle.

The Maxwell's equations, expressed in terms of  $\mathbf{E}(\mathbf{r}, \omega)$  and  $\mathbf{H}(\mathbf{r}, \omega)$ , in an homogeneous dielectric medium in the absence of carriers and charges area are

$$\nabla \cdot \mathbf{D}(\mathbf{r}, \omega) = 0, \quad (1.18)$$

$$\nabla \cdot \mathbf{B}(\mathbf{r}, \omega) = 0, \quad (1.19)$$

$$\nabla \times \mathbf{E}(\mathbf{r}, \omega) = -j\omega \mathbf{B}(\mathbf{r}, \omega), \quad (1.20)$$

$$\nabla \times \mathbf{H}(\mathbf{r}, \omega) = j\omega \mathbf{D}(\mathbf{r}, \omega), \quad (1.21)$$

where  $\mathbf{B}(\mathbf{r}, \omega)$  and  $\mathbf{D}(\mathbf{r}, \omega)$  are the magnetic flux and the electric displacement, respectively, which are generally expressed as

$$\mathbf{B}(\mathbf{r}, \omega) = \mu_0 \mu_r(\mathbf{r}, \omega) \mathbf{H}(\mathbf{r}, \omega), \quad (1.22)$$

$$\mathbf{D}(\mathbf{r}, \omega) = \varepsilon_0 \varepsilon_r(\mathbf{r}, \omega) \mathbf{E}(\mathbf{r}, \omega). \quad (1.23)$$

Here,  $\mu_r(\varepsilon_r)$  is the relative permeability (permittivity) of the material and  $\mu_0(\varepsilon_0)$  denotes their values in the vacuum. Since the waveguides considered here are dielectric structures, i.e. non-magnetic, the relative permeability  $\mu_r$  is assumed to be zero.

These parameters are linked to the wavenumber of light inside the medium as  $\Gamma = \omega \sqrt{\varepsilon_r \mu_r} = \omega n(\mathbf{r}, \omega) \sqrt{\varepsilon_0 \mu_0} = k_0 n(\mathbf{r}, \omega)$ , where  $k_0 = \omega/c_0$  is the wavenumber in vacuum with  $c_0$  as the velocity of light in vacuum, and  $n(\mathbf{r}, \omega)$  the refractive index. For STIN waveguides,  $n(\mathbf{r}, \omega)$  is constant along the waveguide core and cladding regions, see Fig. 1.7 (a), hence the spatial and frequency dependency is neglected and only the real part is considered  $n = \sqrt{\varepsilon_r}$ .

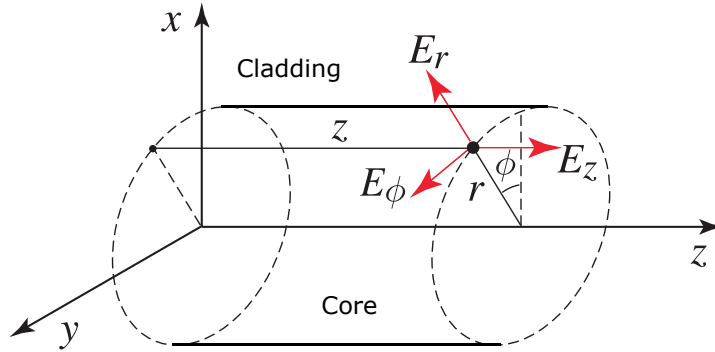


Figure 1.10: Photonic waveguide with cylindrical geometry. A coordinate transformation from cartesian to cylindrical coordinates is required. Extracted from [157].

### 1.2.2.2/ EIGENMODES OF STEP-INDEX CYLINDRICAL WAVEGUIDES

Although a photonic waveguide can take any geometry, most waveguides have a nominally cylindrical shape as depicted in Fig. 1.10. For STIN waveguides with a cylindrical core, applying the curl operation on Eq. 1.20 and using Eq. 1.21, the vector wave equation for the electric and the magnetic field is expressed as

$$\nabla^2 \mathbf{E}(\mathbf{r}, \omega) + \nabla \left( \frac{\nabla \varepsilon_r(\mathbf{r}, \omega)}{\varepsilon_r(\mathbf{r}, \omega)} \cdot \mathbf{E}(\mathbf{r}, \omega) \right) + k_0^2 \varepsilon_r(\mathbf{r}, \omega) \mathbf{E}(\mathbf{r}, \omega) = 0, \quad (1.24)$$

$$\nabla^2 \mathbf{H}(\mathbf{r}, \omega) + \frac{\nabla \varepsilon_r(\mathbf{r}, \omega)}{\varepsilon_r(\mathbf{r}, \omega)} \times (\nabla \times \mathbf{H}(\mathbf{r}, \omega)) + k_0^2 \varepsilon_r(\mathbf{r}, \omega) \mathbf{H}(\mathbf{r}, \omega) = 0, \quad (1.25)$$

which are the so-called Helmholtz equations. In homogeneous media ( $\nabla \varepsilon_r(\mathbf{r}, \omega) \ll \varepsilon_r(\mathbf{r}, \omega)$ ) the second term of the vector wave from Eq. 1.24 and Eq. 1.25 can be neglected and reformulated as

$$\nabla^2 \mathbf{E}(\mathbf{r}, \omega) + k_0^2 \varepsilon_r(\mathbf{r}, \omega) \mathbf{E}(\mathbf{r}, \omega) = 0, \quad (1.26)$$

$$\nabla^2 \mathbf{H}(\mathbf{r}, \omega) + k_0^2 \varepsilon_r(\mathbf{r}, \omega) \mathbf{H}(\mathbf{r}, \omega) = 0. \quad (1.27)$$

For cylindrical STIN waveguides, electric and magnetic field components inside the core and cladding are decoupled, hence the Helmholtz equations are solved separately.

Therefore, from the  $E_z$  component of the electric field of Eq. 1.24, all the other field components can be further derived. When the core of a waveguide has cylindrical geometry, i.e. axially symmetric, it is convenient to write the transverse  $E_z$  component of the electromagnetic field in terms of cylindrical coordinates  $(r, \phi, z)$  (cf. Fig. 1.10) as

$$\begin{aligned} \frac{\partial^2 E_z(r, \phi, z)}{\partial r^2} + \frac{1}{r} \frac{\partial E_z(r, \phi, z)}{\partial r} + \frac{1}{r^2} \frac{\partial^2 E_z(r, \phi, z)}{\partial \phi^2} \\ + \frac{\partial^2 E_z(r, \phi, z)}{\partial z^2} + k_0^2 n^2 E_z(r, \phi, z) = 0. \end{aligned} \quad (1.28)$$

The solution of a plane wave propagating in the  $z$ -direction with propagation constant  $\beta$  is  $2\pi$ -periodic in the  $\phi$ -direction due to the system's cylindrical symmetry, and hence described by

$$E_z(r, \phi, z) = A u(r) e^{-j l \phi + \phi_0} e^{-j \beta z}, \quad l = 0, \pm 1, \pm 2, \quad (1.29)$$

where  $A$  is the amplitude of the electric field,  $u(r)$  is the radial dependency of the solution and  $\phi_0$  is the phase. A differential equation spatially-dependent on  $r$  is obtained by introducing Eq. 1.29 in Eq. 1.28

$$\frac{\partial^2 u(r)}{\partial r^2} + \frac{1}{r} \frac{\partial u(r)}{\partial r} + \left( k_0^2 n^2 - \beta^2 - \frac{l^2}{r^2} \right) u(r) = 0. \quad (1.30)$$

For a complete study, the propagation constants of plane waves propagating in the core ( $k_0 n_{\text{cladding}} < \beta < k_0 n_{\text{core}}$ ) and cladding ( $n_{\text{cladding}} k_0 > \beta$ ) are decoupled, resulting in two new propagation constants expressed as

$$k_T^2 = n_{\text{core}}^2 k_0^2 - \beta^2, \quad (1.31)$$

$$\gamma^2 = \beta^2 - n_{\text{cladding}}^2 k_0^2. \quad (1.32)$$

The characteristics of waveguide modes are determined by these two parameters. The larger the value of  $k_T$ , the more the mode's radial distribution lies within the core region, while the larger  $\gamma$ , the faster the mode is attenuated towards the cladding. Combining Eq. 1.31 and Eq. 1.32 results in

$$\gamma^2 + k_T^2 = k_0^2 (n_{\text{core}}^2 - n_{\text{cladding}}^2) = k_0^2 \text{NA}^2, \quad (1.33)$$

where  $\gamma$  is imaginary for modes  $k_T > k_0(\text{NA})$ , leading to the description of unguided modes that exponentially decay with propagation distance. These parameters can be rewritten by defining two normalized variables as a function of the waveguides' radius  $a$  as

$$\begin{aligned} X &= k_T a, \\ Y &= \gamma a, \end{aligned} \quad (1.34)$$

and the normalized frequency  $V$  from Eq. 1.13 is recovered as

$$X^2 + Y^2 = V^2. \quad (1.35)$$

This demonstrates that the normalized frequency  $V$  remains unaltered independently of the approach, ray-optical or electromagnetic wave-based, and hence it does strictly depend on the waveguide structural parameters  $a$ , NA and  $\lambda_0$ . Then, the differential Eq. 1.30 can be reformulated using the propagation constants  $k_T$  and  $\gamma$  as

$$\frac{\partial^2 u(r)}{\partial r^2} + \frac{1}{r} \frac{\partial u(r)}{\partial r} + \left( k_T^2 - \frac{l^2}{r^2} \right) u(r) = 0, \quad r \leq a \text{ (core)} \quad (1.36)$$

$$\frac{\partial^2 u(r)}{\partial r^2} + \frac{1}{r} \frac{\partial u(r)}{\partial r} - \left( \gamma^2 + \frac{l^2}{r^2} \right) u(r) = 0, \quad r > a \text{ (cladding)}. \quad (1.37)$$

Considering boundary conditions where the electric field converges to 0 for  $r \rightarrow \infty$  and does not diverge for  $r \rightarrow 0$ , the solutions for  $u(r)$  are

$$u(r) \propto \begin{cases} J_l(k_T r), & r \leq a \text{ (core)} \\ K_l(\kappa r), & r > a \text{ (cladding)}. \end{cases} \quad (1.38)$$

The solutions of Eq. 1.38 are Bessel functions of the first kind and order  $l$  for  $J_l(k_T r)$  and modified Bessel functions, i.e. Neumann functions, of the second kind and order  $l$  for  $K_l(\kappa r)$ , respectively. Figure 1.11 depicts exemplary solutions of the radial distribution for (a)  $l = 0$  and (b)  $l = 3$ . The  $z$ -components of the electric  $E_z$  and magnetic  $H_z$  fields must be continuous at the core-cladding interface, hence the complete solutions of the components under these boundary conditions for a STIN cylindrical waveguides are

$$E_z(r, \phi, z) = \begin{cases} A J_l(k_T r) e^{-j l \phi} e^{-j \beta z}, & r \leq a \text{ (core)} \\ A \frac{J_l(k_T)}{K_l(\kappa)} K_l(\kappa r) e^{-j l \phi} e^{-j \beta z}, & r > a \text{ (cladding)}, \end{cases} \quad (1.39)$$

$$H_z(r, \phi, z) = \begin{cases} B J_l(k_T r) e^{-j l \phi + \pi/2} e^{-j \beta z}, & r \leq a \text{ (core)} \\ B \frac{J_l(k_T)}{K_l(\kappa)} K_l(\kappa r) e^{-j l \phi + \pi/2} e^{-j \beta z}, & r > a \text{ (cladding)}. \end{cases} \quad (1.40)$$

The  $z$ -components of the electric  $E_z$  and magnetic  $H_z$  fields are derived in Eq. 1.39 and Eq. 1.40, but the other field components  $E_r$ ,  $E_\phi$ ,  $H_r$  and  $H_\phi$  can as well be obtained by solving Maxwell's equations. The boundary conditions of continuity of  $E_\phi$  and  $H_\phi$  at the core-cladding interface  $r = a$  result in two additional equations, and one determines the dispersion relation that relates the propagation constant  $\beta$  with the core radius  $a$ , the vacuum wavelength  $\lambda_0$  and the refractive index of core ( $n_{\text{core}}$ ) and cladding ( $n_{\text{cladding}}$ ). The dispersion relation provides unique propagation constants  $\beta$  for each azimuthal mode with index  $l$ , which correspond to propagation constants of the different modes and their respective refractive indices as  $\beta_i = k_0 n_{\text{eff},i}$ . From the numerical solution of this equation, the parameters  $\gamma$  and  $k_T$  are determined (from Eq. 1.31 and Eq. 1.32), respectively.

Modes can be further categorized based on their field component values as transverse electric (TE) modes

$$H_r \neq 0; E_\phi \neq 0; H_z \neq 0; E_r = H_\phi = E_z = 0, \quad (1.41)$$

transverse magnetic (TM) modes

$$E_r \neq 0; H_\phi \neq 0; E_z \neq 0; H_r = E_\phi = H_z = 0, \quad (1.42)$$

and for the hybrid (HE and EH) modes, where no field component vanishes.

This description gives a full picture of the modes according to their category (TE, TM, HE and EH) and two positive integers  $l$  and  $m$ , which denote the rotational and axial shape of the modes, i.e.  $TE_{lm}$ ,  $TM_{lm}$ ,  $HE_{lm}$  and  $EH_{lm}$ . The index  $l$  is related to the index of the Bessel function and denotes the rotational shape of the modes, and therefore determines their azimuth symmetry. The index  $m$  denotes the radial shape of the modes, i.e. the number of zeros of the mode's intensities, which depends on  $\gamma$  and  $k_T$ . The vector fields of these modes are exact solutions of Maxwell's equations and therefore these calculations determine all the missing field components for cylindrical STIN waveguides. Importantly, the intensity profile  $I(r, \phi, z)$ , which is the physical quantity that is obtained from experimental analysis, is given by

$$I(r, \phi, z) = |\mathbf{E}(r, \phi, z)|^2 = |E_x(r, \phi, z)|^2 + |E_y(r, \phi, z)|^2 + |E_z(r, \phi, z)|^2. \quad (1.43)$$

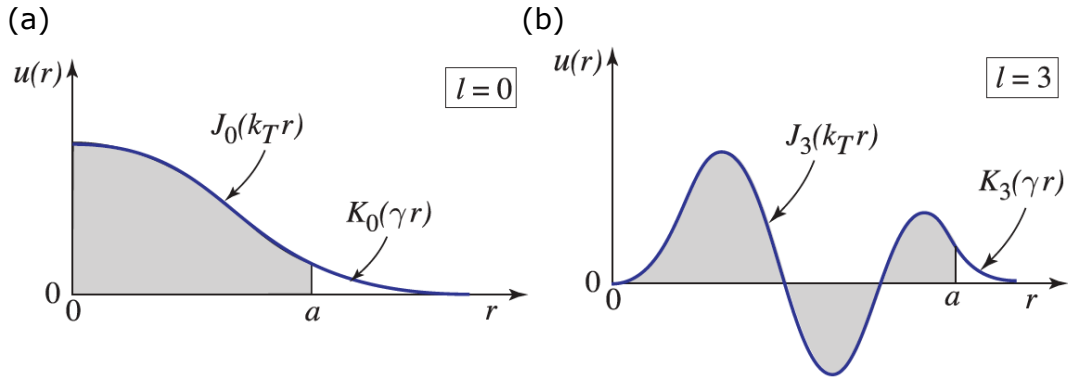


Figure 1.11: Radial distribution  $u(r)$  solutions for (a)  $l = 0$  and (b)  $l = 3$ . Shaded (unshaded) areas correspond to the waveguide core (cladding). The parameters  $\gamma$  and  $k_T$  have been selected such that the radial distribution  $u(r)$  has a continuous derivative at  $r = a$ . Extracted from [157].

### 1.2.2.3/ WEAKLY-GUIDING APPROXIMATION

As previously introduced, when the refractive-index contrast between core and cladding in STIN waveguides is small,  $\Delta n \ll 1$ , the guided rays can be considered paraxial, i.e. approximately parallel to the propagation axis. This considers that light is not strongly confined within the core, and hence the longitudinal components of electric and magnetic fields are much weaker than the transverse ones. The linear polarization in the  $x$  and  $y$  directions creates orthonormal states of polarization, therefore intensity profiles of the transverse electric fields ( $E_x$  and  $E_y$ ) that belong to the same linearly polarized (LP) mode have the same spatial distribution. This allows to simplify the analysis of waveguides and enables to analyse these modes as linearly polarized ( $LP_{lm}$ ), in which the two polarizations of modes ( $l, m$ ) travel with equal propagation constant  $\beta_{lm}$  and equal spatial distribution. Under the weakly-guiding approximation, and considering the condition of

continuity of  $u(r)$  at  $r = a$  and using the normalized parameters from Eq. 1.34, Eq. 1.38 results in

$$X \frac{J_{l\pm 1}(X)}{J_l(X)} = \pm Y \frac{K_{l\pm 1}(Y)}{K_l(Y)}. \quad (1.44)$$

The solution of the dispersion equation Eq. 1.44 corresponds to the combination of  $(l, m)$  indices of the normalized frequency  $V$  given by Eq. 1.35. Figure 1.12 (a) shows the intensity distributions of the  $E_x(E_y)$ -components of the electric field for the  $LP_{lm}$  modes and their respective vector modes ( $TE_{lm}$ ,  $TM_{lm}$ ,  $HE_{lm}$  and  $EH_{lm}$ ). The 2-fold (4-fold) degeneracy of  $LP_{01}$  and  $LP_{12}$  ( $LP_{11}$  and  $LP_{21}$ ) modes is defined by the polarization state of the cylindrical waveguides' modes. Moreover, there are two energetically equal configurations for  $\mathbf{E}(r, \phi, z)$  and  $\mathbf{H}(r, \phi, z)$ . Figure 1.12 (b) depicts the dispersion curves of the  $LP_{lm}$  modes for cylindrical STIN waveguides, where the propagation constant  $\beta$  is obtained by solving the dispersion equations for the different modes  $m$ . As seen, the value of the cut-off of the second lowest order mode  $LP_{11}$  is  $V_{\text{cut-off}} = 2.405$  (see Eq. 1.15).

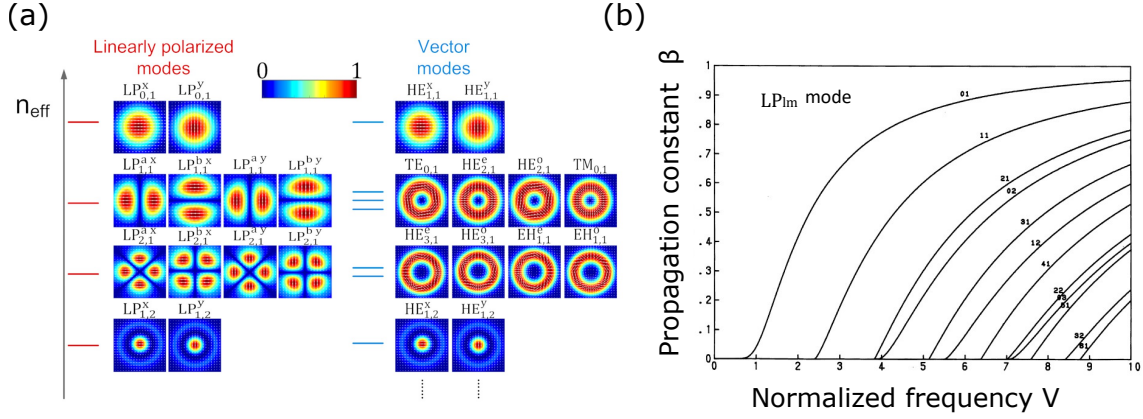


Figure 1.12: Optical modes and their dispersion relation in cylindrical photonic waveguides. (a) Normalized intensity distribution for linearly polarized (LP) modes and their respective representation in vector modes. Extracted from [162]. (b) Propagation constant  $\beta$  as a function of the frequency parameter  $V$  for different  $LP_{lm}$  modes. Extracted from [161].

### 1.2.3/ OPTICAL COUPLING BETWEEN WAVEGUIDES

As discussed, light propagates in a waveguide in the form of optical modes, and their shape depends on the normalized frequency  $V$ , i.e.  $NA = \sqrt{n_{\text{core}}^2 - n_{\text{cladding}}^2}$ , the wavelength  $\lambda_0$  and the core radius  $a$  (see Eq. 1.13). For total internal reflection, an external optical ray needs to be coupled from the input-facet of a waveguide. If the amplitude distribution of the light source matches the one of the mode in the waveguide, i.e. injected and waveguide modes are mode-matched, only one specific mode will be launched. The complex amplitude of the optical field travelling in the  $z$ -direction can be treated as a superposition of modes as

$$E(y, z) = \sum_m a_m u_m(y) e^{-j\beta_m z}, \quad (1.45)$$

where  $a_m$  is the amplitude,  $u_m(y)$  is the transverse distribution and  $\beta_m$  is the propagation constant of a mode  $m$ . The fraction of light transferred into the waveguide is determined by the degree of similarity between the transverse distributions of the light source and the waveguide's mode. The polarization of the incident radiation must also match with the one of the mode, i.e. linearly polarized for LP modes. The degree of resemblance between the light source distribution  $s(y)$  and mode  $u_m(y)$  distributions define the number of modes excited as well as the fraction of light transferred.

For multimode waveguides, the maximum coupling efficiency is achieved when  $0 < \theta < \theta_{max}$ , see Eq. 1.2. Therefore, the coupling efficiency is maximum if the maximum angle of the light source is equal to the waveguide's NA.

For single-mode fibers, to fulfill the condition of maximum coupling efficiency is challenging since the range  $0 < \theta < \theta_{max}$  is narrow due to the single-mode cut-off  $V_{cut-off} = 2.405$  condition. Additionally, diffraction effects cannot be ignored. The fundamental mode of a waveguide can be approximated by a Gaussian beam, since their intensity distributions are similar, and Gaussian light sources are commonly available from commercial lasers. At the focal point  $p$ , the electric field profile of a Gaussian beam's cross-section is defined as

$$\mathbf{E}(x, y, z = p) = \mathbf{E}_0 \cdot e^{-\frac{x^2+y^2}{\omega_0^2}}, \quad (1.46)$$

where  $\mathbf{E}_0$  is the electric field amplitudes and  $\omega_0$  is the waist radius, which is defined as the point where the intensity of the Gaussian beam drops to  $1/e^2$ . At a distance  $z$  away from the focus point  $p$ , the waist radius is given by  $\omega(z) = \omega_0 \sqrt{1 + (z/z_R)^2}$ , where  $z_R = (\pi\omega_0^2 n)/\lambda$  is the Rayleigh range and  $n$  is the refractive index of the medium. The full width at half maximum (FWHM) and the waist radius  $\omega(z)$  of a Gaussian beam at position  $z$  are related as  $FWHM(z) = \omega(z) \sqrt{2 \ln 2}$ . To fulfill the mode-matching condition, the beam waist  $\omega_0$  of the Gaussian distribution must be identical to the one of the fundamental mode in the waveguide.

### 1.2.3.1/ ADIABATIC TAPERS

Generally, the wavelength  $\lambda_0$  of the source beam is fixed and the matching condition to the waveguide's mode is not trivial without continuously adjustable external optical elements, such as lenses. A strategy to adapt between, both, the source and waveguide modes is using a taper, which involves gradually changing the waveguide's core dimensions from an input diameter  $d_{input}$  to an output diameter  $d_{output}$  throughout a length  $l_t$ , and Fig. 1.13 shows its structure.

The analysis of light propagation through tapered waveguides considers the refractive index profile over the cross-section of the taper. If the taper length  $l_t$  is large compared to the Rayleigh length ( $l_t \geq z_R$ ), the electric field distribution and propagation constant changes linearly and the light transmission is conserved. This transition occurs when the so-called adiabatic condition is fulfilled. The propagation constants  $\beta_i = k_0 n_{eff,i}$  for the local modes are obtained for each position along the taper throughout its length  $l_t$ . Assuming that the taper is axisymmetric, which is the case for cylindrical STIN waveguides, the fundamental local mode  $LP_{01}$  can couple only to modes with the same azimuthal symmetry, i.e. local and higher-order  $LP_{0m}$  cladding modes. This condition is satisfied when the

taper's length  $l_t$  is larger than the coupling length between the fundamental mode and the dominant coupling mode. However, if this condition is not satisfied, the field distribution does not change rapidly enough to keep up with the variation of the fundamental mode, and higher-order modes are excited due to the bending of its phase front, leading to light attenuation towards the cladding. The local coupling length between the fundamental and second local mode is given by the beating length  $z_b$  as

$$z_b = \frac{2\pi}{\beta_1 - \beta_2}, \quad (1.47)$$

where  $\beta_1 = \beta_1(z)$  ( $\beta_2 = \beta_2(z)$ ) are the respective propagation constants for fundamental (second) local modes. Accordingly, when  $l_t > z_b$ , negligible coupling occurs and the fundamental mode will propagate adiabatically along the taper with minimal losses, while for  $l_t < z_b$  a significant coupling to higher mode occurs and the fundamental mode does not propagate throughout the taper section.

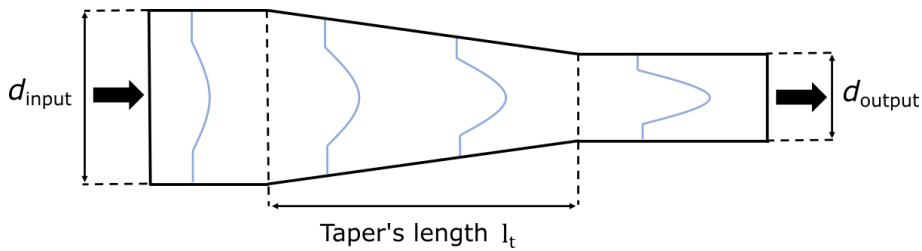


Figure 1.13: Schematic illustration of a taper's geometry used for external mode-matching. The input diameter  $d_{input}$  is tapered throughout a taper-length  $l_t$  until matching the output diameter  $d_{output}$ .

### 1.2.3.2/ COUPLING BETWEEN WAVEGUIDES

The ability to split light between optical components is of vital importance in order to realize optical integrated circuits. Light can be transferred between two waveguides that are sufficiently close to each other, and the coupled-mode theory analyzes their coupling efficiency. The basic principle of waveguide coupling is that when two waveguide cores with refractive indices  $n_{core,1}$  and  $n_{core,2}$ , respectively, are embedded in a medium where  $n_{cladding} < n_{core,1}(n_{core,2})$ , the optical signal can be transferred between the waveguides. Importantly, the waveguides need to be separated by a distance  $g$  sufficiently small to allow their optical fields outside the waveguide cores, i.e. evanescent fields, to overlap.

When two waveguides are far apart, their field amplitudes remain independent as  $a_1(z) = u_1 \exp(-j\beta_1 z)$  and  $a_2(z) = u_2 \exp(-j\beta_2 z)$  (see Eq. 1.45). However, when they come into sufficiently close proximity, their coupling modifies the amplitude of their guided field modes without modifying their transversal spatial distributions and propagation constants. The coupling can be conceived as a scattering effect: the field distribution from one waveguide is scattered into the second waveguide, hence creating a source of light that changes the field amplitude of the second waveguide, and vice versa. The coupling strictly depends on the distance  $g$  due to the exponential decay of the evanescent field outside of the waveguide's core. The mode amplitudes of both waveguides are consequently functions of  $z$ ,  $a_1(z)$  and  $a_2(z)$ , and the coupling between waveguides requires determining  $a_1(z)$  and  $a_2(z)$  under specific boundary conditions.

The most common photonic components in order to study the coupling between waveguides, as depicted in Fig. 1.14, are (a) directional couplers [163], (b) multi-mode interference (MMI) couplers [164] and (c) tapered velocity couplers [165]. The latter leverages the effect of a continuously changing waveguide radius in order to modify propagation conditions such that light is transferred from one input to a number  $M$  of output waveguides. Figure 1.14 (c) schematically illustrates a single-mode inversely-tapered velocity coupler (left panel) and its change of the propagation constant of the fundamental mode (right panel). The interaction of the two modes has its maximum where the propagation constant of the waveguides A and B matches. When this condition is fulfilled, light transfer between different modes of dissimilar cores is enabled. These optical splitters, their 3D fabrication and their experimental characterization are further discussed in Chapter 3.

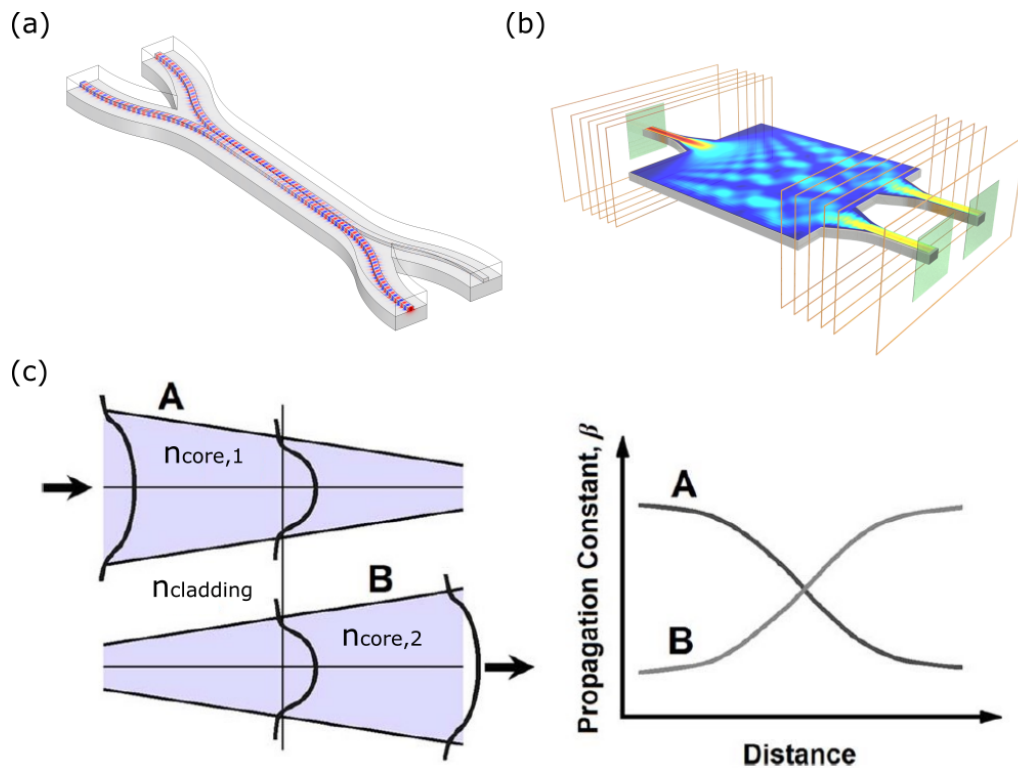


Figure 1.14: Schematic illustration of different mechanisms leveraging optical coupling between waveguides in order to split optical signals. (a) Directional couplers. Extracted from simulations by COMSOL Multiphysics. (b) Multi-mode interference (MMI) units. Extracted from simulations by Lumerical Inc. (c) Tapered velocity couplers. Extracted from [165].

### 1.3/ 3D PHOTONIC INTEGRATION VIA PHOTO-INDUCED POLYMERIZATION

A general overview of state-of-the-art manufacturing platforms towards 2D and 2.5D photonic integration has been presented in the introductory Section 1.1.1. In Section 1.3, an extensive discussion of the 3D photonic integration via photo-induced polymerization is realized [166, 167]. The fabrication of the 3D photonic components presented

in this manuscript leverages the polymerization of monomeric units via femtosecond (fs) laser-based processes [168]. Generally, the excitation produced from the absorption of a single photon, or the simultaneous absorption of two photons, is needed to launch the photo-polymerization process, i.e. transition from monomer solutions to solid polymers [169]. One-photon polymerization (OPP) is a widespread technique implemented during the inter-layer photo-mask fabrication of photonic and electronic semiconductor ICs. However, while OPP is capable of polymerizing large areas in 2D, its capacity for creating complex structures in 3D is severely limited. To this aim, the nonlinear TPP combined with DLW lithography allows the single-step and mask-free additive fabrication, i.e. layer-by-layer, of a wide range of materials such as polymers, metals or ceramics [170, 171, 167]. Combined, these two processes result in the formation of solid structures with sub-diffraction limit resolution, whose optical properties can be dynamically adjusted. All these aspects are of vital interest for the fabrication of 3D waveguides, which are the fundamental units for light guiding in optical communication systems as discussed in Section 1.2.

### 1.3.1/ PHOTO-POLYMERIZATION

Photo-polymerization is the process of using light as the energy source to induce photo-chemical reactions. These reactions constitute a phase transition from small unsaturated molecules in the liquid state, i.e. monomers, towards solid macromolecules via polymerization reactions. The basic component of the starting liquid material is the monomer, and their polymerization is triggered upon illumination under a particular illumination source, typically in the ultra-violet (UV), visible or infra-red (IR) range. Photoresists are classified as positive or negative. When exposed to light, a positive resist becomes soluble and the surrounding material solidifies into a polymer, while for a negative resist, only the region exposed to the light is polymerized. For efficient monomer-to-polymer conversion, usually, a photoinitiator that absorbs the light needs to be present in the initial monomeric solution, yet recent studies have shown polymerization of resins with the absence of photoinitiators [175]. This photoinitiator acts as a catalyst for the chemical reaction. When exposed to light with wavelength  $\lambda$ , the photoinitiator first absorbs energy and consequently produces an active species, i.e. radicals, that react with the monomers in the solution. Once the energy is sufficient to launch the process, the photo-polymerization is started. Typically, both, photoinitiator and monomer are transparent at the same wavelengths to minimize light absorption.

### 1.3.2/ ONE-PHOTON POLYMERIZATION

One-photon polymerization is the process that occurs when a single photon launches the photo-polymerization reaction. Figure 1.15 (a) and (b) show the energy diagram and the reaction's schematics for OPP, respectively. In the initiation step, the photoinitiators are excited electronically from the ground state  $|n\rangle$  to the singlet excited state  $|n+1\rangle$  by absorbing a single photon with energy  $h\nu$ , often in the UV range, see Fig. 1.15 (a). Then, the photoinitiators can either relax to the ground state by emitting fluorescence light, or the excited state population is transferred to a long-living triplet state via intersystem crossing (ISC). This triplet photon-based energy excitation results in the generation of radicals, which trigger the chain propagation by producing new single bonds between monomer

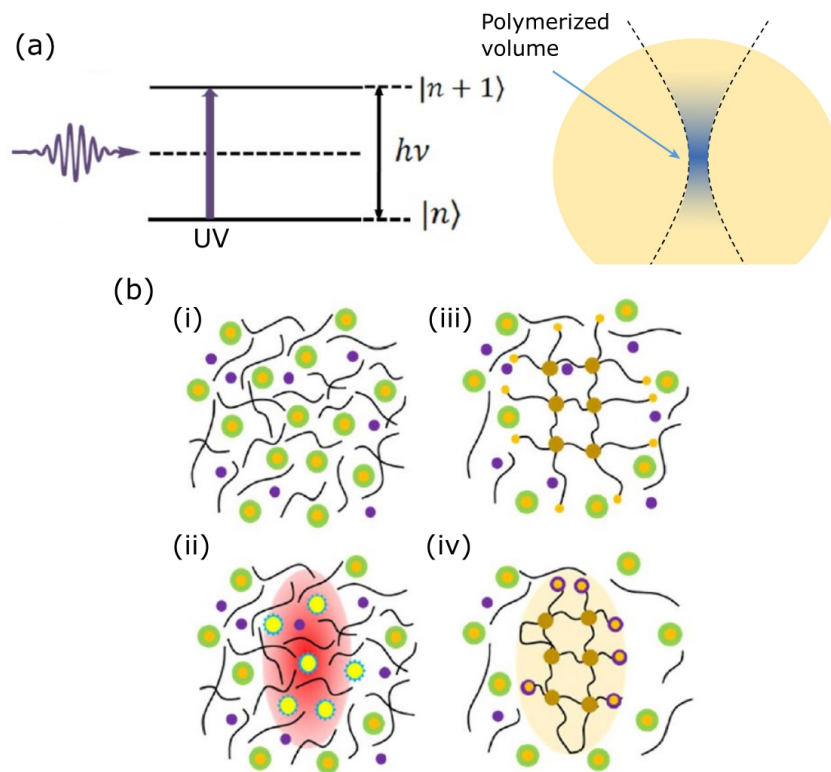


Figure 1.15: General concept of photo-polymerization of photoresists. (a) Schematic representation (left panel) of the energy-level diagram for the absorption of one photon with the energy necessary (UV range) to excite the electronic transition between ground  $|n\rangle$  to excited  $|n+1\rangle$  state. Extracted from [172]. Single photon excitation polymerizes a volume all along the continuous wave (cw) radiation (right panel). Extracted from [173]. (b) Illustration of the reaction process in a liquid photoresist containing monomers/oligomers (black lines), photoinitiators (green rings) with associated radicals (yellow circles), and photoinhibitors (purple dots). (i) State before initiation and (ii) situation after initiation. The red region corresponds to the area exposed to the light source, while the blue corona represents the emitted fluorescence. The sequential steps in the reaction mechanism, including (iii) chain reaction propagation and (iv) termination/quenching processes. The shaded portion in yellow portrays the volume that has undergone photopolymerization. Extracted from [174].

molecules, rapidly increasing the weight of the polymer chain, which fully solidifies in the process. The polymer chain's growth is finalized via a quenching reaction during which a radical or single bond encounters an inhibitor, e.g. oxygen, or a radical and single bond encounter each other as seen in Fig. 1.15 (b). The physical, chemical and mechanical properties of the solidified polymer strictly depend on the nature of the monomer solution, i.e. molecular weight, reactive groups and concentration of both the photoinitiator and photoinhibitor, as well as the optical illumination intensity.

OPP is extensively used in current 2D photo-lithography technology employed for electronic semiconductor and photonic ICs comprising thin material layers. The process utilizes exposing a photosensitive resin through a photo-mask comprising specific design patterns to process, and to usually stack various thin material layers and create 2D structures by repeating this process layer-by-layer. This includes applying the photoresist,

exposing it using a photo-mask, the etching process, and several washing and rinsing steps. For highly repetitively structured patterns like SD (secure digital) memory cards, this results in ICs with up to 100 or more circuit layers. However, stacking several layers using this generically 2D fabrication concept has several drawbacks. Firstly, it requires precise alignment of the photo-mask multiple times in each photo-lithographic step, which is challenging and time-consuming. Secondly, it is the economic appeal, since each process step must be repeated in a loop-like manner between each layer. An economically advantageous approach would be a process where the entire IC's volume is created during just a few such process steps.

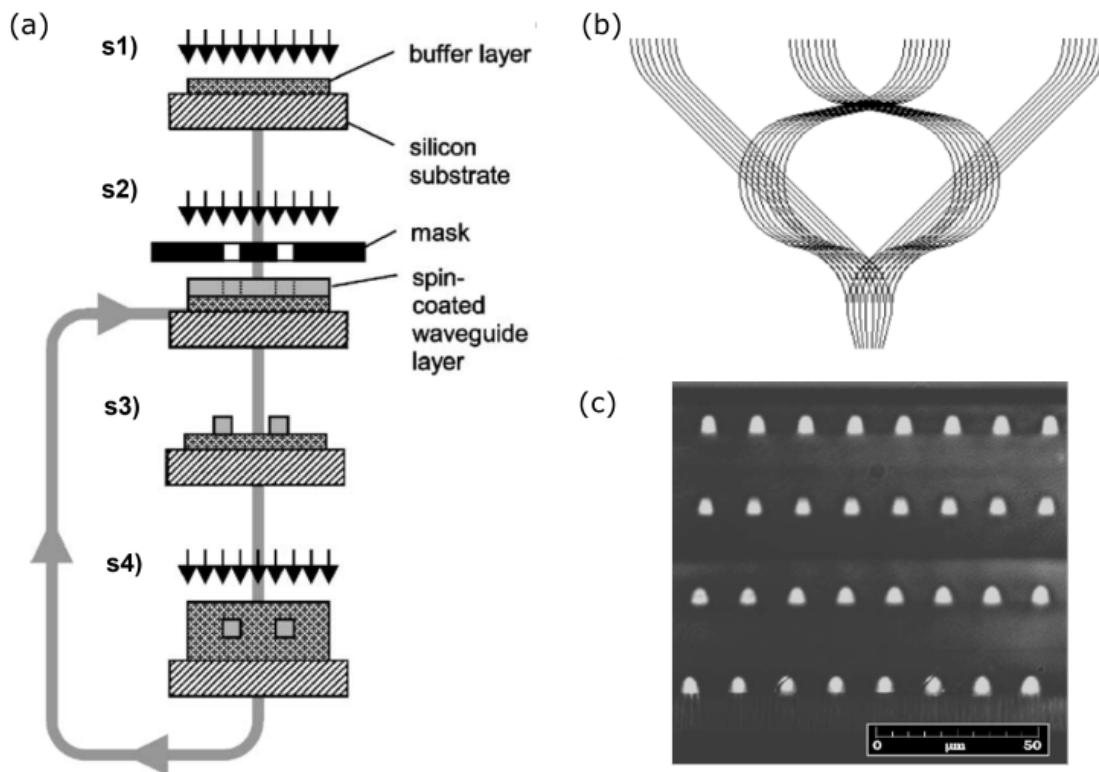


Figure 1.16: Multilayer 3D waveguide fabrication via OPP. Extracted from [176]. (a) Schematic diagram of the fabrication sequence using spin coating and simple direct UV photolithography curing (s1); UV irradiation of the waveguides using a mask (s2); development (s3); UV irradiation of the cladding (s4). (b) Layout of the 3D interconnect polymer structure with an array of 4x8 waveguides. (c) Cross-section microscope optical image of 4x8 stack waveguides.

Generally, the optical exposure dose  $D$  determines the refractive index  $n$  of the polymerized resin [177]. In 2D photo-lithography, the refractive index of a resin is altered via OPP for significantly large volumes, and unintended irradiation doses strongly accumulate in volumes outside the targeted exposure plane. Consequently, precisely controlling a 3D refractive index distribution with high spatial resolution on the scale of an optical wavelength, i.e. a volume hologram, is challenging. OPP is therefore more appropriate for the simultaneous polymerization of large areas, such as in classical 2D lithography, for large uniform volumes of volume holograms with lower spatial resolution. Despite this, stacked 2D lithography has also been used for complex 3D photonic integration, see Figure 1.16, as well as in tomographic volumetric 3D printing [178]. However, this approach

suffers from the aforementioned drawbacks of multiple photo-mask alignment steps and economic relevance.

### 1.3.3/ TWO-PHOTON POLYMERIZATION INDUCED VIA FEMTOSECOND PULSES

Two-photon polymerization leverages the nonlinear, i.e. second-order, nature of two-photon absorption (TPA). TPA is a quantum mechanical three-body process in which a molecule absorbs two photons simultaneously to exceed the energy gap  $h\nu$  between ground  $|n\rangle$  and excited states  $|n+1\rangle$ . As light interacts with a molecule, a virtual state is formed when the first photon with energy  $h\nu/2$  is absorbed. This virtual state persists for a very short duration (on the order of fs), resulting in two-photon absorption if a second photon with energy  $h\nu/2$  is absorbed before the decay of this virtual state. Figure 1.17 (a) illustrates the typical energy-level diagram for the TPA process, in which contrary to OPP the energy of a single photon is in the near-infrared (NIR) range. Consequently, TPA is the physical phenomena behind photo-polymerization via two-photon polymerization.

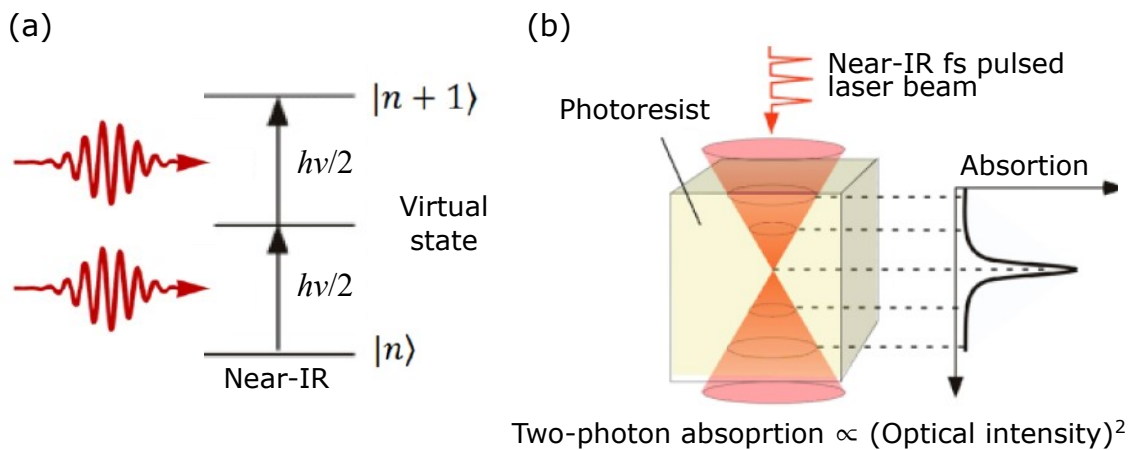


Figure 1.17: Two-photon polymerization process. (a) Schematic representation of the energy-level diagram for the absorption of two photons with the energy necessary (Near-IR range) to assist the electronic transition between ground  $|n\rangle$  to excited  $|n+1\rangle$  state with intermediate, virtual state. Extracted from [174]. (b) Two-photon absorption is proportional to the square of the light intensity, and allows for strong confinement of light at the focal point, enabling the solidification of liquid molecules into solid polymers with submicron dimensions. Extracted from [171].

The fundamental difference between one- and two-photon polymerization is the way a photon's energy for activating the photoinitiators, hence launching the photopolymerization, is delivered. Typically, UV continuous wave (cw) radiation is used to induce OPP, whereas pulsed light in the range of near-IR is required for TPP, see Fig. 1.17 (a) and (b). As TPP is a second-order nonlinear optical process, high-intensity pulsed light sources are required. The ultra-short pulse duration of  $\approx 80$ -100 fs and the high peak power of up to  $10^{20}$  W/cm<sup>2</sup> of a femtosecond laser fulfills these requirements and provides unprecedented extreme physical conditions for micromachining of materials based on high laser power density [179, 180]. When such high optical intensity is employed, the optical absorption  $\alpha$  becomes dependent on the excitation intensity  $I$  according to

$$\alpha(I) = \alpha_0 + \beta_{\text{TPA}}I, \quad (1.48)$$

where  $\alpha_0$  ( $\beta_{\text{TPA}}$ ) are the linear absorption (TPA coefficient), respectively. In TPA processes,  $\beta_{\text{TPA}}$  is strictly associated with the TPA cross-section  $\sigma_{\text{TPA}}$  as

$$\beta_{\text{TPA}} = \frac{N\sigma_{\text{TPA}}}{h\nu}, \quad (1.49)$$

with  $N$  being determined by the concentration of monomers, photoinitiators and photoinhibitors in the primary photoresist solution. From Eq. 1.49, the TPP efficiency is determined by the TPA coefficient  $\beta_{\text{TPA}}$  and, unlike OPP, the photoinitiator needs not only to absorb at one specific wavelength  $\lambda$ , but a high two-photon cross-section ( $\beta_{\text{TPA}} \propto \sigma_{\text{TPA}}$ ) is further required. For most photoinitiators used for TPP, the TPA cross-section is on the order of  $\sigma_{\text{TPA}} = 10^{-50} \text{cm}^4 \text{s/photon}$ .

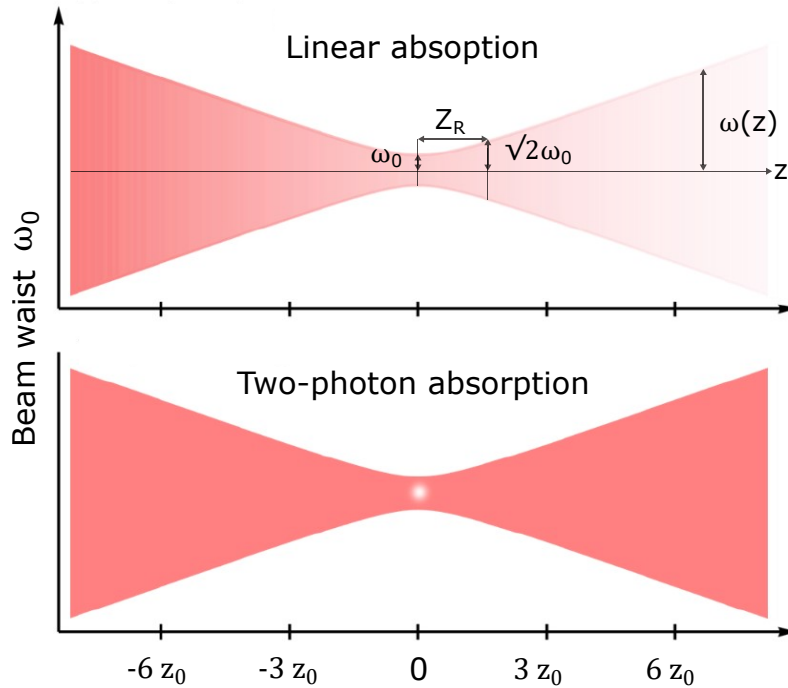


Figure 1.18: Schematic illustration of the focused laser beam's reduction in intensity due to the absorption of either one (top panel) or two (bottom panel) photons. The areas in white represent the degree of attenuation. The vertical axis represents the Gaussian beam width  $\omega(z)$  as a function of distance  $z$  in units of the confocal parameter ( $z_0$ ), which is defined as the distance from the focal plane where the beam waist  $\omega_0$  expands by a factor of  $\sqrt{2}$ , and its related  $z_R$  Rayleigh length. Extracted from [174].

Generally, the intensity of light  $I$  is attenuated exponentially as it propagates throughout a material. When the wavelength is in the range of transparency of the photoresist and photoinitiator, then  $\alpha_0 = 0$ , and the light dissipation rate along the propagation  $z$ -direction is expressed as

$$\frac{dI(z)}{dz} = -\beta_{\text{TPA}}I^2(z), \quad (1.50)$$

where the dissipation rate for a TPA process is quadratically dependent on the light intensity [169]. In contrast with linear processes like OPP, the nonlinear dependency of TPA on light enables very high spatial confinement when the optical excitation is focused using high-intensity fs-pulsed lasers. Figure 1.18 compares light dissipation for one- (top panel) and two-photon (bottom panel) absorption, respectively. As illustrated here, the optical amplitude is exponentially attenuated throughout the medium for linear absorption, while it is tightly confined within the laser focal volume for TPA.

### 1.3.3.1/ DIRECT-LASER WRITING LITHOGRAPHY

Direct-laser writing is a 3D printing technology that benefits from the TPP concept for the construction of sub- $\mu\text{m}$  resolution features. An essential optical element in DLW-TPP is the microscope objective (MO), which is used to tightly focus the fs-laser beam. The lateral resolution achievable via DLW is given by Abbe's diffraction limit as

$$R_{\text{Abbe}} = \frac{\lambda}{2\text{NA}}, \quad (1.51)$$

where  $R_{\text{Abbe}}$  refers to the focal spot radius,  $\lambda$  is the radiation wavelength and  $\text{NA} = n \cdot \sin(\theta)$  is the numerical aperture (see. Eq. 1.2) of the microscope objective. The inset in Fig. 1.19 (a) depicts the operation principle of DLW for different microscope objectives, showing that the shorter the working distance ( $\text{WD}_2 < \text{WD}_1$ ), the greater NA ( $\text{NA}_2 > \text{NA}_1$ ). At the focal spot volume, the smallest printable 3D volume is commonly named TPP-voxel, which is analogous to a 2D pixel. In DLW-TPP, the dimension of the polymerized voxel  $\propto 1/(\text{NA})^4$ , therefore the NA of the microscope objective needs to be large in order to achieve sub-diffraction resolution features.

The additive fabrication of 3D structures with complex shapes via DLW-TPP requires dynamically moving either the fs-laser beam or the sample in all three-spatial dimensions. The focus can be displaced using galvanometric scanners, while the sample can be displaced with high-precision using  $xyz$  piezoelectric stages. A typical galvanometric system is depicted in Fig. 1.19 (a), which comprises a scanning galvo-mirror, whose changing angles steer the optical beam through a focusing microscope objective, and the different angles result in different focal positions within the  $xy$ -plane of the sample. The galvanometric setting allows to polymerize photoresists at high-scanning speeds (up to 5 m/s), based on a layer-by-layer approach. The layout design of a structure is first 'hatched  $h$ ' in the lateral  $xy$ -directions, and then 'sliced  $s$ ' along the  $z$ -direction. Using a high-resolution translation stage, the microscope objective is displaced to different vertical layers to perform the slicing required for large-scale additive fabrication. Contrary, when using only  $xyz$  piezo-stages, the design is not 'sliced', rather the stage is directly moved in all directions by the piezoelectric stages with nm-scale accuracy. 3D structures are therefore created from continuous writing of 3D lines. A clear disadvantage of using piezo-stages compared to galvanometric scanners is the shorter travel distances (up to a few hundred  $\mu\text{m}$  at tens of  $\mu\text{m/s}$ ), yet the accuracy is significantly higher since the beam does not move and is therefore not distorted by passing the microscope objective at potentially higher angles. For this reason, most commercial systems have both galvanometric systems and high-accuracy  $xyz$  piezo-stages, switching between those depending on the requirements.

In standard DLW settings, the short distance between the focal plane and the surface of the objective, i.e. the working distance, is the principal limiting factor to fabricating

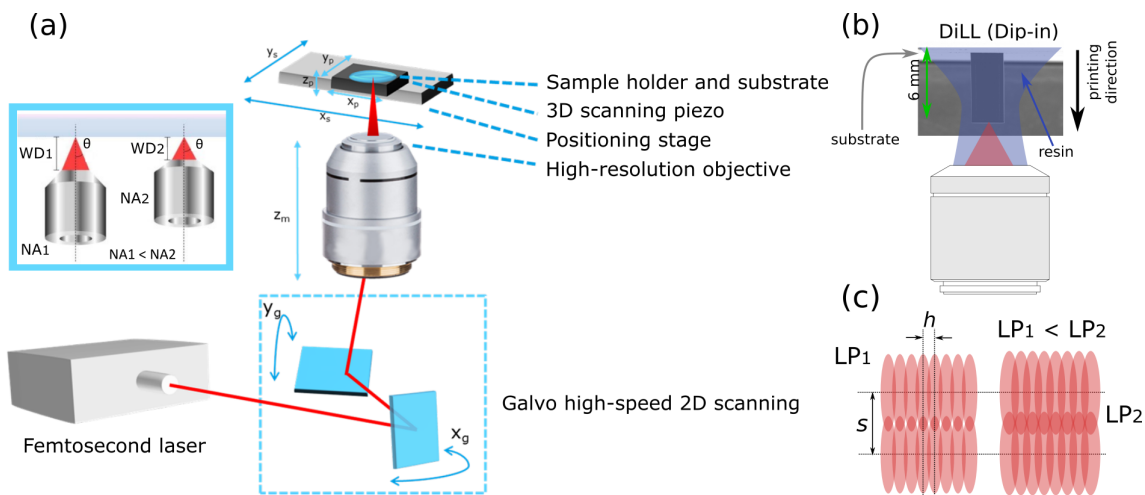


Figure 1.19: Direct-laser writing lithography scheme. Extracted from [114]. (a) The fs-pulsed laser is scanned through the monomer photoresist via high-speed galvo-mirrors. A piezo-stage controls displacement in the  $z$ -position with high-accuracy. (b) DLW fabrication with 'dip-in' technique. The microscope objective, which moves downwards during DLW-printing, tightly focused at the photoresist-substrate interface. The maximum height of 3D printed structures is  $\sim 8$  mm. (b) The resin is polymerized via two-photon absorption, forming voxels that are placed on a 3D lattice determined by hatching (slicing) distance  $h$  ( $s$ ) in the  $(x, y)$ -plane ( $z$ -direction). These parameters as well as the laser power ( $LP$ ) determine the overlapping between neighboring voxels, which defines the minimum feature size and the smoothness of 3D printed structures. A larger (lower) laser power  $LP_2$  ( $LP_1$ ) leads to larger (smaller) voxel sizes.

tall ( $> 1$  mm) structures [181]. This is because the 'slices' of the structure are consecutively created as the sample moves away from the MO, hence the sample distance can be increased as long as a continuous volume of liquid resist is deposited between MO and sample. The 'dip-in' lithography configuration from Fig. 1.19 (b) overcomes this limitation by immersing the microscope objective into a liquid photoresist, hence the WD becomes a non-limiting factor for the polymerization of features up to  $\sim$  cm height [148]. Important for CMOS compatibility, it enables printing on materials that are not transparent at the fs-laser's wavelength. This turns DLW into a mask-free and CMOS compatible technique for the additive manufacturing of complex 3D micro-structures with very high aspect-ratio [182]. However, in order to print large structures ( $\text{mm}^3$ ), it is currently necessary to stitch together different writing fields. This process is similar to the stepper process used in 2D semiconductor lithography. To increase the writing field, a lower NA microscope objective can be chosen, but this results in reduced printing resolution.

The size of a single polymerized voxel relative to the scanning speed of the printing laser is critical for the quality of the produced 3D structure and its integration. The photoinitiation of the chemical reaction is almost instantaneous compared to the writing speed, thus the writing volume is directly dependent on the laser's scanning. However, polymerization is a chemical reaction with a time scale that is typically orders of magnitude slower than the galvo-controlled laser scanning. This is an essential aspect since polymerization occurs for multiple neighboring voxels at overlapping times. Consequently, the polymerization process becomes more uniform, and the resulting structures are not subject to unintended variations in material properties that result from stitching countless small vox-

els together to form a large structure. Figure 1.19 (c) provides a schematic illustration of the overlapping between neighboring polymer voxels and its dependence on the writing laser power  $LP$ , hatching distance  $h$  and slicing  $s$  distance.

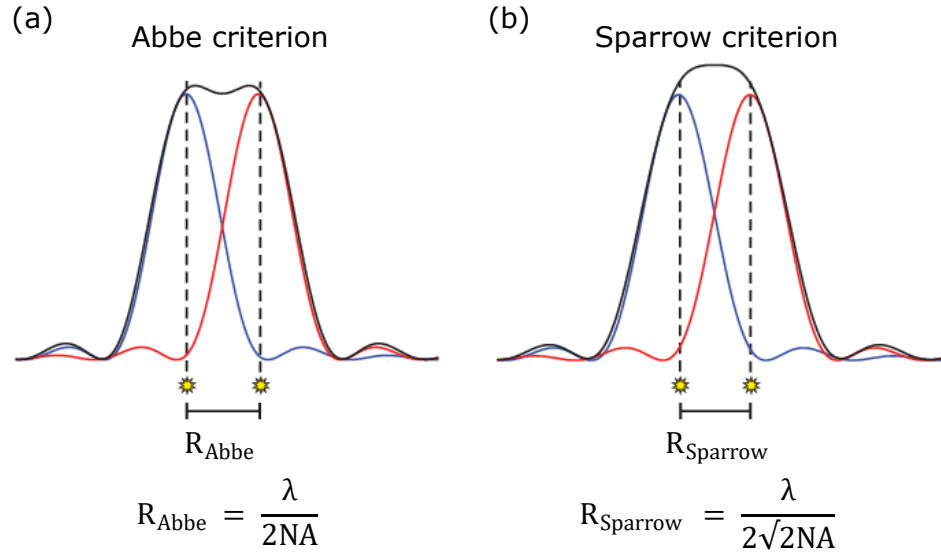


Figure 1.20: Microscope resolution criteria. Extracted from [183]. (a) In the Abbe criterion, two Airy discs get close to each other with a dip recognizable in-between. (b) In the Sparrow criterion, the maximum of the two Airy discs overlaps and hence merge into a flat surface.

In DLW-TPP, the minimum lateral separation  $R_{\text{Sparrow}}$  between two neighboring voxels is given by the two-photon Sparrow criterion [184] as

$$R_{\text{Sparrow}} = \frac{\lambda}{2\sqrt{2}NA}, \tag{1.52}$$

which contrary to Abbe's diffraction limit definition considers that a spectral line pair (broadened by diffraction) is still resolvable as long as there is a local minimum in the middle of the signal [185]. This criterion applies to serial lithography schemes such as DLW-TPP, where sequential exposures accumulate in their entirety. In such cases, the presence of a local minimum in the sum of two shifted point exposures becomes essential for separating singular points, even with a perfectly sharp threshold. To apply this criterion to sequential two-photon exposures, the intensity profiles are replaced with their squares. Figure 1.20 compares the definition of lateral resolution following both the (a) Abbe and (b) Sparrow criterion.

### 1.3.4/ DYNAMIC POWER RANGE OF PHOTORESISTS

In DLW-TPP, it is crucial to consider the degree of polymerization of the photoresist, which determines its refractive index  $n$  through the Clausius relationship. This relationship states that the refractive index of a material is dependent on the number of molecules within a given volume. In the case of certain photoresists, the solid polymer phase exhibits a higher density compared to the liquid resin phase. This density difference is influenced by the kinetics of polymerization, which in turn is driven by, both, the intensity and duration

of light exposure. Consequently, the refractive index of the photoresist can be adjusted with the light exposure [186].

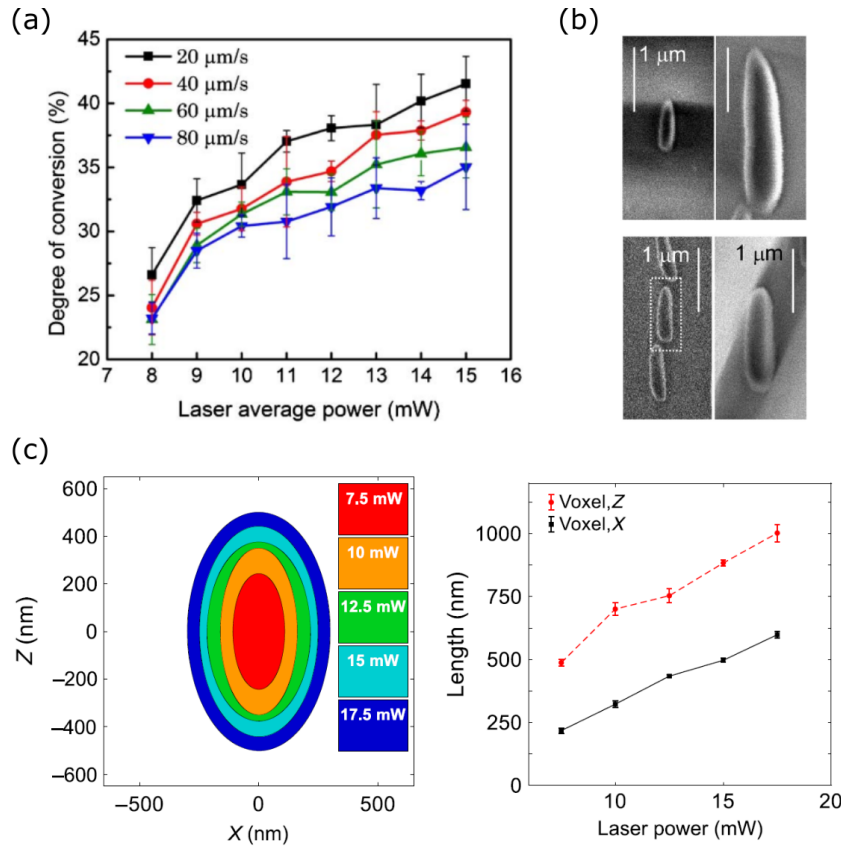


Figure 1.21: Fabrication parameter characterization for the dynamic power range of photoresists. (a) Degree of conversion (polymerization) dependence on the average LP and writing speed. Extracted from [187]. (b) SEM micrograph of typically cigar-shaped TPP-voxels. Extracted from [188]. (c) Best-fit ellipses of TPP-voxel dimensions over average laser power  $LP \in \{7.5 : 2.5 : 17.5\}$  mW. Extracted from [146].

The type of photoresist and dose parameters such as scanning speed and LP primarily influence its degree of polymerization. When the fs-laser peak power is below the TPP-threshold, the energy deposited in the focal spot is not sufficient to trigger the nonlinear TPA process, and the polymerization is not initiated. The laser-induced breakdown is reached when high laser irradiation induces damage in the photoresist by ablation processes, resulting in micro-explosions inside the bulk material. The dynamic power range of the photoresist lies between the TPP-threshold and the breakdown limit, and it can be adjusted by modifying the fabrication parameters ( $h$  and  $s$  distances) and the dose parameters ( $D$ ) to modify the size of the TPP-voxel without introducing additional defects. Therefore, the degree of polymerization, hence the refractive index, of the photoresist can be tailored by gradually modifying the exposure energy  $D$  and its duration within the dynamic power range window.

Figure 1.21 (a) shows the degree of conversion (%) versus the laser power LP (mW) and scan speed ( $\mu\text{m/s}$ ) for the exemplary IP-L 780 photoresist. As seen, its dynamic power range lies between  $LP = 8$  mW and  $LP = 15$  mW, and increasing the LP leads to a higher degree of conversion of the photoresist. For fixed LP, the degree of conversion increases

for lower scan speeds due to a larger effective energy deposition in the writing voxel per time and volume [188]. Generally, the voxel size can be tailored by almost two orders of magnitude within the dynamic power range. Figure 1.21 (b) and (c) show the standard cigar-shape of the TPP-voxel and its size evolution in, both, the  $x$ - and  $z$ -directions versus LP, respectively. As polymerization is a time-dependent process, the hatching and slicing distances equally contribute to the degree of conversion. Increasing the laser power to fabricate 3D structure is preferred over decreasing the voxel-to-voxel distances, as the printing time scales quadratically with the lateral distance. All these parameters need to be precisely adjusted in order to achieve the desired material property of the final 3D printed structure, i.e. refractive index, resolution, roughness and mechanical stability.

### 1.3.5/ ADVANTAGES AND CHALLENGES OF ADDITIVE DLW-TPP FABRICATION

Over the past 15 years, DLW-TPP has become a versatile tool for the fabrication of polymeric structures with sub-micron dimensions [189, 29, 190]. Unlike 2D planar approaches such as electron-beam lithography or mask-based photo-lithography, it enables the fabrication of complex 3D structures [191]. DLW-TPP plays a crucial role in many proof-of-concept designs in fields such as optics, acoustics [192, 193], elasticity [194, 195, 191, 196], robotics [197], and electric transport [198]. However, significant challenges, such as the inclusion of conductive resins [199], quantum-dots (QDs) doped resins [200] and liquid-crystals doped resins [201], are still in the development phase. Recently, there has been significant progress towards parallel DLW, which substantially accelerates the fabrication process [202]. Furthermore, different polymerization concepts are continually being developed, some of which use novel approaches to high-resolution 3D printing based on polymer resins [203]. It is worth noting that the recently demonstrated two-color fabrication method has the potential to substantially increase fabrication speed while moderately improving minimal feature size [204].

Although the clear advantages offered by DLW-TPP towards the creation of 3D photonic free-form structures, it still faces challenges in terms of widespread implementation [205]. From a manufacturing perspective, and compared to classical 2D lithography, TPP is cost-effective, scalable, and capable of constructing complex designs suitable for visible nanophotonic applications, achieving feature sizes of approximately  $\sim 200$  nm [206, 180, 207], see Fig. 1.5. However, for many specific applications, a higher resolution of around  $\sim 10$  nm is required, which can only be achieved through electron-beam or deep ultraviolet (DUV) lithography. Its relatively large fabrication time and spatial resolution limitation restrict the large-scale implementation of TPP. Additional limiting factors are the geometrical artifacts that alter optical properties at a local or global level. These artifacts can arise from the photo-induced polymerization process and modifications during development, including shrinking [208, 209], thermal diffusion [210], striation [211], and undesired photo-polymerization of areas with a low degree of polymerization [208, 177].

Summarizing, the main advantages of additive DLW-TPP fabrication are

- Single-step, single-material and truly 3D fabrication of complex photonic structures.
- Moderate fabrication speed (on the order of  $0.001$ - $0.01$  mm<sup>3</sup>/h), see Fig. 1.5.
- Dynamically control of optical properties such as the degree of polymerization, i.e. refractive index  $n$ , of photoresists.

- Widespread and developing technology. Several companies commercialize DLW-TPP systems while improving overall performances.

and the challenges are

- Medium spatial resolution. Although  $\sim 200$  nm feature sizes are achievable via TPP, a much higher resolution ( $\sim 10$  nm) is commonly required for certain advanced photonic devices and metasurface designs.
- Local and global artifacts appearing during TPP-fabrication, which alter optical properties at a local or global level of the printed structure.
- Spatiotemporal variation of chemical and material properties such as polymerization density, and the inclusion of oligomers in the final structures

### 1.3.6/ DLW-TPP FABRICATION COMMERCIAL SYSTEM

The 3D photonic components presented in this thesis have been fabricated via the commercial Nanoscribe GmbH (Photonic Professional GT) system. Nanoscribe provides all the essential tools and materials enabling the fabrication of 2D, 2.5D and 3D polymeric structures with feature sizes from sub- $\mu\text{m}$  to mm scales, see Fig. 1.5. Via its DLW-TPP fabrication methodology, high-resolution polymer-based objects are printed at high-speeds via galvanometric and  $xyz$  piezo-stages. The system is equipped with a high-intensity fs-laser source with a center wavelength at  $\lambda = 780$  nm, which triggers the nonlinear TPA process when the beam is tightly focused through a high-NA microscope objective into a transparent photoresist.

#### 1.3.6.1/ IP-RESINS OVERVIEW

For DLW-TPP fabrication via Nanoscribe GmbH, the commercial negative-tone IP, i.e. IP-Dip, IP-S and IP-Q, thermosetting photoresists are used [212, 177, 213, 214]. Table 1.1 summarizes their main properties. All the photoresists are essentially transparent from  $\lambda = 633$  nm until  $\lambda = 2400$  nm. Importantly, different combinations of microscope objectives and photoresists determine the smallest feature size and the total printable volume of the 3D printed structures. This defines the fabrication of small (IP-Dip, NA = 1.4), medium (IP-S, NA = 0.8) and large (IP-Q, NA = 0.3) features sizes. The combination of NA and photoresist equally determines the hatching  $h$  and slicing  $s$  distances needed to fabricate smooth 3D structures, and hence the average printing time. For instance, the combination of IP-Dip photoresist and microscope objective (63X, NA = 1.4), hatching (slicing) distances of  $0.2 \mu\text{m}$  ( $0.3 \mu\text{m}$ ) are recommended for the fabrication of high-resolution and well-defined shapes, while for the IP-Q photoresist and microscope objective (10X, NA = 0.3), hatching (slicing) distances of  $1 \mu\text{m}$  ( $5 \mu\text{m}$ ) results in high-speed and mm-size structures. The IP-S photoresist and microscope objective (25X, NA = 0.8) represents an intermediate set for fabricating mm-size structures while achieving  $\mu\text{m}$ -features sizes ( $\sim 0.6 \mu\text{m}$  voxel size).

As previously introduced, for, both, OPP and TPP the refractive index of the polymerized resin is a function of the optical exposure dose  $D$ . Several studies have investigated

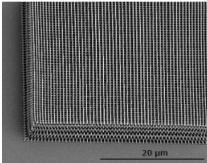
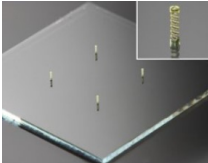

	3D small features	3D medium features	3D large features
<b>TPP resin</b>	IP-Dip	IP-S	IP-Q
<b>Microscope objective</b>	63X, NA = 1.4	25X, NA = 0.8	10X, NA = 0.3
<b>Refractive index (liquid)</b>	1.512 @ 780 nm, 20° C	1.478 @ 780 nm, 20° C	1.480 @ 780 nm, 20° C
<b>Refractive index (once TPP)</b>	1.548 @ 660 nm, 20° C	1.510 @ 660 nm, 20° C	1.510 @ 660 nm, 20° C
<b>Substrate</b>	Fused silica	ITO-coated	Silicon
<b>Max. volume</b>	< 0.1 mm <sup>3</sup>	< 50 mm <sup>3</sup>	< 400 mm <sup>3</sup>
<b>Voxel size (aspect ratio)</b>	~ 0.2 μm (3.5)	~ 0.6 μm (6)	~ 1.2 μm (10)
<b>Hatching <i>h</i> distance</b>	0.2 μm	0.5 μm	1 μm
<b>Slicing <i>s</i> distance</b>	0.3 μm	1 μm	5 μm
<b>Description</b>	Highest 3D resolution and shape accuracy 	Smooth 3D surfaces and high shape accuracy 	High-speed 3D printing of mm-sized features 

Table 1.1: Comparison table for commercial negative-tone IP, i.e. IP-Dip, IP-S and IP-Q, thermosetting photoresists used for TPP-fabrication. Extracted from *Nanoscribe GmbH*.

have studied the intrinsic properties, i.e. refractive index, extinction, luminescence, aging and heat treatment, of such commercial resins over exposure dose  $D$ . Figure 1.22 (a) depicts the refractive index  $n$  over the UV exposure time relation of the commercial IP-S photoresist at  $\lambda = 546$  nm, where a saturation behavior when polymerizing a photoresist via OPP is clearly seen. For lower exposure doses, the refractive index of the IP-S resin quickly increases, while it reaches a plateau where it remains constant for larger  $D$ . Finally, Fig. 1.22 (b) and (c) show the dispersion relation and the extinction coefficient ( $\text{mm}^{-1}$ ) versus wavelength  $\lambda$  between the liquid and UV cured phase for large gamma of commercially available IP photoresists, respectively.

### 1.3.6.2/ OPERATIONAL WORKFLOW

For the fabrication of 3D structures via the DLW-TPP Nanoscribe system, STL (CAD model) files containing the design to be printed are imported into the DeScribe software. This software converts the STL files into GWL print-job files, which provide a visual rendering of the printing process. The resulting GWL file is then loaded into the NanoWrite software, which controls the Nanoscribe system. During the STL to GWL file conversion process, the software computes a sequence of trajectories in the  $xy$ -plane, i.e. the hatching  $h$ , and the  $z$ -direction, i.e. the slicing  $s$ , following an additive layer-by-layer approach. Specifically, the DeScribe program 'slices' the object by intersecting its 3D solid surfaces with a series of parallel planes that are spaced by  $s$  along the  $z$ -direction. Each resulting plane is then intersected with the contour of the surfaces and subsequently filled with multiple hatching lines spaced by  $h$ . Moreover, the DeScribe software enables editing and developing recipes for 3D printing and setting various optimization print parameters, i.e. laser power and scan speed. Finally, the Nanoscribe system is equipped with a microscope camera controlled via the AxioVision software, which provides a live view of the

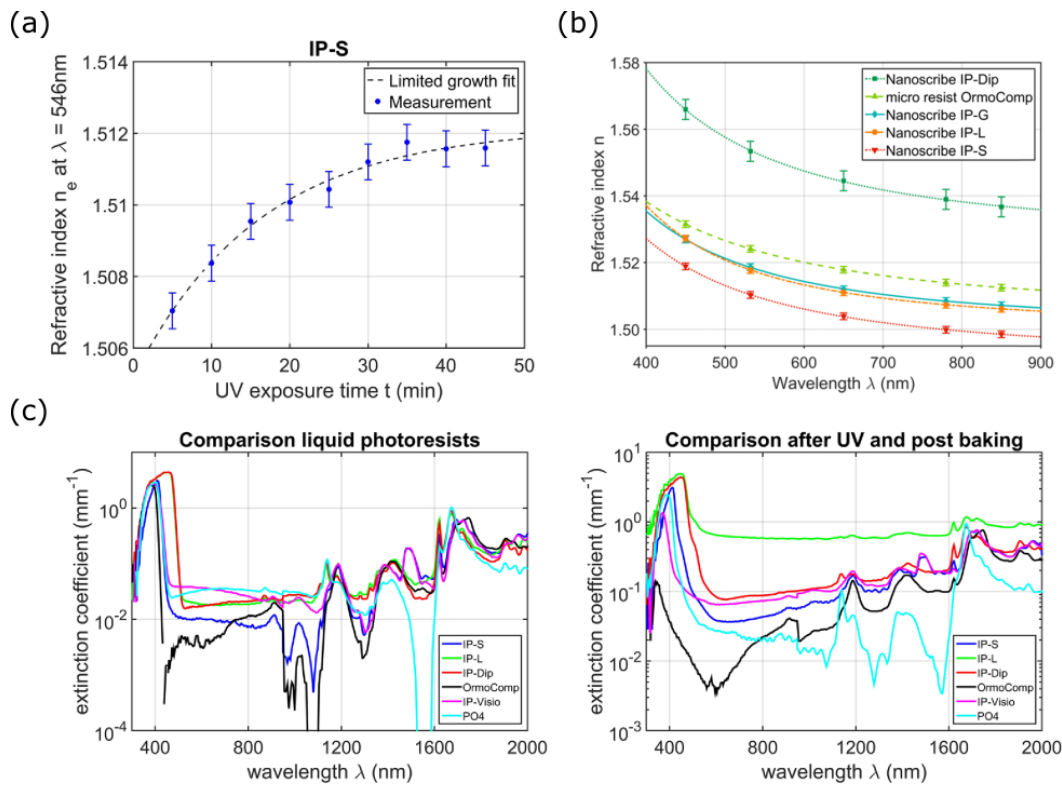


Figure 1.22: Optical properties of the IP family of photoresists used for TPP-fabrication. (a) Refractive index  $n$  dependence over UV dose for the IP-S photoresist. Extracted from [177]. (b) Dispersion relation (refractive index  $n$  versus wavelength  $\lambda$ ) of the commercial IP-Dip, IP-G, IP-L, IP-S and OrmoComp photoresists. Extracted from [213]. (c) Extinction coefficient comparison for the IP-Dip, IP-L, IP-S, IP-Visio, OrmoComp and PO4 photoresists in the liquid state (left panel) and after UV exposure plus post-baking treatment (right panel). The extinction coefficient increases for the polymerized (after UV exposure) state for all the photoresists. Extracted from [177].

printing process.

Figure 1.23 (a) illustrates the standard operational workflow for the fabrication of an exemplary 3D structure via the DLW-TPP Nanoscribe system, which consists of the following steps

- i Preparation of the sample. Choice of the specific recipe, hence the combination of microscope objective and photoresist adequate for the desired application (see Table 1.1), e.g. IP-S photoresist and microscope objective (25X, NA = 0.8). Fix the corresponding substrate to the sample holder.
- ii Deposition of the photoresist on the appropriated substrate avoiding the formation of air bubbles.
- iii Insertion of the sample holder and installation of the microscope objective.
- iv Printing process, which includes importing the STL file into the DeScribe software and loading the produced GWL file into the NanoWrite program. Set the dose parameters LP and scan speed. When the job is started, the microscope objective

is moved towards the substrate and then immersed into the liquid photoresist in a 'dip-in' configuration as depicted in Fig. 1.23 (b) and (c). The printing process can be monitored visually in real-time via the AxioVision software.

- v Sample development. After the printing process, the sample is placed in a bath of propylene-glycol-methyl-ether-acetate (PGMEA) developer for 20 min in order to remove the unpolymerized excess of monomer resin, followed by rinsing in isopropanol (IPA 2-propanol) for 5 min to remove the developer. Developer and developing time might differ upon the recipe as well as the density of the produced structure.

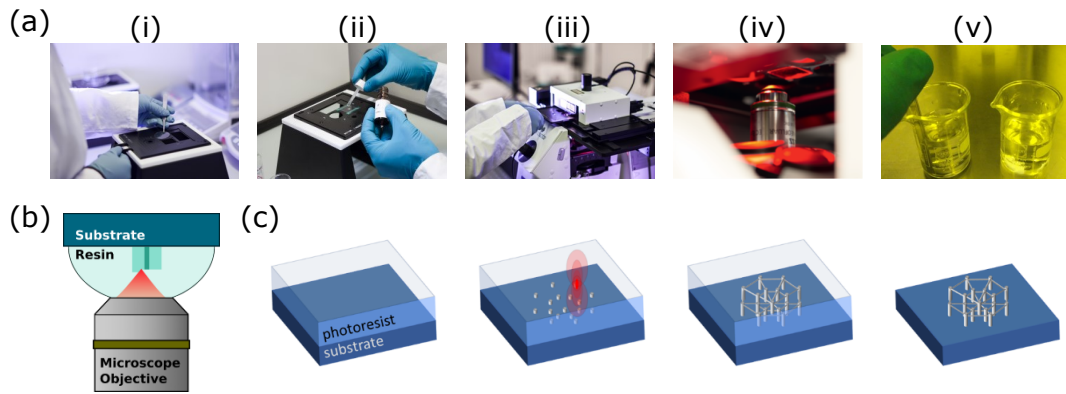


Figure 1.23: DLW-TPP fabrication workflow. Extracted from *Nanoscribe GmbH*. (a) DLW-TPP lithography workflow consisting of (i) fixation of the substrate on a sample holder, (ii) dropping of photoresist on the substrate, (iii) installation of the microscope objective and substrate (with photoresist) inside the lithography machine, (iv) laser-writing procedure and (v) sample development. (b) Configuration of microscope objective and substrate containing photoresist during DLW-TPP printing in the 'dip-in' configuration. (c) After the development process, the non-exposed liquid monomer is removed and only the solidified polymer remains.

### 1.3.7/ (3+1)D PRINTING OF PHOTONIC WAVEGUIDES

Following the concepts introduced in Chapter 1.2, the standard photonic waveguides' guiding concept relies on having a core region with a higher refractive index  $n_{\text{core}}$  than the refractive index of the cladding region  $n_{\text{cladding}}$ , i.e.  $\Delta n = n_{\text{core}} - n_{\text{cladding}} > 0$ . This core-cladding configuration, as shown schematically in Fig. 1.6 (a), allows optical rays with an incidence angle smaller than the critical angle  $\theta_c = \sin^{-1}(1 - n_{\text{cladding}}^2/n_{\text{core}}^2)^{1/2}$  (see Eq. 1.1) to undergo total internal reflection at the core-cladding interface, enabling the confinement and directed propagation of light along a pre-designed path via a solid, integrated core.

The refractive index contrast  $\Delta n$ , the core diameter  $d$  and the wavelength  $\lambda$  are a waveguide's determining characteristics. These determine its numerical aperture  $\text{NA} = \sqrt{n_{\text{core}}^2 - n_{\text{cladding}}^2}$  as well as the number of supported spatial modes  $M \approx V^2/2 = (4\pi d/\lambda)\text{NA}$  for  $M \gg 1$ , see Eqs. 1.13 and 1.14. Here,  $V$  is the normalized frequency, a key parameter of optical waveguides, and for  $V \leq 2.405$ , a waveguide supports a single-mode only, while

higher values of  $V$  enable multiple modes to propagate. Moreover, the refractive index contrast  $\Delta n$  determines the minimum bending radius at which light can be directed with low losses, hence being  $\Delta n$  the limiting towards integration density within photonic ICs.

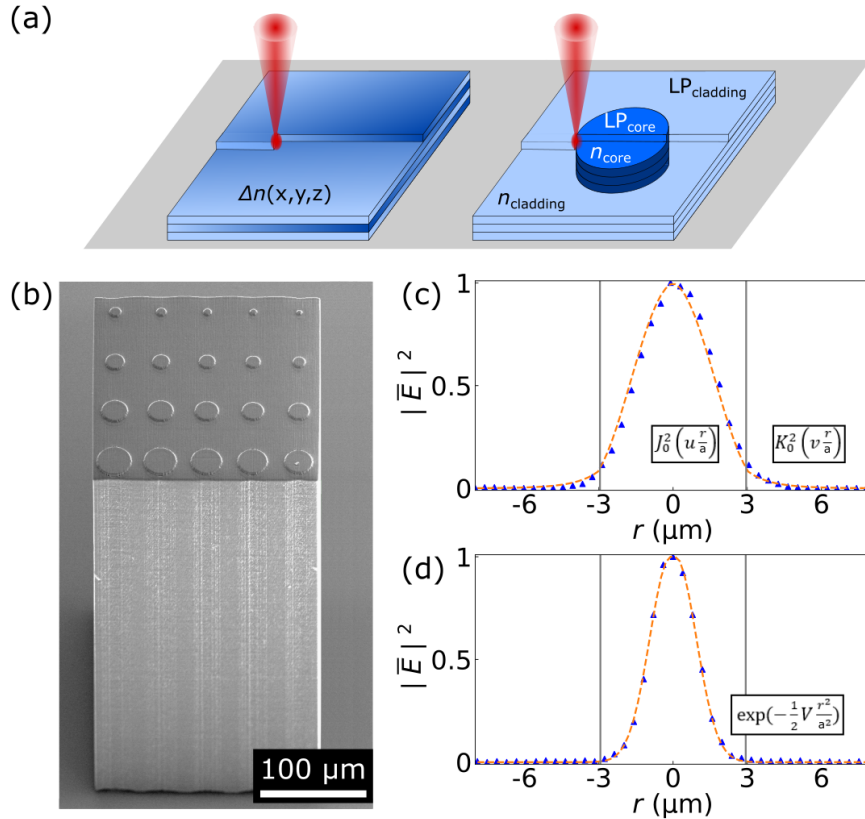


Figure 1.24: Principle of (3+1)D printing of photonic waveguides. Extracted from [111]. (a) During TPP-writing, the refractive index is adjusted by dynamically changing the average LP. Volume gratings (left panel) used for holography and 3D photonic waveguide (right panel) were demonstrated. For the latter, the waveguide cores with  $n_{\text{core}}$  (cladding with  $n_{\text{cladding}}$ ) are printed via TPP using high (low)  $\text{LP}_{\text{core}}$  ( $\text{LP}_{\text{cladding}}$ ) average laser power, resulting in  $\Delta n \approx 2.4 \cdot 10^{-3}$ . (b) SEM micrograph of a (3+1)D printed cuboid embedding 20 STIN waveguides of 300  $\mu\text{m}$  height. Panels (c) and (d) show output intensities profiles and fundamental  $\text{LP}_{01}$  mode fits (dashed lines), respectively. Light is more confined within the core for GRIN waveguides.

DLW-TPP is perfectly suited for the additive fabrication of 3D photonic waveguides [182] as it leverages the spatial refractive index modification of a single host material, i.e. photoresist. This allows to gradually modify the degree of polymerization throughout 3D printing voxels in a single-step using a single-resin by considering the exposure  $D$  as a fourth variable during the TPP-polymerization process, hence the formulation *(3+1)D printing*. For illustrating the concept, 3D photonic waveguides with, both, STIN and GRIN refractive index profiles, cf. Fig. 1.7, are fabricated via (3+1)D printing. The commercially available IP-Dip photoresist ( $n \approx 1.548$ ) and a microscope objective (63X, NA = 1.4) are used for fabrication on a fused silica substrate, see Table 1.1 and Fig. 1.23 for details regarding fabrication recipe and workflow.

Figure 1.24 (a) schematically illustrates volume holograms (left panel) and cylindrical STIN photonic waveguides (right panel) fabricated via (3+1) printing. As seen, the re-

refractive index contrast  $\Delta n$  can be dynamically modified by tailoring the laser power during the printing process. For photonic waveguides, the refractive index of the core region  $n_{\text{core}}$  and the surrounding cladding  $n_{\text{cladding}}$  are printed with respective laser power  $\text{LP}_{\text{core}} > \text{LP}_{\text{cladding}}$ . STIN waveguides are printed using a constant LP all across their core, while for GRIN waveguides the writing power changes from high to low following a parabolic profile when departing from the core's center (see Eq. 1.3). The scanning electron microscope (SEM) micrograph from Fig. 1.24 (b) shows an exemplary 3D cuboid containing 20 STIN waveguides fabricated via (3+1)D printing, and the entire photonic chip volume is fabricated via TPP.

To investigate the optical performance of the photonic waveguides, the output intensities for diameters  $d$  below the cut-off condition of second mode propagation are analyzed. The  $\text{LP}_{01}$  ground mode's output intensity of cylindrical STIN waveguides (cf. Fig. 1.11 (a)) is given by  $J_0^2(u_a^L)$  for  $|r| < a$  and  $K_0^2(v_a^L)$  for  $|r| > a$ , whereas the GRIN waveguides output is given by an infinite parabolic profile as  $\exp -\frac{1}{2}V\frac{r^2}{a^2}$ . Figure 1.24 depicts the fit of the fundamental  $\text{LP}_{01}$  mode to the normalized output for (c) STIN and (d) GRIN waveguides with radius  $a = 3 \mu\text{m}$ . Average numerical aperture of  $\langle \text{NA} \rangle = 0.08 \pm 0.01$  for STIN and  $\langle \text{NA} \rangle = 0.18 \pm 0.02$  for GRIN waveguides are obtained, considering the refractive index of the core constant ( $n_{\text{core}} \approx 1.548$ ). STIN waveguides with polymer cladding have a refractive index contrast on the order of  $\Delta n \approx 2.4 \cdot 10^{-3}$ , see Fig. 1.5. The core confinement of GRIN waveguides is significantly higher than for STIN waveguides due to the inner core refractive index distribution, providing a vital benefit for photonic integration schemes [146], as anticipated in Section 1.2.1.2. These results show the flexibility of (3+1)D printing towards 3D photonic integration based on DLW-TPP, which is demonstrated by the fact that optical manipulation using integrated and monolithic 3D structures can either use separate components, such as waveguides, or employ continuous manipulation of free optical propagation, such as volume holograms.

### 1.3.8/ OPTICAL CHARACTERIZATION

To evaluate the optical performance of 3D photonic waveguides (propagation losses, injection losses and modal analysis) such as the ones introduced in the previous Section 1.3.7, a free-space optical set up is required. The optical set up used to characterize the 3D printed photonic waveguides presented in this thesis is depicted in Fig. 1.25. The fiber-pigtailed laser diode (LD) (Thorlabs, LP660-SF20) with Gaussian output is first collimated using the microscope objective  $\text{MO}_1$  (Olympus PLN10X, NA = 0.3). After passing the polarizer and the  $\lambda/2$  wave-plate, the polarization of the light is set to linear. Then the linearly polarized light is focused on the top-surface of the sample using a second microscope objective  $\text{MO}_2$  (Olympus PLN10X, NA = 0.3). The sample is mounted in a (xyz)-stage (Thorlabs 3-Axis Nanomax system), by which the beam focus spot is precisely aligned to the input-facet of the 3D photonic waveguides. After injecting the light into the 3D photonic waveguides, the optical output signal is collected by a third microscope objective  $\text{MO}_3$  (Olympus PLN50x, NA = 0.8) and further imaged on the transmission camera  $\text{CAM}_T$  (iDS U3-3482LE, pixel size  $2.2 \mu\text{m}$ ) using an achromatic lens (Thorlabs AC254-100-AB-ML) with 100 mm focal length. At the top-surface of the sample, the incoming light is back-reflected and then similarly imaged on a second camera  $\text{CAM}_R$  (iDS U3-3482LE, pixel size  $2.2 \mu\text{m}$ ) using an achromatic lens (Thorlabs AC254-100-AB-ML) with a 100 mm focal length. A light-emitting diode (LED) at  $\lambda = 660 \text{ nm}$  is used for broad wavelength illumination of the sample. Both, the transmission (reflection) cameras  $\text{CAM}_T$  ( $\text{CAM}_R$ ) are

connected to the computer equipped with the specialized iDS  $\mu$ Eye software for further image acquisition and analysis.

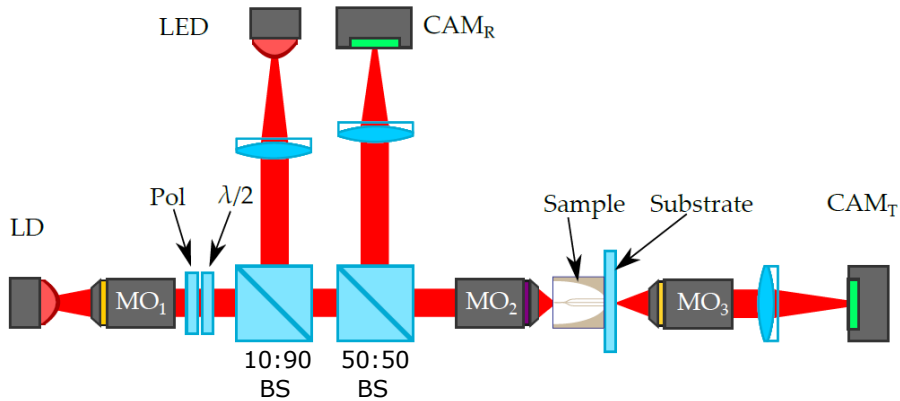


Figure 1.25: Experimental set up for the optical characterization of 3D printed photonic waveguides. The beam from the fiber-pigtailed laser-diode LD ( $\lambda = 660$  nm) is collimated in  $MO_1$ . The laser system is optically decoupled with the polarizer and the  $\lambda/2$ -waveplate and focused on the waveguide's input-facet with  $MO_1$ . The waveguide's output is collected with  $MO_3$  and imaged with the lens system on the transmission camera  $CAM_T$ .

This optical set up is used to evaluate the optical performance of waveguides presented in this thesis. To this aim, for all the waveguides the total transmission  $T_{total}$  is analyzed. A reference image is taken, where the injection beam is focused on top of the glass substrate at an area without waveguides or support structures. The reference intensity  $T_{ref}$  is computed by numerically integrating the intensity distribution over an area around the peak of the Gaussian input. The area for the integration is chosen to be bigger than the width of the Gaussian input, i.e.  $4 \times 4 \mu\text{m}$ , to integrate the vast majority of the transmitted signal. After focusing and aligning the beam at the waveguide's input-facet, the integration is repeated for each waveguide and its output transmission  $T_{output}$  is determined. Finally, the total transmission is obtained by dividing the output intensity by the reference intensity  $T_{total} = T_{output}/T_{ref}$ . The global losses are obtained by expressing  $T_{total}$  in logarithmic scale as  $10 \log_{10}(T_{total})$ .

## FLASH-TPP: COMBINING ONE- AND TWO-PHOTON POLYMERIZATION

In Chapter 2, the novel lithographic *flash*-TPP configuration is presented [215]. The *flash*-TPP concept leverages a combination of one- and two-photon polymerization towards the fabrication of 3D photonic waveguides. To speed up conventional DLW-TPP fabrication settings while enhancing overall performances, three distinct ingredients for creating three vital components of a photonic waveguide circuit are integrated leveraging different concepts and parameters: (i) waveguide cores, (ii) waveguide claddings, and (iii) mechanical support to ensure the stability of the 3D integrated circuit. Importantly, the majority of an integrated photonic circuit consists of a material with a uniform refractive index lower than that of the waveguide cores. Here, the entire circuit is polymerized using a single-shot blanket OPP via UV irradiation according to a precisely controlled exposure dosage to achieve the desired refractive index contrast  $\Delta n$ .

The relevant information presented in Chapter 2 is based on results published in: *Grabulosa, A., Moughames, J., Porte, X. and Brunner, D. "Combining one and two photon polymerization for accelerated high performance (3+1)D photonic integration" Nanophotonics, vol. 11, no. 8, 2022, pp. 1591-1601. DOI: 10.1515/nanoph-2021-0733.*

### 2.1/ ACCELERATE 3D WAVEGUIDE PRINTING WITH FLASH-TPP

A vital challenge encountered in, both, classical DLW-TPP and (3+1)D printing schemes is the impractical fabrication time when printing  $\text{mm}^3$  volume circuits, often exceeding 20 hours. In 3D ICs, the essential elements are the waveguide cores, while the waveguide cladding is naturally formed by the surrounding, 'unstructured' larger volume with a lower refractive index  $n_{\text{cladding}}$ . It is advantageous to restrict the high-resolution and hence time-consuming TPP process to the creation of waveguide cores, while employing a rapid and indiscriminate single-step blanket UV exposure above the absorption energy of the resin's photoinitiator to swiftly polymerize the entire remaining chip in a single *flash*. This approach enables reducing operation times in the fabrication procedure.

The working principle of *flash*-TPP is illustrated in Fig. 2.1, where (a) depicts the typical 'dip-in' DLW-TPP printing procedure, where the microscope objective is directly immersed into the resin. The printed structure is subsequently developed using the steps discussed in Section 1.3.6.2. After development, the unexposed photoresist (monomer) outside the enclosed volume is removed and the entire 3D photonic circuit is then transferred to a

UV chamber (Rolence Enterprise Inc., LQ-Box model, 405 nm wavelength, 150 mW/cm<sup>2</sup> average light intensity) as shown in Fig. 2.1 (b), polymerizing the unexposed monomer volume inside the photonic chip. The OPP dosage  $D$  is adjusted via the duration of the UV exposure [177].

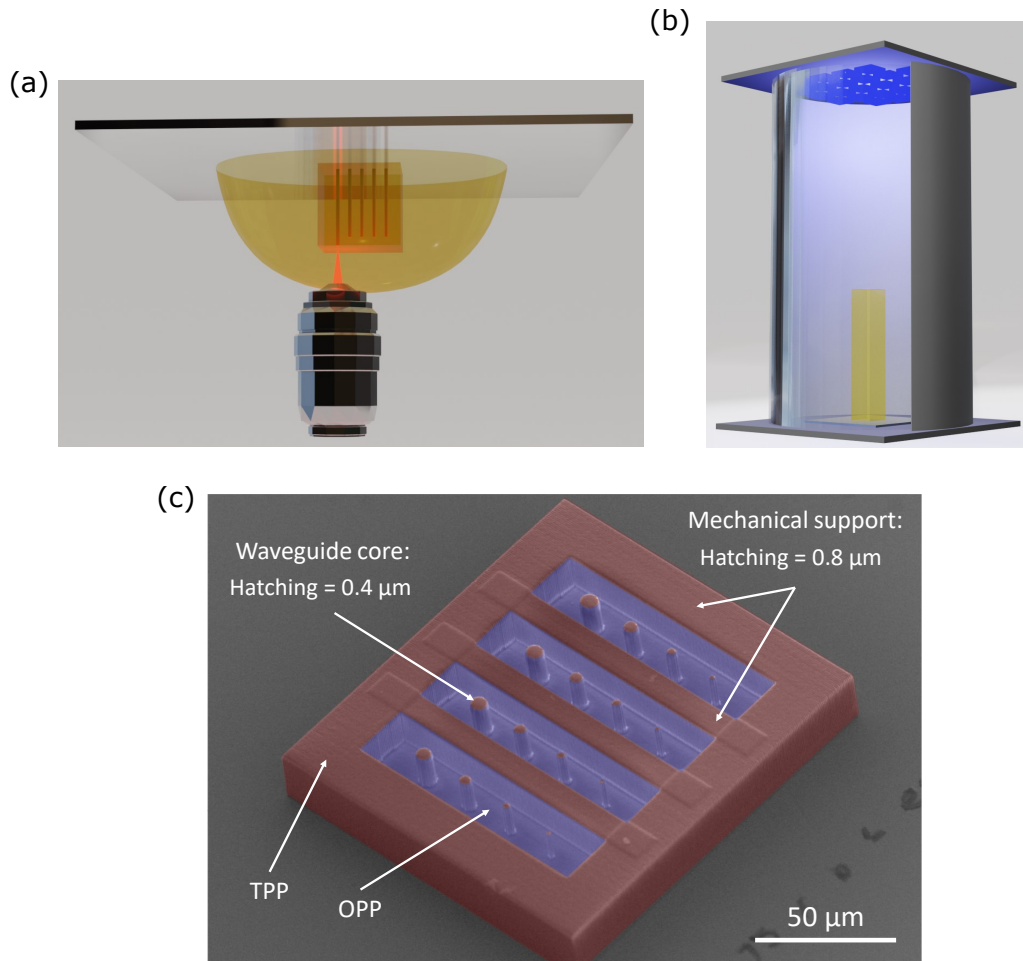


Figure 2.1: *Flash*-TPP lithography concept for 3D photonic integration. Extracted from [215]. (a) Schematic illustration of the 'dip-in' configuration during DLW-writing. (b) After development, where the unexposed photoresist at the outer regions of the 3D cuboid is removed, the 3D photonic chip is exposed under a UV light source that polymerizes the remaining regions via OPP. *Flash*-TPP leverages the combination of both one-(OPP) and two-photon polymerization (TPP). (c) SEM micrograph showing the cross-section of a 3D cuboid containing 16 waveguides. The waveguide cores (mechanical supports) are printed with high(low)-resolution. The regions that are polymerized via TPP (OPP) are depicted in red (blue) colors, respectively.

To further accelerate the fabrication process, the TPP writing conditions are local and dynamically adjusted based on the specific functionality of each component of the photonic circuit. Achieving minimal propagation losses require reducing roughness at the core-cladding interface. This is accomplished by employing a small voxel spacing in the  $(x, y)$ -plane, corresponding to a small hatching distance  $h$ , while the vertical distance between consecutive slices, or slicing distance  $s$ , is maximized. The latter does not significantly affect the roughness of the waveguide's interface, while considerably impacting upon ac-

celerating the printing process. Other sections of the circuit, such as the outer cladding or internal support columns, do not interact with optical signals and primarily require mechanical sturdiness. Therefore, the hatching distance for these sections is maximized. Importantly, since the printing time scales as  $\propto (h^2s)^{-1}$ , increasing the hatching distance has a substantial impact on reducing the overall fabrication time. The SEM micrograph in Fig. 2.1 (c) schematically illustrates the overall *flash*-TPP fabrication concept, where the photonic circuit is initially fabricated in a single-step via DLW-TPP lithography (red region). After development, the entire circuit is polymerized via OPP under UV irradiation (blue region) for several seconds.

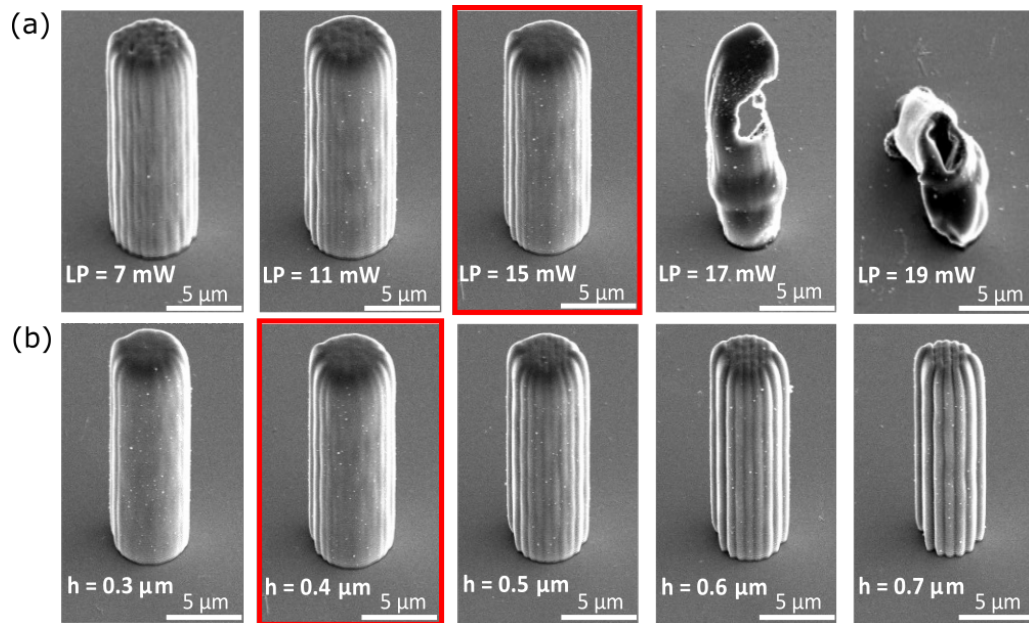


Figure 2.2: TPP fabrication parameters optimization for waveguide cores. Extracted from [215]. (a) SEM micrograph of a free-standing cylinder with  $d = 5 \mu\text{m}$  and  $20 \mu\text{m}$  height reassembling waveguide cores fabricated with laser power  $LP \in \{7, \dots, 19\}$  mW. The hatching (slicing) distances are fixed to  $h = 0.4 \mu\text{m}$  ( $s = 1 \mu\text{m}$ ). The combination with better performance is highlighted in red. (b) SEM micrograph as in (a) but showing the impact of  $h \in \{0.3 : 0.1 : 0.7\} \mu\text{m}$ , with fixed  $s = 1 \mu\text{m}$  and  $LP = 15$  mW. The combination with better performance is highlighted in red.

### 2.1.1/ TWO-PHOTON POLYMERIZATION FABRICATION PARAMETERS

The first step for *flash*-TPP fabrication of 3D photonic waveguides is to maximize the smoothness of the waveguide's core surfaces in order to ensure low propagation losses. It is of vital relevance the characterization of the dynamic power range, see Section 1.3.4, of the photoresist. This is done by investigating the writing laser power in order to obtain high-quality structures as well as specific refractive index  $n$ . Moreover, the fabrication parameters that determine the resolution in the  $(x, y)$ -plane ( $z$ -direction), which are the hatching  $h$  (slicing  $s$ ) distances, need to be precisely optimized. To this aim, a series of five independent free-standing pillars that emulate waveguide cores of  $20 \mu\text{m}$  height and diameter  $d = 5 \mu\text{m}$  are printed on a fused silica substrate. The fabrication is done with the negative-tone IP-S photoresist, with  $n = 1.510$  when fully TPP-polymerized at  $\lambda = 660$  nm,

cf. Fig. 1.22, using a microscope objective (25X, NA = 0.8), see Table 1.1.

The first fabrication optimization involves employing various TPP laser powers (LP) while maintaining a constant hatching distance  $h = 0.4 \mu\text{m}$ . A scanning speed of 10 mm/s and slicing distance  $s = 1 \mu\text{m}$  are set as globally fixed fabrication parameters for all the fabrication. Figure 2.2 (a) depicts a SEM micrograph after the development of waveguide cores printed with  $LP \in \{7, \dots, 19\}$  mW. The initial two images exhibit waveguide cores with  $LP = 7$  mW and  $LP = 11$  mW, which results in rough and inhomogeneous surfaces. Increasing the LP up to 15 mW leads to larger TPP voxels and a smoother surface. However, for  $LP > 17$  mW the waveguides are over-polymerized and burnt, as depicted in the last two images of Fig. 2.2 (a). Consequently, a laser power  $LP = 15$  mW is chosen for the next optimization step (highlighted in red in Fig. 2.2 (a)).

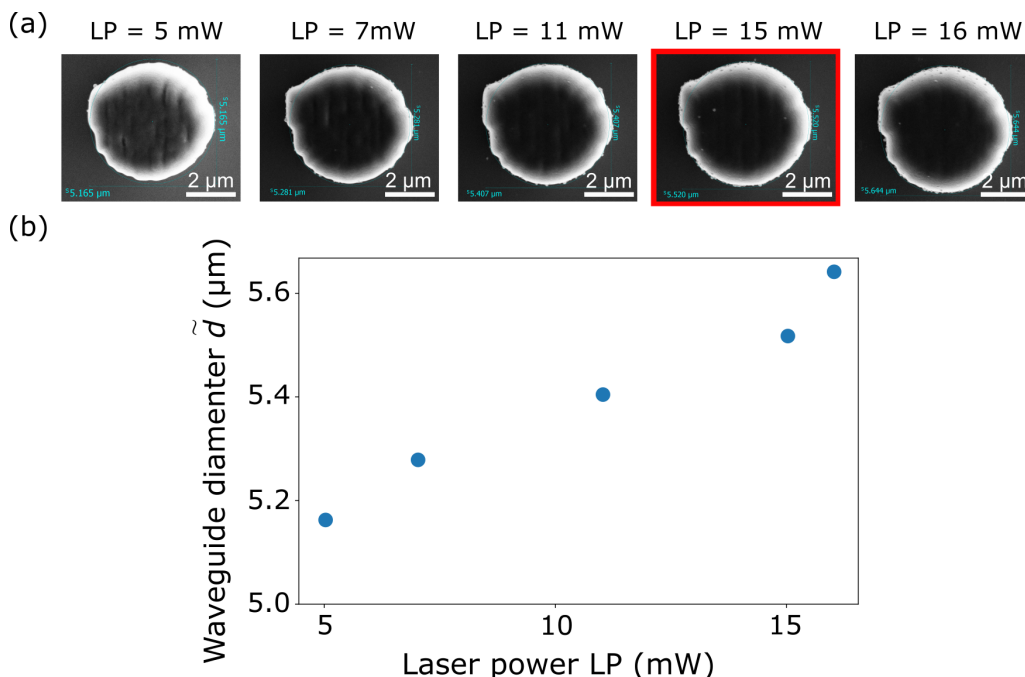


Figure 2.3: Impact of the TPP-voxel size on the waveguide core diameter. (a) SEM micrographs of the top-surface of waveguide cores with designed diameter  $d = 5 \mu\text{m}$  printed with  $LP \in \{5, \dots, 16\}$  mW,  $h = 0.4 \mu\text{m}$  and  $s = 1 \mu\text{m}$ . The waveguide core diameter increases for larger LP due to the TPP exposure-dependent voxel size. Best combination highlighted in red. (b) Waveguide core diameter  $\tilde{d}$  dependence over LP from (a). This leads to an effective waveguide core diameter of  $\tilde{d} = d + d_0$ .

The hatching distance  $h$  is optimized by a scan from  $0.3 \mu\text{m}$  to  $0.7 \mu\text{m}$  while the LP is fixed to 15 mW. The SEM micrographs in Fig. 2.2 (b) reveal that the first two waveguide cores, corresponding to  $h$  values of  $0.3 \mu\text{m}$  and  $0.4 \mu\text{m}$ , exhibit smoother surfaces in comparison to the last three. The surface quality is comparable for  $h = 0.3 \mu\text{m}$  and  $h = 0.4 \mu\text{m}$ , but the latter reduces the fabrication time by a factor of 1.8. Also, for  $h = 0.3 \mu\text{m}$ , results are not always reproducible, which are attributed to spontaneous micro-burnings within waveguide cores due to increased TPP irradiation produced by the smaller hatching distance. Therefore, the hatching distance  $h = 0.4 \mu\text{m}$  is selected, see highlighted in red in Fig. 2.2 (b).

Additionally, to investigate the effect of the TPP exposure dose over the TPP-voxel

size [188], a set of waveguide cores with diameter  $d = 5 \mu\text{m}$  are printed with the optimized  $h = 0.4 \mu\text{m}$ , while scanning  $\text{LP} \in \{5, \dots, 16\}$  mW within the dynamic power range of the IP-S photoresist. The analysis of the SEM micrographs shown in Fig. 2.3 (a) reveals that the waveguide cores exceed the design diameter  $d$  due to the non-negligible TPP voxel size. Consequently, an effective diameter  $\tilde{d} = d + d_0$  is considered for further investigations. Figure 2.3 (b) depicts the typically observed relation between  $\tilde{d}$  and the laser power.

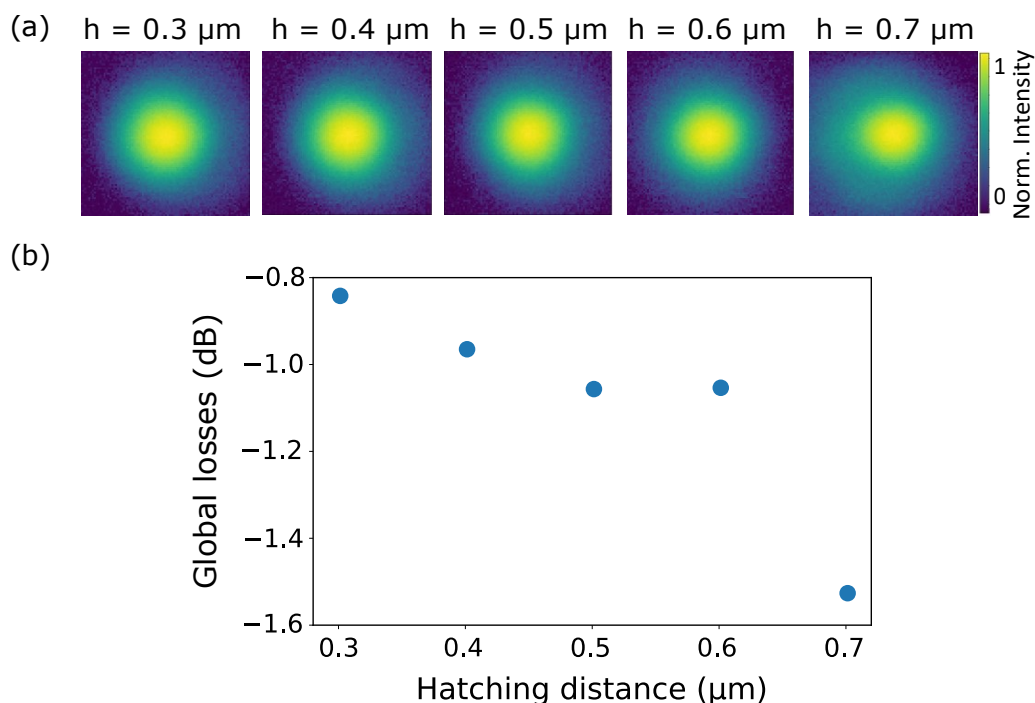


Figure 2.4: Optical characterization of TPP-printed waveguide cores. Extracted from [215]. (a) Output intensity profiles of photonic waveguides with  $\tilde{d} = 3.3 \mu\text{m}$  and  $300 \mu\text{m}$  height fabricated using  $h \in \{0.3 : 0.1 : 0.7\} \mu\text{m}$ ,  $s = 1 \mu\text{m}$  and  $\text{LP} = 15 \text{ mW}$ . Sample exposed under UV light for 20s. For the largest  $h = 0.7 \mu\text{m}$ , the optical confinement is weaker and the scattering increased. (b) Global losses versus  $h$  for the waveguides from (a).

The impact of  $h$  on the propagation losses is investigated by evaluating five waveguides of  $300 \mu\text{m}$  length at  $\lambda = 660 \text{ nm}$ . The fabrication parameters used are identical to those from Fig. 2.2 (b). Figure 2.4 (a) shows the output intensities of the waveguides with  $h$  ranging from  $0.3$  to  $0.7 \mu\text{m}$ , where  $\tilde{d} = 3.3 \mu\text{m}$  and  $\text{LP} = 15 \text{ mW}$ . After the development process, the samples are exposed under UV irradiation for 20 seconds. The first four outputs exhibit nearly identical intensity distributions, with a significant reduction in optical confinement observed only for  $h = 0.7 \mu\text{m}$ . This trend is also demonstrated in Fig. 2.4 (b), which shows the overall optical losses (injection, propagation, outcoupling) corresponding to different  $h$  values. The global optical losses gradually increase with  $h$  until experiencing a sharp rise at  $h = 0.7 \mu\text{m}$ .

Overall, a combination of hatching distance  $h = 0.4 \mu\text{m}$  and laser power  $\text{LP} = 15 \text{ mW}$ , with a globally fixed scanning speed of  $10 \text{ mm/s}$  and slicing distance  $s = 1 \mu\text{m}$ , is selected for fabricating the TPP-printed waveguide cores. To reduce printing time, the mechanical supports, i.e. side-walls, are printed with a lower resolution and  $h = 0.8 \mu\text{m}$ . Addition-

ally, walls between rows of waveguides are introduced to ensure a flat top surface of the cuboids, counteracting the shrinkage effect during sample development that otherwise leads to waveguide collapsing [208]. The entire concept is exemplary illustrated in Fig. 2.1 (c).

## 2.2/ FLASH-TPP WAVEGUIDE PROPERTIES

After precisely optimizing the fabrication parameters, propagation losses and temporal stability of photonic waveguides printed via *flash*-TPP are characterized.

### 2.2.1/ MODAL CONFINEMENT

The first study on waveguide performance is investigating their modal confinement. To this aim, a set of 3D cuboids embedding 16 waveguides with diameters ranging from  $\tilde{d} \in \{1.3 : 0.4 : 7.3\} \mu\text{m}$  and height  $300 \mu\text{m}$  are fabricated. The different cuboids are UV exposed for 0, 5, 20 and 60s, which results in OPP irradiation doses  $D$  of 0, 750, 3000 and  $9000 \text{ mJ/cm}^2$ , respectively.

As previously done in Section 1.3.7 for (3+1)D printed waveguides, by fitting the experimental output intensities for different diameters, the waveguide's normalized frequency  $V = \frac{\pi}{\lambda_0} \tilde{d} \text{NA}$  is obtained, where  $\text{NA} = \sqrt{n_{\text{core}}^2 - n_{\text{cladding}}^2}$  is the numerical aperture and  $n_{\text{core}} \approx 1.510$  ( $n_{\text{cladding}}$ ) are the refractive indices of core (cladding), respectively. Each intensity is fitted to the fundamental  $\text{LP}_{01}$  mode for diameters below the cut-off condition for a second propagating mode, as shown in Fig. 2.5 (a) for an exemplary waveguide of  $\tilde{d} = 4.5 \mu\text{m}$  UV exposed with  $D = 3000 \text{ mJ/cm}^2$ . Figure 2.5 (b) shows the experimental characterization for all effective waveguide diameters  $\tilde{d}$  exposed to different UV doses  $D$  extracted by individually determining the normalized frequency  $V = \sqrt{u^2 + v^2}$ . As seen, it is clear that the shorter the circuit is exposed to UV light, the larger the normalized frequency  $V$ . From the slope of the linear regression (dashed lines) in Fig. 2.5 (b), the average NA for each UV exposure is obtained.

In Fig. 2.5 (c) one can observe that the NA shows a slight decrease as the waveguides' diameter increases. This effect is attributed to the diffusion process occurring during development, which results in a smoother transition of refractive index between the waveguide core and cladding. Consequently, this transition converts the effective GRIN profile at smaller diameters to an effective STIN at larger diameters, which results in an increase of NA for waveguides with smaller diameters. Importantly, Fig. 2.5 (c) does not show some UV unexposed waveguides (see for  $D = 0 \text{ mJ/cm}^2$ ). This is due to mechanical failure observed for small diameter waveguides  $\tilde{d} < 2.3 \mu\text{m}$ , either immediately after fabrication or after several weeks ( $>2$  weeks).

Finally, Fig. 2.5 (d) depicts the evolution of the average  $\langle \text{NA} \rangle$  and  $\langle n_{\text{cladding}} \rangle$  as a function of  $D$ . The remarkable agreement with the fitted logistic curve demonstrates the ability to precisely adjust the NA of different waveguides, which decreases exponentially till it reaches a plateau. The same trend is observed in other investigations, cf. Fig. 1.22 (a), for such saturation processes, which again confirms the excellent agreement found across different studies. The refractive index is approximately constant once the resin is fully TPP-polymerized. Therefore, any variations in NA with respect to the expo-

sure dose  $D$  can be attributed to changes in the refractive index of the cladding, following the relation  $n_{\text{cladding}} = (n_{\text{core}}^2 - \text{NA}^2)^{1/2} = A/(1 - \exp(\kappa D))$ , with  $\kappa = 1.16 \times 10^{-3} \text{ mJ}^{-1} \text{ cm}^2$  obtained from the fit.

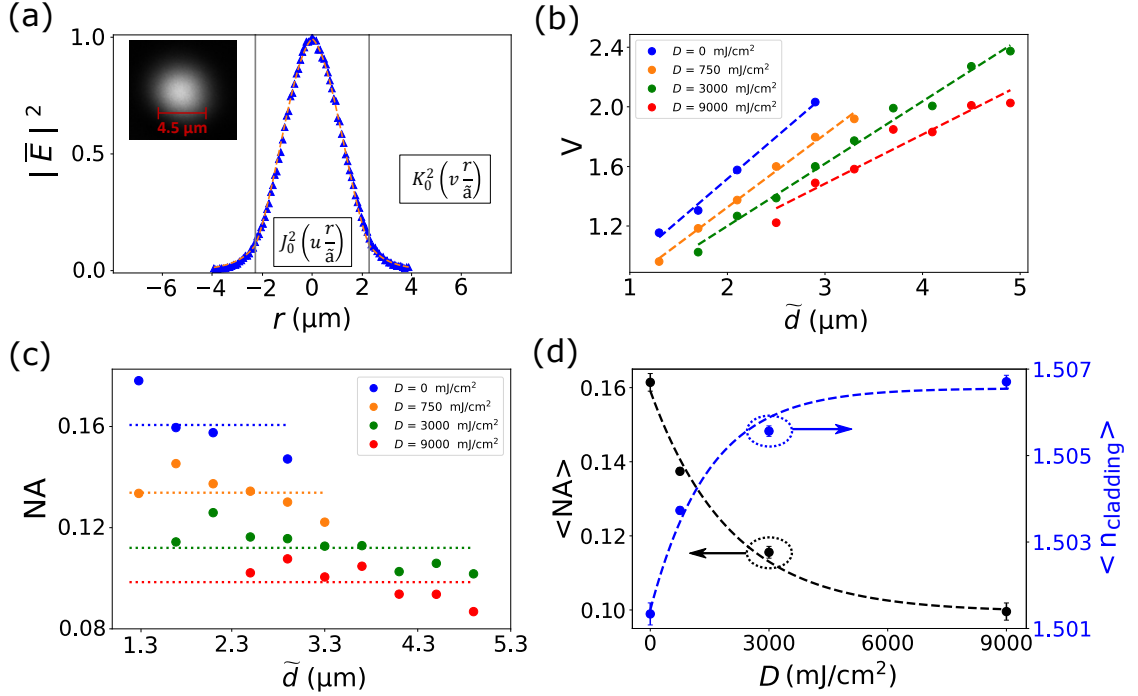


Figure 2.5: Modal confinement of photonic waveguides printed via *flash*-TPP. Extracted from [215]. (a) Output intensity profile (blue triangles) and fundamental  $\text{LP}_{01}$  mode fit (dashed orange lines) for a waveguide of  $\tilde{d} = 4.5 \mu\text{m}$  and UV-cured with  $D = 3000 \text{ mJ}/\text{cm}^2$ . (b) Normalized frequency  $V$  versus effective diameter  $\tilde{d}$  for OPP dosages  $D$  of 0 (blue dots), 750 (orange dots), 3000 (green dots) and 9000 (red dots)  $\text{mJ}/\text{cm}^2$ . Linear regression of the experimental data is indicated by the dashed lines. (c) Numerical aperture  $\text{NA}$  values versus  $\tilde{d}$  dependence. Dashed lines represent the average  $\langle \text{NA} \rangle$  for each UV dose  $D$ . (d) Averaged  $\langle \text{NA} \rangle$  (black color) and  $\langle n_{\text{cladding}} \rangle$  (blue color) over UV dosage  $D$ . Logistic fit curve of the experimental data is indicated by the dashed lines.

This  $\Delta n \approx 5 \cdot 10^{-3}$  allows single-mode propagation for waveguide diameters  $\tilde{d} \leq 4.2 \mu\text{m}$  ( $\tilde{d} \leq 9.8 \mu\text{m}$ ) at  $\lambda = 660 \text{ nm}$  ( $\lambda = 1550 \text{ nm}$ ) and over relatively large distances ( $\approx 6 \text{ mm}$ ), which is standard with the current DLW-TPP fabrication technology, see Fig. 1.5. A further modal analysis is done via COMSOL Multiphysics by numerically simulating both the optical confinement and mode evolution in waveguides with  $\Delta n \approx 5 \cdot 10^{-3}$ . Figure 2.6 (a) shows the numerical confinement factor versus  $\tilde{d}$  for  $\lambda \in \{660, 760, 960, 1550\} \text{ nm}$  and both the fundamental  $\text{LP}_{01}$  (solid line) and second  $\text{LP}_{11}$  (dashed line) propagation modes. For all  $\lambda$ , the optical confinement rapidly increases to unity once the total internal reflection condition is fulfilled for diameters below the cut-off condition. The simulated cut-off diameter of the second propagation  $\text{LP}_{11}$  mode is  $\tilde{d} \approx 4.2 \mu\text{m}$  for  $\lambda = 660 \text{ nm}$ , which perfectly agrees with the experimental results. Figure 2.6 (b) depicts the intensity profiles normalized by the maximum of each distribution for different waveguide diameters  $\tilde{d}$  for the exemplary cases of  $\lambda = 660 \text{ nm}$  and  $\lambda = 1550 \text{ nm}$ , which clearly show the discussed effects of optical confinement over  $\tilde{d}$ .

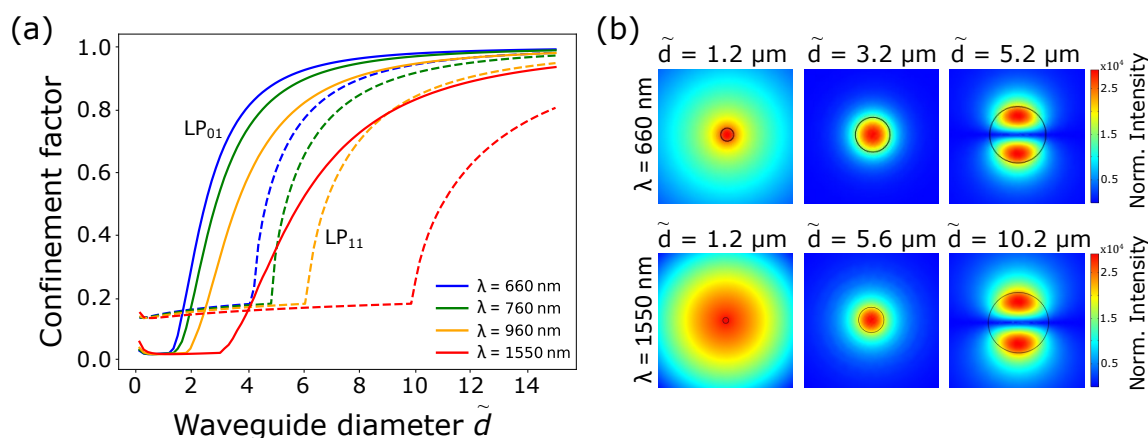


Figure 2.6: Optical confinement for low refractive index waveguides. Simulations are done via COMSOL Multiphysics. (a) Confinement factor versus  $\tilde{d}$  for  $\lambda \in \{660, 760, 960, 1550\}$  nm and  $\Delta n \approx 5 \cdot 10^{-3}$ . The curves for the fundamental (second) propagation modes are represented in solid (dashed) lines. The cut-off diameter  $\tilde{d}$  for the second propagation LP<sub>11</sub> mode increases over  $\lambda$ . (b) Simulated output intensity profiles of waveguides with  $\tilde{d} \in \{1.2, 3.2, 5.2\}$   $\mu\text{m}$  ( $\tilde{d} \in \{1.2, 5.6, 10.2\}$   $\mu\text{m}$ ) for  $\lambda = 660$  nm ( $\lambda = 1550$  nm). The cut-off diameter for the second propagation mode is  $\tilde{d} = 5.2$   $\mu\text{m}$  ( $\tilde{d} = 10.2$   $\mu\text{m}$ ) for  $\lambda = 660$  nm ( $\lambda = 1550$  nm), respectively.

### 2.2.2/ PROPAGATION AND INJECTION LOSSES

To evaluate propagation and injection losses, a series of waveguides ranging from 0.1 to 6 mm in length are fabricated. The diameter of the waveguides is set to  $\tilde{d} = 3.7$   $\mu\text{m}$  and the UV expose dose to  $D = 3000$  mJ/cm<sup>2</sup>, which provide high NA while remaining single-mode (see Fig. 2.5 (c) and (d)). To minimize injection losses, it is necessary to adiabatically modify the diameter of the waveguide core to smoothly transition the input size mode from free-space to that of the waveguide, i.e. via adiabatic tapers [124]. As introduced in Section 1.2.3.1, it is crucial to maintain the angle of the taper, i.e. the taper-rate, sufficiently small to avoid exciting higher-order modes and satisfy the condition for adiabatic transition. An optimization process is carried out in order to minimize the injection losses and to determine the most efficient taper's dimension in order to achieve mode-matching coupling. This involves fabricating a set of tapers with taper-length  $l_t \in \{20 : 10 : 60\}$   $\mu\text{m}$  and  $\tilde{d} \in \{4.1 : 0.4 : 6.1\}$   $\mu\text{m}$ . From Fig. 2.6 (a), the optimal taper is identified to be starting from an input diameter  $\tilde{d} = 4.9$   $\mu\text{m}$  to the target waveguide diameter of 3.7  $\mu\text{m}$  during a taper-length  $l_t = 40$   $\mu\text{m}$ .

Figure 2.7 (b) depicts the global losses of the fundamental LP<sub>01</sub> mode on a semi-logarithmic scale. Propagation losses of 1.36 dB/mm and injection losses of 0.26 dB are obtained from the linear fit, see Fig. 1.5. These results show highly reproducible measurements across the wide range of lengths examined, in particular considering that each waveguide longer than 0.5 mm is fabricated on a different substrate as for 'dip-in' DLW schemes the working distance of the microscope objective limits the distance between neighboring structures, see Section 1.3.3.1. Figure 2.7 (c) shows a macroscopic image of the 6 mm long waveguide printed for this study, imaged next to a match for scaling purposes. This emphasizes the excellent reproducibility and high-quality of the *flash*-TPP fabrication technique as well as the optical characterization procedure.

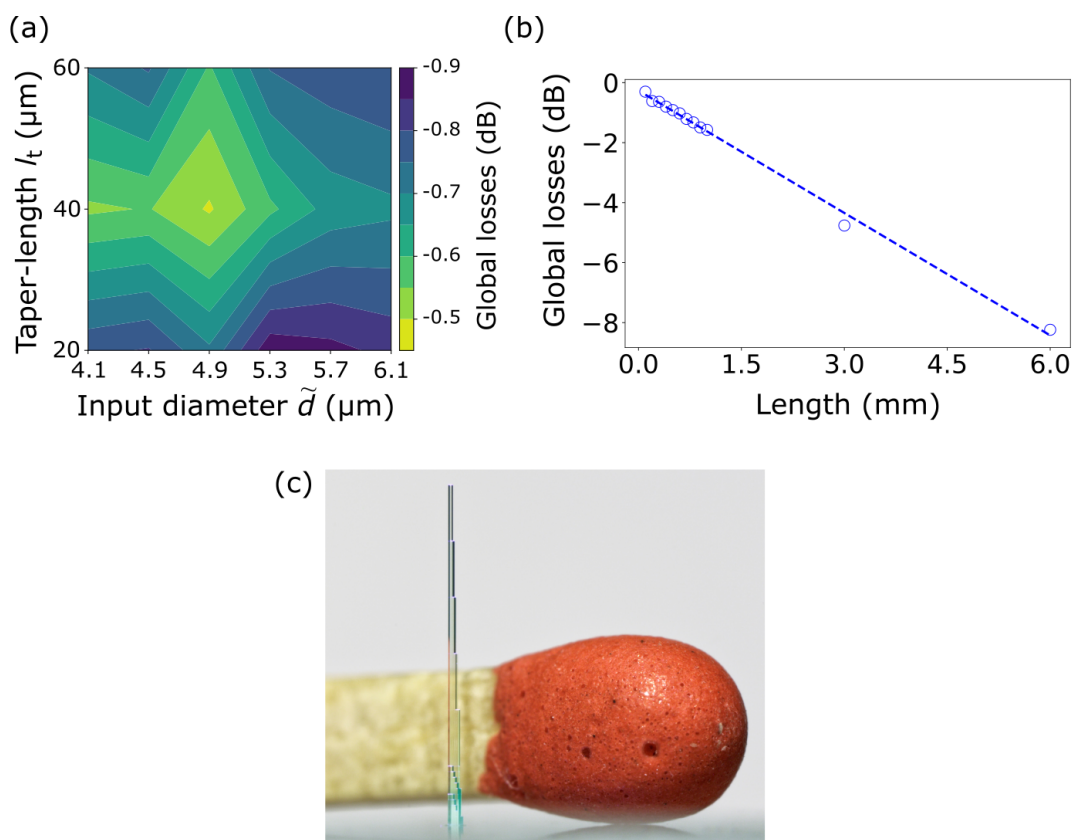


Figure 2.7: Taper optimization and propagation losses of photonic waveguides printed via *flash*-TPP. Extracted from [215]. (a) 2D scatter plot of fabricated tapers with taper-length  $l_t \in \{20 : 10 : 60\} \mu\text{m}$  and input diameter  $\tilde{d} \in \{4.1 : 0.4 : 6.1\} \mu\text{m}$ . (b) Propagation (injection) losses of 1.36 dB/mm (0.26 dB) extracted from the linear fit of the fundamental  $\text{LP}_{01}$  mode for waveguides with  $\tilde{d} = 3.7 \mu\text{m}$  and  $D = 3000 \text{ mJ/cm}^2$  UV dose. (c) Photography of a 3D cuboid integrating the 6 mm long waveguide scaled to a match for size comparison.

### 2.2.3/ TEMPORAL STABILITY

As a final investigation, the aging of waveguides printed via *flash*-TPP is evaluated under 'rest' (exposed to ambient laboratory light levels) and 'operation' (guiding optical signals) conditions. Temporal stability is crucial for ensuring reliability in practical applications. Aging can arise from various factors, including thermal diffusion, shrinkage, or unintended photo-polymerization in areas with a low degree of polymerization [208]. The latter is crucial for (3+1)D-TPP printing since the concept is based on the partial polymerization of the waveguide cladding areas, and some photoinitiators may remain active after only partial polymerization via OPP or TPP. If unintended optical exposure occurs after development, this can activate the remaining photoinitiators and lead to further polymerization of the waveguide cladding and further increase of its refractive index. Consequently, the change of the refractive index contrast  $\Delta n$  and related optical properties would be altered over time. To investigate the temporal stability of the waveguides, the NA of the waveguides is monitored over time. For the case of 'rest' conditions, all structures are kept in the laboratory under ambient room light with no special protection shield from standard irradiation intensity. Figure 2.8 (a) shows that under these 'resting' conditions the NA of all waveguides examined in the previous sections remains unchanged throughout a

continuous characterization period of  $\approx 3000$  hours.

For the evaluation of the degradation under continuous 'operation' conditions, light at  $\lambda = 660$  nm with a power of 0.25 mW was injected into a waveguide ( $\tilde{d} = 2.9$   $\mu\text{m}$ , 300  $\mu\text{m}$  height and  $D = 3000$   $\text{mJ}/\text{cm}^2$  OPP dose), and the NA was measured over time. The NA of the waveguide was monitored during  $\approx 600$  hours of continuous 'operation', and Fig. 2.8 (b) shows the obtained average  $\langle \text{NA} \rangle = 0.1014$  (dashed line) with a standard deviation of  $\sigma(\text{NA}) = 3 \cdot 10^{-4}$ . This demonstrates that the optical properties remain stable within the limits of the measurement resolution, and hence confirms the reliability of *flash*-TPP in practical applications. Importantly, the NA of the same waveguide used for this evaluation is measured more than 1 year after. The obtained  $\text{NA} = 0.1018$  remains within the previously obtained standard deviation. This result certifies the long-term ( $>1$  year) stability of waveguides printed via *flash*-TPP and further demonstrates the high-quality and sturdiness of this technique.

Finally, the resilience of the waveguides to direct-sun exposure was tested by placing a sample on a window sill in central Europe during the summer months. As shown in Fig. 2.9, the almost complete polymerization of the cladding area was observed after  $\approx 15$  days, resulting in the vanishing of the light-guiding structures. It is evident that the direct and unprotected UV radiation from the sun is above the threshold to trigger the reaction of the remaining photoinitiators and initiate the polymerization process. Importantly, the impact of direct-sun exposure was equally examined for waveguides fabricated via (3+1)D printing using a low TPP power dose, i.e. 1, 2, and 3 mW, for the cladding regions. No difference compared to the *flash*-TPP technique was observed, since all structures are equally erased by direct-sun exposure. Consequently, the aging effect under direct exposure to sunlight is primarily attributed to an overall increase in the degree of polymerization and is not dependent on the specific polymerization technique, i.e. *flash*-TPP or (3+1)D printing, used during fabrication.

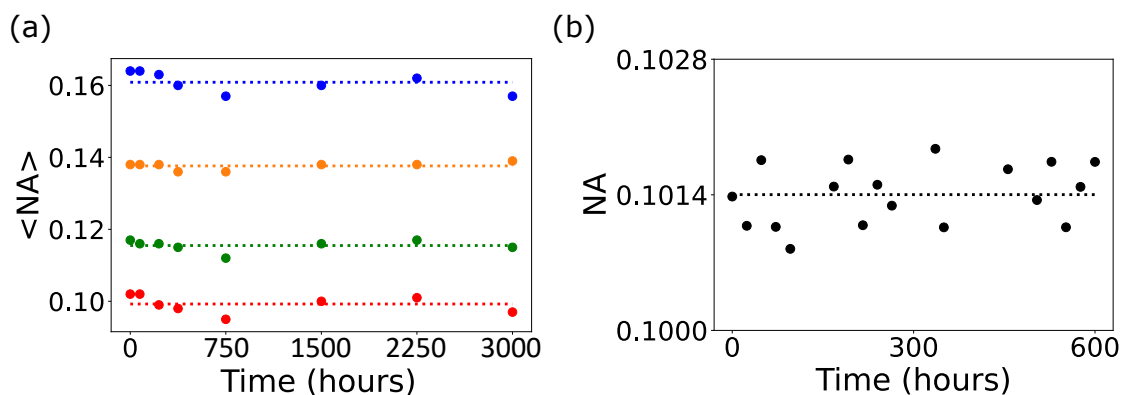


Figure 2.8: Temporal stability for 3D *flash*-TPP printed waveguides. Extracted from [215]. (a) Average  $\langle \text{NA} \rangle$  over time of 3D photonic waveguides under laboratory conditions. (b) Numerical aperture NA over time after continuous injection of light with 0.25 mW,  $\lambda = 660$  nm. No aging effect is found for the here evaluated time.

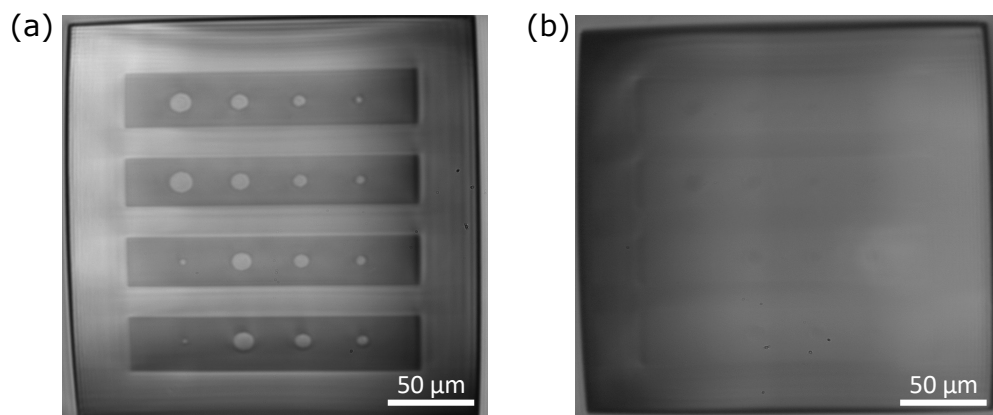


Figure 2.9: Effect of direct-sun exposure on photonic waveguides printed via *flash*-TPP. The optical microscope images show the effect of direct-sun exposure for  $\approx 15$  days during August of a 3D printed cuboid, before (left panel) and after (right panel) exposure. Full-polymerization is obtained for photonic chips fabricated via (3+1) printing and *flash*-TPP.

### 2.3/ FLASH-TPP PRINTING TIME

Printing time is typically proportional to the volume of a circuit, and the potential time saved with *flash*-TPP depends on the ratio of areas that require TPP and OPP exposure. Here, it is assumed that this ratio remains constant throughout different positions along the circuit's  $z$ -direction, and that waveguides with a radius of  $a \approx 2.5 \mu\text{m}$  are separated by a cladding of around  $6 \mu\text{m}$  to ensure minimal interaction, i.e. cross-talking between waveguide cores. The level of cross-talk depends on the interplay between confinement and separation, and the scaling of both the cladding width  $l$  and waveguide radius  $a$  should remain similar for integrated single-mode circuits with a comparable refractive index contrast  $\Delta n$ . When using only TPP to fabricate the entire circuit, the time required is  $T_{\text{TPP}} \propto (l + 2a)^2$ , whereas via *flash*-TPP scales as  $T_{\text{flash}} \propto \pi a^2$ . As a result, the relative duration  $\Gamma$  of *flash*-TPP relative to classic TPP is given by

$$\Gamma = \frac{\pi a^2}{(l + 2a)^2} = \frac{\pi}{4} \frac{1}{(1 + l/2a)^2}, \quad (2.1)$$

which is also the filling factor of waveguide cores within a 3D integrated photonic chip. Hence, even when considering a circuit with the highest possible density of photonic waveguide, which is typically the main objective of circuit integration, the fabrication time is significantly reduced to approximately  $\Gamma \approx 16 \%$  when compared to using TPP-alone. This agrees with the experimental observations, as using *flash*-TPP reduces the printing time to around  $\Gamma \approx 10 \%$  compared to conventional TPP. As a clear example, printing the 6 mm macroscopic structures from Fig. 2.7 (c) exclusively using TPP would take  $\approx 24$  h, while fabricating via *flash*-TPP only requires  $\approx 3$  h, which corresponds to a reduction of approximately  $\Gamma \approx 12 \%$ .

When fabricating tall waveguides, it is necessary to print an outer cladding serving as mechanical support. Typically, printing mechanical support represents a bottleneck when only a few waveguides are involved, but it becomes less significant when dealing with a large number of waveguides. The relationship between printing waveguides and mechanical support can be described using similar considerations as the simple speed factor

mentioned in Eq. (2.1). For waveguides with radius  $a$  and separation  $l$ , the area occupied by a waveguide core is given by  $A_{\text{core}} = \pi a^2$ . Using thickness  $t$  for the mechanical supports, and considering a circuit with  $N_c$  columns and  $N_a$  rows, along with a mechanical support wall present every  $k$  rows with thickness  $\alpha t$ , the total area of the circuit's mechanical support is denoted as

$$A_{\text{mec}} = t^2 \left[ 1 + \frac{1}{t} (N_c + N_a + \frac{\alpha}{k} N_c N_a) \right]. \quad (2.2)$$

To calculate the ratio  $R$  of printing time between the waveguide core and the mechanical support, normalizing by  $A_{\text{core}}$  and assuming a square circuit profile ( $N_c = N_a = \sqrt{N}$ ) with and hatching distances  $h_m$  ( $h_c$ ) for mechanical support (core), respectively, the obtained expression is

$$R \propto \frac{h_c}{h_m} \frac{t^2}{\pi r^2} \left( \frac{1}{N} + \frac{1}{t} \frac{2}{\sqrt{N}} + \frac{\alpha}{k} \right). \quad (2.3)$$

For large circuits, the additional time for fabricating the mechanical support therefore reduces to

$$R \Big|_{N \rightarrow \infty} \propto \frac{h_c}{h_m} \frac{t^2}{\pi a^2} \frac{\alpha}{k}. \quad (2.4)$$

This ratio is constant and depends on the relative ratio of core and mechanical hatching distances  $\frac{h_m}{h_c}$ , of the ratio between the areas of the mechanical support's unit cell and waveguide's core  $\frac{t^2}{\pi a^2}$ , and of the properties of the intra-wall support  $\frac{\alpha}{k}$ . This is  $R \Big|_{N \rightarrow \infty} \propto \frac{0.4}{0.8} \frac{100 \mu\text{m}^2}{7.1 \mu\text{m}^2} \frac{0.5}{1} = 3.52$ , and printing mechanical support and waveguides therefore takes comparable amounts of time. However, the spacing between individual waveguides here is  $30 \mu\text{m}$ . Using a denser fabrication with  $l = 6 \mu\text{m}$ , it is likely to remove the mechanical support, and in this case, the scaling is  $R \Big|_{N \rightarrow \infty} \propto \frac{1}{\sqrt{N}}$ . Therefore, the mechanical support takes less and less time relative to the photonic guiding regions.

## 2.4/ CONCLUSIONS AND OUTLOOK

Chapter 2 covered the principles of the *flash*-TPP printing strategy. *Flash*-TPP is a simple and fast lithography configuration based on combining OPP and TPP for the fabrication of polymer-cladded single-mode 3D photonic waveguides. The *flash*-TPP concept synergistically combines three principles. Firstly, waveguide cores are printed via DLW-TPP, employing precise calibration of TPP laser power and large lateral resolution by minimizing hatching distances between voxels ( $h = 0.4 \mu\text{m}$ ). This ensures minimal propagation losses and smooth core-cladding interfaces. Secondly, areas serving as mechanical support like side walls, do not interact with the guided light, hence no precise control of the spacing between TPP voxels is required. These areas are printed with a larger hatching distance ( $h = 0.8 \mu\text{m}$ ). Finally, instead of employing DLW-TPP for the cladding region, the entire photonic circuit is polymerized in a single-step under UV blanket irradiation via OPP. By combining these three aspects, the overall printing time is reduced by  $\approx 90 \%$  compared to conventional TPP-only fabrication. Moreover, for integrated photonic chips,

where the packing density is adjusted to minimize the signal's cross-talking, a similar acceleration in fabrication is generally to be expected.

Via *flash*-TPP, and here demonstrated with the commercially available IP-S photoresist, a precise control over the refractive index contrast  $\Delta n$  between the waveguide core and cladding is achieved by adjusting the UV exposure dose  $D$  during the blanket OPP illumination, covering a range from 0 to 9000 mJ/cm<sup>2</sup>. The optical properties of the waveguides are analyzed by fitting the output intensities to the LP<sub>01</sub> mode for different UV exposure doses  $D$  and diameters  $\tilde{d}$  below the cut-off condition of the second LP<sub>11</sub> mode. From these fits, the waveguide's NA as a function of the UV dosage  $D$  is investigated. The experimentally obtained data exhibited excellent agreement with the expected exponential trend observed in saturation processes such as UV curing, resulting in numerical aperture values ranging from NA = 0.10 to NA = 0.16 with low propagation (injection) losses of 1.36 dB/mm (0.26 dB). The temporal stability of the waveguides is demonstrated over  $\approx$  3000 hours under 'rest' conditions in ambient laboratory conditions. An important aspect of the aging study is assessing the reliability of the *flash*-TPP method under 'operating' conditions. This is studied under continuous injection of 0.25 mW of light into a waveguide over  $\approx$  600 hours, and no signs of deterioration are found under these conditions.

Propagation losses do not yet reach the bulk absorption  $\approx$  0.055 dB/mm of the IP-S photoresist at  $\lambda = 660$  nm [177], cf. Fig. 1.22 (c). Currently, the propagation losses are approximately one order of magnitude higher than those of standard silicon photonic waveguides [41], see Fig.1.5. However, when compared to waveguides fabricated via DLW inscription in fused silica glass, propagation losses are comparable at  $\lambda = 660$  nm, while the injection losses are more than an order of magnitude lower [216]. Notably, these results represent a five-fold improvement compared to waveguides fabricated via (3+1)D printing. Furthermore, the potential of post-fabrication thermal annealing in reducing losses for waveguides fabricated via DLW in fused silica could be addressed in future investigations. Such annealing processes reduced losses from similar levels to  $\approx$  0.08 dB/cm, which indicates a promising approach towards reaching the material's absorption limit [217].

When 3D printing complex shapes, achieving homogeneous UV exposure can be challenging due to the presence of 'shadows' cast by TPP structures. To overcome this, a possible solution is to employ multiple UV sources positioned at different locations around the sample to ensure more uniform exposure [177]. Additionally, post-curing the UV exposed sample can help accelerate and homogenize the polymerization process. In the case of the liquid IP-S resist, which exhibits strong absorption at  $\lambda = 405$  nm (cf. Fig. 1.22 (c)), the OPP process can be attenuated at mm-depths within large-scale ICs. However, in the structures here demonstrated, this effect is not observed, most likely due to their high aspect-ratio that enables UV exposure through the nearby side-walls. To achieve uniform OPP exposure levels within mm-scale circuits with aspect-ratios close to unity, one approach could involve shifting the OPP wavelength closer to the edge of the photo-initiator's absorption range.

The integration of DLW-TPP with UV lithography has been previously demonstrated for the production of finely detailed 3D microstructures [218, 219]. However, in contrast to *flash*-TPP, these approaches are based on the polymerization of two distinct photoresists in two separate manufacturing stages. Likewise, these techniques are most efficient for 2D fabrication and can become time-intensive when applied to 3D fabrication, mainly due to the layer-by-layer processing method. Compared to P $\mu$ SL methods (see Sec-

tion 1.1.2.1), *flash*-TPP achieves a printing rate of  $0.014 \text{ mm}^3/\text{h}$ , which is a significant improvement compared to the  $0.002 \text{ mm}^3/\text{h}$  achieved by TPP alone, see Fig. 1.5. Furthermore, the speed of *flash*-TPP could be further enhanced by employing multiplexing techniques that convert a single writing voxel into multiple voxels through phase modulation with a spatial light modulator [220]. This approach can be seamlessly integrated with the *flash*-TPP method, making both highly complementary concepts.

Overall, the efficiency of *flash*-TPP as a highly capable manufacturing technique for fabricating polymer-based 3D integrated photonic circuits is established. This concept is particularly advantageous in applications where the integration of complex 3D topologies is required, where standard 2D integration remains impractical.

## 3D PRINTED ADIABATIC 1 TO M BROADBAND COUPLERS AND FRACTAL SPLITTER NETWORKS

The information presented in Chapter 3 exploits the practical capabilities of the *flash*-TPP fabrication methodology, covered in Chapter 2, towards the creation of complex photonic components. Here, single-mode adiabatic 1 to M broadband couplers and fractal splitters networks are demonstrated via *flash*-TPP. Most photonic ICs rely on optical splitters/combiners, and their implementation in 3D presents intriguing possibilities for creating optical routing ranging from one to multiple outputs [115]. All without the need for delicate optical interference units such as directional and MMI couplers [163, 164], cf. Fig. 1.14 (a) and (b). In 3D, the realization of 1 to M optical couplers becomes feasible by strategically arranging multiple output waveguides around the input waveguide, which is impractical to achieve in a purely 2D planar integration scheme [30, 14]. Most of previous studies have been focused on the 2D approach where coupling is limited to a one to one connection between optical components.

The relevant information presented in Chapter 3 is based on results published in: *Grabulosa, A., Porte, X., Jung E., Moughames, J., Kadic M. and Brunner, D. "(3+1)D printed adiabatic 1-to-M broadband couplers and fractal splitter networks" Opt. Express, vol. 31, no. 12, 2023, pp. 20256-20264. DOI: 10.1364/OE.486235.*

### 3.1/ 3D ADIABATIC 1 TO M COUPLERS

Low-loss single-mode optical coupling is a crucial tool in, both, classical and quantum photonic applications. Various methods have been employed to realize this [221], and among them, the most prevalent and well-established techniques are diffraction grating-based optical coupling [222, 223, 224], end-fibre coupling [225], and adiabatic coupling [226, 227]. As introduced in Section 1.2.3.2, adiabatic coupling offers efficient and low-loss single-mode optical transfer via evanescent waves [165]. In this process, the optical mode adiabatically transitions from the tapered core of an input waveguide (leaking into the cladding) towards the inversely-tapered cores of the output waveguides [228], therefore enabling highly efficient and broadband single-mode field transfer from 1 to M waveguides. Adiabatic coupling has become a widely adopted technique in the current 2D photonic integrated circuit technology [229, 230]. The optical transfer between the in-

and output waveguides is achieved through evanescent coupling, where the optical mode gradually leaks from the core of the tapering input waveguides into the cladding and then into the inversely-tapering output waveguides [231].

Adiabatically coupled waveguides offer great potential for sensing and characterizing on-chip, wafer-scale photonic components like microdisk arrays, planar microrings, and photonic crystal waveguides [232]. Additionally, this principle has been proposed as an efficient method for mode-selective coupling in optical communications involving multiple spatial modes [165, 233]. Likewise, adiabatic coupling serves as a crucial element in the development of photonic lanterns, which find numerous applications. Previous investigations have predominantly focused on studying adiabatic coupling between tapered optical fibers and various nanophotonic devices. Impressive achievements have been made in single-mode coupling of guided light from a tapered fiber to a photonic waveguide, with efficiencies reaching up to 97 %. This represents a highly promising pathway for the realization of photonic ICs [110]. Importantly, achieving ultra-low losses remains of vital importance for the scalable large-scale photonic integration of optical quantum networks and repeaters [234, 235].

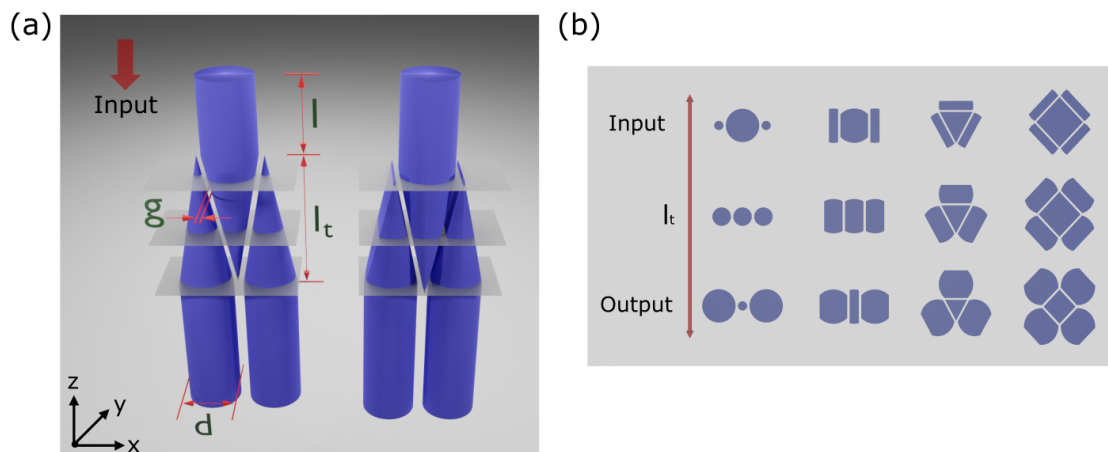


Figure 3.1: Design layout for adiabatic 1 to M couplers. Extracted from [236]. (a) Schematic illustration of conical (left panel) and truncated rod (right panel) tapering geometries of 1 to 2 splitters. (b) Top-view of the waveguides' cross-sections along taper-length  $l_t$  for 1 to 2 couplers with conical and truncated rod geometry, followed by 1 to 3 and 1 to 4 truncated rod splitters (from left to right).

### 3.1.1/ DESIGN AND FABRICATION

For illustrating the concept, Fig. 3.1 (a) depicts the generic case of 1 to 2 splitters employing two different tapering strategies, where the left (right) panels show conical (truncated rod) geometries, respectively. For the conical tapering geometry, the waveguide core gradually decreased in size along the  $(x, y)$ -directions at a uniform rate of  $d/l_t$ , where  $d$  represents the input diameter and  $l_t$  corresponds to the taper-length. For the truncated rod tapering geometry, the core is inwardly cut along the  $x$ -direction while retaining its original shape along the  $y$ -direction. This configuration restricts coupling to be parallel to the splitting direction, therefore increasing the effective interface area between the coupled waveguides, and hence by deliberately guiding the evanescent leakage. The taper-

rate  $d/l_t$  for both tapering geometries is intrinsically linked to the beating length  $z_b = \lambda/\Delta n$  for adiabaticity, see Eq. 1.47. Figure 3.1 (b) depicts the waveguides' cross-sections along the tapering regions for the different 1 to M splitters and tapering strategies.

To ensure efficient adiabatic overlapping, the waveguide cores are inversely-tapered for both the in- and output waveguides, employing equal taper-rates and geometric symmetry to match their relevant effective modal indices. The neighboring waveguides are separated by a gap  $g \in \{0.4, 0.8, 1.2\} \mu\text{m}$  to investigate the evanescent coupling efficiency over the distance between the coupled waveguides. To minimize cross-talk outside the tapered sections, a straight section with a length  $l = 30 \mu\text{m}$  is added to all output ports. The same tapering strategy is used for fabricating 1 to 3 (1 to 4) splitters, for which triangular (quadrangular) pyramid waveguides' cross-sections are required for the tapers employing truncated rod geometric symmetry. These configurations are depicted in the last two illustrations in Fig. 3.1 (b).

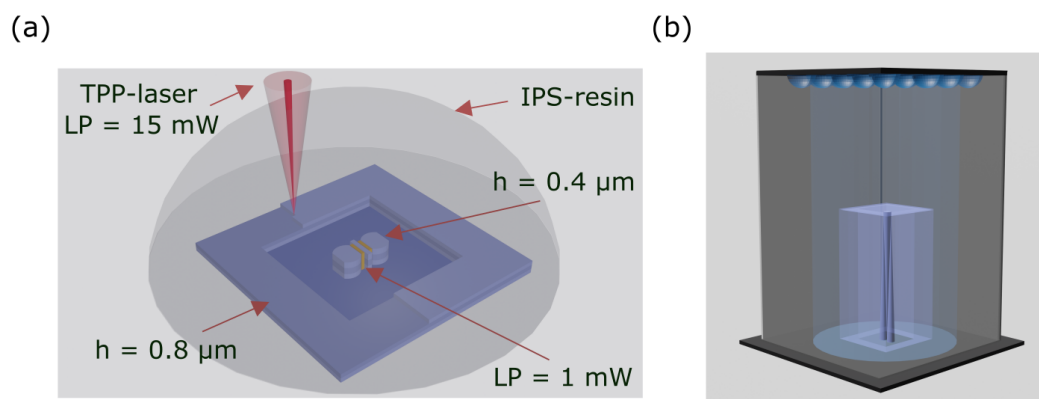


Figure 3.2: *Flash*-TPP fabrication of adiabatic 1 to M couplers. Extracted from [236]. (a) The waveguide cores (mechanical supports) are printed with hatching distances of  $h = 0.4 \mu\text{m}$  ( $h = 0.8 \mu\text{m}$ ) with laser power  $LP = 15 \text{ mW}$  and using the IP-S photoresist. Section in-between waveguides are printed with  $LP = 1 \text{ mW}$ . (b) After the development procedure, the 3D photonic chip is polymerized via OPP in a UV chamber.

The 1 to M adiabatic couplers are fabricated via *flash*-TPP and using the liquid negative-tone IP-S photoresist as shown in Fig. 3.2 (a). As discussed in Chapter 2, the waveguide cores are TPP-printed with  $LP = 15 \text{ mW}$  and  $h = 0.4 \mu\text{m}$ , while the mechanical supports are fabricated using  $h = 0.8 \mu\text{m}$ . The slicing distance is fixed to  $s = 1 \mu\text{m}$ . To maintain a constant gap  $g$  between the waveguides throughout the tapering regions, the volume in-between the tapers is polymerized with a low TPP laser power ( $LP = 1 \text{ mW}$ ). This improves the mechanical adhesion between the individual tapers without significantly modifying the gap's refractive index. This ensures that disjoint taper-sections do not drop during printing. After completing the TPP step, the unexposed photoresist outside the cuboid's surface is removed via a standard two-step development process. Finally, the entire 3D circuit is irradiated under UV blanket light with  $D = 3000 \text{ mJ/cm}^2$ , see Fig. 3.2 (b).

### 3.1.2/ OPTICAL PERFORMANCE

The evaluation of the optical performance of the splitters is done by examining the optical near-field of the output modes as well as the global losses, which include injection, coupling and propagation losses. All the optical characterization is done using the optical

set up shown in Fig. 1.25 with a wavelength of  $\lambda = 660$  nm. Figure 3.3 (a) illustrates the output intensities of truncated rod optical splitters for 2, 3, and 4 outputs. The core diameter is  $d = 3.3$   $\mu\text{m}$ , which ensures high mode confinement within the waveguide core while remaining single-mode, see Fig. 2.6 (a). The arrangement of the individual output intensities in Fig. 3.3 (a) perfectly agrees with the designed 1 to M splitters output configuration, cf. Fig. 3.1 (b). This demonstrates the high fidelity of the design and achieved layout.

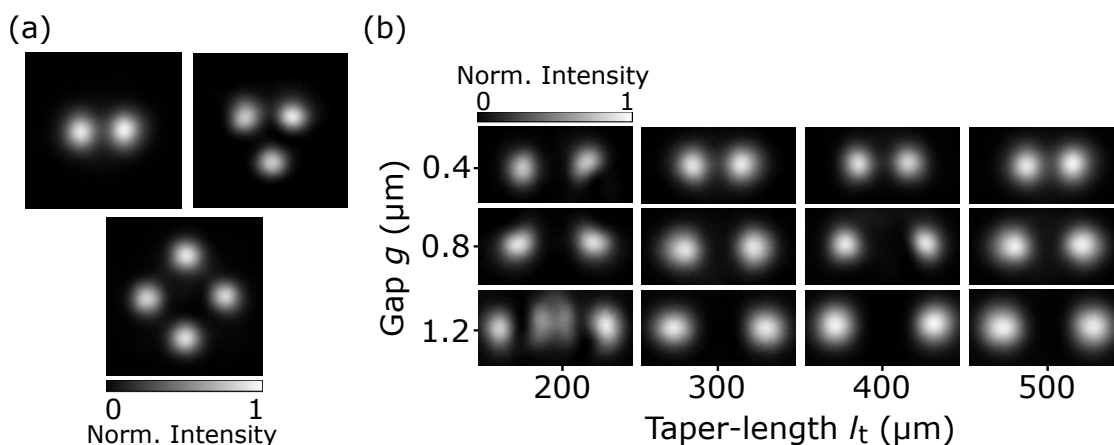


Figure 3.3: Adiabatic criterion for 1 to M splitters. Extracted from [236]. (a) Output intensity profiles of 1 to 2, 3 and 4 splitters with truncated rod geometry. (b) Output intensity profiles of the 1 to 2 optical splitters for taper-length  $l_t \in \{200, 300, 400, 500\}$   $\mu\text{m}$  (left to right panels) and gap distances  $g \in \{0.4, 0.8, 1.2\}$   $\mu\text{m}$  (top to bottom panels).

The analysis of the output intensity profiles in Fig. 3.3 (b) shows that for  $l_t = 200$   $\mu\text{m}$  the output profiles do not correspond to the fundamental  $\text{LP}_{01}$  mode, and for  $g = 1.2$   $\mu\text{m}$  (bottom panel) the individual output modes are not sufficiently decoupled. In contrast, a complete splitting of  $\text{LP}_{01}$  single-modes is observed for  $l_t \in \{300, 400, 500\}$   $\mu\text{m}$  for all  $g$ . Therefore, the adiabatic criterion of the 1 to 2 splitters is satisfied for a taper-length  $l_t > 200$   $\mu\text{m}$ , which is consistent with the theoretical value of  $z_b = 132$   $\mu\text{m}$  at the injection wavelength of  $\lambda = 660$  nm.

The numerical validation for adiabaticity was conducted via 2D simulations using COMSOL Multiphysics. The fundamental eigenmode is launched at the input-facet of the waveguide via *Port* boundary conditions, and then propagated throughout a 2D projection of the splitters depicted in Fig. 3.1 (a), employing scattering boundary conditions and considering refractive index contrast of  $\Delta n \approx 5 \times 10^{-3}$ . Figure 3.4 depicts the 2D numerical simulations of 1 to 2 adiabatic splitters with  $l_t = 100$   $\mu\text{m}$  (top panel) and  $l_t = 500$   $\mu\text{m}$  (bottom panel) for  $g \in \{0.4, 0.8, 1.2\}$   $\mu\text{m}$ . The inspection of the field intensity distributions throughout the 1 to 2 splitters agrees with the experimental observation of complete splitting of single-mode intensities on the  $l_t$  and  $g$ . This confirms the adiabatic nature of the truncated rod 3D optical splitters.

The global losses of 1 to 2 splitters with conical and truncated rod geometries over  $g$  are investigated. From Fig. 2.7 (b), injection losses of 0.26 dB were determined, which are here used to determine the propagation-coupling losses of the adiabatic splitters. As shown in Fig. 3.5 (a), the truncated rod splitters exhibit lower coupling losses compared to the conical counterparts across all gaps  $g$ . This improved performance can be attributed to the discussed enhanced directionality and increased effective transfer area

for this geometry. Consequently, the truncated rod geometry is chosen for the following investigations.

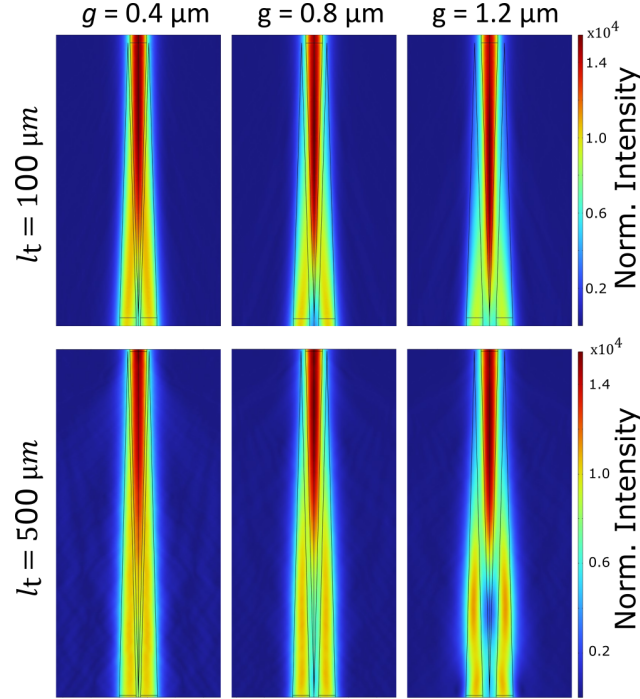


Figure 3.4: Adiabatic criterion simulations for 1 to 2 splitters. Simulations with  $l_t = 100 \mu\text{m}$  (top panel) and  $l_t = 500 \mu\text{m}$  (bottom panel) and gap distances  $g \in \{0.4, 0.8, 1.2\} \mu\text{m}$  (left to right panels). As in the experiments, full optical splitting is achieved for larger  $l_t$ . Simulations done in 2D via COMSOL Multiphysics considering  $\Delta n \approx 5 \times 10^{-3}$ .

Figure 3.5 (b) depicts the coupling losses of the 1 to 2 splitters with truncated rod geometry for  $g \in \{0.4, 0.8, 1.2\} \mu\text{m}$ , while varying the taper-length  $l_t$  from 100 to 500  $\mu\text{m}$ . The optimal coupling condition is identified for  $l_t = 500 \mu\text{m}$  and  $g = 0.4 \mu\text{m}$ , which corresponds to global losses of 0.32 dB, hence remarkably low coupling losses of 0.06 dB. Moreover, the intensities at the two output ports are highly uniform and only differ by  $\sim 3.4\%$ . Subsequently, these optimal values ( $l_t = 500 \mu\text{m}$  and  $g = 0.4 \mu\text{m}$ ) are used to fabricate 1 to 3 and 1 to 4 splitters, cf. Fig. 3.3 (a), which exhibit coupling losses of 0.4 dB and intensity differences between output ports of 4.6 % (6.1 %) for 1 to 3 (1 to 4) splitters. Notably, the coupling losses for the 1 to 3 and 1 to 4 splitters are nearly identical. Figure 3.5 (c) summarizes the coupling losses versus the number of output ports for the different 1 to M splitters.

Finally, the coupling losses are as well numerically investigated via 2D simulations using COMSOL Multiphysics with the same boundary conditions as previously. Figure 3.6 depicts the numerical results of the coupling losses of 1 to 2 adiabatic as in Fig. 3.5 (b) of reduced losses for large  $l_t$  and small gaps  $g$ . This again certifies the adiabatic signature of the splitters. However, the simulated splitters perform better than the fabricated ones, which could potentially be attributed to the fact that the simulations are performed in 2D instead of 3D. In this 2D scenario, most of the electric field intensity that is damped towards the cladding situated outside the in-between tapers along the  $(x, y)$  waveguide core is neglected. The complete and realistic analysis of coupling losses in such 3D mm-size structures is so far not possible due to the available computer RAM memory of 250 GB.

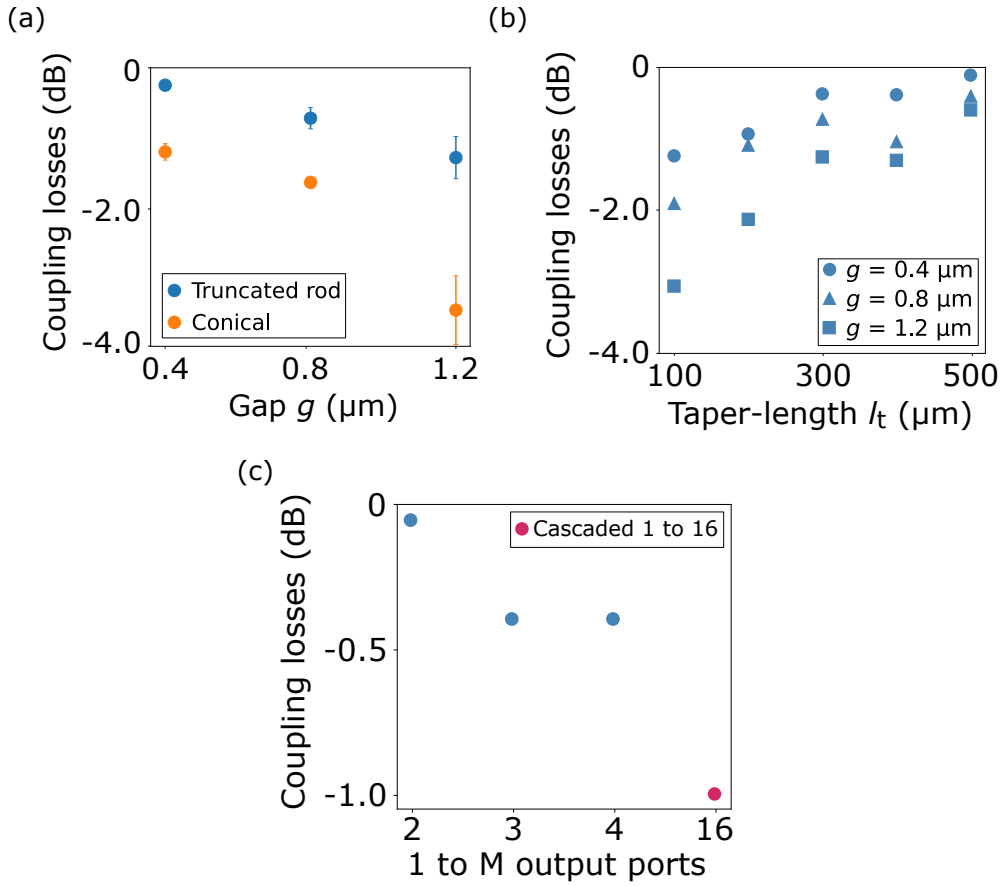


Figure 3.5: Optical performance of adiabatic 1 to M couplers. Extracted from [236]. (a) Coupling losses dependence over gaps  $g \in \{0.4, 0.8, 1.2\} \mu\text{m}$  for 1 to 2 splitters with conical (blue color) and truncated rod (orange color) geometry. Taper's length fixed to  $l_t = 300 \mu\text{m}$ . (b) Coupling losses versus gaps  $g$  of 1 to 2 splitters with truncated rod geometry and taper-lengths  $l_t \in \{100 : 100 : 500\} \mu\text{m}$ . (c) Coupling losses versus number of 1 to M output ports for adiabatic splitters with truncated rod geometry, i.e. 1 to 2, 1 to 3, 1 to 4 (blue color) and cascaded 1 to 16 (purple color).

### 3.1.3/ BROADBAND FUNCTIONALITY

Compared to interference-based directional couplers, cf. Fig. 1.14 (a) and (b), adiabatic power transfer offers a significant advantage in terms of reduced sensitivity to wavelength variations on the splitting ratios [164]. The broadband functionality of the truncated rod 1 to 2 adiabatic splitters with  $l_t = 500 \mu\text{m}$  is investigated by injecting different input light with wavelengths ranging from  $\lambda = 520 \text{ nm}$  to  $\lambda = 980 \text{ nm}$ . Figure 3.7 (a) shows the global losses for the 1 to 2 splitters, which remain below 2 dB throughout this nearly octave-spanning wavelength range. For  $\lambda \geq 660 \text{ nm}$ , the global losses start to increase due to a reduced modal confinement that results in a larger gap  $g$  for adiabaticity as well as increased scattering at the core-cladding interface. At  $\lambda = 520 \text{ nm}$ , which is close to the single-mode cut-off wavelength situated at  $\lambda \approx 480 \text{ nm}$ , the excitation of higher-order modes leads to increase global losses and the evanescent coupling decrease due to reduced modal overlap.

Figure 3.7 (b) illustrates the output intensity profiles of the 1 to 2 splitters throughout the

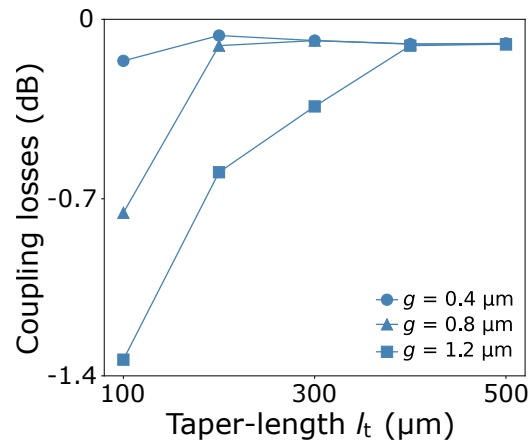


Figure 3.6: Simulated coupling losses versus gaps  $g \in \{0.4, 0.8, 1.2\} \mu\text{m}$  of 1 to 2 splitters with truncated rod geometry and taper-lengths  $l_t \in \{100 : 100 : 500\} \mu\text{m}$ . A similar behavior is observed as in the experiments. Simulations done in 2D via COMSOL Multiphysics considering  $\Delta n \approx 5 \times 10^{-3}$ .

entire range of wavelengths investigated here, providing clear evidence of the aforementioned effects of higher-order modes and non-separated single-modes. However, for a complete interpretation of these results, one would also have to consider the dispersion relation of the IP-S photoresist, which describes the wavelength dependency on the effective refractive index  $n_{\text{eff}}$  in the waveguide's core, see Fig. 1.22 (b). The dispersion relation affects the optimal coupling distance required for achieving adiabaticity. Importantly, the bulk absorption of the IP-S photoresist is not of crucial relevance for the length  $l_t$  across the entire range of wavelengths here examined, Fig. 1.22 (c).

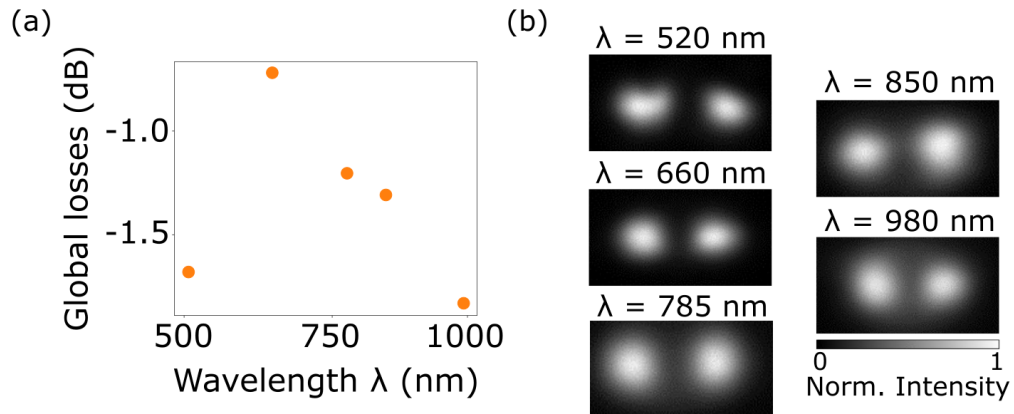


Figure 3.7: Broadband functionality. Extracted from [236]. (a) Global losses at different wavelength  $\lambda$  of the 1 to 2 splitters with  $l_t = 500 \mu\text{m}$  and  $g = 0.8 \mu\text{m}$ . (b) Output intensity profiles from (a) over  $\Delta\lambda \sim 500 \text{ nm}$ .

### 3.2/ FRACTAL NETWORKS OF 3D SPLITTERS

In photonic ICs, throughput efficiency drops exponentially in a 'deep' circuit that cascades multiple components in series [15]. To enable the future integration of photonic circuits in

applications relying on large-scale interconnects, achieving parallel and efficient scalability of spatially multiplexing photonic signals is crucial. These applications require connecting numerous in- and output channels while maintaining parallelism. Fractal topologies, i.e. self-similar branching structures, have been demonstrated as a suitable strategy for routing optical signals in three-dimensions [30]. Notably, fractal coupling architectures distribute an input signal across a growing number of outputs, which exponentially increases with the number of splitters along the signal's pathway. This distribution pattern maintains losses linearly relative to the number of output channels. This implies that the architecture of the tree is determined by the spacing between the output waveguides  $D_L$  and the height  $H_L$ , where  $L$  represents the number of specific bifurcation layers. Likewise, the dimensions across the bifurcation layers 'scales' as  $D_l = \sqrt{b} D_{(l+1)}$  and  $H_l = \sqrt{b} H_{(l+1)}$ , where  $b$  represents the number of splitting branches. In the case of cascading 1 to 4 splitters ( $l_t = 500 \mu\text{m}$ ,  $g = 0.4 \mu\text{m}$ ) in a double-layer results in 16 outputs, being  $b = 4$  the splitting branches, and after consecutive layers the values of  $D_L$  and  $H_L$  are doubled.

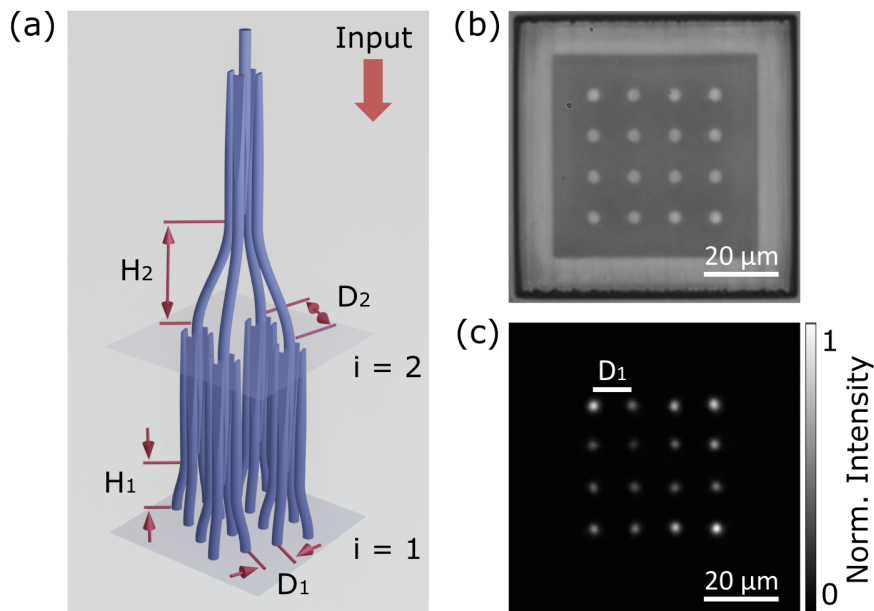


Figure 3.8: Fractal network splitters leveraging adiabatic coupling. Extracted from [236]. (a) Design of double-layer cascaded 1 to 4 splitters with truncated rod geometry ( $l_t = 500 \mu\text{m}$ ,  $g = 0.4 \mu\text{m}$ ) resulting in 16 outputs. (b) Optical microscope image under incoherent illumination showing the output (bottom surface). (c) Output intensity profiles from (a-b).

In such a configuration, the outputs of a 1 to  $M$  splitter serve as inputs to another splitter with the same splitting ratio. These geometries exhibit an exponential increase in the number of output channels with the number of cascaded splitters in a sequence. Cascading 1 to 4 splitters in two layers leads to one coupler in the first layer and four couplers in the second layer. This arrangement enables the realization of 16 output ports, which is schematically illustrated in Fig. 3.8 (a), where the ports between the two layers are connected through bent waveguides that follow a cosine-like shape, with dimensions  $D_1 = 10 \mu\text{m}$ ,  $H_1 = 200 \mu\text{m}$ ,  $D_2 = 20 \mu\text{m}$ , and  $H_2 = 400 \mu\text{m}$ .

Figures 3.8 (b) and (c) depict an optical microscope image of the output facet under incoherent illumination and the optical output of the 1 to 16 splitters, respectively. The

coupling losses are only 1 dB, and individual outputs are single-mode, see Fig. 3.5 (c). The performance of the cascaded 1 to 16 coupler is slightly better than that of the individual splitters, considering the propagation losses linked to bent waveguides in the output ports. The uniformity of splitting ratios is reduced compared to the individual splitters, where on average each output contains  $(5.81 \pm 2.31)\%$  of the injected intensity, which is close to the ideal value of 6.25%. However, this also shows that the individual coupling ratios to the 16 output waveguides significantly deviate from this average value. At present, this difference is attributed to slight variations of distances  $g$  in-between tapers between the four outputs of the 1 to 4 splitters, which may result in inhomogeneous splitting ratios throughout the cascaded layers, or potential refractive index fluctuations inside the gap due to the effects discussed in [237]. Further investigation is underway to fully understand this effect.

### 3.3/ CONCLUSIONS AND OUTLOOK

Chapter 3 demonstrates the fabrication of single-mode optical splitters via *flash*-TPP. These splitters leverage adiabatic power transfer to couple optical signals between one input and up to 4 output waveguides. By optimizing the waveguides' geometry and comparing conical and truncated rod tapering strategies for 1 to 2 splitters, low global (coupling) losses of 0.32 dB (0.06 dB) are achieved with only a difference of 3.4% between the two output port intensities. The functionality of the adiabatic splitters is investigated across a broad spectral window spanning almost an octave, revealing broadband mode splitting behavior ranging from  $520 \text{ nm} \leq \lambda \leq 980 \text{ nm}$ , during which global losses remain below 2 dB. Furthermore, the same concept is used to show efficient scalability of optical interconnects by cascading 1 to 4 optical splitters in a fractal, self-similar configuration, resulting in 16 single-mode output ports with only 1 dB coupling losses. However, the splitting ratio of the 1 to 16 cascade splitters still exhibits noticeable variations, which can be improved by exploring potential refractive index or thickness variations of the gap separating the tapers and inverse tapers.

Alternative approaches, such as coupling structures based on multi-mode interferometers (MMI), require intricate designs involving extensive numerical calculations for performance optimization [163, 164]. Additionally, similar to directional couplers, the splitting ratios of these structures exhibit significant variations with changes in the input wavelength. In contrast, the adiabatic power transfer concept exhibits intriguing properties, making it highly appealing for further exploration.

The potential of photonic circuits for future parallel and scalable optical interconnects, specially in the context of modern photonic NNs, is highly promising. As seen, reducing the gap between in- and output waveguides offers advantages in terms of minimizing coupling losses, cf. Fig. 3.5 (b), while enhancing integration compactness. However, there exists a fundamental limitation imposed by the generalized two-photon Sparrow criterion, see Fig. 1.20 (b), which determines the minimum lateral distance required for resolving modifications of neighboring voxels [185]. The adiabatic couplers presented here are fabricated using a fs-laser operating at  $\lambda = 780 \text{ nm}$  and a microscope objective (25X, NA = 0.8), the minimum lateral separation is  $0.344 \text{ }\mu\text{m}$ , which aligns well with the selected  $g = 0.4 \text{ }\mu\text{m}$ .

Overall, the adiabatic splitters demonstrated in Chapter 3 offer a promising solution for

efficient scalability of optical interconnects as well as decreasing the power consumption for NN computing hardware schemes. Traditional 2D circuits are not capable of achieving the necessary scalability, highlighting the significance of 3D photonic integration, see Fig. 1.5. An important consideration is that all the resins and processes employed in this study are CMOS compatible. This fulfillment of CMOS compatibility is a vital prerequisite, as it enables synergistic combinations of electronic and photonic circuits. By leveraging this compatibility, the integration of electronic and photonic components could lead to enhanced functionality and performance.

# SINGLE-MODE AND AIR-CLADDED WAVEGUIDES FOR INCREASED 3D PHOTONIC INTEGRATION

The photonic waveguides and splitters demonstrated in Chapter 2 and Chapter 3 leverage the combination of one- and two-photon polymerization of a single-material, i.e. IP-S photoresist, which intrinsically results in a low refractive index contrast of  $\Delta n \approx 5 \times 10^{-3}$  ( $NA \approx 0.12$ ) and as a result allows for comfortable integration of single-mode waveguides across visible and NIR wavelengths. However, the minimal bending radius for which light can be directed along a curved waveguide without exceedingly high losses is also determined by  $\Delta n$ . The small  $\Delta n$  of such polymer-cladded waveguides leads to large bending radii of 15 mm (7 mm) at  $\lambda = 1550$  nm ( $\lambda = 650$  nm), and in turn limiting a photonic circuit's integration density.

Polymer waveguides with air cladding have a relatively large  $\Delta n \approx 0.5$  ( $NA \approx 1.13$ ) with strong confinement [238], which enables extremely small bending radii of 25  $\mu\text{m}$  (14  $\mu\text{m}$ ) at  $\lambda = 1550$  nm ( $\lambda = 660$  nm), and in turn dense photonic integration [239]. However, these waveguides allow a large number of propagating modes (see Eq. 1.14), and the diameter of the core required for single-mode waveguides at  $\lambda = 660$  nm is  $d = 0.45$   $\mu\text{m}$ . This is not feasible due to the minimum resolution achievable via DLW-TPP fabrication, hence an alternative strategy is necessary.

In Chapter 4, the geometry and dimensions of air-cladded waveguides are carefully adjusted for achieving high mode-matching between the injection laser intensity distribution and that of the propagating fundamental mode. By doing so, inter-modal cross-talking to higher-order modes is minimized. Likewise, a detailed modal decomposition approach is developed to evaluate the degree of single-mode operation for such large index contrast waveguides, where the weakly-guiding approximation ( $\Delta n \ll 1$ ) is not valid. The single-mode operation is evaluated for s- and u-like bends, and their optical performance compared between classical circular and Euler geometries. Finally, single-mode and air-cladded splitters leveraging adiabatic coupling are demonstrated.

The relevant information presented in Chapter 4 is the result of investigations done in collaboration with Erik Jung in the framework of a master thesis project at Femto-ST, which can be found in: Jung, E., "Design and Analysis of 3D high index contrast optical Waveguide Circuit Components". Furthermore, a publication is in preparation.

#### 4.1/ ANALYSIS METHOD FOR HIGHLY-CONFINED WAVEGUIDES

In photonic waveguides, light propagates as superpositions of eigenmodes. The weakly-guiding approximation is not valid for air-claddeed waveguides due to their increased optical confinement and large refractive index contrast ( $\Delta n \approx 0.5$ ). For such waveguides, a detailed modal decomposition is required in order to analyze how much of the injected light is transferred to which eigenmode. The transmission per eigenmode coefficient  $T_i$  is calculated by analyzing the obtained output intensities after the optical characterization from 3D waveguides, as introduced in Section 1.3.8. Considering that the camera  $CAM_T$  used in the experimental set up, cf. Fig. 1.25, works based on the photoelectric effect, the electric field profiles for the fit are needed. For that reason, an analysis method is here developed to fit the normalized measured intensity profiles  $I_{\text{meas}}(x, y)$  from the output intensity with the absolute value of the eigenmodes electric field profiles  $E_{x,i}(x, y)$  and  $E_{y,i}(x, y)$  as

$$\tilde{I}_{\text{meas}}(x, y) \approx \left| \sum_{i=1} a_i E_{x,i}(x, y) \right|^2 + \left| \sum_{i=1} a_i E_{y,i}(x, y) \right|^2, \quad (4.1)$$

where the complex expansion coefficients  $a_i$  are determined. Since the electric fields  $E_{x,i}(x, y)$  and  $E_{y,i}(x, y)$  form an orthonormal base, the following condition is fulfilled

$$\sum_i |a_i|^2 = 1. \quad (4.2)$$

The value of  $|a_i|^2$  represents how much intensity remains in the eigenmode  $i$  after propagating a certain distance. For a squared expansion coefficient of  $|a_i|^2 = 1$  all the intensity is contained in eigenmode  $i$ , while for  $|a_i|^2 = 0$  null intensity is scattered to eigenmode  $i$ .

The transmission per eigenmode coefficient  $T_i$  is calculated by multiplying the absolute value  $|a_i|^2$  with the total transmission coefficient  $T_{\text{total}}$ . The first 20 eigenmodes of a STIN cylindrical waveguide are used to fit the experimentally measured intensity with the mode's electric field profiles obtained from simulations via COMSOL multiphysics. For those eigenmodes, the majority of the intensity is confined within the waveguides' core, and in order to reduce the computational time, only the intensity  $I_{\text{meas}}(x, y)$  contained within or in close proximity of the core is fitted. The dominant  $E_x$  and  $E_y$  components of the electric field are imported with a resolution of 50 data-points/ $\mu\text{m}$  and then normalized. This high-resolution provides a fine-grained interpolation of the function related to the electric field profiles. Backlight offset intensity  $I_0$  is accounted for, see Eq. 4.3. Possible rotations and translations of the electric field profiles compared to the experimental intensity profile must be taken into account, see Eq. 4.4.

$$\tilde{I}_{\text{meas}}(x, y) \approx I_{\text{fit}}(x, y) = \left| \sum_{i=1}^{N_{\text{fit}}} a_i \tilde{E}_{x,i}(\tilde{x}, \tilde{y}) \right|^2 + \left| \sum_{i=1}^{N_{\text{fit}}} a_i \tilde{E}_{y,i}(\tilde{x}, \tilde{y}) \right|^2 + I_0 \quad (4.3)$$

$$\begin{pmatrix} \tilde{x} \\ \tilde{y} \end{pmatrix} = \begin{pmatrix} \cos(\theta) & -\sin(\theta) \\ \sin(\theta) & \cos(\theta) \end{pmatrix} \cdot \begin{pmatrix} \frac{1}{S} \cdot (x + x_0) \\ \frac{1}{S} \cdot (y + y_0) \end{pmatrix}. \quad (4.4)$$

Via the fitting procedure, the real and imaginary parts of the expansion coefficients  $a_i$ , the translations  $x_0$  and  $y_0$ , the rotation angle  $\theta$  and the intensity offset  $I_0$  are determined. The

total number of fit parameters  $p$  is therefore  $p = 2 \cdot N_{fit} + 4$ . Finally, an additional coefficient  $R^2$  is included in the fit procedure as

$$R^2 = 1 - \left( \frac{n_{pix} - 1}{n_{pix} - p} \right) \frac{SSE}{SST}. \quad (4.5)$$

where  $n_{pix}$  is the number of fitted pixels and SSE (STT) is the sum of squared residuals (variances), respectively. The quantity  $R^2$  is a determination of the fit quality.

## 4.2/ STRAIGHT AND TAPERED WAVEGUIDES

The fundamental mode of a waveguide can be well approximated by a Gaussian beam of the same waist size due to the similarity of their intensity distribution. Here, the fiber-pigtailed laser diode (Thorlabs, LP660-SF20) is used for the optical characterization, cf. Fig. 1.25, which has a Gaussian output intensity distribution. Injecting only the waveguide's fundamental mode requires the Gaussian beam waist radius  $\omega_0$  of the propagating mode matching to the one of the mode distribution profile of the injection laser. Considering that  $\lambda$  and  $\Delta n$  are fixed by the experimental set up and the fabrication process, the waveguide radius  $a$  is the parameter that needs to be adjusted.

For experimentally determining the optimal mode-matching condition for air-cladded waveguides while minimizing injection losses, a set of straight waveguides with diameter  $d = 2 \mu\text{m}$  and  $50 \mu\text{m}$  height including tapers with taper-length  $l_t \in \{5, 5, 20\} \mu\text{m}$  and input diameter  $d \in \{2.8 : 0.2 : 4.2\} \mu\text{m}$  are printed. This fine sweep of the taper's dimensions is crucial to minimize inter-modal cross-talking to higher-order modes when targeting single-mode propagation in such air-cladded waveguides, hence a very precise optimization is crucial. For the optical characterization, the microscope objective MO<sub>2</sub> for the injection, cf. Fig. 1.25, is replaced by a different MO (Olympus PLN20X, NA = 0.4) for optimal mode-matching. As shown in Fig. 4.1 (a), the taper's dimensions are identified to be starting from an input diameter  $d = 3.4 \mu\text{m}$  to the target diameter of  $2 \mu\text{m}$ , during a taper-length  $l_t = 15 \mu\text{m}$ . As expected, this  $l_t$  is significantly shorter compared to polymer-cladded waveguides ( $l_t = 40 \mu\text{m}$ ), due to the increased optical confinement within the waveguide core and hence shorter Rayleigh length  $z_R$ , see Fig. 1.18.

The detailed eigenmode evaluation for these air-cladded waveguides is performed via the modal decomposition routine presented in Section 4.1. Figure 4.1 (b) depicts the SEM micrograph of the top-surface (top panel) and the output intensity profile (bottom panel), reassembling the fundamental EH<sub>11</sub> mode, of the optimized waveguide ( $d = 2 \mu\text{m}$  and  $50 \mu\text{m}$  height). The results obtained via the fitting routine are shown in Fig. 4.1, as (c) the measured intensity distribution normalized by the integrated intensity  $I/I_{int}$ , (d) the fit results, (e) the residuals  $R^2$  and (f) the transmission per eigenmode coefficients  $T_i$  for 20 eigenmodes. The high-quality of this fitting method is clearly seen, as the measured profile can be accurately approximated by the intensity profile of the fundamental EH<sub>11</sub> eigenmode. Likewise, the value of the residuals  $R^2 = 0.981$  close to unity also reveals the performance of this fitting methodology. Here, the transmission of the two-times degenerate fundamental mode is  $T_{fund} = 70 \%$  (red color), whereas the transmission of all the higher-order modes  $T_{high}$  (blue color) is almost negligible at a combined sum of  $T_{high} = 0.02 \%$ , see Fig. 4.1 (f).

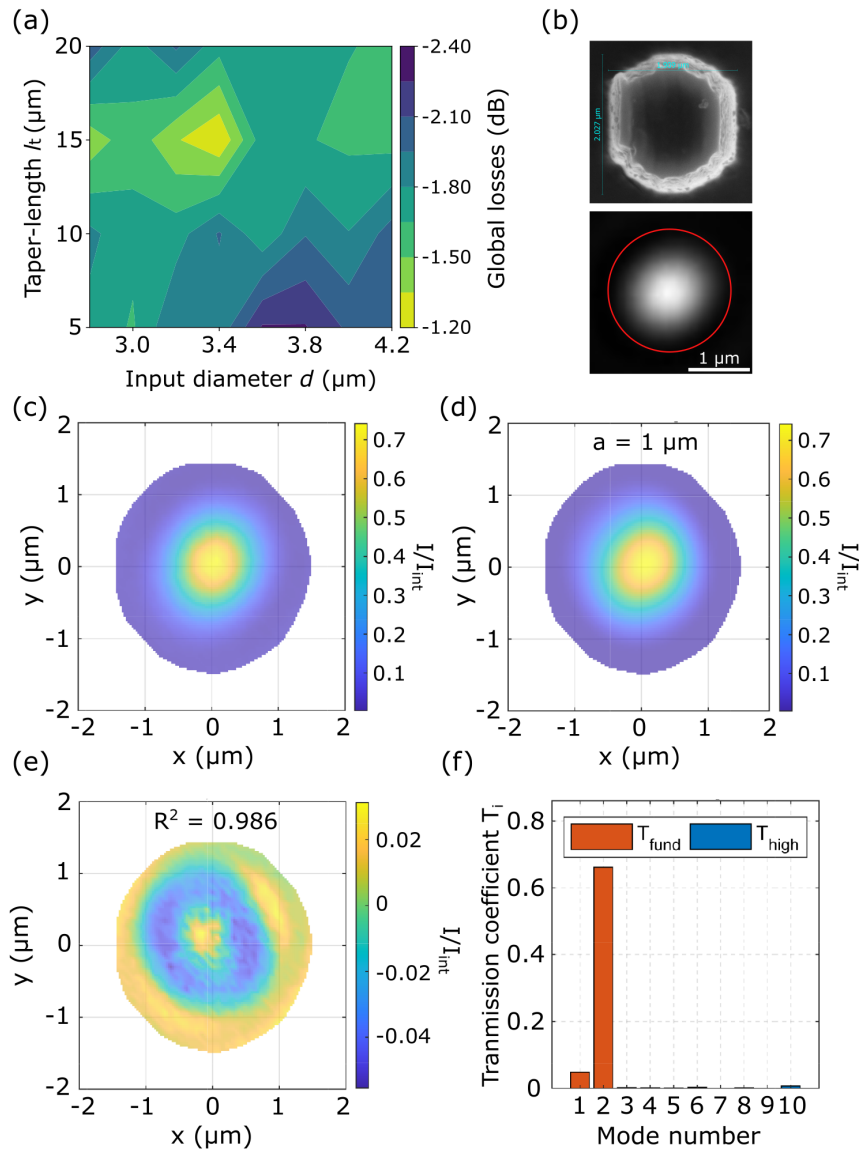


Figure 4.1: Taper optimizations and modal decomposition for air-cladded waveguides. (a) 2D scatter plot of fabricated tapers with taper-length  $l_t \in \{5 : 5 : 20\} \mu\text{m}$  and input diameter  $d \in \{2.8 : 0.2 : 4.2\} \mu\text{m}$ . Global losses are minimized for tapers with  $d = 3.4 \mu\text{m}$  and  $l_t = 15 \mu\text{m}$ . (b) SEM micrograph of the top-surface of an air-cladded waveguide core with  $d = 2 \mu\text{m}$  (top panel) and its output intensity profile (bottom panel). The modal evaluation of the output intensity from (b) is analyzed, with (c) the resulting measured intensity, (d) fit with first 20 eigenmodes, (e) residuals  $R^2$  and (f) modal decomposition for a waveguide with core radius  $a = 1 \mu\text{m}$  with relative transmission coefficient  $T_i$  for each eigenmode.

### 4.3/ CURVED WAVEGUIDES: CIRCULAR AND EULER-BENDS

Compared to standard straight waveguides, the electromagnetic analysis of curved waveguides is notably challenging, as the effective refractive index  $n_{\text{eff}}$  spatially depends on the bend radius  $R$ . The complexity of the study considerably increases when targeting single-mode operation in such air-cladded bent waveguides [125, 126]. Some consid-

erations are therefore essential when investigating such waveguides. First, a conformal transformation of the radial coordinates over the refractive index profile  $n(r)$  within the waveguide core is done [240, 241] for solving the Helmholtz from Eq. 1.28. To this aim, the radial part of Eq. 1.30 is reformulated as

$$r = R \cdot e^{\frac{g}{R}}, \quad (4.6)$$

$$g = R \ln\left(\frac{r}{R}\right) \text{ with } g, r > 0, \quad (4.7)$$

where  $R$  is the bending radius relative to the waveguide's center. A comparison of coordinates transformation is depicted in Fig. 4.2 (a) for (i) bent and (ii) straight waveguides. As seen, this transformation allows to solve a bent waveguide described by Eq. 4.6 using the approximation of a straight waveguide as in Eq. 4.7.

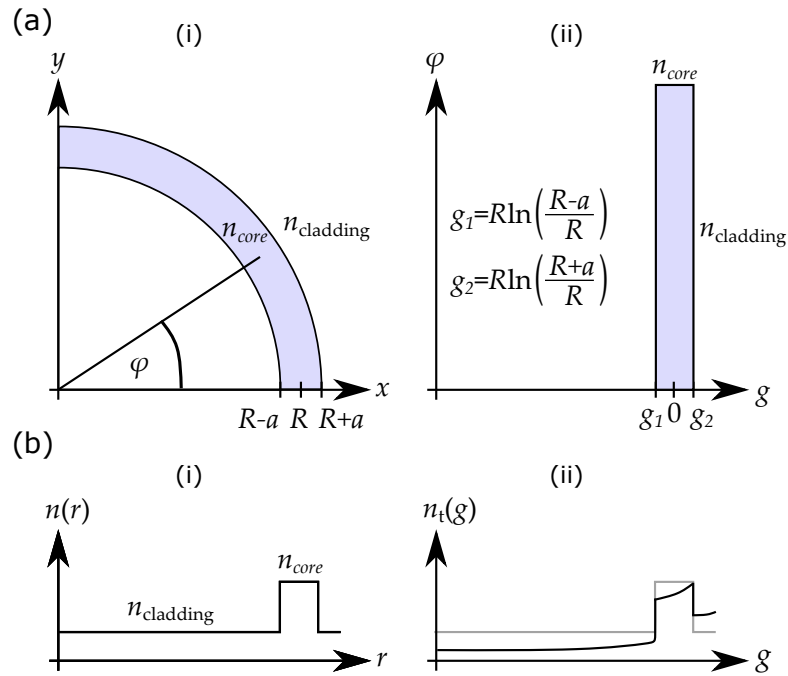


Figure 4.2: Conformal transformation for bent waveguides. Extracted from [241]. (a) Bent waveguide (i) that is transformed via a conformal transformation to a straight waveguide (ii). (b) Refractive index profile before (i) and after (ii) the conformal transformation.

With  $n_t(g)$  ( $\beta_t$ ) as the new refractive index distribution (propagation constant), the transformed Helmholtz equation for bent waveguides is expressed as

$$n_t(g) = n\left(R \cdot e^{\frac{g}{R}}\right), \quad (4.8)$$

$$\beta_t = \frac{\beta}{R}. \quad (4.9)$$

where the refractive index profile of the waveguides  $n(r)$  is modified by the transformation  $n_t(g)$  as illustrated in Fig. 4.2 (b).

This coordinate transformation subsequently alters the electric field distribution of the eigenmodes. When light propagates within bent waveguides, instead of concentrating at the center of the waveguide's core, the optical modes are displaced towards the position where the transformed refractive index  $n_t(g)$  has its maximum value. As the waveguide bends more significantly, the intensity distribution undergoes a larger shift, hence increasing its transition towards the cladding where it is exponentially attenuated. Crucially, the curvature, i.e. bending radius  $R$ , fundamentally affects the total light transmission as well as the inter-modal cross-talking of eigenmodes into higher-order modes propagating within the waveguide [242].

### 4.3.1/ DESIGN AND FABRICATION

The design of low-loss air-cladded bent waveguides with few optical modes propagating is not a trivial task [243]. Several geometries are considered for the realization of such bent waveguides, i.e. simple cosine or sine-like shapes, classical circular bends and more sophisticated Euler or Bezier curves [244]. Here, curved waveguides with circular and Euler geometries are investigated [245]. Compared to the classical circular curvatures following  $(x, y) = (R \cos(\alpha), R \sin(\alpha))$  with arc length  $L = \alpha R$ , the more intricate geometry of the Euler-bend is based on the so-called clothoid [246]. The clothoid is a spiral whose curvature  $\frac{1}{R}$  linearly increases with arc length  $L$  as

$$L = \frac{1}{R} \cdot A^2, \quad (4.10)$$

where the proportionality variable  $A$  is a positive real constant.

Figure 4.3 (a) schematically illustrates the curves for both the classical circular (red color) and Euler (blue color) bending geometries. For Euler-bends, following the description for a circular arc length  $L$ , the differential arc length  $dL = R \cdot d\alpha$  is integrated as  $\alpha = \int \frac{L}{A^2} dL = \frac{L}{2R}$ . For a clothoid,  $dx$  and  $dy$  are expressed in the  $(xy)$ -plane using cylindrical coordinates as  $(dx, dy) = (\cos(\alpha)dL, \sin(\alpha)dL)$ , which leads to its vectorial representation

$$\begin{pmatrix} x \\ y \end{pmatrix} = \int \begin{pmatrix} \cos\left(\frac{L}{2R}\right) \\ \sin\left(\frac{L}{2R}\right) \end{pmatrix} dL. \quad (4.11)$$

Importantly, for small angles, it is valid to approximate Eq. 4.11 by a Taylor expansion of the argument and by integrating as

$$\begin{pmatrix} x \\ y \end{pmatrix} = L \cdot \begin{pmatrix} 1 - \frac{\alpha^2}{2! \cdot 5} + \frac{\alpha^4}{4! \cdot 9} \pm \dots \\ \frac{\alpha}{3} - \frac{\alpha^3}{3! \cdot 7} + \frac{\alpha^5}{5! \cdot 11} \pm \dots \end{pmatrix}. \quad (4.12)$$

For achieving a symmetric Euler-bent shape with a bending angle  $\alpha$ , it is crucial to combine two identical clothoid spirals with bending angle  $\frac{\alpha}{2}$ , as the geometric shape defined by Eq. 4.11 resembles a clothoid spiral. Figure 4.3 (b) illustrates the shape and curvature of such an Euler-bend compared to a circular bend with radius  $R = 1 \mu\text{m}$ . As seen, the Euler-bend begins with no curvature at the starting point to ensure a smooth transition from a straight section. The curvature progressively increases until it reaches  $\frac{\alpha}{2}$ , which represents the minimum radius  $R_{\min}$  of the circular bend  $R$ . Beyond this point, the curvature decreases linearly until the end of the bend.

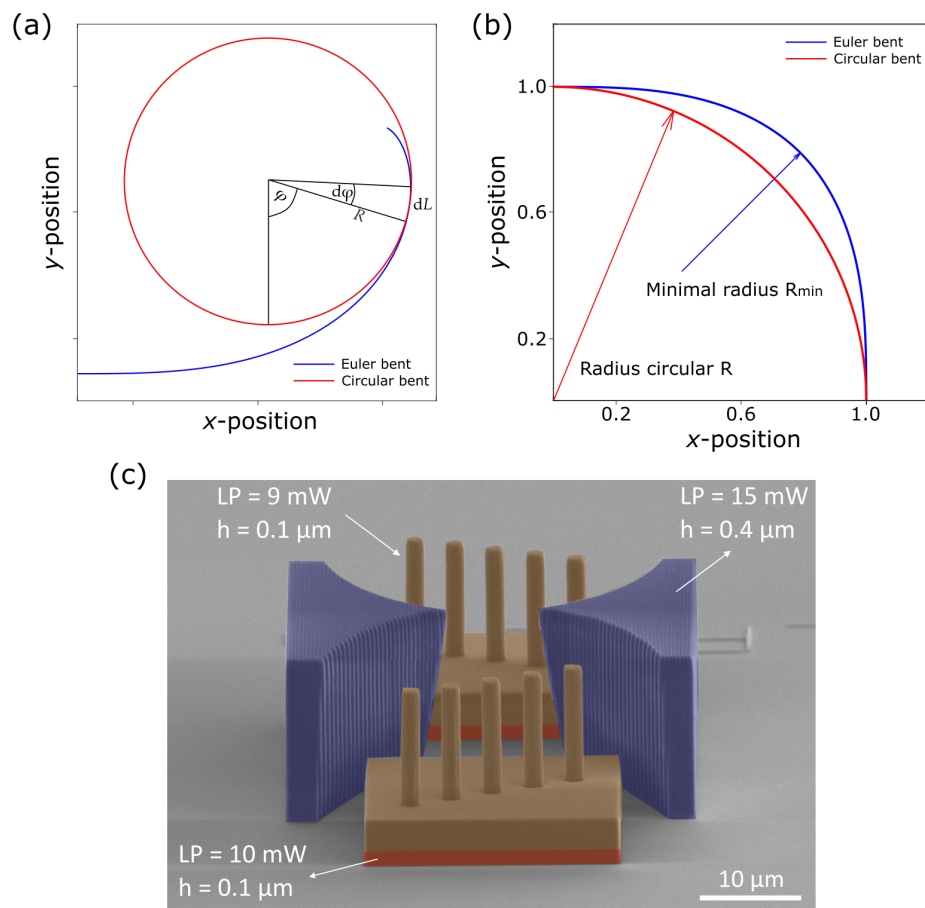


Figure 4.3: Euler versus circular bends and DLW-TPP fabrication. (a) Approximation of a clothoid for an infinitesimally small angle  $d\varphi$  through a circle with the same radius. (b) Comparison of the shape of  $90^\circ$  Euler and circular bends. (c) SEM micrograph of a 3D photonic circuit's cross-section containing a set of s-bends with bending radii  $R \in \{6, \dots, 15\} \mu\text{m}$  using the IP-Dip photoresist and a 63X microscope objective. The waveguide cores (mechanical supports) are printed with high(low)-resolution using hatching distances  $h = 0.1 \mu\text{m}$  ( $h = 0.4 \mu\text{m}$ ) and laser power  $LP = 9 \text{ mW}$  ( $LP = 15 \text{ mW}$ ), respectively. A pedestal is added to improve the adherence of the waveguide cores on the substrate, and its bottom is printed with  $LP = 10 \text{ mW}$ .

For the fabrication, circular and Euler-bent waveguides are fabricated via DLW-TPP using the liquid negative-tone IP-Dip photoresist, which provides a higher printing resolution than IP-S and hence, at least in principle, smoother surfaces in curved waveguides. Prior to the TPP-fabrication, the fused silica substrate is activated via a standard oxygen plasma treatment for improving photoresist adhesion. Figure 4.3 (c) shows the cross-section of an exemplary photonic chip containing a set of curved waveguide cores (yellow color) printed using an optimal laser power ( $LP = 9 \text{ mW}$ ) and minimal hatching distance ( $h = 0.1 \mu\text{m}$ ) to ensure smooth surfaces. These air-cladded waveguides are extremely fragile and tend to collapse after the development procedure. This is solved by engineering a customized mechanical support for improving the overall stability of such waveguides. These special mechanical supports (purple color) are printed with a larger hatching distance ( $h = 0.4 \mu\text{m}$ ) and laser power ( $LP = 15 \text{ mW}$ ) to reduce printing times. For additional adherence, a pedestal accommodating the curved waveguides is constructed ( $h =$

0.1  $\mu\text{m}$ ), where the first layers (orange color) are printed using larger TPP-dosage (LP = 10 mW). The slicing distance is fixed to  $s = 0.1 \mu\text{m}$  for all the photonic chip, since for curved waveguides it crucially affects the surface's roughness as well as their stability in the third-dimension.

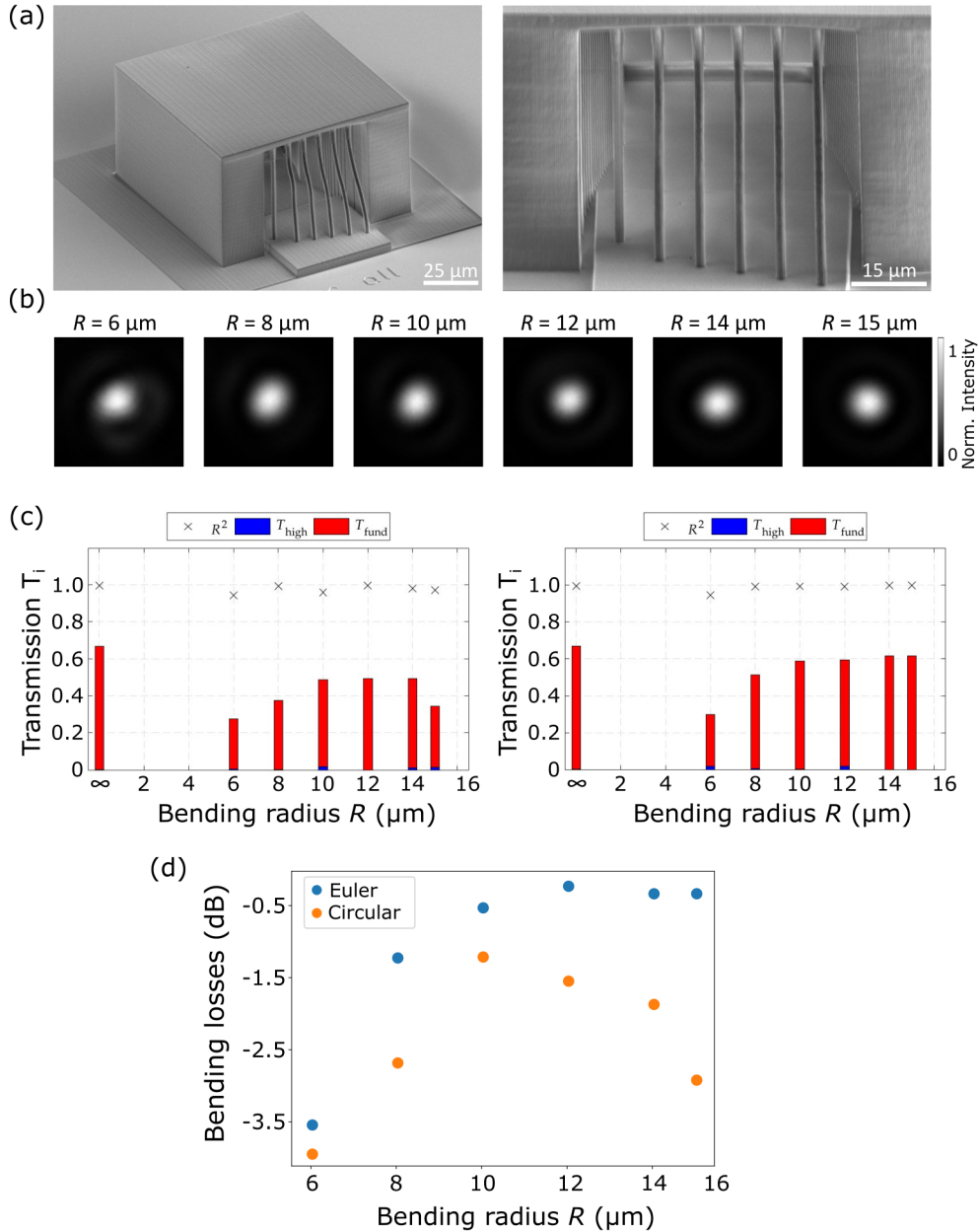


Figure 4.4: Comparison of the optical performance for s-bends with Euler and circular geometries and angle  $\alpha = 45^\circ$ . (a) SEM micrographs of an exemplary 3D photonic circuit printed via DLW-TPP containing a set of Euler s-bends of  $d = 2 \mu\text{m}$  and bending radii  $R \in \{6, \dots, 15\} \mu\text{m}$ . A straight waveguide ( $R = \infty \mu\text{m}$ ) is included for reference. (b) Experimental output intensity profiles from the s-bends with Euler geometry from (a). (c) Transmission coefficient  $T_i$  per eigenmode over bending radii  $R \in \{6, \dots, 15\} \mu\text{m}$  for circular (left panel) and Euler (right panel) s-bends after a modal decomposition of the output intensities from (b) for 20 eigenmodes. (d) Bending losses versus bending radii  $R$  for circular (orange color) and Euler (blue color) s-bends.

### 4.3.2/ S-BENDS

The first investigations of curved waveguides involve fabricating circular and Euler-bends following an s-like shape with  $\alpha = 45^\circ$  [247]. The bending losses of such s-bends are evaluated over bending radii spanning  $R \in \{6, \dots, 15\} \mu\text{m}$ . The diameter of s-bent waveguides is set to  $d = 2 \mu\text{m}$ , and including the optimized taper as shown in Fig. 4.1 (a). The SEM micrographs of Figure 4.4 (a) depict an exemplary structure integrating a set of Euler s-bends over bending radius  $R$  and a tapered straight waveguide for reference. The visual inspection of the output intensity profiles of s-bends with Euler geometry from Fig. 4.4 (b) shows that for small bending radii  $R = 6 \mu\text{m}$  the intensity distribution profile is multi-mode, not fully centered at the center of the waveguide core. For bending radii  $R \geq 10 \mu\text{m}$ , the output intensities correspond to the fundamental  $\text{EH}_{11}$  eigenmode, well-centered at the waveguide's core. This bending radius is therefore the transition value  $R$  by which the cross-scattering from the fundamental  $\text{EH}_{11}$  mode to higher-order modes is minimized for Euler s-bends.

Figure 4.4 (c) shows the evaluation of the optical performance for such curved waveguides, where the transmission coefficient  $T_i$  is analyzed via fitting circular (left panel) and Euler (right panel) s-bends for different  $R$ . The cross-scattering to higher-order modes is comparatively low and  $T_{\text{fund}} \gg T_{\text{high}}$  for all the entire  $R$  range. Importantly, the large value of the residuals  $R^2$  (black crosses) close to unity again confirms the validity of this fitting approach.

Finally, the output intensity of the straight waveguide ( $R = \infty \mu\text{m}$ ) printed in the same 3D structure is used as a reference intensity in order to extract the bending losses for circular (orange color) and Euler (blue color) s-bent waveguides, see Fig. 4.4 (d). It is clear that the bending losses for both the s-bends start to increase until reaching a plateau (0.4 dB) for  $R \geq 10 \mu\text{m}$ . However, the s-bends with Euler geometry exhibit better performance (lower bending losses) compared to circular s-bends for all  $R$ , drastically increasing for  $R > 12 \mu\text{m}$ . This shows the clear advantage of Euler bends compared to classical circular curvatures in terms of low-losses and single-mode operation, and these are therefore chosen for the following investigations.

### 4.3.3/ U-BENDS

A further investigation of curved waveguides is done by constructing Euler-bends following a u-like shape with  $\alpha = 180^\circ$ , where the same evaluation procedure followed for s-bends is used to determine their optical performance. For such u-bent waveguides, one particularity is that both the light injection and collection happen from the same side of the substrate, which consequently requires some modifications regarding the optical characterization, see Fig. 1.25. Here, the input (output) light is injected (collected) with the same microscope objective MO (Olympus PLN20X, NA = 0.4), while the reference intensity  $T_{\text{ref}}$  (used to measure the optical losses) is obtained by placing a silver mirror (99 % reflectivity) at the focal point. For the fabrication, two tapered sections are added to, both, the waveguide's input and output, which also provides additional mechanical stability.

The SEM micrographs of Figure 4.5 (a) depict a set of u-bends with an Euler geometry fabricated with a bending radius ranging  $R \in \{4, \dots, 10\} \mu\text{m}$ , where the discussed features of such u-bends are visible. From the visual inspection of the output intensity profiles

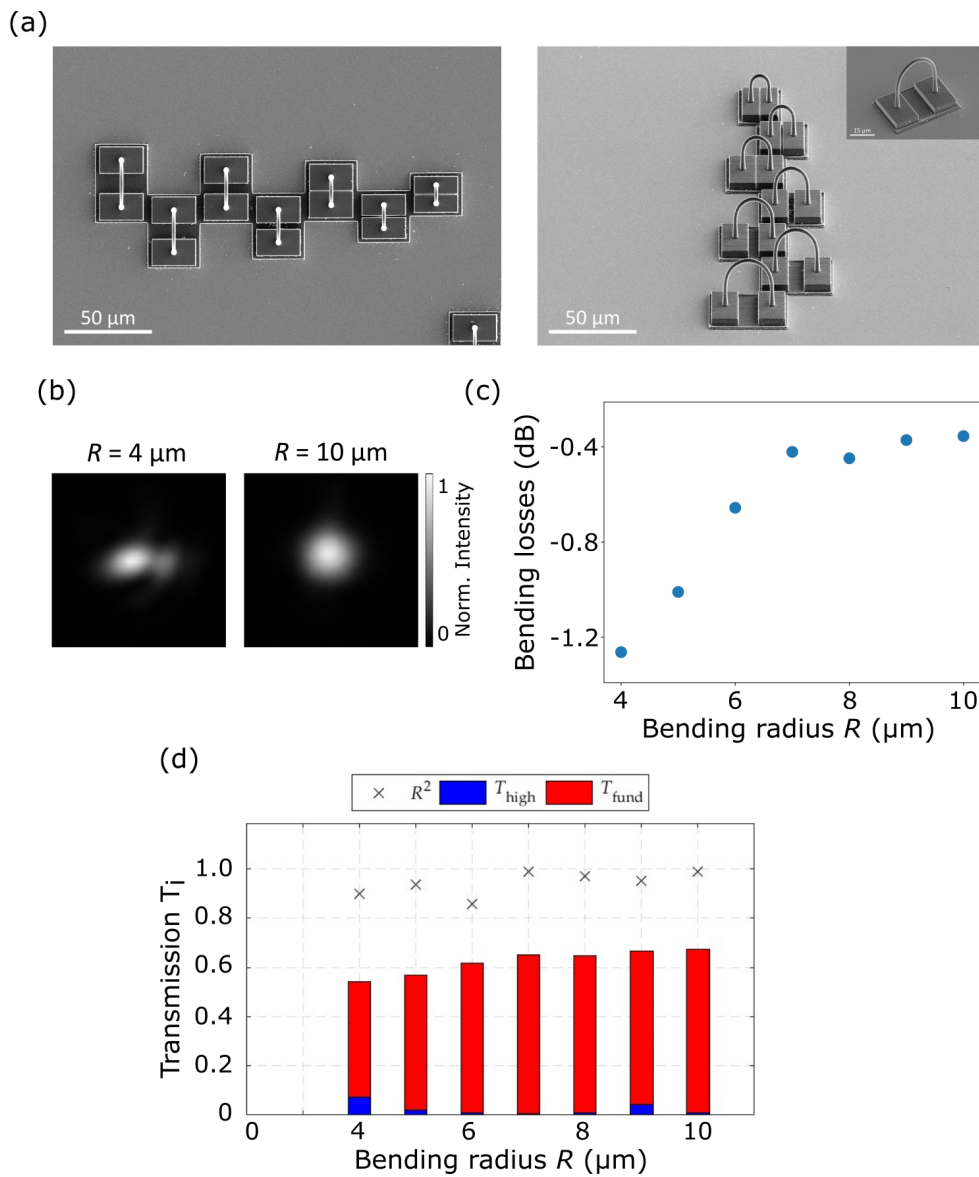


Figure 4.5: Optical performance of u-bends with Euler geometry and angle  $\alpha = 180^\circ$ . (a) SEM micrographs of an exemplary 3D photonic circuit printed via DLW-TPP containing a set of Euler u-bends of  $d = 2 \mu\text{m}$  and bending radii  $R \in \{4, \dots, 10\} \mu\text{m}$ . (b) Experimental output intensity profiles from the Euler u-bends from (a) with  $R = 4 \mu\text{m}$  and  $R = 10 \mu\text{m}$ . (c) Bending losses versus bending radii  $R \in \{4, \dots, 10\} \mu\text{m}$  for u-bends with Euler geometry. (d) Transmission coefficient  $T_i$  per eigenmode over bending radii  $R$  for Euler u-bends after a modal decomposition of the output intensities for 20 eigenmodes.

of Fig. 4.5 (b), large cross-scattering from the fundamental  $\text{EH}_{11}$  mode to higher-order modes is observed for a tight bending radius  $R = 4 \mu\text{m}$ . For  $R = 10 \mu\text{m}$ , the output intensity is clearly single-mode. Regarding bending losses, a similar behavior compared to s-bends is observed, where losses decrease until reaching a plateau at 0.4 dB for  $R > 7 \mu\text{m}$ , see Fig. 4.5 (c). Importantly, the bending losses for larger bending radii are similar for, both, the s- and u-bends with Euler geometry, showing reproducible optical performances. A bending radius of  $R = 10 \mu\text{m}$  offers the best performance in terms of fundamental  $\text{EH}_{11}$  mode propagation as well as lower bending losses for both the curvatures.

Finally, Fig. 4.5 (d) shows the transmission coefficient  $T_i$  per eigenmode over  $R$  obtained via the fitting procedure, demonstrating their good performance regarding single-mode operation. Future investigations include fabricating u-bends with larger bending radius  $R > 10 \mu\text{m}$  in order to study the limitation on mechanical stability until breakdown for such bends.

#### 4.4/ AIR-CLADDED 3D SPLITTERS

For the efficient integration of 3D photonic circuits, it is crucial to split/combine optical signals into/from multiple ports. As demonstrated in Chapter 3, high-quality adiabatic 1 to  $M$  broadband couplers and fractal splitter networks are feasible via *flash*-TPP. Here, both, the radius and cross-section's shape of air-cladded waveguides are engineered for leveraging adiabatic power transfer. The layout design of such air-cladded splitters is illustrated in Fig. 4.6 (a) for the case of 1 to 3 outputs, where the cross-section of the input waveguide is extruded along a path described by

$$\begin{pmatrix} x \\ y \\ z \end{pmatrix} = \begin{pmatrix} \cos(i \cdot 2\pi/n) & -\sin(i \cdot 2\pi/n) & 0 \\ \sin(i \cdot 2\pi/n) & \cos(i \cdot 2\pi/n) & 0 \\ 0 & 0 & 1 \end{pmatrix} \cdot \begin{pmatrix} \frac{g}{2}(\cos(\pi t) - 1) \\ 0 \\ l_{\text{split}} \cdot t \end{pmatrix}, \quad (4.13)$$

where the rotation matrix describes the spatial orientation of the branching  $i \in \{1, n\}$ , the distance/gap  $g$  between waveguides,  $l_{\text{split}}$  is the splitting distance and  $t \in \{0, \dots, 1\}$  is the index of the parametric path.

The SEM micrographs of Fig. 4.6 (b) depict a set of 1 to 3 air-cladded splitters leveraging adiabatic power transfer with  $l_{\text{split}} = 52 \mu\text{m}$  and gap  $g \in \{1.0 : 0.5 : 3.0\} \mu\text{m}$ . A tapered straight waveguide is included for reference and the waveguide's diameter ( $d = 2 \mu\text{m}$ ), with equal taper dimensions as for Euler s- and u-bends. From the single-mode output intensity profiles shown in Fig. 4.6 (c), it is clear that the arrangement of the individual output intensities perfectly agrees with the designed distances  $g$ . This demonstrates the high fidelity of the design and fabricated splitter's layout.

Figure 4.6 (d) shows the splitting losses of such air-cladded 1 to 3 splitters over  $g \in \{1.0 : 0.5 : 3.0\} \mu\text{m}$ , where the global losses increase for larger  $g$ . For  $g = 1.0 \mu\text{m}$ , the output intensity profiles are not yet fully decoupled, with some intensity contribution from the input waveguide visible in the center between the three output waveguides. A complete splitting of fundamental mode outputs, with negligible cross-talking, is identified for  $g = 1.5 \mu\text{m}$ . For the latter, the associated splitting losses are 0.60 dB (excluding injection and bending losses), with intensity differences between output ports of only 8.0 %.

Finally, the transmission coefficient  $T_i$  per eigenmode for such splitters is evaluated via the modal decomposition of output intensity profiles, see Fig. 4.6 (e). As seen, the cross-scattering to higher-order modes is larger than for the s- and u-bends, while the fundamental mode still strongly dominates for all  $g$  as  $T_{\text{fund}} \gg T_{\text{high}}$ , with values of  $R^2$  close to unit. Here, the intensity contribution of the individual outputs waveguides is accounted for, since for the different  $g$  the  $T_i$  is divided to each relative intensities relate to the three outputs. These results demonstrate that the injected eigenmode is conserved to a high-degree for all  $g$ . Noteworthy, 1 to 3 splitters with  $g = 0.5 \mu\text{m}$  were fabricated during these

investigations. However, the successful fitting analysis of output intensity profiles is not possible due to their overlapping at the output ports. Compared to polymer-cladded splitters from Chapter 2, the here obtained global losses are notably increased. Future efforts include reducing losses by realizing splitters with longer splitting lengths  $l_{\text{split}}$  with fixed splitting distances.

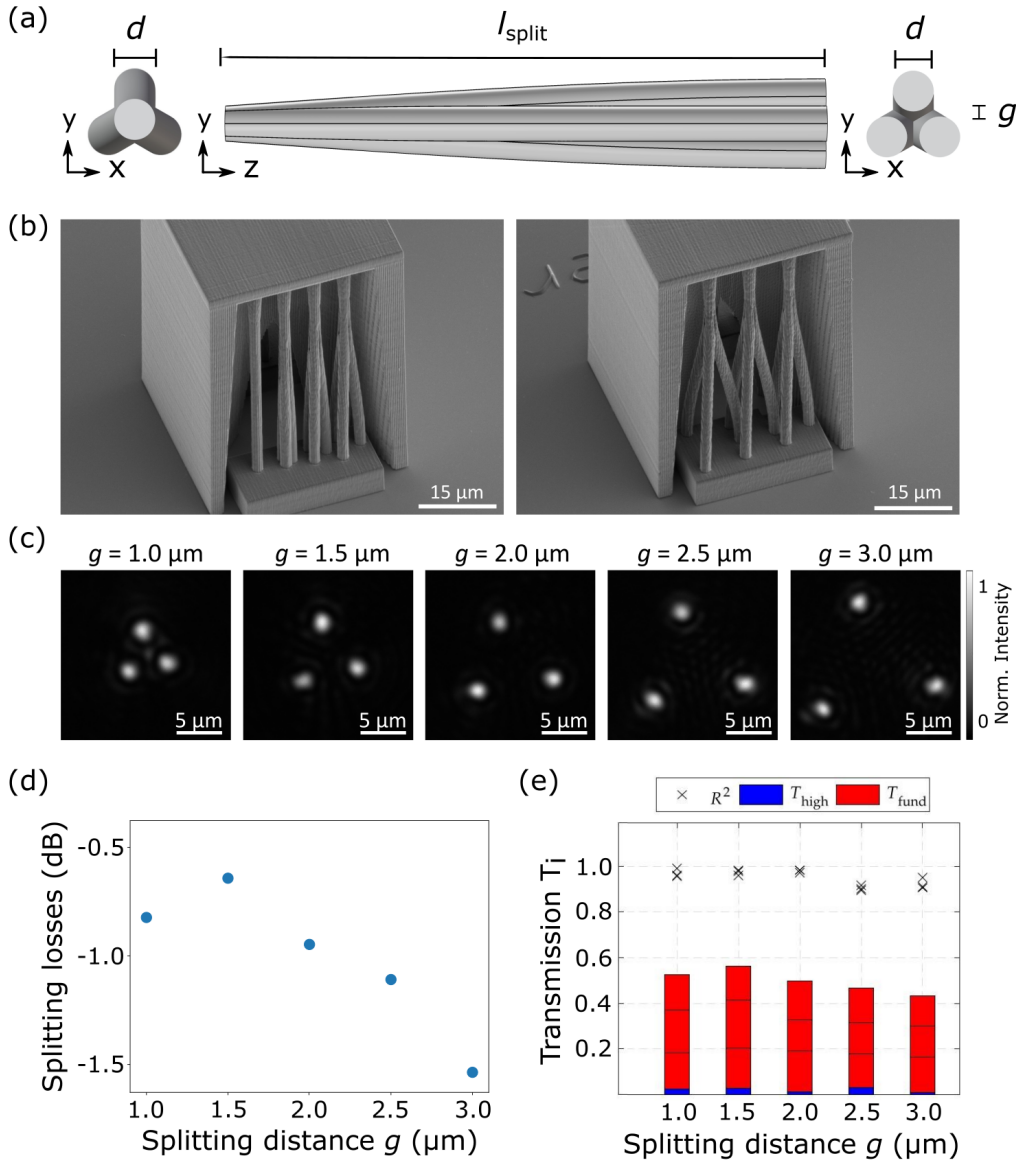


Figure 4.6: Air-cladded splitter waveguides optical performance. (a) Design layout of an adiabatic 1 to 3 splitter with diameter  $d$ , splitting distance  $g$  and splitting length  $l_{\text{split}}$ . The input (left panel), splitting (middle panel) and output (right panel) sections are depicted. (b) SEM micrographs of an exemplary 3D photonic circuit printed via DLW-TPP containing a set of air-cladded 1 to 3 adiabatic splitters with splitting distances  $g \in \{1.0 : 0.5 : 3.0\} \mu\text{m}$ . (c) Experimental output intensity profiles of the 1 to 3 adiabatic splitters with splitting distance  $g \in \{1.0 : 0.5 : 3.0\} \mu\text{m}$ ,  $l_{\text{split}} = 52 \mu\text{m}$  and  $d = 2 \mu\text{m}$ . (d) Splitting losses versus splitting distance  $g$  of 1 to 3 adiabatic splitters. (e) Transmission coefficient  $T_i$  per eigenmode over splitting distance  $g$  for air-cladded 1 to 3 adiabatic splitters after a modal decomposition of the output intensities from (c) for 20 eigenmodes.

## 4.5/ CONCLUSIONS AND OUTLOOK

Chapter 4 shows the realization of low-loss, single-mode and air-cladded waveguides via DLW-TPP printing. Tapered straight waveguides with air cladding are first investigated, where a self-developed modal decomposition method based on COMSOL Multiphysics is used in order to determine the relative transmission per eigenmode propagating within the waveguides. The relative transmission of the fundamental mode  $T_{\text{fund}}$  relative to the one of higher-order modes  $T_{\text{high}}$  is close to unit ( $T_{\text{fund}} \gg T_{\text{high}}$ ), which shows the high-quality of the fabricated waveguides as well as the customized analysis method.

Furthermore, curved waveguides following a s- and u-like shape and based on two geometries, i.e. circular and Euler, are compared in terms of optical losses and single-mode operation. For Euler curves, coupling losses are considerably reduced compared to classical circular geometries, and both the s- and u-bends with Euler curvatures show similar coupling losses of 0.4 dB for large bending radii  $7 < R < 16 \mu\text{m}$ . This shows the advantage offered by these more intricate Euler curvatures in terms of low bending losses as well as minimizing inter-modal cross-talking towards higher-order modes.

Finally, following investigations introduced in Chapter 3, 1 to 3 splitters leveraging adiabatic transfer are fabricated, yet with an air cladding. The full splitting of single-mode outputs ( $T_{\text{fund}} \gg T_{\text{high}}$ ) is achieved over gaps  $g$ . However, the splitting losses are larger (0.60 dB) and future efforts include minimizing injection losses as well as increasing the splitting length  $l_{\text{split}}$  with unchanged splitting distance. Overall, the dimensions of such optical splitters are significantly reduced from hundreds of  $\mu\text{m}$  ( $l_1 = 300 - 500 \mu\text{m}$ ) for polymer-cladded couplers to tens of  $\mu\text{m}$  ( $l_{\text{split}} = 52 \mu\text{m}$ ) for their air-cladded counterparts. Such air-cladded waveguide and splitter circuits are prime candidates for highly-dense photonic integration due to their low bending radii (in the order tens of  $\mu\text{m}$ ), being an important tool for the next generation of intra- and inter-chip optical communication as well as for parallelization in photonic NNs.



# INTERFACING 3D PHOTONIC CIRCUITS WITH SEMICONDUCTOR QUANTUM DOT MICROPILLAR ARRAYS

Chapter 5 targets the realization of the first integrated system combining quantum light sources such as quantum dot micro-lasers (QDMLs) and the 3D printing technology established in the framework of this thesis, forming the backbone of next generation optical NN architectures. Merging 3D waveguides and QDMLs in a single hardware system represents a crucial step for promising applications in advanced photonic information processing. Many investigations have focused on the deterministic on-chip fabrication of semiconductor architectures for enhanced light-matter interactions harnessing cavity quantum-electrodynamics (cQED), which is the study of the interaction between light tightly confined in an optical cavity and quantum states [248]. Using quantum dots (QDs) as two-level quantum systems present a way to realize functionality out of scope of classical systems, such as the realization of solid-state single-photon emitters [249], representing a clear breakthrough towards future quantum communication technologies [250]. Crucially, the 3D printing technology presented in Chapter 2, Chapter 3 and Chapter 4 is CMOS and semiconductor compatible.

What is here demonstrated is one of the first realizations of its kind, hence various fundamental challenges arise related to DLW-TPP fabrication onto semiconductor substrates [119]. The QD micropillars' architecture is first described, including a general discussion of the diverse growth and etching processes required for their fabrication. Likewise, a careful optimization of the TPP-writing parameters, i.e. laser power and hatching (slicing) distance  $h$  ( $s$ ), is crucial when printing onto opaque substrates such as semiconductor materials. This is required to avoid the over-polymerization of the photoresist during TPP-writing, which is induced due to specular reflections at the semiconductor's surface, which in turn increases the optical dose in writing volumes near the semiconductor-resin interface. A further requisite is to precisely construct the 3D photonic chip at specific locations of the on-chip patterned devices. To this aim, an accurate alignment protocol using the tools available in the Nanoscribe GmbH (Photonic Professional GT) lithography system is proposed.

The main technology requirements to coherently coupling the quantum emission states of QDMLs via 3D photonic waveguides for creating one single integrated device are presented. Conceptually, the 3D waveguides to be interfaced on top of the QD micropillar arrays will result in the optical coupling of the QD emission of the micro-cavities into

the 3D waveguides. The short coupling lengths (100  $\mu\text{m}$ ) mean that coupling delays ( $< 0.1$  ps) are substantially shorter than the dephasing rates of cavity photons and QD excitons (3...100 ps), and hence the creation of a coherent superposition of quantum states of various QDs is fundamentally achievable considering transform limited quantum emitters [250, 251]. However, QDMLS do not operate at room temperature and therefore need to be cooled to cryogenic temperatures [252]. Such cooling is required to reduce the non-radioactive losses by thermal escape, and the ensemble of QDs' gain profile is adjusted to spectrally match with the fundamental mode at such temperatures [253]. The set up used for cooling down and optically pumping the micropillars for further QD emission collection via 3D waveguides is here detailed. As a final investigation, a quantitative study of 3D photonic waveguides printed via *flash*-TPP on top of QDMLS is evaluated at 4 K, where the characteristic lasing curves as well as the optical spectra of micropillars-alone and micropillars-waveguides hybrid devices are compared. Preliminary results show good performances in terms of low global losses and high coupling efficiency to the QDMLS.

The semiconductor samples integrating QDMLS used for these investigations were produced by the research group at the Technical University of Berlin (TUB) led by Prof. Stephan Reitzenstein in the framework of the Volkswagen Foundation NeuroQNet II project [253, 254]. Furthermore, a short-term ( $\sim 2$  months) research internship funded by the German Academic Exchange Service (DAAD) was realized in order to strengthen an already fruitful collaboration of synergetic research between both the Femto-ST and TUB research units.

## 5.1/ QUANTUM DOT MICRO-CAVITY LASERS

The choice of working with QD micropillars is made for several reasons. QDMLS are semiconductor lasers, and their response time is dominated by the carrier's relaxation oscillation frequency, which readily reaches 10 GHz [255]. A semiconductor laser has numerous sources of non-linearity such as the lasing threshold, gain saturation or amplitude-phase coupling [256]. Moreover, the QDMLS' pumping can be done optically, which allows for scalability since complex wiring schemes are not required. Using the same principle, input information can be injected all-optically [257]. The quantum dot micropillar arrays (QDMPAs) must adhere to two fundamental characteristics: a regular spacing of the micropillars and homogeneity of the emission wavelength across the QDMPA. Fulfilling this, QDMLS are promising candidates to act as the nonlinear nodes of a photonic NN, see Fig. 1.2 (a). In such an NN scheme, the QDMLS that are arranged in a 2D plane act as artificial neurons, while their dense parallel interconnectivity is realized out-of-plane via 3D waveguides, see Fig. 1.2 (c).

The fabrication of QDMLS is based on multiple steps. First, the QD micro-cavities, which are typically based on planar Al(Ga)As heterostructures, are grown by metal-organic chemical vapour deposition (MOCVD). In order to assure light confinement in the three-dimensions, the micropillar consists of a central GaAs cavity, which in its center includes layers of InGaAs QDs active layer providing optical gain. This central cavity layer is sandwiched between distributed Bragg reflectors (DBR) comprising alternating Al(Ga)As and GaAs mirror pairs, see Fig. 5.1 (a). Key-aspects of such a resonant cavity are the mode volume and the quality (Q) factor [258]. This strongly depends on the composition and the number of mirror pairs in the DBR section. For cQED studies, high-Q factors and small mode volumes are required in order to maximize the exciton-photon coupling [252, 250].

In recent investigations done by the group led by Prof. Stephan Reitzenstein at TUB, resonator cavities based on AlAs/GaAs layer stacks, with 32/36 mirror pairs in the upper/lower DBR, exhibiting Q-factor of 150.000 and mode volumes in the order of the cube-wavelength have been demonstrated [259].

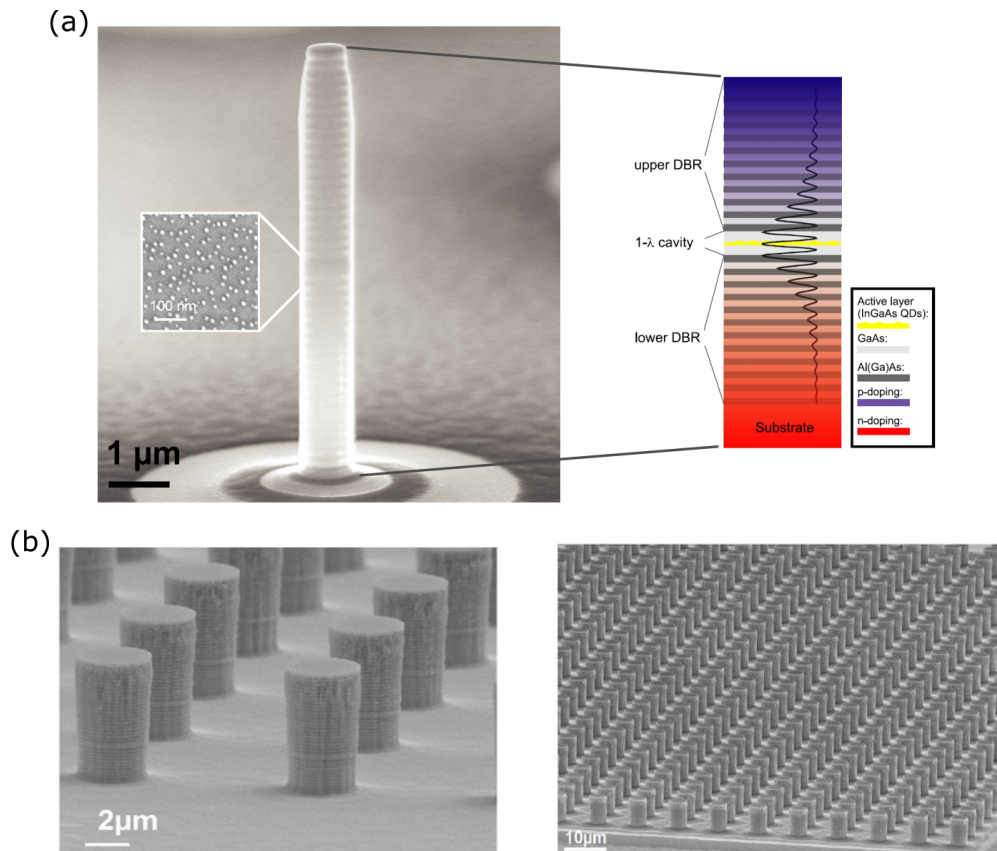


Figure 5.1: Quantum dot micropillar arrays structure layout. (a) SEM micrograph (left panel) and schematic illustration (right panel) of a cylindrical micro-cavity where a central one- $\lambda$  thick gain section based on InGaAs self-assembled quantum dots (inset zoom-in) that is vertically sandwiched between top and bottom distributed Bragg reflectors (DBR) alternating Al(Ga)As and GaAs mirror pairs. Extracted from [252]. (b) SEM micrographs of 900 quantum dot micro-lasers (QDMLs). Individual micropillars have a pillar center-to-center pitch 10  $\mu\text{m}$  with a diameter (height) of 5.0  $\mu\text{m}$  (5.8  $\mu\text{m}$ ). Extracted from [253].

A crucial aspect to consider is the fabrication of QDs embedded in such an optical micro-cavity, which requires a sophisticated fabrication methodology. Control of the physical properties (size, emission energy and oscillator strength) of the InGaAs active layer is required to achieve a large oscillator strength and ensuring sufficient gain for lasing operation. The QD layers are fabricated via controlled growth of monoatomic layers of InAs on top of GaAs [260]. Beyond a critical thickness, growth continues through nucleation and coalescence of islands, which form the QDs, see the inset in Fig. 5.1 (a). For micropillars with a diameter  $>4 \mu\text{m}$ , the gain medium is composed of several thousand QDs, and their quantum states provide optical gain by light-matter interaction with the cavity mode. However, due to the QD's inhomogeneous broadening, only a small part, typically 10 %, aligns a particular cavity resonance and contributes to lasing emission [261, 262].

The micropillar processing into a cylindrical shape is a crucial step that provides 3D light

confinement and high-Q to the micro-cavity [252]. The need for smooth and vertical micropillar surfaces is of vital importance to reduce the photon escape from the cavity, which is the dominant loss mechanism for such devices. Following the sample growth, the still planar sample, comprising of the DBR pairs with the QD layer sandwich between them, is spin-coated with an electron-beam sensitive resist (PMMA) and the cross-sections of the pillars are patterned via electron-beam lithography (EBL). After this step, the resist is developed and the inductively coupled plasma–reactive ion etching (ICP-RIE) method is used to shape the micropillars out of the semiconductor material.

The SEM micrographs of Fig. 5.1 (b) show an array of 30x30 QD micropillars with smooth and vertical sidewalls growth following this fabrication methodology. In this work, a surface's thickness disparity of about 2 % was addressed by adjusting the resonance wavelength of each micropillar via its diameter [253]. This diameter-tuning was realized for a large array of 900 quantum dot micropillars with high spectral homogeneity (0.23 nm) of the fundamental mode's emission wavelength, which allows large-scale connectivity for applications in photonic information processing. The QDMLs used in these investigations were optimized to operate at low temperatures (77 K).

## 5.2/ CHALLENGES OF INTEGRATING DLW-TPP FABRICATION AND SEMICONDUCTOR TECHNOLOGY

First challenges of integrating single-step, monolithic and direct-laser 3D additive fabrication approaches with semiconductor or CMOS platforms start from the interaction of such materials with the fs-pulsed laser required for TPP-fabrication. In standard DLW-TPP settings, the interaction between the fs-laser and the glass substrate is negligible since the substrate material, i.e. fused silica, is transparent at the wavelength of the fs-pulsed laser ( $\lambda = 780$  nm), see Table 1.1. The direct band-gap energy of semiconductor materials such as InP, InAs, GaAs, GaN or Silicon is below to that of the writing laser, and printing structures through such an opaque substrate essentially is impossible.

To this aim, and contrary to DLW into bulk glass seen in Section 1.1.1, the 'dip-in' lithography configuration is clearly advantageous for fabricating mm-size structures while avoiding aberrations during laser-writing directly onto semiconductor materials, since it does not require illuminating the resin through the supporting substrate. However, the large refractive index  $n$  of the semiconductor materials at the fs-laser wavelength leads to high specular reflections at the substrate's surface. This results in the unintended over-polymerization of the photoresist if not adjusted for [263]. The optical reflection of intensity by planar GaAs substrate surfaces is  $R = \left(\frac{n_{\text{GaAs}} - n_{\text{IPS}}}{n_{\text{GaAs}} + n_{\text{IPS}}}\right)^2 = 0.177$ , where  $n_{\text{GaAs}} = 3.696$  (at  $\lambda = 780$  nm) and  $n_{\text{IPS}} = 1.510$  are the refractive indices of GaAs and the IPS photoresist, respectively. For ideally flat substrates, the degree of polymerization of a photoresist is increased by 17.7 % on GaAs substrates for a fs-laser addressing a voxel in close proximity between the GaAs-resin interface compared to the same TPP dosage when fabricating on transparent substrates. However, since the CMOS technology is based on stacking multiple thin layers of semiconductor materials in a loop-like manner, there is a non-homogeneous thickness distribution after several fabrication steps. These thickness variations throughout a semiconductor's surface lead to multiple reflections in different directions, and hence a radially-dependent degree of polymerization of photoresists. The single-step and single-material DLW-TPP approach avoids the sequential alignment of

photo-masks and later UV exposure of large volumes of photoresist compared to standard CMOS technology. However, a precise optimization of the TPP dosage  $D$ , potentially as a function of distance to the semiconductor-resin interface, when fabricating onto opaque substrates is therefore crucial to obtain high-performance 3D structures with the desired optical properties.

A further challenge is the alignment of the fs-laser TPP-writing coordinates with respect to the positioning of patterned devices on the semiconductor substrate. Therefore, a careful coordinate system transformation is required for precisely fabricating photonic components onto the targeted on-chip locations. Importantly, the Nanoscribe (Photonics Professional GT) system is equipped with an advanced set of tools enabling to automatically address for substrate tilt corrections, while providing for an in-built adjustment of the camera coordinate system with respect to the lithography's coordinate system for high-accuracy alignment.

## 5.3/ DLW-TPP FABRICATION ON SEMICONDUCTOR SUBSTRATES

In this section, the principal hurdles encountered during DLW-TPP fabrication, with the 'dip-in' configuration, and directly onto CMOS and semiconductor material platforms are detailed. The preliminary evaluation of optical performance and mechanical stability of 3D printed waveguides on top of QD micropillar arrays are presented. The experimentally obtained results show the successful overcoming of the aforementioned roadblocks towards the hybrid integration of both the DLW-TPP and CMOS technologies [168].

### 5.3.1/ TPP FABRICATION PARAMETER CALIBRATION

As first fabrication optimization step, the TPP parameters, i.e. fs-laser power and hatching distance  $h$ , are calibrated by printing a set of 3D cuboids directly on top of substrates capped with semiconductor GaAs layers. These test samples are grown via MOCVD during the top-DBR wafer calibration phase, hence no central gain section of InGaAs self-assembled quantum dots (QDs) is present. As globally fixed parameters in all the fabrications, the scanning speed (slicing distance) is set to 10 mm/s ( $s = 1 \mu\text{m}$ ).

Figure 5.2 (a) depicts the layout design (left panel), SEM micrograph (central panel) and optical microscope image (right panel) of 3D cuboids ( $60 \times 60 \times 8 \mu\text{m}^3$ ) arranged in  $5 \times 5$  arrays. Here, both the laser power  $LP \in \{1.0 : 2.5 : 11.0\}$  mW and hatching distances  $h \in \{0.4 : 0.1 : 0.7\}$   $\mu\text{m}$  are scanned. From the optical microscope image in Fig. 5.2 (a), it is clear that the TPP-printed cuboids with  $LP = 11.0$  mW ( $LP = 1.0$  mW) show over(under)-polymerization of the IP-S photoresist for all  $h$ . These two situations are related to the limits of the so-called dynamic power range of the photoresist, see Section 1.3.4. Importantly, the here obtained breakdown point ( $LP = 11.0$  mW) aligns well with the expected LP when fabricating on GaAs material, since this is reduced by  $\approx 17.7\%$  compared to printing on transparent substrates ( $LP = 17.0$  mW) for IP-S photoresist, see Fig. 2.2. Likewise, the degree of polymerization, i.e. refractive index  $n$ , of the photoresist within the dynamic power range can be further adjusted by adapting the hatching distance  $h$ . Here, the influence of the hatching distance  $h$  is clearly seen as for fixed LP, the degree of polymerization of the 3D cuboids increases due to the accumulated TPP-irradiation for smaller  $h$  (see bottom to top in Fig. 5.2 (a)). After identifying the LP required to avoiding

over(under)-polymerization at  $LP = 11.0$  mW ( $LP = 1.0$  mW) for the IP-S photoresist onto GaAs, a second fine-sweep ranging  $LP \in \{4.5 : 1.0 : 8.5\}$  mW for the same 3D cuboids is realized, and Fig. 5.2 (b) shows the results. As seen in the optical microscope image of Fig. 5.2 (b), the 3D printed cuboids with  $LP \in \{5.5, 6.5, 7.5\}$  mW show clean surfaces with no visible defects for all  $h$ . These fabrication parameters are therefore selected for the following investigations.

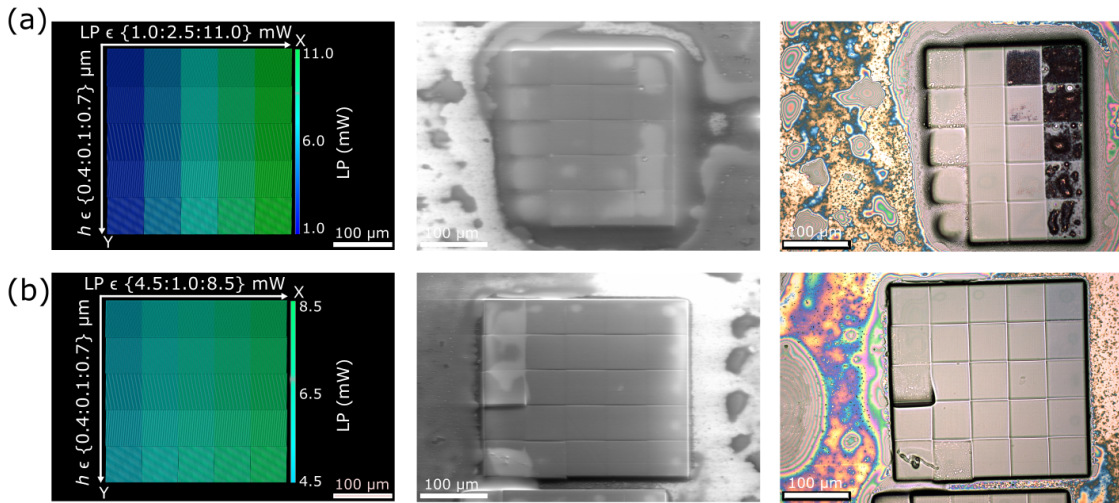


Figure 5.2: Dynamic power range characterization of TPP-printed cuboids on top of semiconductor GaAs substrates using the IP-S photoresist. (a) Layout design (left panel), SEM micrograph (central panel) and optical microscope image (right panel) of 3D printed cuboids with dimensions of  $60 \times 60 \times 8 \mu\text{m}^3$  arranged in  $5 \times 5$  arrays with spanning  $LP \in \{1.0 : 2.5 : 11.0\}$  mW ( $x$ -axis) and hatching distances  $h \in \{0.4 : 0.1 : 0.7\}$  μm ( $y$ -axis). (b) Same as in (a) but with  $LP \in \{4.5 : 1.0 : 8.5\}$  mW with equal  $h$ .

A second investigation involves leveraging DLW-TPP fabrication onto semiconductor substrates containing more complex structures such as QDMLs arrays, cf. Fig. 5.1 (b). For these experiments, the substrate layout is composed of several patterns of QD micropillar cavities arranged in  $30 \times 30$  arrays, where individual micropillars have a diameter (height) of  $5.0 \mu\text{m}$  ( $5.8 \mu\text{m}$ ), and are separated by a constant pillar center-to-center pitch of  $10 \mu\text{m}$  [253].

An initial evaluation of DLW-TPP fabrication onto such micro-lasers is carried out by replicating the previous experiment of 3D cuboids, using the experimentally optimized parameters found in Fig. 5.2 (b). Figure 5.3 (a) shows the layout design (top panel) and SEM micrograph (bottom panel) for 3D cuboids constructed using a constant LP distribution along the  $z$ -direction, i.e. STIN profile. The SEM micrograph shows a 3D cuboid with non-homogeneous surfaces revealing hole-like patterns located above the micropillars. This finding is attributed to the interface mismatching between the micropillar's top-surface and the fs-laser focus during TPP-writing, which leads to uneven voxel-to-voxel overlapping along the  $z$ -direction (slicing distance  $s$ ). After the development process, these regions collapse since they are not fully polymerized, which leads to the formation of such hole-like patterns observed in Fig. 5.3 (a).

This effect is solved by constructing 3D cuboids with GRIN profile via (3+1)D printing. As demonstrated in Section 1.3.7, this printing approach relies on locally modifying the TPP-voxel size by spatially adjusting the TPP dosage  $D$  of the fs-laser during DLW, cf.

Fig. 1.24 (a). Figure 5.3 (b) depicts the layout design (top panel) and SEM micrograph (bottom panel) for (3+1)D printed cuboids with GRIN profile, where the LP is dynamically adjusted along the  $z$ -direction following a linear modulation with slope  $\Delta LP_z = \frac{LP_f - LP_i}{z_f - z_i}$ . This refractive index modulation is done by increasing an initial  $LP_i = 5.5$  mW by 0.5 mW for each  $\Delta z = 2$   $\mu\text{m}$ -thick layer. Compared to STIN cuboids, the resulting (3+1)D printed cuboids with GRIN profile on top of QDMLs show clean and homogeneous surfaces. Via (3+1)D fabrication, the interface mismatching during laser-writing is successfully corrected, hence achieving high-quality structures with smooth surfaces. Further efforts include fabricating these GRIN cuboids following a parabolic-like modulation of LP as a function of the distance to the substrate-resin interface, accounting for the summation of intensities while TPP-printing onto opaque substrates, which corresponds to the convolution of two Gaussian beams, see Fig. 1.18.

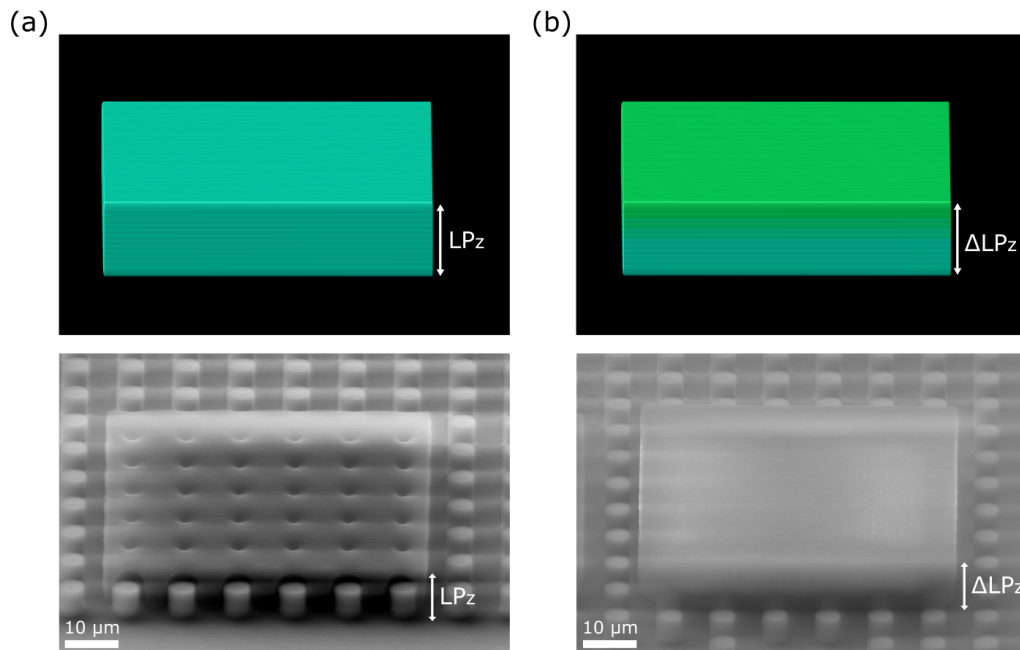


Figure 5.3: Layout design (top panel) and SEM micrograph (bottom panel) of 3D cuboids with  $60 \times 60 \times 8$   $\mu\text{m}^3$  dimensions based on (a) STIN and (b) GRIN refractive index profiles printed on top of semiconductor GaAs quantum dot micropillars array.

### 5.3.2/ ALIGNMENT PROTOCOL

To ensure optimal coupling between 3D waveguides and QDMLs, a high-accuracy ( $<100$  nm) and precise control over the three-spatial coordinates of the fs-laser beam with respect to target coordinates on the chip is vital. In order to reliably detect these positions, a marker-based port detection and coordinate transformation technique is here proposed. This involves a coordinate transformation that correlates the position of an object observed in the camera, which is equipped with the Photonic Professional GT, to its position expressed in the lithography's circuitry coordinates, see Fig. 1.19.

In the DLW-TPP configuration, the spatial positions of a point related to the lithography coordinates  $\vec{R}_L = (X_L, Y_L, Z_L)$  correspond to the positions that the piezoelectric transducers need to address in order to locate a specific point in the fs-laser's focus during the writing

process. Importantly, the coordinates of the lithography system are parallel to that of the piezo-stage, with the origin located at the piezo's zero position. The TPP-writing starts at the fs-laser focus  $Z_L$ , and it can manually (opaque substrates) or automatically (transparent substrates) be detected via the Photonic Professional GT system on the sample's surface. For a well-aligned system, the focal plane is set by optimizing the projection of the camera-view axis to the plane with the sharpest sight, where the offset between the lithography height and the sharpest image is  $Z_{\text{offset}} = 0$ . The protocol of coordinates transformation between the camera-view  $\vec{R}_C = (X_C, Y_C, C)$  and the lithography  $\vec{R}_L$  coordinates system starts by identifying their offset. To this aim, the location of two different points, which are to be known from the layout design, are considered from the camera-view. Commonly used reference markers for mask-alignment in 2D lithography are lines or square geometries.

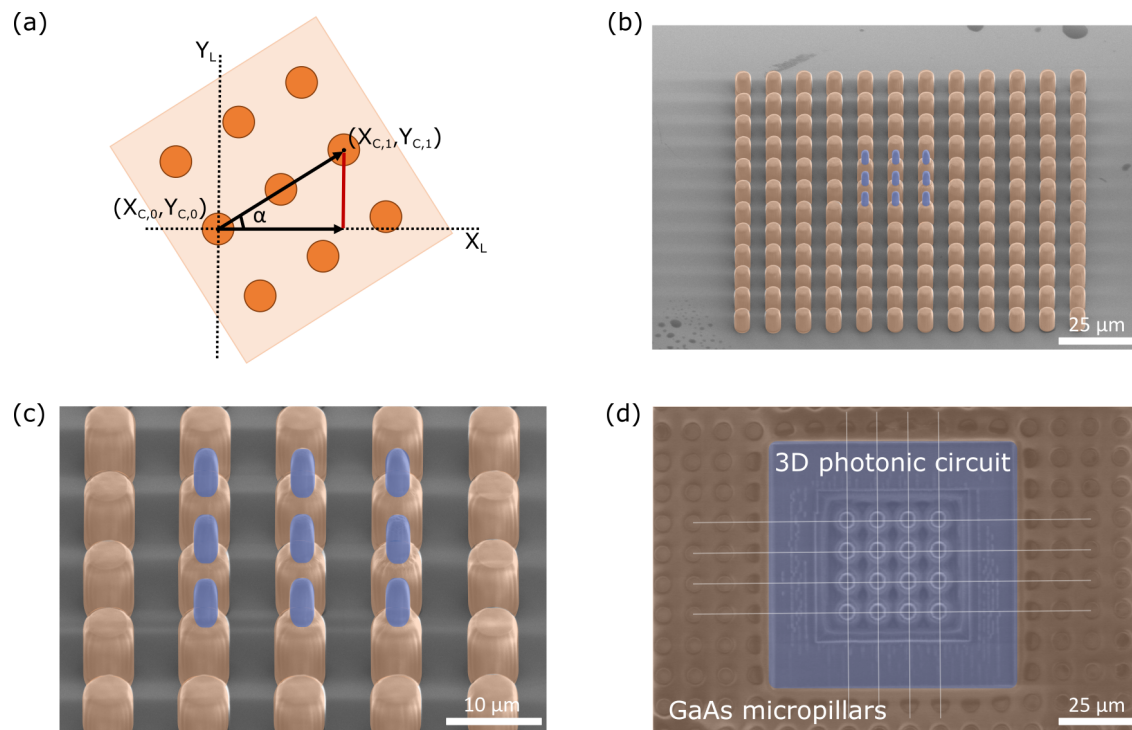


Figure 5.4: Alignment protocol for integrating 3D printed photonic circuits with semiconductor substrates containing quantum dot micropillar arrays. (a) Schematic representation of the angle  $\alpha$  correction of the lithography coordinates  $\vec{R}_L = (X_L, Y_L, Z_L)$  with respect to the camera-view coordinates  $\vec{R}_C = (X_C, Y_C, Z_C)$ . (b) Set of TPP-printed cylinders (3x3 array) emulating waveguide cores (blue color) fabricated onto further cylinders (12x12 array) emulating GaAs micropillars after a two-step DLW-TPP procedure where an induced tilting angle  $\alpha$  is corrected. (c) Zoom-in of (b). (d) SEM micrograph of a 3D printed cross-section cutting through a cuboid integrating 16 photonic waveguides (5.6  $\mu\text{m}$  diameter and 100  $\mu\text{m}$  height) on top of semiconductor GaAs quantum dot micropillars.

First, the on-chip coordinates  $(X_{C,0}, Y_{C,0})$  and  $(X_{C,1}, Y_{C,1})$  of such markers are obtained via the in-built coordinate lithography system associated to the piezoelectric transducers stage, see Fig. 5.4 (a). Since both coordinate systems are parallel in their  $z$ -axis, the rotation matrix  $R_z(\alpha)$  is applied, and for a translation along the lithography  $x$ -axis their angle  $\alpha$  is given by  $\tan(\alpha) = (Y_{C,1} - Y_{C,0}) / (X_{C,1} - X_{C,0}) = \Delta Y_C / \Delta X_C$ . Then, the rotation angle  $\alpha$  is identified and the lithography coordinates  $\vec{R}_L$  with respect to the camera coordinates

$\vec{R}_C$  are corrected. This step is possible by (i) manually rotating the 3D design layout structure or (ii) automatically via the Photonic Professional GT system.

To show the effectiveness of such a protocol, a set of free-standing cylinders (3x3 array) emulating photonic waveguides (5  $\mu\text{m}$  height,  $d = 2.8 \mu\text{m}$  diameter) are printed on top of previously fabricated cylinders emulating GaAs micropillars (5  $\mu\text{m}$  height,  $d = 5.2 \mu\text{m}$  diameter) via a two-step DLW-TPP procedure. The cylinders' center-to-center pitch is set to 10  $\mu\text{m}$ . After fabricating the TPP-micropillars (12x12 array) and the subsequent development process, where the non-polymerized photoresist is removed, a tilt angle  $\alpha$  is introduced by deliberately rotating the fused silica substrate before starting the second fabrication step. Next, following the here discussed alignment protocol, the angle  $\alpha$  between lithography and camera-view coordinate system is adjusted. Importantly, the TPP-writing starting location  $Z_L$  is set equal to the height of the TPP-micropillars ( $Z_L = Z_{\text{offset}} = 5 \mu\text{m}$ ) in order to assure good structure adherence, i.e. vertical voxel-to-voxel overlapping. The SEM micrographs of Fig. 5.4 (b-c) demonstrate the high-quality of this alignment approach, here illustrated with TPP-printed cylinders reassembling waveguide cores (blue color) constructed onto cylinders emulating semiconductor micropillars (orange color).

Finally, the reliability of this alignment protocol in a practical context is demonstrated by leveraging TPP-printing of waveguides on top of semiconductor substrates containing QDMLs, cf. Fig. 5.1 (b). The layout design consists of waveguide cores ( $d = 5.6 \mu\text{m}$  and 100  $\mu\text{m}$  height) arranged in a 4x4 array with a waveguide center-to-center pitch (equal to the micropillar's) of 10  $\mu\text{m}$ . A (3+1)D printed pedestal (80x80x10  $\mu\text{m}^3$ ) with GRIN profile is constructed using the same LP range as in Fig. 5.3 (b), and the complete 3D integrated circuit is embedded within mechanical supports ensuring the overall stability. The SEM micrograph of Fig. 5.4 (d) shows a cross-section of such a 3D photonic circuit (blue color) printed on top of QDMLs (orange color). As seen, the fabricated waveguide cores (4x4 array) are perfectly aligned with respect to the micro-laser's pitch and positioning.

### 5.3.3/ OPTICAL REFLECTION PERFORMANCE

As a last investigation, the optical performance of 3D photonic waveguides interfaced with GaAs micropillars is evaluated. Via *flash*-TPP, a set of waveguides of 80  $\mu\text{m}$  height and diameters ranging  $d \in \{4.0 : 0.8 : 5.6\} \mu\text{m}$  are fabricated. After the DLW-TPP process, the undeveloped monomer resin forming part of the 3D photonic chip is contained by the cuboid enclosing the entire circuit like a box, which is consequently polymerized via OPP with an exposure dose  $D = 3000 \text{ mJ/cm}^2$ . The injection losses are minimized by adding tapers at the input-facet of the waveguide cores, cf. Fig. 2.7 (a).

For the performance evaluation, the optical reflection from the QDMLs coming back through the waveguides printed on top of individual QD micropillars is analyzed. The injection wavelength for this investigation is set to  $\lambda = 976 \text{ nm}$ , which is close to the fundamental mode's wavelength of the QD emission of the micro-lasers from Fig. 5.1 (b). The optical reflection coming from micropillars-alone (without waveguides or support structures) is used as reference intensity  $T_{\text{ref}}$  to extract the global losses, which include injection and propagation losses. According to data shown in Fig. 5.5 (a), the global losses remain below 0.4 dB for the entire range of  $d \in \{4.0 : 0.8 : 5.6\} \mu\text{m}$ , which slowly decrease for larger  $d$  due to the increased optical confinement within the waveguides' core over  $d$ , see Fig. 2.6 (a-b).

Figure 5.5 (b) depicts an optical microscope image (under incoherent illumination) of

the top-surface's 3D cuboid embedding photonic waveguides used for this study. Here, the laser beam ( $\lambda = 976$  nm) is focused on the mechanical supports (left panel) and the waveguides' input-facet (right panel), respectively. As seen, the reflected light intensity coming from the micropillar through the waveguide is highly confined within its core, whereas it is clearly scattered in all directions when focusing on the mechanical support. This shows the high-performance of the here presented fabrication/alignment procedure and their reliability towards the hybrid integration of 3D printing technology and GaAs-based QDMLs.

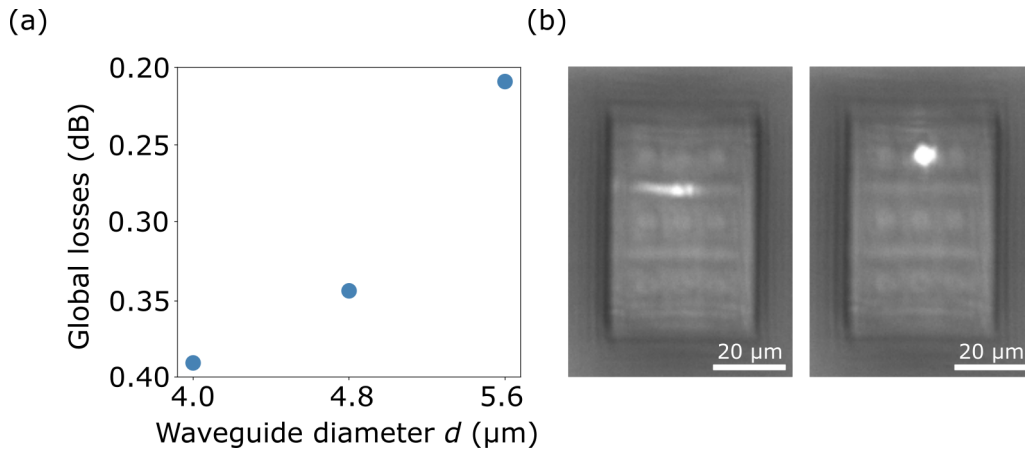


Figure 5.5: Optical characterization at injection wavelength  $\lambda = 976$  nm of 3D photonic waveguides integrated with semiconductor micro-lasers. (a) Global losses versus waveguide diameter  $d \in \{4.0 : 0.8 : 5.6\}$   $\mu\text{m}$  for 80  $\mu\text{m}$  high waveguides printed on top of GaAs quantum dot micropillars. (b) Optical microscope image showing the top surface of a 3D cuboid integrating photonic waveguides where the laser focus is located on mechanical supports (left panel) and waveguides' input-facet (right panel).

## 5.4/ OPTICAL PUMPING AND EMISSION OF QDMLS VIA 3D WAVEGUIDES

Here, cQED experiments involving the optical pumping of QDMLs and their lasing (QD emission) are performed. The optical set up integrating a cryogenic system used for these investigations is first presented. Furthermore, the characteristic lasing curves for such micro-lasers are analyzed, while their optical spectrum is evaluated in order to locate the emission wavelength peak and study the overall spectral homogeneity. Lastly, preliminary investigations of 3D photonic chips printed onto individual micro-lasers show excellent performances in terms of spectral homogeneity and QD emission collection via 3D waveguides.

### 5.4.1/ CRYOGENIC SYSTEM AND OPTICAL CHARACTERIZATION

The optical set up used for the here presented investigations is depicted in Fig. 5.6 (a). The reference laser at  $\lambda = 976$  nm (Thorlabs BL976-SAG300) with Gaussian output is first collimated using the lens  $L_1$  (Thorlabs AC254-035-B-ML). After passing the polarizer

and then a  $\lambda/2$  wave-plate, the polarization of the light is set to linear. The transmitted linearly polarized light, after crossing the beam splitter  $BS_1$  (CCM1-BS014/M, 50:50),  $BS_2$  (CCM1-BS014/M, 90:10) and dichroic mirror, is focused via a silver mirror (Thorlabs PF10-03-P01) on the top-surface of the sample through the vacuum chamber of the cryostat system (Attocube, attoDRy800) using a microscope objective MO (Olympus PLN10X IR, NA = 0.3). The sample is mounted on a  $(xyz)$ -piezo stage, by which the focal spot is precisely aligned to the top-surface of the QD micropillars. The optical reflection from the micropillars is imaged in the camera  $CAM_1$  (iDS UI-1222LE-M, pixel size  $6 \mu\text{m}$ ) after passing first an achromatic lens  $L_2$  (Thorlabs AC254-150-B-ML) and then a long-pass filter  $F_{LP}$  (LP, Thorlabs FELH0950). The long-pass filter  $F_{LP}$  removes cross-talk from the pump laser by suppressing its photons by 15 orders of magnitude.

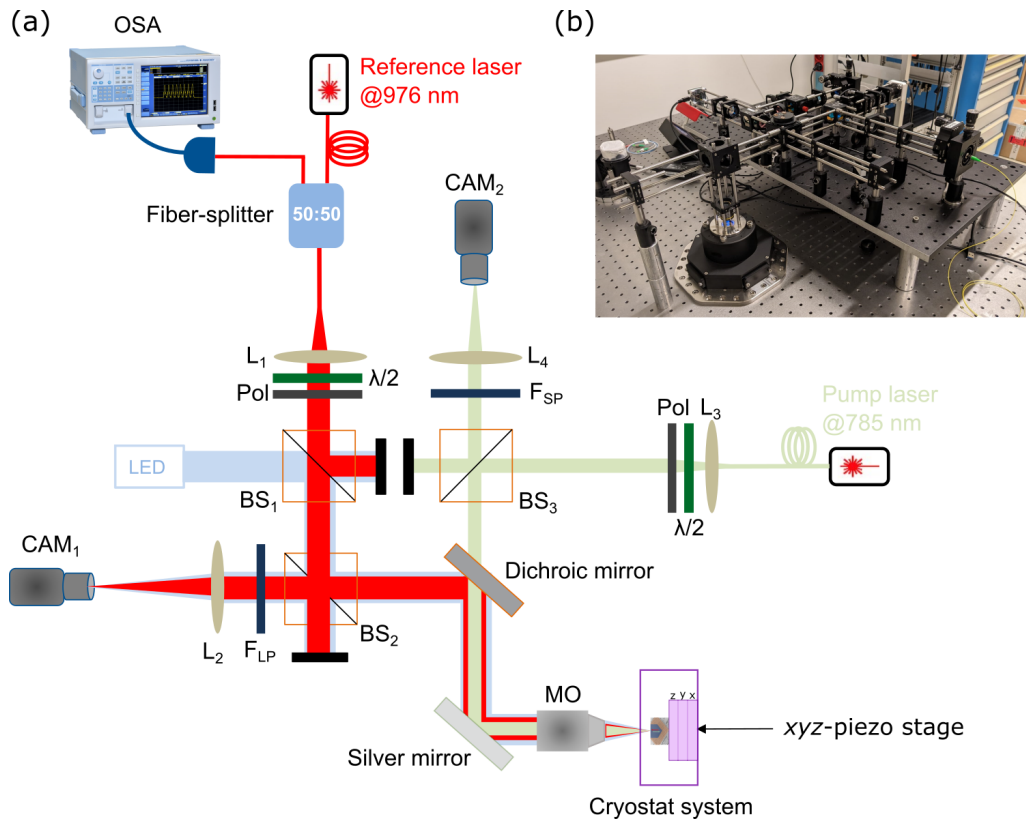


Figure 5.6: Experimental QDMLS scheme and cryogenic system. (a) The reference laser at  $\lambda = 976 \text{ nm}$  is used to adjust the focal distance of the microscope objective (MO) relative to the QDMLs. The pump laser at  $\lambda = 785 \text{ nm}$  is focused on top of the QD micropillars to induce population inversion and further lasing. (b) Image of the optical set up from (a).

For the optical pumping of the QDMLs, a pump laser at  $\lambda = 785 \text{ nm}$  (Thorlabs FPL785S-250) with Gaussian output is collimated using the achromatic lens  $L_3$  (Thorlabs AC254-035-B-ML) and set to linearly polarized after passing a polarizer and  $\lambda/2$  wave-plate. After passing through the beam-splitter  $BS_3$  (CCM1-BS014/M, 50:50), the dichroic mirror and the silver mirror, the beam is focused on the sample using the same microscope objective MO. The optical reflection is imaged on the camera  $CAM_2$  (iDS UI-3482LE-M, pixel size  $6 \mu\text{m}$ ) after passing the achromatic lens  $L_4$  (Thorlabs AC254-100-AB-ML) and a short-pass filter  $F_{SP}$  (SP, Thorlabs FESH0900). This short-pass filter  $F_{SP}$  suppresses the QDMLs emission intensity by more than 50 dB. The recordings from both cameras undergo post-processing to consider the transmission coefficients of each component along

their respective beam paths, with the aim of deriving the pump and emission intensities at the top of each QDML. Crucially, the reflected intensity coming from the micropillars, i.e. QD emission, is collected and its optical spectrum analyzed via an Optical Spectrum Analyzer (OSA) (YOKOGAWA, AQ6370D) through collection by a confocal system. Figure 5.6 (b) depicts both the optical set up and cryogenic system used for these investigations.

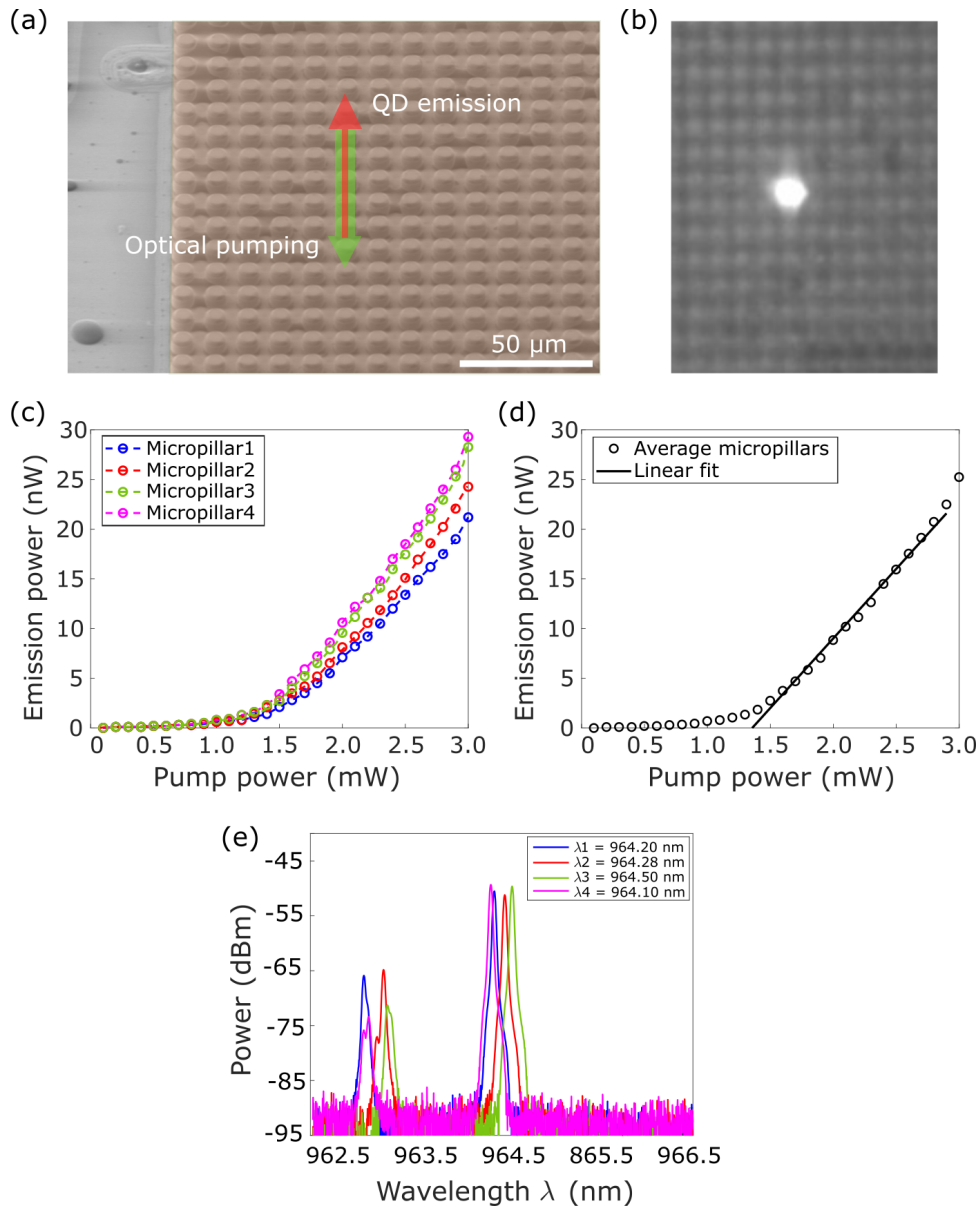


Figure 5.7: Optical pumping and emission of individual QDMLs. (a) Schematic illustration of the optical pumping of a micropillar. The pump laser (green color) is precisely focused on top of a micropillar, and the QD emission (red color) is collected by a confocal system. (b) Pump laser focused on a sample containing QDMLs. (c) Distinctive lasing curves, i.e. emission power versus pump power, of four individual micropillars characterized for different pump powers  $P_{\text{pump}} \in \{0.0 : 0.1 : 3.0\}$  mW. (d) Average lasing curves from (c). An averaged lasing threshold of  $\langle P_{\text{thr}} \rangle = 1.350$  mW is obtained from the linear fit (solid line). (e) Optical spectrum of the four micropillars from (c).

### 5.4.2/ OPTICAL PUMPING AND EMISSION OF QDMLS PERFORMANCE

The QDMLS are optically pumped [254]. The role of the pump laser is to supply energy to the QDMLS, and for maximizing the pumping efficiency, it is essential to optimize the spatial profile of the pump laser's focal spot on the surface of the micropillars. The overlap integral between the pump laser's and the QDML's spatial mode ideally should approach unity. For a micropillar with a diameter of 5  $\mu\text{m}$ , its emission has a single-mode spatial profile for the confined mode. Therefore, the pump laser must be single-mode and its mode diameter must match with the QDML's mode.

Figure 5.7 (a) schematically illustrates the overall concept, where the pump laser at  $\lambda = 785 \text{ nm}$  (green color) is precisely focused on the top-surface of a single QD micropillar. For a pump power  $P_{\text{pump}}$  above lasing threshold, electron-hole pairs, i.e. excitons, are created inducing population inversion in the band-gap energies of quantum states and resonate in the micro-cavity, which is the essential requirement for the QDMLS' stimulated emission. This QD emission (red color) is simultaneously collected using the same optical path as the injected light.

First investigations with QDMLS involve optically pumping individual QD micropillars with pump powers  $P_{\text{pump}} \in \{0.0 : 0.1 : 3.0\} \text{ mW}$  in order to extract their distinctive lasing curve, which relates how the light output power responds to injected optical power. To this aim, the pump laser is focused on top of individual micropillars. Figure 5.7 (b) depicts the sample, cf. Fig. 5.1 (b), under LED ( $\lambda = 940 \text{ nm}$ ) illumination and the pump laser focused on the top-surface of a micropillar-alone. The sample is cooled down at 4 K for optimal micro-lasers' performance. The lasing curves of four different QD micropillars are depicted in Fig. 5.7 (c), showing the typically observed input-output lasing behavior, where the emission power rapidly increases above a certain pump power named lasing threshold  $P_{\text{thr}}$ . A  $P_{\text{thr}} = 1.350 \pm 0.053 \text{ mW}$  is obtained via the linear fit (solid line) of the lasing curve of such micropillars, see Fig. 5.7 (d). All the here tested micropillars are lasing and show similar lasing behavior with comparable lasing threshold  $P_{\text{thr}}$ .

Finally, the optical spectrum of these micropillars at  $P_{\text{pump}} = 3 \text{ mW}$  is measured by the OSA through collection by a confocal system, and the results are shown in Fig. 5.7 (e). The fundamental  $\text{HE}_{11}$  mode is located at the peaks with a higher power, with an average resonance wavelength  $\lambda = 964.270 \pm 0.147 \text{ nm}$  for the four micropillars measured [252]. Likewise, when the pump power is large enough, higher-order modes start to appear, which are shifted towards shorter (higher) wavelengths (energies) due to the excitation of higher quantum energy levels. This high spectral homogeneity of the resonance wavelength exhibited is crucial for applications in photonic information processing [253]. It shows the high-quality of the sample fabricated by the group at TUB as well as the reliability of the optical set up.

### 5.4.3/ OPTICAL PUMPING AND EMISSION OF QDMLS VIA 3D WAVEGUIDES PERFORMANCE

As a concluding study, the lasing collection of QD micropillars via 3D waveguides is evaluated. To this aim, the previous 3D cuboid, cf. Fig. 5.5 (b), integrating photonic waveguides with a diameter ranging  $d \in \{4.0 : 0.8 : 5.6\} \mu\text{m}$  and 80  $\mu\text{m}$  height are used. Figure 5.8 (a) schematically shows the overall concept, where the pump laser is focused at the input-facet of the waveguides, which are used to both optically pump and collect the emission

of the micro-lasers. Crucially, the NA, i.e. optical confinement, of the waveguide must be adapted to work at the single-mode operation regime for, both, the pumping (emission) wavelengths  $\lambda = 785 \text{ nm}$  ( $\lambda = 964 \text{ nm}$ ) of the QDMLS. As seen in Fig. 2.6 (a), for photonic waveguides printed via *flash*-TPP with  $\Delta n \approx 5 \cdot 10^{-3}$ , the cut-off diameter for the second propagation mode is for  $d = 4.8 \text{ }\mu\text{m}$  ( $d = 6.1 \text{ }\mu\text{m}$ )  $\lambda = 760 \text{ nm}$  ( $\lambda = 960 \text{ nm}$ ). The selected waveguide diameter range  $d \in \{4.0 : 0.8 : 5.6\} \text{ }\mu\text{m}$  therefore serves as a first broad test to evaluate the pumping-emission efficiency for such waveguide-micropillar integrated devices.

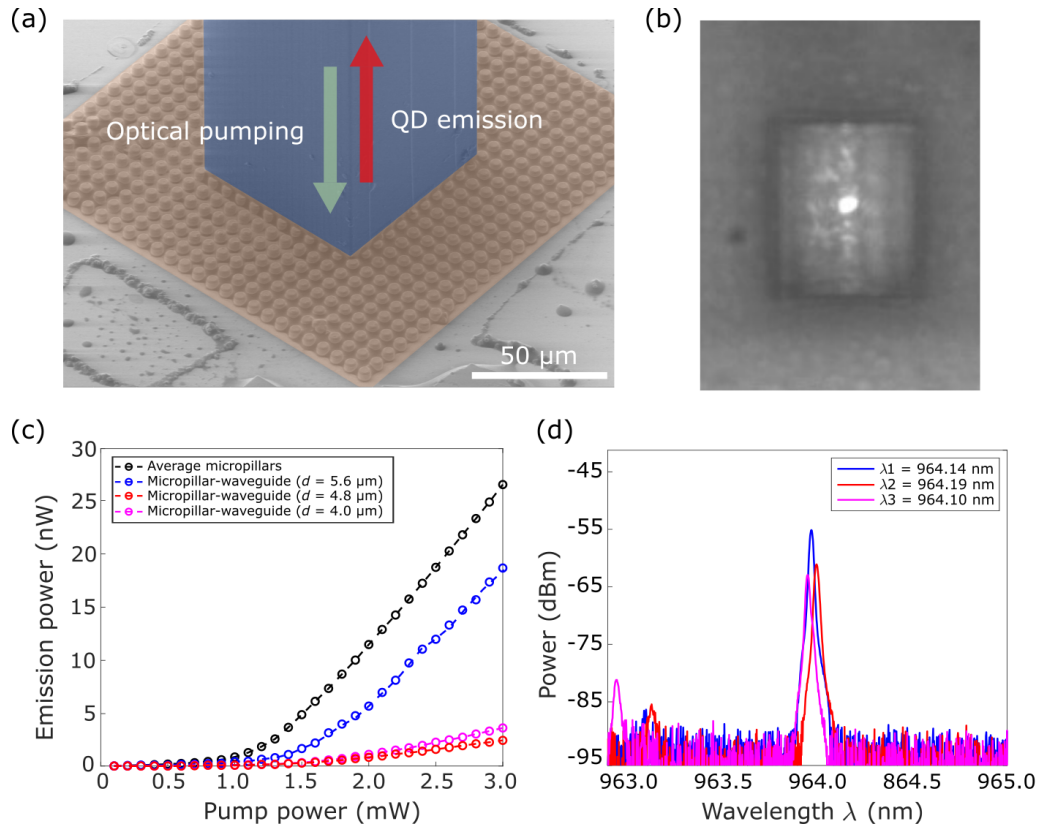


Figure 5.8: Optical pumping and emission of QDMLS via interfaced 3D waveguides. (a) Schematic illustration of the optical pumping of a micropillar via 3D waveguides. The pump laser (green color) is focused on top of the waveguides, and the QD emission (red color) is collected by a confocal system. (b) Optical microscope image showing the top surface of the 3D cuboid integrating 3D waveguides printed on top of QDMLS. (c) Average lasing curves for micropillars-alone (black color), and combined waveguide-micropillar with core diameter  $d = 4.0 \text{ }\mu\text{m}$  (purple color),  $d = 4.8 \text{ }\mu\text{m}$  (red color) and  $d = 5.6 \text{ }\mu\text{m}$  (blue color). (d) Optical spectrum of three individual interfaced waveguide-micropillar structures from (c).

After cooling the system to 4 K, see Fig. 5.8 (b), the distinctive lasing curves for each of the photonic waveguides printed on top of the micro-lasers are measured for the same set of QDMLS as reported previously. Figure 5.8 (c) shows the averaged lasing curves for micropillars-alone (black color), and interfaced waveguide-micropillar with core diameter  $d = 4.0 \text{ }\mu\text{m}$  (purple color),  $d = 4.8 \text{ }\mu\text{m}$  (red color) and  $d = 5.6 \text{ }\mu\text{m}$  (blue color). Importantly, the evaluated lasing curves are averaged for three different waveguides for each  $d$  (total of nine waveguides), while four individual QDMLS are accounted for the lasing curve of

micropillars-alone, see Fig. 5.7 (c). From the linear fit of the lasing curves, the resulting lasing thresholds are  $P_{\text{thr}} = 1.502$  mW ( $d = 4.0$   $\mu\text{m}$ ),  $P_{\text{thr}} = 1.548$  mW ( $d = 4.8$   $\mu\text{m}$ ) and  $P_{\text{thr}} = 1.474$  mW ( $d = 5.6$   $\mu\text{m}$ ). Compared to the previously obtained  $P_{\text{thr}} = 1.350$  mW for micropillars-alone, it is clear that sufficient and similar light is coupled into the waveguides in order to pump the micro-lasers.

A clear dependence of the QD emission collection via 3D waveguides is observed over  $d$ , where the emission power is maximum for  $d = 5.6$   $\mu\text{m}$ , while is drastically reduced for  $d = 4.0$   $\mu\text{m}$  and  $d = 4.8$   $\mu\text{m}$ . The reflection losses obtained in Fig. 5.5 (a) are used to extract the coupling losses of the QD emission into waveguides for all  $d$ . For  $d = 5.6$   $\mu\text{m}$ , the coupling losses are only 1.1 dB. This high-performance for larger  $d$  is related to the improved mode-matching between the mode profiles of both the QD emission and waveguides for  $d = 5.6$   $\mu\text{m}$ , which results in an enhancement of light collection. Likewise, the higher optical confinement of the waveguides at  $\lambda = 960$  nm, cf. Fig. 2.6 (a), contribute to reducing coupling losses when collecting the QDMLs emission into the waveguide. This is apparently only for collecting the lasing emissions, since the thresholds for different  $d$  are almost identical, hence this effect is essentially restricted to the coupling efficiency of the pump laser. For  $d < 5.6$   $\mu\text{m}$ , the coupling efficiency is drastically reduced, showing the described effect of increasing collection losses. Finally, Fig. 5.8 (d) shows the optical spectrum for three micropillars integrating waveguides at constant  $P_{\text{pump}} = 3$  mW, where an average resonance wavelength of  $\lambda = 964.143 \pm 0.036$  nm is obtained, which totally agrees with the previously obtained from micropillars-alone ( $\lambda = 964.270 \pm 0.147$  nm).

## 5.5/ CONCLUSIONS AND OUTLOOK

In Chapter 5, the first steps towards the realization of a new approach merging semiconductor quantum dot micro-lasers (QDMLs) and 3D photonics circuits are introduced. Crucially, the favourable realization of such a co-integrated device has the potential to reshape fully-optical and fully-parallel NN architectures in hardware [13]. The semiconductor samples used for these investigations consist of micro-cavities based on planar Al(Ga)As heterostructures having a central GaAs cavity, which acts as InGaAs QDs active layer, that is sandwiched between distributed Bragg reflectors (DBR) alternating Al(Ga)As and GaAs mirror pairs, see Fig. 5.1 (a). Several challenges of constructing 3D waveguides via DLW-TPP onto semiconductor substrates are here successfully overcome. These include the adjustment of the TPP dosage (laser power) for compensating specular reflections of the fs-laser onto the semiconductor substrates as well as elaborating an alignment protocol proficient on positioning photonic waveguides on top of individual micropillars with high-precision.

Using an optical set up integrating a cryogenic system for cooling temperatures down to 4 K, cf. Fig. 5.6, cQED experiments involving optical pumping and emission detection of QDMLs are performed. The characteristic lasing curves and lasing thresholds ( $P_{\text{thr}}$ ) for a set of micropillar-alone and micropillar-waveguide structures are extracted by optically pumping such devices with pump powers ranging  $P_{\text{pump}} \in \{0.0 : 0.1 : 3.0\}$  mW. For micropillars-alone, the optical spectrum of four individual micro-lasers shows a considerably high spectral homogeneity (0.147 nm standard deviation) of QD emission, with the fundamental  $\text{EH}_{11}$  mode emission peak centered at  $\lambda = 964.270$  nm. In future investigations, the analysis of the spectral homogeneity will be evaluated over a larger area of micropillars (30x30 array) in order to confirm this behavior in a large-scale framework.

For hybrid micropillar-waveguide structures, coupling losses of only 1.1 dB are obtained after optically pumping micropillars and subsequent QD emission collection via photonic waveguides ( $d = 5.6 \mu\text{m}$ ). The optical spectrum reveals large spectral homogeneity of the fundamental  $\text{EH}_{11}$  mode emission of  $\lambda = 964.143 \pm 0.036 \text{ nm}$ , which is comparable to that of micropillars-alone. However, the collection efficiency drastically drops when reducing the waveguides' diameter, showing the relevance of matching the waveguide's and the QDML's modes. Future efforts include exploring optimal waveguide diameter  $d$  for single-mode operation for, both, the pumping (emission) wavelengths  $\lambda = 785 \text{ nm}$  ( $\lambda = 964 \text{ nm}$ ), which will further improve injection/coupling behavior for such micropillar-waveguide hybrid devices. Overall, these results show encouraging performances in terms of optical losses and mechanical stability of polymer-based photonic circuits at cryogenic temperatures, further confirming the compatibility of DLW-TPP with CMOS and semiconductor materials.

## GENERAL CONCLUSIONS AND PERSPECTIVES

Neural networks are computing concepts fundamentally linked to interconnecting elements via their network topology [264, 18]. Such circuitry is fundamentally hampered in electronics and too space consuming for standard photonic ICs [9]. Likewise, photonic waveguides do not suffer bandwidth limitations by length [265], and hence a 3D photonic waveguide network offers a highly promising strategy for creating the first fully implemented and large-scale network worldwide. Despite the significantly larger feature size compared to integrated electronics, photonics has the cutting-edge advantage over electronic substrates for establishing the network substrate [266]. Efforts exclusively focus on realizing nodes and connections in 2D substrates, dwindled by the quadratic scaling of connections, which makes this strategy fundamentally impractical [10]. Here, this bottleneck is overcome by exploiting all three-dimensions. In 3D topologies, input and output channels occupy a discrete 2D plane, while the third dimension allows the circuit's volume to be utilized for interconnections [30, 14]. This leverages the fundamental relationship between area and volume to achieve scalability of the overall architecture, which is a vital requirement for the consolidation of NN architectures fully integrated on-chip [54]. This realization has the potential to serve as a demonstration that the concept of NN computation demands a potentially equally dedicated hardware platform as the complementary Turing/von Neumann computing already has at its disposal [13].

In this thesis, essential building blocks with the potential to playing a pivotal role in the next generation of 3D photonic ICs are presented. These are fundamental tools for realizing large-scale and parallel interconnection required in NN computing, which are challenging to implement via the state-of-the-art 2D/2.5D integration platform technologies reviewed in Chapter 1. The here demonstrated 3D printed photonic devices are fabricated leveraging additive photo-induced polymerization of commercial photoresists, with all the involved processes and materials being CMOS compatible. Based on OPP and TPP and combined with DLW settings, a complete toolbox of photonic components is presented, and their performances are evaluated.

In Chapter 2, a novel manufacturing methodology merging DLW-TPP and OPP, i.e. *flash*-TPP, is developed for the fabrication of polymer-cladded STIN photonic waveguides. This single-step and monolithic lithography principle is capable of reducing the printing time by  $\approx 90\%$  compared to fabricating an equal circuitry volume by using only DLW-TPP, i.e. (3+1)D printing. This is achieved by incorporating diverse fabrication strategies for the different sections of a photonic IC. The waveguide cores are printed with high-resolution by

precisely adjusting fabrication parameters, i.e. hatching (slicing) and  $h$  ( $s$ ) distances and TPP dosage  $D$ , ensuring smooth surfaces, and hence low propagation losses. Structures serving simply as mechanical supports, which do not interact with the guided light, are instead printed with indiscriminate TPP parameters. After the development process, where the non-polymerized photoresist outside the 3D photonic's chip volume is removed, the entire IC is polymerized via OPP in a single-instance. Via *flash*-TPP, the refractive index contrast between the waveguides' core and cladding is in the order of  $\Delta n \approx 5 \cdot 10^{-3}$  ( $NA = 0.12$ ), which can be further adjusted by dynamically modifying the OPP exposure dose  $D$ . This low  $\Delta n \ll 1$  enables the propagation of the fundamental  $LP_{01}$  mode over large distances (6 mm), with low 1.36 dB/mm (0.26 dB) propagation (injection) losses at  $\lambda = 660$  nm, see Fig. 1.5. Crucially, investigations reveal that the optical performance under operation conditions of these waveguides does not vary over time, recently evaluated for  $>1$  year.

Future efforts include combining recently developed concepts such as two-photon grayscale lithography, which enables mass production of 3D microstructures using the latest generation of 3D printers [267, 268]. This new generation of printers achieve scanning speeds of up to 6.25 m/s, a significant improvement from the previous speed of 0.625 m/s. This remarkable scaling potential of the fabrication technique highlights the promising prospects for *flash*-TPP, which can readily be adapted. Crucially, the recently demonstrated two-color fabrication method can potentially increase fabrication speed substantially [204], while also offering a moderate improvement in terms of minimal feature size.

Via *flash*-TPP, Chapter 3 shows the realization of broadband and low-loss adiabatic 1 to M splitters leveraging adiabatic coupling. These splitters are the backbone of any standard photonic circuits enabling to split/combine optical signals and are clearly advantageous for applications in NNs, where the fundamental appeal is exploiting the parallelism by connecting numerous inputs to a comparable number of output channels. Single-mode optical splitters leveraging adiabatic transfer from one input to up to 4 outputs in a single component are demonstrated, achieving record optical coupling losses of 0.06 dB with very symmetric (3.4 %) splitting ratios. For the latter, the wavelength-independent splitting signature for such splitters is tested showing almost octave-spanning broadband functionality from 520 nm to 980 nm, during which losses remain below 2 dB. Finally, fractal splitting networks with 1 to 16 single-mode outputs are demonstrated, with only 1 dB global losses and with the entire IC occupying a minimal volume of  $(0.08 \times 0.08 \times 1.5)$  mm<sup>3</sup>. However, this footprint is still far from the ideal (tens to hundreds of  $\mu\text{m}^3$ ) integration density needed for realistic NN computing.

Future efforts include improving the homogeneity of the splitting ratio of the cascaded 1 to 16 fractal splitters, which still exhibit notable variations. This involves investigating potential refractive index or thickness variations in the sections in-between tapered and inversely-tapered waveguides [237]. The currently large footprint of such splitters can be further reduced by integrating so-called short-cuts strategies for adiabaticity [269]. This relies on exploiting the analogy between quantum mechanics and waveguide optics for light manipulation in optical devices such as directional couplers [270], coupled nonlinear triple waveguides [271] and photonic waveguides [272].

To this aim, Chapter 4 shows the realization of air-cladded waveguides and bends that are prime candidate for an increased integration density due to their higher optical confinement and large  $\Delta n = 0.5$ . This enables having low bending radii compared to polymer-cladded counterparts (from tens of  $\mu\text{m}$  to tens of mm), which is a key element for achiev-

ing high circuit integration within a compact volume. The fundamental  $\text{EH}_{11}$  propagating mode is launched into such waveguides by optimizing the mode-matching between the mode distribution profile of both the injection laser and waveguide. Likewise, circular and Euler bent waveguides following u- and s-like curvatures are fabricated, and their optical performance is evaluated for single-mode operation. Coupling losses of Euler bent waveguides are reduced to 0.4 dB for both the u- and s-curvatures for bending radii ranging  $7 < R < 16 \mu\text{m}$ . Finally, air-cladded 1 to 3 splitters leveraging adiabatic coupling with very symmetric (8.0 % variation) splitting ratios and single-mode operation are demonstrated. Compared to optical splitters constructed via *flash*-TPP, the footprint of these air-cladded counterparts is reduced to  $(2 \times 2 \times 52) \mu\text{m}^3$ , manifesting the benefits in terms of highly-dense photonic integration of these devices.

Future efforts include combining polymer- and air-cladded waveguides [247], benefiting from the strengths of each configuration in a single platform, i.e. air-cladding waveguides providing highly-dense photonic integration with their small bending radii, while STIN waveguides serving as tools for single-mode propagation over large distances. The combination of air- and polymer-cladded waveguides could enable dense integration with simultaneous precise control over optical signal properties such as mode number, polarization and phase. Initial recent investigations are showing encouraging results in terms of performance and stability for such air- and polymer-cladded transition waveguides.

As a last investigation, Chapter 5 shows the first-of-its-kind integrated device merging quantum dot micro-lasers (QDMLs) and 3D photonic waveguides in a single and hybrid platform. This new approach lays the foundations to build future generations of all-optical NNs, with QDMLs serving as nonlinear nodes arranged in a 2D plane, while the highly-dense interconnection is performed out-of-plane via 3D waveguides. Crucially, this shows the CMOS and semiconductor compatibility of the here developed *flash*-TPP lithography configuration. A customized protocol for fabricating structures via DLW-TPP onto semiconductor (GaAs) materials is proposed, including a detailed optimization of TPP parameters as well as a precise alignment methodology. Individual micro-lasers are optically pumped at cryogenic temperatures (4 K) via interfaced 3D photonic waveguides, yielding very high emission collection efficiency into the waveguides, with coupling losses of only 1.1 dB. Importantly, such QDMLs exhibit very high spectral homogeneity (0.147 nm), which is essential for applications in large optical NN architectures.

Future efforts include fabricating more intricate photonic components such as adiabatic polymer- or air-cladded splitters onto QDMLs, forming new hybrid platforms highly appealing for the realization of connected networks. Likewise, the possibility of reducing the lasing threshold of such QDMLs by two orders of magnitude is to be considered for future work [273]. In particular, new investigations showing a combination of Q-factor engineering and tailoring of the optical gain on the nm-scale via stacked site-controlled QDs are highly innovative techniques, together never explored for the design of semiconductor laser arrays [274, 275]. Combined with 3D photonic waveguides and optical splitters, such implementation is a promising alternative (or synopsis) to already existing optical computing approaches based on on-chip coherent meshes of MZIs [276].



# BIBLIOGRAPHY

- [1] T. B. Brown, B. Mann, N. Ryder, M. Subbiah, J. Kaplan, P. Dhariwal, A. Neelakantan, P. Shyam, G. Sastry, A. Askell, S. Agarwal, A. Herbert-Voss, G. Krueger, T. Henighan, R. Child, A. Ramesh, D. M. Ziegler, J. Wu, C. Winter, C. Hesse, M. Chen, E. Sigler, M. Litwin, S. Gray, B. Chess, J. Clark, C. Berner, S. McCandlish, A. Radford, I. Sutskever, and D. Amodei, “Language models are few-shot learners,” *arXiv*, 2020.
- [2] P. P. Ray, “Chatgpt: A comprehensive review on background, applications, key challenges, bias, ethics, limitations and future scope,” *Internet of Things and Cyber-Physical Systems*, vol. 3, pp. 121–154, 2023.
- [3] W. Oremus, “Ai chatbots lose money every time you use them. that is a problem.,” *The Washington Post*, 2023.
- [4] D. Patterson, J. Gonzalez, U. Holzle, Q. Le, C. Liang, L. Munguia, D. Rothchild, D. R. So, M. Texier, and J. Dean, “The carbon footprint of machine learning training will plateau, then shrink,” *Computer*, vol. 55, pp. 18–28, jul 2022.
- [5] E. Strubell, A. Ganesh, and A. McCallum, “Energy and policy considerations for deep learning in nlp,” *arXiv*, 2019.
- [6] A. M. Turing, “Computability and lambda-definability,” *The Journal of Symbolic Logic*, vol. 2, no. 4, p. 153–163, 1937.
- [7] P. Bernays, “Alonzo church. an unsolvable problem of elementary number theory. american journal of mathematics, vol. 58 (1936), pp. 345–363.,” *The Journal of Symbolic Logic*, vol. 1, no. 2, p. 73–74, 1936.
- [8] F. Cai, J. M. Correll, S. H. Lee, Y. Lim, V. Bothra, Z. Zhang, M. P. Flynn, and W. D. Lu, “A fully integrated reprogrammable memristor–cmos system for efficient multiply–accumulate operations,” *Nature Electronics*, vol. 2, pp. 290–299, 2019.
- [9] S. Borkar, “Design challenges of technology scaling,” *IEEE Micro*, vol. 19, no. 4, pp. 23–29, 1999.
- [10] W. M. M., “The chips are down for moore’s law,” *Nature*, vol. 530(7589), p. 144–147, 2016.
- [11] J. T. Boyd, R. W. Wu, D. E. Zelmon, A. Naumaan, H. A. Timlin, and H. E. Jackson, “Planar And Channel Optical Waveguides Utilizing Silicon Technology,” in *Integrated Optical Circuit Engineering I* (D. B. Ostrowsky and S. Sriram, eds.), vol. 0517, p. 100, jan 1985.
- [12] S. R. A. and J. P. Lorenzo, “All-Silicon Active and Passive Guided-Wave Components for  $\lambda = 1.3$  and  $1.6 \mu\text{m}$ ,” *IEEE Journal of Quantum Electronics*, vol. QE-22, no. 6, p. 873, 1986.

- [13] G. Moody, V. J. Sorger, D. J. Blumenthal, P. W. Juodawlkis, W. Loh, C. Sorace-Agaskar, A. E. Jones, K. C. Balram, J. C. F. Matthews, A. Laing, M. Davanco, L. Chang, J. E. Bowers, N. Quack, C. Galland, I. Aharonovich, M. A. Wolff, C. Schuck, N. Sinclair, M. Lončar, T. Komljenovic, D. Weld, S. Mookherjea, S. Buckley, M. Radulaski, S. Reitzenstein, B. Pingault, B. Machielse, D. Mukhopadhyay, A. Akimov, A. Zheltikov, G. S. Agarwal, K. Srinivasan, J. Lu, H. X. Tang, W. Jiang, T. P. McKenna, A. H. Safavi-Naeini, S. Steinhauer, A. W. Elshaari, V. Zwiller, P. S. Davids, N. Martinez, M. Gehl, J. Chiaverini, K. K. Mehta, J. Romero, N. B. Lingaraju, A. M. Weiner, D. Peace, R. Cernansky, M. Lobino, E. Diamanti, L. T. Vidarte, and R. M. Camacho, “2022 roadmap on integrated quantum photonics,” *Journal of Physics: Photonics*, vol. 4, p. 012501, jan 2022.
- [14] N. U. Dinc, D. Psaltis, and D. Brunner, “Optical neural networks: The 3d connection,” *Photoniques*, no. 104, pp. 34–38, 2020.
- [15] K. Boahen, “Dendrocentric learning for synthetic intelligence,” *Nature*, vol. 612, no. December 2020, pp. 43–50, 2022.
- [16] M. Roser, “The internet’s history has just began,” *Our World in Data*, 2018.
- [17] N. P. Jouppi, C. Young, N. Patil, D. Patterson, G. Agrawal, R. Bajwa, S. Bates, S. Bhatia, N. Boden, A. Borchers, R. Boyle, P.-I. Cantin, C. Chao, C. Clark, J. Coriell, M. Daley, M. Dau, J. Dean, B. Gelb, T. V. Ghaemmaghami, R. Gottipati, W. Gulland, R. Hagmann, C. R. Ho, D. Hogberg, J. Hu, R. Hundt, D. Hurt, J. Ibarz, A. Jaffey, A. Jaworski, A. Kaplan, H. Khaitan, D. Killebrew, A. Koch, N. Kumar, S. Lacy, J. Laudon, J. Law, D. Le, C. Leary, Z. Liu, K. Lucke, A. Lundin, G. MacKean, A. Maggiore, M. Mahony, K. Miller, R. Nagarajan, R. Narayanaswami, R. Ni, K. Nix, T. Norrie, M. Omernick, N. Penukonda, A. Phelps, J. Ross, M. Ross, A. Salek, E. Samadiani, C. Severn, G. Sizikov, M. Snellman, J. Souter, D. Steinberg, A. Swing, M. Tan, G. Thorson, B. Tian, H. Toma, E. Tuttle, V. Vasudevan, R. Walter, W. Wang, E. Wilcox, and D. H. Yoon, “In-datacenter performance analysis of a tensor processing unit,” *SIGARCH Comput. Archit. News*, vol. 45, p. 1–12, jun 2017.
- [18] W. S. McCulloch and W. Pitts, “A logical calculus of the ideas immanent in nervous activity,” *The bulletin of mathematical biophysics*, vol. 5, pp. 115–133, 1943.
- [19] Y. LeCun, Y. Bengio, and G. Hinton, “Deep learning,” *Nature*, vol. 521, pp. 436–444, 2015.
- [20] B. Ding, H. Qian, and J. Zhou, “Activation functions and their characteristics in deep neural networks,” in *2018 Chinese Control And Decision Conference (CCDC)*, pp. 1836–1841, 2018.
- [21] K. Rupp, “40 years of microprocessor trend data,” *GitHub*, 2018.
- [22] D. E. Rumelhart, G. E. Hinton, and R. J. Williams, “Learning representations by back-propagating errors,” *Nature*, vol. 323, pp. 533–536, 1986.
- [23] X. Guo, J. Xiang, Y. Zhang, and Y. Su, “Integrated neuromorphic photonics: Synapses, neurons, and neural networks,” *Advanced Photonics Research*, vol. 2, no. 6, p. 2000212, 2021.

- [24] B. Xu, Y. Huang, Y. Fang, Z. Wang, S. Yu, and R. Xu, "Recent progress of neuromorphic computing based on silicon photonics: Electronic and photonic co-design, device, and architecture," *Photonics*, vol. 9, no. 10, 2022.
- [25] P. Simard, D. Steinkraus, and J. Platt, "Best practices for convolutional neural networks applied to visual document analysis," in *Seventh International Conference on Document Analysis and Recognition, 2003. Proceedings.*, pp. 958–963, 2003.
- [26] V. Venkatadri, B. Sammakia, K. Srihari, and D. Santos, "A Review of Recent Advances in Thermal Management in Three Dimensional Chip Stacks in Electronic Systems," *Journal of Electronic Packaging*, vol. 133, p. 041011, 12 2011.
- [27] S. Rangarajan, S. N. Schiffres, and B. Sammakia, "A review of recent developments in "on-chip" embedded cooling technologies for heterogeneous integrated applications," *Engineering*, 2023.
- [28] H. Esmailzadeh, E. Blem, R. St. Amant, K. Sankaralingam, and D. Burger, "Dark silicon and the end of multicore scaling," *IEEE Micro*, vol. 32, no. 3, pp. 122–134, 2012.
- [29] J. Moughames, S. Jradi, T. M. Chan, S. Akil, Y. Battie, A. E. Naciri, Z. Herro, S. Guenneau, S. Enoch, L. Joly, J. Cousin, and A. Bruyant, "Wavelength-scale light concentrator made by direct 3D laser writing of polymer metamaterials," *Scientific Reports*, vol. 6, p. 33627, 10 2016.
- [30] J. Moughames, X. Porte, M. Thiel, G. Ulliac, L. Larger, M. Jacquot, M. Kadic, and D. Brunner, "Three-dimensional waveguide interconnects for scalable integration of photonic neural networks," *Optica*, vol. 7, pp. 640–646, Jun 2020.
- [31] A. Rickman, "The commercialization of silicon photonics," *Nature Photonics*, vol. 8, pp. 579–582, 2014.
- [32] G. T. Reed, W. R. Headley, and C. E. J. Png, "Silicon photonics: the early years," in *Optoelectronic Integration on Silicon II* (J. A. Kubby and G. E. Jabbour, eds.), vol. 5730, pp. 1 – 18, International Society for Optics and Photonics, SPIE, 2005.
- [33] R. Soref and J. Lorenzo, "Single-crystal silicon: a new material for 1.3 and 1.6  $\mu\text{m}$  integrated-optical components," *Electronics Letters*, vol. 21, pp. 953–954(1), October 1985.
- [34] D. Thomson, A. Zilkie, J. E. Bowers, T. Komljenovic, G. T. Reed, L. Vivien, D. Marris-Morini, E. Cassan, L. Viot, J.-M. Fédéli, J.-M. Hartmann, J. H. Schmid, D.-X. Xu, F. Boeuf, P. O'Brien, G. Z. Mashanovich, and M. Nedeljkovic, "Roadmap on silicon photonics," *Journal of Optics*, vol. 18, p. 073003, jun 2016.
- [35] B. Jalali and S. Fathpour, "Silicon photonics," *Journal of Lightwave Technology*, vol. 24, no. 12, pp. 4600–4615, 2006.
- [36] S. Y. Siew, B. Li, F. Gao, H. Y. Zheng, W. Zhang, P. Guo, S. W. Xie, A. Song, B. Dong, L. W. Luo, C. Li, X. Luo, and G.-Q. Lo, "Review of silicon photonics technology and platform development," *Journal of Lightwave Technology*, vol. 39, no. 13, pp. 4374–4389, 2021.

- [37] F. Morichetti, A. Canciamilla, C. Ferrari, M. Torregiani, A. Melloni, and M. Martinelli, "Roughness induced backscattering in optical silicon waveguides," *Phys. Rev. Lett.*, vol. 104, p. 033902, Jan 2010.
- [38] P. Cheben, P. J. Bock, J. H. Schmid, J. Lapointe, S. Janz, D.-X. Xu, A. Densmore, A. Del age, B. Lamontagne, and T. J. Hall, "Refractive index engineering with sub-wavelength gratings for efficient microphotonic couplers and planar waveguide multiplexers," *Opt. Lett.*, vol. 35, pp. 2526–2528, Aug 2010.
- [39] R. Halir, P. J. Bock, P. Cheben, A. Ortega Mo ux, C. Alonso-Ramos, J. H. Schmid, J. Lapointe, D.-X. Xu, and S. Janz, "Waveguide sub-wavelength structures: a review of principles and applications," *Laser & Photonics Reviews*, vol. 9, no. 1, pp. 25–49, 2015.
- [40] G. Z. Mashanovich, M. M. Milo evi , M. Nedeljkovic, N. Owens, B. Xiong, E. J. Teo, and Y. Hu, "Low loss silicon waveguides for the mid-infrared," *Opt. Express*, vol. 19, pp. 7112–7119, Apr 2011.
- [41] Y. A. Vlasov and S. J. McNab, "Losses in single-mode silicon-on-insulator strip waveguides and bends," *Opt. Express*, vol. 12, pp. 1622–1631, Apr 2004.
- [42] J. F. Bauters, M. J. R. Heck, D. D. John, M.-C. Tien, W. Li, J. S. Barton, D. J. Blumenthal, J. E. Bowers, A. Leinse, and R. G. Heideman, "Ultra-low-loss single-mode  $\text{Si}_3\text{N}_4$  waveguides with 0.7 db/m propagation loss," in *37th European Conference and Exposition on Optical Communications*, p. Th.12.LeSaleve.3, Optica Publishing Group, 2011.
- [43] S. C. Mao, S. H. Tao, Y. L. Xu, X. W. Sun, M. B. Yu, G. Q. Lo, and D. L. Kwong, "Low propagation loss silicon optical waveguide prepared by optimal low-hydrogen module," *Opt. Express*, vol. 16, pp. 20809–20816, Dec 2008.
- [44] H. E. Dirani, L. Youssef, C. Petit-Etienne, S. Kerdiles, P. Grosse, C. Monat, E. Pargon, and C. Sciancalepore, "Ultralow-loss tightly confining  $\text{Si}_3\text{N}_4$  waveguides and high-q microresonators," *Opt. Express*, vol. 27, pp. 30726–30740, Oct 2019.
- [45] J. M. De Teresa, *Nanofabrication*. 2053-2563, IOP Publishing, 2020.
- [46] C. Mack, *Fundamental Principles of Optical Lithography*. John Wiley & Sons, Ltd, 2007.
- [47] S. Landis, *Lithography*. John Wiley & Sons, Inc., 2013.
- [48] A. Lugnan, S. G.-C. Carrillo, C. D. Wright, and P. Bienstman, "Rigorous dynamic model of a silicon ring resonator with phase change material for a neuromorphic node," *Opt. Express*, vol. 30, pp. 25177–25194, Jul 2022.
- [49] M. Weinhold and P. J. Klar, "Patterning 2d materials for devices by mild lithography," *RSC Adv.*, vol. 11, pp. 29887–29895, 2021.
- [50] V. Vakarın, D. Melati, T. T. D. Dinh, X. Le Roux, W. K. K. Kan, C. Dupr , B. Szelag, S. Monfray, F. Boeuf, P. Cheben, E. Cassan, D. Marris-Morini, L. Vivien, and C. A. Alonso-Ramos, "Metamaterial-engineered silicon beam splitter fabricated with deep uv immersion lithography," *Nanomaterials*, vol. 11, no. 11, 2021.

- [51] T. Meany, "Femtosecond-laser direct-written waveguides produce quantum circuits in glass," *Laser Focus World*, vol. 50, pp. 25–27, 07 2014.
- [52] L. Li, W. Kong, and F. Chen, "Femtosecond laser-inscribed optical waveguides in dielectric crystals: a concise review and recent advances," *Advanced Photonics*, vol. 4, no. 2, p. 024002, 2022.
- [53] Y. Shen, N. C. Harris, S. Skirlo, M. Prabhu, T. Baehr-Jones, M. Hochberg, X. Sun, S. Zhao, H. Larochelle, D. Englund, and M. Soljačić, "Deep learning with coherent nanophotonic circuits," *Nature Photonics*, vol. 11, pp. 441–446, 2017.
- [54] J. Feldmann, N. Youngblood, M. Karpov, H. Gehring, X. Li, T. J. Kippenberg, W. H. P. Pernice, and H. Bhaskaran, "Parallel convolutional processing using an integrated photonic tensor core," *Nature*, vol. 589, p. 52–58, 2021.
- [55] N. Psaila, R. Thomson, H. Bookey, A. Kar, N. Chiodo, R. Osellame, G. Cerullo, G. Brown, A. Jha, and S. Shen, "Femtosecond laser inscription of optical waveguides in bismuth ion doped glass," *Opt. Express*, vol. 14, pp. 10452–10459, Oct 2006.
- [56] A. Arriola, S. Gross, N. Jovanovic, N. Charles, P. G. Tuthill, S. M. Olaizola, A. Furbach, and M. J. Withford, "Low bend loss waveguides enable compact, efficient 3d photonic chips," *Opt. Express*, vol. 21, pp. 2978–2986, Feb 2013.
- [57] F. Chen and J. R. V. de Aldana, "Optical waveguides in crystalline dielectric materials produced by femtosecond-laser micromachining," *Laser & Photonics Reviews*, vol. 8, no. 2, pp. 251–275, 2014.
- [58] C. Grivas, "Optically pumped planar waveguide lasers: Part ii: Gain media, laser systems, and applications," *Progress in Quantum Electronics*, vol. 45-46, pp. 3–160, 2016.
- [59] R. Martínez-Vazquez, R. Osellame, G. Cerullo, R. Ramponi, and O. Svelto, "Fabrication of photonic devices in nanostructured glasses by femtosecond laser pulses," *Opt. Express*, vol. 15, pp. 12628–12635, Oct 2007.
- [60] G. Corrielli, S. Atzeni, S. Piacentini, I. Pitsios, A. Crespi, and R. Osellame, "Symmetric polarization-insensitive directional couplers fabricated by femtosecond laser writing," *Opt. Express*, vol. 26, pp. 15101–15109, Jun 2018.
- [61] L. A. Fernandes, J. R. Grenier, P. R. Herman, J. S. Aitchison, and P. V. S. Marques, "Femtosecond laser fabrication of birefringent directional couplers as polarization beam splitters in fused silica," *Opt. Express*, vol. 19, pp. 11992–11999, Jun 2011.
- [62] M. R. Vázquez, B. Sotillo, S. Rampini, V. Bharadwaj, B. Gholipour, P. Fernández, R. Ramponi, C. Soci, and S. M. Eaton, "Femtosecond laser inscription of nonlinear photonic circuits in gallium lanthanum sulphide glass," *Journal of Physics: Photonics*, vol. 1, p. 015006, dec 2018.
- [63] P. Vildoso, R. A. Vicencio, and J. Petrovic, "Ultra-low-loss broadband multiport optical splitters," *Opt. Express*, vol. 31, pp. 12703–12716, Apr 2023.
- [64] Y. Jia, S. Wang, and F. Chen, "Femtosecond laser direct writing of flexibly configured waveguide geometries in optical crystals: fabrication and application," *Opto-Electron Adv*, vol. 3, no. 10, pp. 190042–1–190042–12, 2020.

- [65] Y. Yao, W. Wang, and B. Zhang, "Designing mmi structured beam-splitter in linbo3 crystal based on a combination of ion implantation and femtosecond laser ablation," *Opt. Express*, vol. 26, pp. 19648–19656, Jul 2018.
- [66] Y. Jia and F. Chen, "Compact solid-state waveguide lasers operating in the pulsed regime: a review," *Chin. Opt. Lett.*, vol. 17, p. 012302, Jan 2019.
- [67] M. Ams, G. Marshall, P. Dekker, J. Piper, and M. Withford, "Ultrafast laser written active devices," *Laser & Photonics Reviews*, vol. 3, no. 6, pp. 535–544, 2009.
- [68] Y. Duan, P. Dekker, M. Ams, G. Palmer, and M. J. Withford, "Time dependent study of femtosecond laser written waveguide lasers in yb-doped silicate and phosphate glass," *Opt. Mater. Express*, vol. 5, pp. 416–422, Feb 2015.
- [69] R. R. Thomson, H. T. Bookey, N. D. Psaila, A. Fender, S. Campbell, W. N. MacPherson, J. S. Barton, D. T. Reid, and A. K. Kar, "Ultrafast-laser inscription of a three dimensional fan-out device for multicore fiber coupling applications," *Opt. Express*, vol. 15, pp. 11691–11697, Sep 2007.
- [70] R. S. Luís, G. Rademacher, B. J. Puttnam, T. A. Eriksson, H. Furukawa, A. Ross-Adams, S. Gross, M. Withford, N. Riesen, Y. Sasaki, K. Saitoh, K. Aikawa, Y. Awaji, and N. Wada, "1.2 pb/s throughput transmission using a 160  $\mu\text{m}$  cladding, 4-core, 3-mode fiber," *Journal of Lightwave Technology*, vol. 37, no. 8, pp. 1798–1804, 2019.
- [71] L. Sansoni, F. Sciarrino, G. Vallone, P. Mataloni, A. Crespi, R. Ramponi, and R. Osellame, "Two-particle bosonic-fermionic quantum walk via integrated photonics," *Phys. Rev. Lett.*, vol. 108, p. 010502, Jan 2012.
- [72] F. Flamini, N. Spagnolo, and F. Sciarrino, "Photonic quantum information processing: a review," *Reports on Progress in Physics*, vol. 82, p. 016001, nov 2018.
- [73] G. D. Marshall, A. Politi, J. C. F. Matthews, P. Dekker, M. Ams, M. J. Withford, and J. L. O'Brien, "Laser written waveguide photonic quantum circuits," *Opt. Express*, vol. 17, pp. 12546–12554, Jul 2009.
- [74] T. A. Birks, I. Gris-Sánchez, S. Yerolatsitis, S. G. Leon-Saval, and R. R. Thomson, "The photonic lantern," *Adv. Opt. Photon.*, vol. 7, pp. 107–167, Jun 2015.
- [75] M. Lenzner, J. Krüger, S. Sartania, Z. Cheng, C. Spielmann, G. Mourou, W. Kautek, and F. Krausz, "Femtosecond optical breakdown in dielectrics," *Phys. Rev. Lett.*, vol. 80, pp. 4076–4079, May 1998.
- [76] M. Bellec, A. Royon, B. Bousquet, K. Bourhis, M. Treguer, T. Cardinal, M. Richardson, and L. Canioni, "Beat the diffraction limit in 3d direct laser writing in photosensitive glass," *Opt. Express*, vol. 17, pp. 10304–10318, Jun 2009.
- [77] E. N. Glezer, M. Milosavljevic, L. Huang, R. J. Finlay, T.-H. Her, J. P. Callan, and E. Mazur, "Three-dimensional optical storage inside transparent materials," *Opt. Lett.*, vol. 21, pp. 2023–2025, Dec 1996.
- [78] S. K. Sundaram and E. Mazur, "Inducing and probing non-thermal transitions in semiconductors using femtosecond laser pulses," *Nature Materials*, vol. 1, pp. 217–224, 2002.

- [79] K. M. Davis, K. Miura, N. Sugimoto, and K. Hirao, "Writing waveguides in glass with a femtosecond laser," *Opt. Lett.*, vol. 21, pp. 1729–1731, Nov 1996.
- [80] J. Burghoff, S. Nolte, and A. Tünnermann, "Origins of waveguiding in femtosecond laser-structured linbo<sub>3</sub>," *Applied Physics A*, vol. 89, pp. 127–132, 2007.
- [81] B. McMillen, C. Athanasiou, and Y. Bellouard, "Femtosecond laser direct-write waveplates based on stress-induced birefringence," *Opt. Express*, vol. 24, pp. 27239–27252, Nov 2016.
- [82] D. Tan, B. Zhang, and J. Qiu, "Ultrafast laser direct writing in glass: Thermal accumulation engineering and applications," *Laser & Photonics Reviews*, vol. 15, no. 9, p. 2000455, 2021.
- [83] C. Cai and J. Wang, "Femtosecond laser-fabricated photonic chips for optical communications: A review," *Micromachines*, vol. 13, no. 4, 2022.
- [84] T. Feng, P. K. Sahoo, F. R. Arteaga-Sierra, C. Dorrer, and J. Qiao, "Pulse-propagation modeling and experiment for femtosecond-laser writing of waveguide in nd:yag," *Crystals*, vol. 9, no. 8, 2019.
- [85] C. Cheng, C. Romero, J. R. V. R. V. de Aldana, and F. Chen, "Superficial waveguide splitters fabricated by femtosecond laser writing of LiTaO<sub>3</sub> crystal," *Optical Engineering*, vol. 54, no. 6, p. 067113, 2015.
- [86] S. Gross and M. J. Withford, "Ultrafast-laser-inscribed 3d integrated photonics: challenges and emerging applications," *Nanophotonics*, vol. 4, no. 3, pp. 332–352, 2015.
- [87] S. Heiskanen, Z. Geng, J. Mastomäki, and I. J. Maasilta, "Nanofabrication on 2d and 3d topography via positive-tone direct-write laser lithography," *Advanced Engineering Materials*, vol. 22, no. 2, p. 1901290, 2020.
- [88] R. Osellame, G. Cerullo, and R. Ramponi, *Femtosecond Laser Micromachining. Photonic and Microfluidic Devices in Transparent Materials*, vol. 123. Springer Heidelberg Dordrecht London New York, 2012.
- [89] R. R. Gattass and E. Mazur, "Femtosecond laser micromachining in transparent materials," *Nature Photonics*, vol. 2, pp. 219–225, 2008.
- [90] J. Siegel, J. M. Fernández-Navarro, A. García-Navarro, V. Diez-Blanco, O. Sanz, J. Solis, F. Vega, and J. Armengol, "Waveguide structures in heavy metal oxide glass written with femtosecond laser pulses above the critical self-focusing threshold," *Applied Physics Letters*, vol. 86, p. 121109, 03 2005.
- [91] X. Li, N. Youngblood, C. Rios, Z. Cheng, C. D. Wright, W. H. Pernice, and H. Bhaskaran, "Fast and reliable storage using a 5bit, nonvolatile photonic memory cell," *Optica*, vol. 6, pp. 1–6, Jan 2019.
- [92] C. Ríos, M. Stegmaier, P. Hosseini, C. D. Wang, Di and Wright, H. Bhaskaran, and W. H. P. Pernice, "Integrated all-photonic non-volatile multi-level memory," *Nature Photonics*, vol. 9, no. 6167, pp. 725–732, 2015.

- [93] T. Herr, V. Brasch, J. D. Jost, C. Y. Wang, N. M. Kondratiev, M. L. Gorodetsky, and T. J. Kippenberg, "Temporal solitons in optical microresonators," *Nature Photonics*, vol. 8, pp. 145–152, 2014.
- [94] A. S. Raja, A. S. Voloshin, H. Guo, S. E. Agafonova, J. D. Jost, M. L. Gorodetsky, and T. J. Kippenberg, "Electrically pumped photonic integrated soliton microcomb," *Nature Communications*, vol. 10, p. 680, 2019.
- [95] P. Trocha, M. Karpov, D. Ganin, M. H. P. Pfeiffer, A. Kordts, S. Wolf, J. Krockenberger, P. Marin-Palomo, C. Weimann, S. Randel, W. Freude, T. J. Kippenberg, and C. Koos, "Ultrafast optical ranging using microresonator soliton frequency combs," *Science*, vol. 359, no. 6378, pp. 887–891, 2018.
- [96] A. Silva, F. Monticone, G. Castaldi, V. Galdi, A. Alù, and N. Engheta, "Performing mathematical operations with metamaterials," *Science*, vol. 343, no. 6167, pp. 160–163, 2014.
- [97] B. Xu, Y. Huang, Y. Fang, Z. Wang, S. Yu, and R. Xu, "Recent progress of neuromorphic computing based on silicon photonics: Electronic-photonic co-design, device, and architecture," *Photonics*, vol. 9, no. 10, 2022.
- [98] V. Bangari, B. A. Marquez, H. Miller, A. N. Tait, M. A. Nahmias, T. F. de Lima, H.-T. Peng, P. R. Prucnal, and B. J. Shastri, "Digital electronics and analog photonics for convolutional neural networks (deap-cnns)," *IEEE Journal of Selected Topics in Quantum Electronics*, vol. 26, no. 1, pp. 1–13, 2020.
- [99] B. J. Shastri, A. N. Tait, T. Ferreira de Lima, H. Pernice, Wolfram H. P. and Bhaskaran, C. D. Wright, and P. R. Prucnal, "Photonics for artificial intelligence and neuromorphic computing," *Nature Photonics*, vol. 15, pp. 102–114, 2021.
- [100] D. A. B. Miller, "Self-configuring universal linear optical component," *Photon. Res.*, vol. 1, pp. 1–15, Jun 2013.
- [101] M. H. P. Pfeiffer, A. Kordts, V. Brasch, M. Zervas, M. Geiselmann, J. D. Jost, and T. J. Kippenberg, "Photonic damascene process for integrated high-q microresonator based nonlinear photonics," *Optica*, vol. 3, pp. 20–25, Jan 2016.
- [102] J. Liu, A. S. Raja, M. Karpov, B. Ghadiani, M. H. P. Pfeiffer, B. Du, N. J. Engelsen, H. Guo, M. Zervas, and T. J. Kippenberg, "Ultralow-power chip-based soliton microcombs for photonic integration," *Optica*, vol. 5, pp. 1347–1353, Oct 2018.
- [103] S. Maruo, K. Ikuta, and H. Korogi, "Force-controllable, optically driven micromachines fabricated by single-step two-photon microstereolithography," *Journal of Microelectromechanical Systems*, vol. 12, no. 5, pp. 533–539, 2003.
- [104] Q. Ji, J. Moughames, X. Chen, G. Fang, J. J. Huaroto, V. Laude, G. Ulliac, C. Clévy, P. Lutz, K. Rabenorosoa, V. Guelpa, A. Spangenberg, J. Liang, A. Mosset, and M. Kadic, "4d thermomechanical metamaterials for soft microrobotics," *Communications Materials*, vol. 2, no. 93, p. 2662, 2021.
- [105] J. D. Pitts, P. J. Campagnola, G. A. Epling, and S. L. Goodman, "Submicron multiphoton free-form fabrication of proteins and polymers: Studies of reaction efficiencies and applications in sustained release," *Macromolecules*, vol. 33, no. 5, pp. 1514–1523, 2000.

- [106] P. Dietrich, M. Blaicher, I. Reuter, M. Billah, T. Hoose, A. Hofmann, C. Caer, R. Dangel, B. Offrein, U. Troppenz, M. Moehrle, W. Freude, and C. Koos, "In situ 3d nanoprinting of free-form coupling elements for hybrid photonic integration," *Nature Photonics*, vol. 12, no. 4, pp. 241–247, 2018.
- [107] H. B. Sun and S. Kawata, *Two-Photon Photopolymerization and 3D Lithographic Microfabrication*. Springer-Verlag, 2004.
- [108] T. Ergin, N. Stenger, P. Brenner, J. B. Pendry, and M. Wegener, "Three-Dimensional Invisibility Cloak at Optical Wavelengths," *Science*, vol. 328, pp. 337–339, 4 2010.
- [109] S. Ristok, S. Thiele, A. Toulouse, A. M. Herkommer, and H. Giessen, "Stitching-free 3d printing of millimeter-sized highly transparent spherical and aspherical optical components," *Optical Materials Express*, vol. 10, p. 2370, 10 2020.
- [110] N. Lindenmann, G. Balthasar, D. Hillerkuss, R. Schmogrow, M. Jordan, J. Leuthold, W. Freude, and C. Koos, "Photonic wire bonding: a novel concept for chip-scale interconnects," *Opt. Express*, vol. 20, pp. 17667–17677, Jul 2012.
- [111] X. Porte, N. U. Dinc, J. Moughames, G. Panusa, C. Juliano, M. Kadic, C. Moser, D. Brunner, and D. Psaltis, "Direct (3+1)d laser writing of graded-index optical elements," *Optica*, vol. 8, pp. 1281–1287, Oct 2021.
- [112] T. Gissibl, S. Thiele, A. Herkommer, and H. Giessen, "Two-photon direct laser writing of ultracompact multi-lens objectives," *Nature Photonics*, vol. 10, no. 8, pp. 554–560, 2016.
- [113] N. U. Dinc, J. Lim, E. Kakkava, C. Moser, and D. Psaltis, "Computer generated optical volume elements by additive manufacturing," *Nanophotonics*, vol. 9, no. 13, pp. 4173–4181, 2020.
- [114] A. Grabulosa, J. Moughames, X. Porte, M. Kadic, and D. Brunner, "Additive 3d photonic integration that is cmos compatible," *Nanotechnology*, vol. 34, p. 322002, may 2023.
- [115] J. Moughames, X. Porte, L. Larger, M. Jacquot, M. Kadic, and D. Brunner, "3d printed multimode-splitters for photonic interconnects," *Optical Materials Express*, vol. 10, p. 2952, 11 2020.
- [116] G. Panusa, Y. Pu, J. Wang, C. Moser, and D. Psaltis, "Fabrication of sub-micron polymer waveguides through two-photon polymerization in polydimethylsiloxane," *Polymers*, vol. 12, no. 11, 2020.
- [117] M. R. Billah, M. Blaicher, T. Hoose, P.-I. Dietrich, P. Marin-Palomo, N. Lindenmann, A. Nestic, A. Hofmann, U. Troppenz, M. Moehrle, S. Randel, W. Freude, and C. Koos, "Hybrid integration of silicon photonics circuits and inp lasers by photonic wire bonding," *Optica*, vol. 5, pp. 876–883, Jul 2018.
- [118] A. Nestic, M. Blaicher, T. Hoose, A. Hofmann, M. Laueremann, Y. Kutuvantavida, M. Nöllenburg, S. Randel, W. Freude, and C. Koos, "Photonic-integrated circuits with non-planar topologies realized by 3d-printed waveguide overpasses," *Optics Express*, vol. 27, p. 17402, 6 2019.

- [119] M. Sartison, K. Weber, S. Thiele, L. Bremer, S. Fischbach, T. Herzog, S. Kolatschek, M. Jetter, S. Reitzenstein, A. Herkommer, P. Michler, S. L. Portalupi, and H. Giessen, "3d printed micro-optics for quantum technology: Optimised coupling of single quantum dot emission into a single-mode fibre," *Light: Advanced Manufacturing*, vol. 2, no. 1, p. 103, 2021.
- [120] J. Feldmann, K. Weber, S. Thiele, L. Bremer, S. Fischbach, T. Herzog, S. Kolatschek, M. Jetter, S. Reitzenstein, A. Herkommer, P. Michler, S. L. Portalupi, and H. Giessen, "Parallel convolutional processing using an integrated photonic tensor core," *Nature*, no. 589, p. 52–58, 2021.
- [121] J. Pyo, J. T. Kim, J. Lee, J. Yoo, and J. H. Je, "3d printed nanophotonic waveguides," *Advanced Optical Materials*, vol. 4, no. 8, pp. 1190–1195, 2016.
- [122] G. Della Valle, R. Osellame, and P. Laporta, "Micromachining of photonic devices by femtosecond laser pulses," *Journal of Optics A: Pure and Applied Optics*, vol. 11, p. 049801, 4 2009.
- [123] T. G. Tiecke, K. P. Nayak, J. D. Thompson, T. Peyronel, N. P. de Leon, V. Vuletić, and M. D. Lukin, "Efficient fiber-optical interface for nanophotonic devices," *Optica*, vol. 2, pp. 70–75, Feb 2015.
- [124] S. Khan, S. M. Buckley, J. Chiles, R. P. Mirin, S. W. Nam, and J. M. Shainline, "Low-loss, high-bandwidth fiber-to-chip coupling using capped adiabatic tapered fibers," *APL Photonics*, vol. 5, no. 5, p. 056101, 2020.
- [125] A. Nesic, M. Blaicher, E. Orlandini, T. Olariu, M. Paszkiewicz, F. Negrodo, P. Kraft, M. Sukhova, A. Hofmann, W. Dörfler, C. Rockstuhl, W. Freude, and C. Koos, "Transformation-optics modeling of 3d-printed freeform waveguides," *Opt. Express*, vol. 30, pp. 38856–38879, Oct 2022.
- [126] P. K. Gill and D. M. Marom, "Single mode, air-cladded optical waveguides supported by a nano-fin fabricated with direct laser writing," *Applied Sciences*, vol. 11, no. 14, 2021.
- [127] R. L. Gallawa and Y. Tu, "Analysis of circular bends in planar optical waveguides," *Fiber and Integrated Optics*, vol. 8, no. 2, pp. 87–97, 1989.
- [128] M. Montiel, A. S. Aguado, and E. Zaluska, "Topology in fractals," *Chaos, Solitons & Fractals*, vol. 7, no. 8, pp. 1187–1207, 1996.
- [129] P.-I. Dietrich, M. Blaicher, I. Reuter, M. Billah, T. Hoose, M. Moehrle, W. Freude, and C. Koos, "In situ 3d nanoprinting of free-form coupling elements for hybrid photonic integration," *Nature Photonics*, vol. 12, no. 4, p. 241–247, 2018.
- [130] Y. Hanai, J. Nishimura, and T. Kuroda, "Haar-like filtering for human activity recognition using 3d accelerometer," in *2009 IEEE 13th Digital Signal Processing Workshop and 5th IEEE Signal Processing Education Workshop*, pp. 675–678, 2009.
- [131] P. Viola and M. Jones, "Rapid object detection using a boosted cascade of simple features," in *Proceedings of the 2001 IEEE Computer Society Conference on Computer Vision and Pattern Recognition. CVPR 2001*, vol. 1, pp. I–I, 2001.

- [132] L. Alzubaidi, J. Zhang, A. J. Humaidi, A. Al-Dujaili, Y. Duan, O. Al-Shamma, J. Santamaría, M. A. Fadhel, M. Al-Amidie, and L. Farhan, "Review of deep learning: concepts, cnn architectures, challenges, applications, future directions," *Journal of Big Data*, vol. 8, p. 53, 2021.
- [133] S. Albawi, T. A. Mohammed, and S. Al-Zawi, "Understanding of a convolutional neural network," in *2017 International Conference on Engineering and Technology (ICET)*, pp. 1–6, 2017.
- [134] N. U. Dinc, A. Saba, J. Madrid-Wolff, C. Gigli, A. Boniface, C. Moser, and D. Psaltis, "From 3d to 2d and back again," *Nanophotonics*, vol. 12, no. 5, pp. 777–793, 2023.
- [135] N. Lindenmann, S. Dottermusch, M. L. Goedecke, T. Hoose, M. R. Billah, T. P. Onanuga, A. Hofmann, W. Freude, and C. Koos, "Connecting silicon photonic circuits to multicore fibers by photonic wire bonding," *J. Lightwave Technol.*, vol. 33, pp. 755–760, Feb 2015.
- [136] T. Vallaitis, S. Bogatscher, L. Alloatti, P. Dumon, R. Baets, M. L. Scimeca, I. Biaggio, F. Diederich, C. Koos, W. Freude, and J. Leuthold, "Optical properties of highly nonlinear silicon-organic hybrid (soh) waveguide geometries," *Opt. Express*, vol. 17, pp. 17357–17368, Sep 2009.
- [137] G. Shao, R. Hai, and C. Sun, "3D Printing Customized Optical Lens in Minutes," *Advanced Optical Materials*, vol. 8, no. 4, 2020.
- [138] C.-F. Lee, W.-F. Hsu, T.-H. Yang, and R.-J. Chung, "Three-dimensional (3d) printing implemented by computer-generated holograms for generation of 3d layered images in optical near field," *Photonics*, vol. 8, no. 7, 2021.
- [139] S.-C. Kim and E.-S. Kim, "Effective generation of digital holograms of three-dimensional objects using a novel look-up table method," *Appl. Opt.*, vol. 47, pp. D55–D62, Jul 2008.
- [140] H. Zheng, Y. Yu, T. Wang, and A. Asundi, "Computer-generated kinoforms of real-existing full-color 3d objects using pure-phase look-up-table method," *Optics and Lasers in Engineering*, vol. 50, no. 4, pp. 568–573, 2012. Computational Optical Measurement.
- [141] Y. Zhao, L. Cao, H. Zhang, D. Kong, and G. Jin, "Accurate calculation of computer-generated holograms using angular-spectrum layer-oriented method," *Opt. Express*, vol. 23, pp. 25440–25449, Oct 2015.
- [142] J. Jia, J. Si, and D. Chu, "Fast two-step layer-based method for computer generated hologram using sub-sparse 2d fast fourier transform," *Opt. Express*, vol. 26, pp. 17487–17497, Jun 2018.
- [143] D. E. Düzgün and K. Nadolny, "Continuous liquid interface production (CLIP) method for rapid prototyping," *Journal of Mechanical and Energy Engineering*, vol. 2, no. 1, pp. 5–12, 2018.
- [144] S. Kawata, H.-B. Sun, and K. Tanaka, Tomokazu and Takada, "Finer features for functional microdevices," *Nature*, vol. 412, pp. 697–698, 2001.

- [145] X. Chen, W. Liu, B. Dong, J. Lee, H. O. T. Ware, H. F. Zhang, and C. Sun, "High-Speed 3D Printing of Millimeter-Size Customized Aspheric Imaging Lenses with Sub 7 nm Surface Roughness," *Advanced Materials*, vol. 30, 5 2018.
- [146] C. R. Ocier, C. A. Richards, D. A. Bacon-Brown, K. C. Toussaint, L. L. Goddard, and P. V. Braun, "Direct laser writing of volumetric gradient index lenses and waveguides," *Light: Science and Applications*, vol. 9, no. 196, 2020.
- [147] C. A. Richards, C. R. Ocier, J. Zhu, L. L. Goddard, and P. V. Braun, "Toward the realization of subsurface volumetric integrated optical systems," *Applied Physics Letters*, vol. 119, no. 13, p. 130503, 2021.
- [148] T. Bückmann, N. Stenger, M. Kadic, J. Kaschke, A. Frölich, T. Kennerknecht, C. Eberl, M. Thiel, and M. Wegener, "Tailored 3d mechanical metamaterials made by dip-in direct-laser-writing optical lithography," *Advanced Materials*, vol. 24, no. 20, pp. 2710–2714, 2012.
- [149] D. E. Marschner, S. Pagliano, P.-H. Huang, and F. Niklaus, "A methodology for two-photon polymerization micro 3d printing of objects with long overhanging structures," *Additive Manufacturing*, vol. 66, p. 103474, 2023.
- [150] M. Mao, J. He, X. Li, B. Zhang, Q. Lei, Y. Liu, and D. Li, "The emerging frontiers and applications of high-resolution 3d printing," *Micromachines*, vol. 8, no. 4, 2017.
- [151] G. Korotcenkov and E. Rusu, "How to Improve the Performance of Porous Silicon-Based Gas and Vapor Sensors? Approaches and Achievements," *physica status solidi (a)*, vol. 216, no. 22, p. 1900348, 2019.
- [152] J. F. Bauters, M. L. Davenport, M. J. R. Heck, J. K. Doylend, A. Chen, A. W. Fang, and J. E. Bowers, "Silicon on ultra-low-loss waveguide photonic integration platform," *Opt. Express*, vol. 21, pp. 544–555, Jan 2013.
- [153] W. A. Zortman, D. C. Trotter, and M. R. Watts, "Silicon photonics manufacturing," *Opt. Express*, vol. 18, pp. 23598–23607, Nov 2010.
- [154] Y. Zou, S. Chakravarty, C.-J. Chung, X. Xu, and R. T. Chen, "Mid-infrared silicon photonic waveguides and devices," *Photon. Res.*, vol. 6, pp. 254–276, Apr 2018.
- [155] R. Martinez-Vazquez, R. Osellame, G. Cerullo, R. Ramponi, and O. Svelto, "Fabrication of photonic devices in nanostructured glasses by femtosecond laser pulses," *Opt. Express*, vol. 15, pp. 12628–12635, 10 2007.
- [156] M. Macias-Montero, F. Muñoz, and B. Sotillo, "Femtosecond laser induced thermophoretic writing of waveguides in silicate glass," *Scientific Reports*, vol. 11, p. 8390, 04 2021.
- [157] B. E. A. Saleh and M. C. Teich, *Fundamentals of photonics; 2nd ed.* Wiley series in pure and applied optics, New York, NY: Wiley, 2007.
- [158] K. Okamoto, *Fundamentals of Optical Waveguides (Second Edition)*. Burlington: Academic Press, second edition ed., 2006.
- [159] A. W. Snyder and J. D. Dove, *Optical Waveguide Theory*. Chapman and Hall, 1983.

- [160] D. Marcuse, *Theory of Dielectric Optical Waveguides (Second Edition)*. Academic Press, second edition ed., 1991.
- [161] C.-L. Chen, *Foundations for Guided-Wave Optics*. John Wiley and Sons, Ltd, second edition ed., 2006.
- [162] Z. Wang, J. Tu, S. Gao, Z. Li, C. Yu, and C. Lu, "Transmission and generation of orbital angular momentum modes in optical fibers," *Photonics*, vol. 8, no. 7, 2021.
- [163] G. F. R. Chen, J. R. Ong, and T. Y. L. Ang, "Broadband silicon-on-insulator directional couplers using a combination of straight and curved waveguide sections," *Scientific Reports*, vol. 7, p. 7246, 3 2017.
- [164] Y. Luo, Y. Yu, and M. Ye, "Integrated dual-mode 3db power coupler based on tapered directional coupler," *Scientific Reports*, vol. 6, p. 23516, 3 2016.
- [165] N. Riesen and J. D. Love, "Tapered velocity mode-selective couplers," *Journal of Lightwave Technology*, vol. 31, no. 13, pp. 2163–2169, 2013.
- [166] H.-B. Sun and S. Kawata, *Two-Photon Photopolymerization and 3D Lithographic Microfabrication*, pp. 169–273. Berlin, Heidelberg: Springer Berlin Heidelberg, 2004.
- [167] X. Wang, H. Yu, P. Li, Y. Zhang, Y. Wen, Y. Qiu, Z. Liu, Y. Li, and L. Liu, "Femtosecond laser-based processing methods and their applications in optical device manufacturing: A review," *Optics and Laser Technology*, vol. 135, p. 106687, 2021.
- [168] M. Malinauskas, A. Žukauskas, V. Purlys, K. Belazaras, A. Momot, D. Paipulas, R. Gadonas, A. Piskarskas, H. Gilbergs, A. Gaidukevičiūtė, I. Sakellari, M. Farsari, and S. Juodkazis, "Femtosecond laser polymerization of hybrid/integrated micro-optical elements and their characterization," *Journal of Optics*, vol. 12, p. 124010, nov 2010.
- [169] V. Hahn, F. Mayer, M. Thiel, and M. Wegener, "3-d laser nanoprinting," *Opt. Photon. News*, vol. 30, pp. 28–35, Oct 2019.
- [170] D. Perevoznic, R. Nazir, R. Kiyani, K. Kurselis, B. Koszarna, D. T. Gryko, and B. N. Chichkov, "High-speed two-photon polymerization 3d printing with a microchip laser at its fundamental wavelength," *Opt. Express*, vol. 27, pp. 25119–25125, Sep 2019.
- [171] S. Maruo and J. Fourkas, "Recent progress in multiphoton microfabrication," *Laser and Photonics Reviews*, vol. 2, no. 1-2, pp. 100–111, 2008.
- [172] W. Lin, D. Chen, and S.-C. Chen, "Emerging micro-additive manufacturing technologies enabled by novel optical methods," *Photon. Res.*, vol. 8, pp. 1827–1842, Dec 2020.
- [173] E. D. Lemma, B. Spagnolo, M. De Vittorio, and F. Pisanello, "Studying cell mechanobiology in 3d: The two-photon lithography approach," *Trends in Biotechnology*, vol. 37, no. 4, pp. 358–372, 2019.
- [174] A. J. G. Otuka, N. B. Tomazio, K. T. Paula, and C. R. Mendonça, "Two-photon polymerization: Functionalized microstructures, micro-resonators, and bio-scaffolds," *Polymers*, vol. 13, no. 12, 2021.

- [175] G. Panusa, Y. Pu, J. Wang, C. Moser, and D. Psaltis, "Photoinitiator-free multi-photon fabrication of compact optical waveguides in polydimethylsiloxane," *Opt. Mater. Express*, vol. 9, pp. 128–138, Jan 2019.
- [176] U. Streppel, P. Dannberg, C. Wächter, A. Bräuer, L. Fröhlich, R. Houbertz, and M. Popall, "New wafer-scale fabrication method for stacked optical waveguide interconnects and 3d micro-optic structures using photoresponsive (inorganic–organic hybrid) polymers," *Optical Materials*, vol. 21, no. 1-3, pp. 475–483, 2003.
- [177] M. Schmid, D. Ludescher, and H. Giessen, "Optical properties of photoresists for femtosecond 3d printing: refractive index, extinction, luminescence-dose dependence, aging, heat treatment and comparison between 1-photon and 2-photon exposure," *Opt. Mater. Express*, vol. 9, pp. 4564–4577, Dec 2019.
- [178] J. Madrid-Wolff, A. Boniface, D. Loterie, P. Delrot, and C. Moser, "Controlling light in scattering materials for volumetric additive manufacturing," *Advanced Science*, vol. 9, no. 22, p. 2105144, 2022.
- [179] G. D. Valle, R. Osellame, and P. Laporta, "Micromachining of photonic devices by femtosecond laser pulses," *Journal of Optics A: Pure and Applied Optics*, vol. 11, p. 013001, dec 2008.
- [180] X. Zhou, Y. Hou, and J. Lin, "A review on the processing accuracy of two-photon polymerization," *AIP Advances*, vol. 5, no. 3, p. 030701, 2015.
- [181] W. Chu, Y. Tan, P. Wang, J. Xu, W. Li, J. Qi, and Y. Cheng, "Centimeter-height 3d printing with femtosecond laser two-photon polymerization," *Advanced Materials Technologies*, vol. 3, no. 5, p. 1700396, 2018.
- [182] G. Berglund, A. Wisniowiecki, J. Gawedzinski, B. Applegate, and T. S. Tkaczyk, "Additive manufacturing for the development of optical/photonic systems and components," *Optica*, vol. 9, pp. 623–638, Jun 2022.
- [183] W. Li, "Single molecule cryo-fluorescence microscopy," *Semantic Scholar*, 2016.
- [184] R. Barakat, "Application of apodization to increase two-point resolution by the sparrow criterion. i. coherent illumination," *J. Opt. Soc. Am.*, vol. 52, pp. 276–283, Mar 1962.
- [185] J. Fischer and M. Wegener, "Three-dimensional optical laser lithography beyond the diffraction limit," *Laser & Photonics Reviews*, vol. 7, no. 1, pp. 22–44, 2013.
- [186] L. Yang, A. Münchinger, M. Kadic, V. Hahn, F. Mayer, E. Blasco, C. Barner-Kowollik, and M. Wegener, "On the schwarzschild effect in 3d two-photon laser lithography," *Advanced Optical Materials*, vol. 7, no. 22, p. 1901040, 2019.
- [187] L. J. Jiang, Y. S. Zhou, W. Xiong, Y. Gao, X. Huang, L. Jiang, T. Baldacchini, J.-F. Silvain, and Y. F. Lu, "Two-photon polymerization: investigation of chemical and mechanical properties of resins using raman microspectroscopy," *Opt. Lett.*, vol. 39, pp. 3034–3037, May 2014.
- [188] H.-B. Sun, K. Takada, M.-S. Kim, K.-S. Lee, and S. Kawata, "Scaling laws of voxels in two-photon photopolymerization nanofabrication," *Applied Physics Letters*, vol. 83, pp. 1104–1106, 08 2003.

- [189] M. Deubel, G. Von Freymann, M. Wegener, S. Pereira, K. Busch, and C. M. Soukoulis, "Direct laser writing of three-dimensional photonic-crystal templates for telecommunications," *Nature materials*, vol. 3, no. 7, pp. 444–447, 2004.
- [190] N. Anscombe, "Direct laser writing," *Nature Photonics*, vol. 4, no. 1, pp. 22–23, 2010.
- [191] L. Wang, G. Ulliac, B. Wang, J. A. Iglesias Martínez, K. K. Dudek, V. Laude, and M. Kadic, "3d auxetic metamaterials with elastically-stable continuous phase transition," *Advanced Science*, p. 2204721, 2022.
- [192] J. A. Iglesias Martínez, J. Moughames, G. Ulliac, M. Kadic, and V. Laude, "Three-dimensional phononic crystal with ultra-wide bandgap at megahertz frequencies," *Applied Physics Letters*, vol. 118, no. 6, p. 063507, 2021.
- [193] T. Frenzel, J. Köpfler, E. Jung, M. Kadic, and M. Wegener, "Ultrasound experiments on acoustical activity in chiral mechanical metamaterials," *Nature communications*, vol. 10, no. 1, pp. 1–6, 2019.
- [194] X. Chen, J. Moughames, Q. Ji, J. A. I. Martínez, H. Tan, G. Ulliac, V. Laude, and M. Kadic, "3d lightweight mechanical metamaterial with nearly isotropic inelastic large deformation response," *Journal of the Mechanics and Physics of Solids*, vol. 169, p. 105057, 2022.
- [195] X. Chen, Q. Ji, J. A. I. Martinez, H. Tan, G. Ulliac, V. Laude, and M. Kadic, "Closed tubular mechanical metamaterial as lightweight load-bearing structure and energy absorber," *Journal of the Mechanics and Physics of Solids*, vol. 167, p. 104957, 2022.
- [196] K. K. Dudek, J. A. I. Martínez, G. Ulliac, and M. Kadic, "Micro-scale auxetic hierarchical mechanical metamaterials for shape morphing," *Advanced Materials*, vol. 34, no. 14, p. 2110115, 2022.
- [197] Q. Ji, J. Moughames, X. Chen, G. Fang, J. J. Huaroto, V. Laude, J. A. I. Martínez, G. Ulliac, C. Clévy, P. Lutz, *et al.*, "4d thermomechanical metamaterials for soft microrobotics," *Communications Materials*, vol. 2, no. 1, pp. 1–6, 2021.
- [198] C. Kern, M. Kadic, and M. Wegener, "Experimental evidence for sign reversal of the hall coefficient in three-dimensional metamaterials," *Physical Review Letters*, vol. 118, no. 1, p. 016601, 2017.
- [199] E. Blasco, J. Müller, P. Müller, V. Trouillet, M. Schön, T. Scherer, C. Barner-Kowollik, and M. Wegener, "Fabrication of conductive 3d gold-containing microstructures via direct laser writing," *Advanced Materials*, vol. 28, no. 18, pp. 3592–3595, 2016.
- [200] F. Mayer, S. Richter, P. Hübner, T. Jabbour, and M. Wegener, "3d fluorescence-based security features by 3d laser lithography," *Advanced Materials Technologies*, vol. 2, no. 11, p. 1700212, 2017.
- [201] A. Münchinger, L.-Y. Hsu, F. Fűrniß, E. Blasco, and M. Wegener, "3d optomechanical metamaterials," *Materials Today*, vol. 59, pp. 9–17, 2022.
- [202] P. Kiefer, V. Hahn, E. Blasco, and M. Wegener, "Parallelizing direct laser writing: Multitasking on the nanoscale," in *Light-Matter Interactions Towards the Nanoscale*, pp. 323–324, Springer, 2022.

- [203] V. Hahn, P. Rietz, F. Hermann, P. Müller, C. Barner-Kowollik, T. Schlöder, W. Wenzel, E. Blasco, and M. Wegener, “Light-sheet 3d microprinting via two-colour two-step absorption,” *Nature Photonics*, vol. 16, no. 11, pp. 784–791, 2022.
- [204] v. Hahn, T. Messer, and N. Bojanowski, “Two-step absorption instead of two-photon absorption in 3D nanoprinting,” *Nature Photonics*, vol. 15, 12 2021.
- [205] K. Godineau, S. Lavernhe, and C. Tournier, “Calibration of galvanometric scan heads for additive manufacturing with machine assembly defects consideration,” *Additive Manufacturing*, vol. 26, pp. 250–257, 2019.
- [206] A. Selimis, V. Mironov, and M. Farsari, “Direct laser writing: Principles and materials for scaffold 3d printing,” *Microelectronic Engineering*, vol. 132, pp. 83–89, 2015. Micro and Nanofabrication Breakthroughs for Electronics, MEMS and Life Sciences.
- [207] K.-S. Lee, D.-Y. Yang, S. H. Park, and R. H. Kim, “Recent developments in the use of two-photon polymerization in precise 2d and 3d microfabrications,” *Polymers for Advanced Technologies*, vol. 17, no. 2, pp. 72–82, 2006.
- [208] A. Ovsianikov, X. Shizhou, M. Farsari, M. Vamvakaki, C. Fotakis, and B. N. Chichkov, “Shrinkage of microstructures produced by two-photon polymerization of zr-based hybrid photosensitive materials,” *Opt. Express*, vol. 17, pp. 2143–2148, Feb 2009.
- [209] C. Davidson and A. Feilzer, “Polymerization shrinkage and polymerization shrinkage stress in polymer-based restoratives,” *Journal of Dentistry*, vol. 25, no. 6, pp. 435–440, 1997.
- [210] Z. Zhang, P. Zhao, P. Lin, and F. Sun, “Thermo-optic coefficients of polymers for optical waveguide applications,” *Polymer*, vol. 47, pp. 4893–4896, 6 2006.
- [211] C. M. Rackson and R. R. McLeod, “Improving print accuracy and eliminating striations in volumetric additive manufacturing: a novel approach to tomographic optimization, and a latent image printing method,” in *3D Printed Optics and Additive Photonic Manufacturing III* (A. M. Herkommer, G. von Freymann, and M. Flury, eds.), vol. PC12135, p. PC1213503, International Society for Optics and Photonics, SPIE, 2022.
- [212] Y. Li, S. Park, M. McLamb, M. Lata, S. Schöche, D. Childers, I. D. Aggarwal, M. K. Poutous, G. Boreman, and T. Hofmann, “Uv to nir optical properties of ip-dip, ip-l, and ip-s after two-photon polymerization determined by spectroscopic ellipsometry,” *Opt. Mater. Express*, vol. 9, pp. 4318–4328, Nov 2019.
- [213] T. Gissibl, S. Wagner, J. Sykora, M. Schmid, and H. Giessen, “Refractive index measurements of photo-resists for three-dimensional direct laser writing,” *Opt. Mater. Express*, vol. 7, pp. 2293–2298, Jul 2017.
- [214] M. Hasan and S. Blair, “Maximizing transmittance in two-photon 3d printed materials for micro-optics in the visible,” *Opt. Mater. Express*, vol. 12, pp. 895–906, Mar 2022.
- [215] A. Grabulosa, J. Moughames, X. Porte, and D. Brunner, “Combining one and two photon polymerization for accelerated high performance (3 + 1)d photonic integration,” *Nanophotonics*, vol. 11, no. 8, pp. 1591–1601, 2022.

- [216] V. A. Amorim, J. M. Maia, D. Viveiros, and P. V. S. Marques, "Loss mechanisms of optical waveguides inscribed in fused silica by femtosecond laser direct writing," *Journal of Lightwave Technology*, vol. 37, pp. 2240–2245, 5 2019.
- [217] J. J. Witcher, W. J. Reichman, L. B. Fletcher, N. W. Troy, and D. M. Krol, "Thermal annealing of femtosecond laser written structures in silica glass," *Opt. Mater. Express*, vol. 3, pp. 502–510, Apr 2013.
- [218] C. Eschenbaum, D. Großmann, K. Dopf, S. Kettlitz, T. Bocksrocker, S. Valouch, and U. Lemmer, "Hybrid lithography: Combining UV-exposure and two photon direct laser writing," *Optics Express*, vol. 21, no. 24, p. 29921, 2013.
- [219] M. P. Lim, X. Guo, E. L. Grunblatt, G. M. Clifton, A. N. Gonzalez, and C. N. LaFratta, "Augmenting mask-based lithography with direct laser writing to increase resolution and speed," *Optics Express*, vol. 26, no. 6, p. 7085, 2018.
- [220] L. Yang, A. El-Tamer, U. Hinze, J. Li, Y. Hu, W. Huang, J. Chu, and B. N. Chichkov, "Parallel direct laser writing of micro-optical and photonic structures using spatial light modulator," *Optics and Lasers in Engineering*, vol. 70, pp. 26–32, 2015.
- [221] G. Son, S. Han, J. Park, K. Kwon, and K. Yu, "High-efficiency broadband light coupling between optical fibers and photonic integrated circuits," *Nanophotonics*, vol. 7, pp. 1845–1864, oct 2018.
- [222] A. Bozzola, L. Carroll, D. Gerace, I. Cristiani, and L. C. Andreani, "Optimising apodized grating couplers in a pure soi platform to -0.5 db coupling efficiency," *Opt. Express*, vol. 23, pp. 16289–16304, Jun 2015.
- [223] M. L. Dakss, L. Kuhn, P. F. Heidrich, and B. A. Scott, "Grating coupler for efficient excitation of optical guided waves in thin films," *Applied Physics Letters*, vol. 16, no. 12, pp. 523–525, 1970.
- [224] S. Peng and T. Tamir, "Directional blazing of waves guided by asymmetrical dielectric gratings," *Optics Communications*, vol. 11, no. 4, pp. 405–409, 1974.
- [225] C. H. Bulmer, S. K. Sheem, R. P. Moeller, and W. K. Burns, "High-efficiency flip-chip coupling between single-mode fibers and linbo3 channel waveguides," *Applied Physics Letters*, vol. 37, no. 4, pp. 351–353, 1980.
- [226] S. M. Spillane, T. J. Kippenberg, and K. J. Vahala, "Ultralow-threshold raman laser using a spherical dielectric microcavity," *Nature*, vol. 415, no. 4, pp. 621–623, 2002.
- [227] L. Collot, V. Lefèvre-Seguin, M. Brune, J. M. Raimond, and S. Haroche, "Very high-q whispering-gallery mode resonances observed on fused silica microspheres," *Europhysics Letters (EPL)*, vol. 23, pp. 327–334, aug 1993.
- [228] A. Dewanjee, J. N. Caspers, J. S. Aitchison, and M. Mojahedi, "Demonstration of a compact bilayer inverse taper coupler for si-photonics with enhanced polarization insensitivity," *Opt. Express*, vol. 24, pp. 28194–28203, Dec 2016.
- [229] T. Tsuchizawa, K. Yamada, H. Fukuda, T. Watanabe, J. ichi Takahashi, M. Takahashi, T. Shoji, E. Tamechika, S. Itabashi, and H. Morita, "Microphotonics devices based on silicon microfabrication technology," *IEEE Journal of Selected Topics in Quantum Electronics*, vol. 11, no. 1, pp. 232–240, 2005.

- [230] R. Marchetti, C. Lacava, L. Carroll, K. Gradkowski, and P. Minzioni, "Coupling strategies for silicon photonics integrated chips," *Photon. Res.*, vol. 7, pp. 201–239, Feb 2019.
- [231] C. P. Michael, M. Borselli, T. J. Johnson, C. Chrystal, and O. Painter, "An optical fiber-taper probe for wafer-scale microphotonic device characterization," *Opt. Express*, vol. 15, pp. 4745–4752, Apr 2007.
- [232] P. E. Barclay, K. Srinivasan, M. Borselli, and O. Painter, "Efficient input and output fiber coupling to a photonic crystal waveguide," *Opt. Lett.*, vol. 29, pp. 697–699, Apr 2004.
- [233] N. Riesen and J. D. Love, "Ultra-Broadband Tapered Mode-Selective Couplers for Few-Mode Optical Fiber Networks," *IEEE Photonics Technology Letters*, vol. 25, pp. 2501–2504, dec 2013.
- [234] R. Van Meter, T. D. Ladd, A. G. Fowler, and Y. Yamamoto, "Distributed quantum computation architecture using semiconductor nanophotonics," *International Journal of Quantum Information*, vol. 08, no. 01n02, pp. 295–323, 2010.
- [235] H. J. Kimble, "The quantum internet," *Nature*, vol. 453, pp. 1023–1020, 2008.
- [236] A. Grabulosa, X. Porte, E. Jung, J. Moughames, M. Kadic, and D. Brunner, "(3+1)d printed adiabatic 1-to-m broadband couplers and fractal splitter networks," *Opt. Express*, vol. 31, pp. 20256–20264, Jun 2023.
- [237] A. J. Littlefield, D. Xie, C. A. Richards, C. R. Ocier, H. Gao, J. F. Messinger, L. Ju, J. Gao, L. Edwards, P. V. Braun, and L. L. Goddard, "Enabling high precision gradient index control in subsurface multiphoton lithography," *ACS Photonics*, vol. 10, no. 9, pp. 3008–3019, 2023.
- [238] S. M. Eaton, M. L. Ng, T. Rafique, and P. R. Herman, "High refractive index contrast in fused silica waveguides by tightly focused, high-repetition rate femtosecond laser," in *Conference on Lasers and Electro-Optics/International Quantum Electronics Conference*, p. CFT3, Optica Publishing Group, 2009.
- [239] J. Lapointe, J.-P. Bérubé, Y. Ledemi, A. Dupont, V. Fortin, and R. Vallée, "Nonlinear increase, invisibility, and sign inversion of a localized fs-laser-induced refractive index change in crystals and glasses," *Advanced Materials*, vol. 9, no. 64, pp. 2047–7538, 2020.
- [240] R. N. Sheehan, S. Horne, and F. H. Peters, "The design of low-loss curved waveguides," *Optical and Quantum Electronics*, vol. 40, no. 14, pp. 1211–1218, 2008.
- [241] R. T. Schermer, "Mode scalability in bent optical fibers," *Opt. Express*, vol. 15, pp. 15674–15701, Nov 2007.
- [242] C. J. Oton, O. Lemonnier, M. Fournier, and C. Kopp, "Adiabatic bends in silicon multimode waveguides," in *2016 IEEE 13th International Conference on Group IV Photonics (GFP)*, pp. 108–109, 2016.
- [243] M. Bahadori, M. Nikdast, Q. Cheng, and K. Bergman, "Universal design of waveguide bends in silicon-on-insulator photonics platform," *Journal of Lightwave Technology*, vol. 37, no. 13, pp. 3044–3054, 2019.

- [244] G. Farin, "Algorithms for rational bézier curves," *Computer-Aided Design*, vol. 15, no. 2, pp. 73–77, 1983.
- [245] X. Jiang, H. Wu, and D. Dai, "Low-loss and low-crosstalk multimode waveguide bend on silicon," *Opt. Express*, vol. 26, pp. 17680–17689, Jun 2018.
- [246] D. S. Meek and D. J. Walton, "Clothoid spline transition spirals," *Mathematics of Computation*, vol. 59, no. 199, pp. 117–133, 1992.
- [247] T. Baghdasaryan, K. Vanmol, H. Thienpont, F. Berghmans, T. Geernaert, and J. V. Erps, "Design and two-photon direct laser writing of low-loss waveguides, tapers and s-bends," *Journal of Physics: Photonics*, vol. 3, p. 045001, aug 2021.
- [248] W. W. Chow and S. Reitzenstein, "Quantum-optical influences in optoelectronics—An introduction," *Applied Physics Reviews*, vol. 5, p. 041302, 10 2018.
- [249] C. Schneider, T. Heindel, A. Huggenberger, P. Weinmann, C. Kistner, M. Kamp, S. Reitzenstein, S. Höfling, and A. Forchel, "Single photon emission from a site-controlled quantum dot-micropillar cavity system," *Applied Physics Letters*, vol. 94, p. 111111, 03 2009.
- [250] J. P. Reithmaier, G. Sek, C. Hofmann, A. Löffler, C. Hofmann, S. Kuhn, S. Reitzenstein, L. V. Keldysh, V. D. Kulakovskii, T. L. Reinecke, and A. Forchel, "Strong coupling in a single quantum dot–semiconductor microcavity system," *Nature*, vol. 432, pp. 197–200, 2004.
- [251] S. M. Ulrich, C. Gies, S. Ates, J. Wiersig, S. Reitzenstein, C. Hofmann, A. Löffler, A. Forchel, F. Jahnke, and P. Michler, "Photon statistics of semiconductor microcavity lasers," *Phys. Rev. Lett.*, vol. 98, p. 043906, Jan 2007.
- [252] S. Reitzenstein and A. Forchel, "Quantum dot micropillars," *Journal of Physics D: Applied Physics*, vol. 43, p. 033001, jan 2010.
- [253] T. Heuser, J. Große, A. Kaganskiy, D. Brunner, and S. Reitzenstein, "Fabrication of dense diameter-tuned quantum dot micropillar arrays for applications in photonic information processing," *APL Photonics*, vol. 3, p. 116103, 09 2018.
- [254] L. Andreoli, X. Porte, T. Heuser, J. Große, B. Moeglen-Paget, L. Furfaro, S. Reitzenstein, and D. Brunner, "Optical pumping of quantum dot micropillar lasers," *Opt. Express*, vol. 29, pp. 9084–9097, Mar 2021.
- [255] K. Liu, C. R. Ye, S. Khan, and V. J. Sorger, "Review and perspective on ultrafast wavelength-size electro-optic modulators," *Laser & Photonics Reviews*, vol. 9, no. 2, pp. 172–194, 2015.
- [256] C. Henry, "Theory of the linewidth of semiconductor lasers," *IEEE Journal of Quantum Electronics*, vol. 18, no. 2, pp. 259–264, 1982.
- [257] D. Brunner, M. C. Soriano, C. R. Mirasso, and I. Fischer, "Parallel photonic information processing at gigabyte per second data rates using transient states," *Nature Communications*, vol. 4, p. 1364, 2013.
- [258] A. Löffler, J. P. Reithmaier, G. Sek, C. Hofmann, S. Reitzenstein, M. Kamp, and A. Forchel, "Semiconductor quantum dot microcavity pillars with high-quality factors and enlarged dot dimensions," *Applied Physics Letters*, vol. 86, p. 111105, 03 2005.

- [259] S. Reitzenstein, C. Hofmann, A. Gorbunov, M. Strauß, S. H. Kwon, C. Schneider, A. Löffler, S. Höfling, M. Kamp, and A. Forchel, "AlAsGaAs micropillar cavities with quality factors exceeding 150.000," *Applied Physics Letters*, vol. 90, p. 251109, 06 2007.
- [260] D. J. Eaglesham and M. Cerullo, "Dislocation-free stranski-krastanow growth of ge on si(100)," *Phys. Rev. Lett.*, vol. 64, pp. 1943–1946, Apr 1990.
- [261] S. Reitzenstein, C. Böckler, A. Bazhenov, A. Gorbunov, A. Löffler, M. Kamp, V. Kulakovskii, and A. Forchel, "Single quantum dot controlled lasing effects in high-q micropillar cavities," *Opt. Express*, vol. 16, pp. 4848–4857, Mar 2008.
- [262] S. Kreinberg, W. W. Chow, J. Wolters, C. Schneider, C. Gies, F. Jahnke, S. Höfling, M. Kamp, and S. Reitzenstein, "Emission from quantum-dot high-beta microcavities: transition from spontaneous emission to lasing and the effects of superradiant emitter coupling," *Light: Science & Applications*, vol. 6, pp. 4848–4857, 2017.
- [263] E. Perez, C. Haws, M. Davanco, J. Song, L. Sapienza, and K. Srinivasan, "Direct-laser-written polymer nanowire waveguides for broadband single photon collection from epitaxial quantum dots into a gaussian-like mode," *arXiv*, 2023.
- [264] N. Brown and T. Sandholm, "Libratus: The superhuman ai for no-limit poker," in *Proceedings of the Twenty-Sixth International Joint Conference on Artificial Intelligence, IJCAI-17*, pp. 5226–5228, 2017.
- [265] D. Miller and H. Ozaktas, "Limit to the bit-rate capacity of electrical interconnects from the aspect ratio of the system architecture," *Journal of Parallel and Distributed Computing*, vol. 41, no. 1, pp. 42–52, 1997.
- [266] L. Galdino, A. Edwards, W. Yi, E. Sillekens, Y. Wakayama, T. Gerard, W. S. Pelouch, S. Barnes, T. Tsuritani, R. I. Killey, D. Lavery, and P. Bayvel, "Optical fibre capacity optimisation via continuous bandwidth amplification and geometric shaping," *IEEE Photonics Technology Letters*, vol. 32, no. 17, pp. 1021–1024, 2020.
- [267] M. Thiel, A. Bertocini, T. Hoose, and M. Blaicher, "Advancement in two-photon grayscale lithography," in *Advanced Fabrication Technologies for Micro/Nano Optics and Photonics XVI* (G. von Freymann, E. Blasco, and D. Chanda, eds.), vol. PC12433, p. PC124330B, International Society for Optics and Photonics, SPIE, 2023.
- [268] T. Aderneuer, O. Fernández, and R. Ferrini, "Two-photon grayscale lithography for free-form micro-optical arrays," *Opt. Express*, vol. 29, pp. 39511–39520, Nov 2021.
- [269] D. Guéry-Odelin, A. Ruschhaupt, A. Kiely, E. Torrontegui, S. Martínez-Garaot, and J. G. Muga, "Shortcuts to adiabaticity: Concepts, methods, and applications," *Rev. Mod. Phys.*, vol. 91, p. 045001, Oct 2019.
- [270] S.-Y. Tseng, R.-D. Wen, Y.-F. Chiu, and X. Chen, "Short and robust directional couplers designed by shortcuts to adiabaticity," *Opt. Express*, vol. 22, pp. 18849–18859, Aug 2014.
- [271] V. Evangelakos, E. Paspalakis, and D. Stefanatos, "Efficient light transfer in coupled nonlinear triple waveguides using shortcuts to adiabaticity," *Scientific Reports*, vol. 13, p. 1368, 01 2023.

- [272] H.-C. Chung, S. Martínez-Garaot, X. Chen, J. G. Muga, and S.-Y. Tseng, "Shortcuts to adiabaticity in optical waveguides," *Europhysics Letters*, vol. 127, p. 34001, sep 2019.
- [273] C.-W. Shih, I. Limame, S. Krüger, C. C. Palekar, A. Koulas-Simos, D. Brunner, and S. Reitzenstein, "Low-threshold lasing of optically pumped micropillar lasers with Al<sub>0.2</sub>Ga<sub>0.8</sub>As/Al<sub>0.9</sub>Ga<sub>0.1</sub>As distributed Bragg reflectors," *Applied Physics Letters*, vol. 122, p. 151111, 04 2023.
- [274] A. Kaganskiy, S. Kreinberg, X. Porte, and S. Reitzenstein, "Micropillar lasers with site-controlled quantum dots as active medium," *Optica*, vol. 6, pp. 404–409, Apr 2019.
- [275] J. Große, M. von Helversen, A. Koulas-Simos, M. Hermann, and S. Reitzenstein, "Development of site-controlled quantum dot arrays acting as scalable sources of indistinguishable photons," *APL Photonics*, vol. 5, p. 096107, 09 2020.
- [276] K. H. R. Mojaver, B. Zhao, E. Leung, S. M. R. Safaee, and O. Liboiron-Ladouceur, "Addressing the programming challenges of practical interferometric mesh based optical processors," *Opt. Express*, vol. 31, pp. 23851–23866, Jul 2023.



